PLACE IN RETURN BOX to remove this checkout from your record.
TO AVOID FINES return on or before date due.
MAY BE RECALLED with earlier due date if requested.

DATE DUE	DATE DUE	DATE DUE

5/08 K:/Proj/Acc&Pres/CIRC/DateDue.indd

UNCOVERING THE SINGLE TOP: OBSERVATION OF ELECTROWEAK TOP QUARK PRODUCTION

By

Jorge Armando Benitez

A DISSERTATION

Submitted to
Michigan State University
in partial fulfillment of the requirements
for the Degree of

DOCTOR OF PHILOSOPHY

Physics and Astronomy

2009

ABSTRACT

UNCOVERING THE SINGLE TOP:
OBSERVATION OF ELECTROWEAK QUARK TOP PRODUCTION

By

Jorge Armando Benitez

The **top quark** is generally produced in quark and anti-quark pairs. However, the Standard Model also predicts the production of only one top quark which is mediated by the electroweak interaction, known as "Single Top." Single Top quark production is important because it provides a unique and direct way to measure the CKM matrix element V_{tb}, and can be used to explore physics possibilities beyond the Standard Model predictions.

This dissertation presents the results of the observation of Single Top using 2.3 fb^{-1} of Data collected with the DØ detector at the Fermilab Tevatron collider. The analysis includes the Single Top muon+jets and electron+jets final states and employs Boosted Decision Tress as a method to separate the signal from the background. The resulting Single Top cross section measurement is:

$$\sigma(p\bar{p} \rightarrow tb + X, tqb + X) = 3.74 \, ^{+0.95}_{-0.74} \text{ pb}, \quad (1)$$

where the errors include both statistical and systematic uncertainties. The probability to measure a cross section at this value or higher in the absence of signal is $p = 1.9 \times 10^{-6}$. This corresponds to a standard deviation Gaussian equivalence of 4.6. When combining this result with two other analysis methods, the resulting cross section measurement is:

$$\sigma(p\bar{p} \rightarrow tb + X, tqb + X) = 3.94 \pm 0.88 \text{ pb}, \quad (2)$$

and the corresponding measurement significance is 5.0 standard deviations.

This dissertation is dedicated to my family
and specially to my love, Catherine.

ACKNOWLEDGMENTS

I would like to thank all those who have been a part of this process and have guided me throughout my research. In particular, I would like to thank:

My advisor, Chip Brock, for his invaluable support and encouragement in the pursue of excellence in research in experimental high energy physics, and for his tremendous insights and words of wisdom that have guided me as a graduate student.

Reinhard Schwienhorst for sharing his stellar understanding of physics, for our many scientific discussions, and for his unique motivation techniques.

Dugan O'Neil for many useful BDT discussions and careful eye when examining results.

C.-P. Yuan and Q.-H Cao for inspiring me to study Single Top physics. It was an honor to have co-authored my first published paper with these esteemed theorists.

Carlos Avila for introducing me to high energy physics as an undergraduate student and for his influence on me to pursue graduate studies.

The members of my guidance committee for reviewing my dissertation: C.-P. Yuan, Reinhard Schwienhorst, Hendrik Schatz and S. D. Mahanti.

All the DØ collaborators, spokespeople, and Fermilab staff for keeping the experiment running, and permitting scientists to study the world around us. The L1 Calorimeter trigger group for their practical knowledge and formidable work, specially to Dan and Philippe for sharing their engineering methods and expertise with me.

The Single Top group, for carrying through this very complex endeavor. The conveners, Ann, Cecilia, and Reinhard for their unique perspectives, and for setting the bar high to make this analysis possible. Special thanks to Dag for his commitment to BDT, and to my fellow analyzers, Monica, Andres, Zhiyi, Thomas, Aran, Yann, Supriya, Liang, Ernest, Gustavo, and Ike for their dedication, and for always burning the midnight oil.

Michigan State University and the Department of Physics and Astronomy, for

providing me with a wonderful and memorable grad school experience. To all the PA staff, especially Brenda and Debbie for always being helpful.

All my friends who have made my grad school years unforgettable and for giving me many good (and sometimes much needed) laughs. To my friends in Colombia for all their support and to my friends in the US who have become my extended family. Special thanks to Monica, Joel, Sergio, Khang, Luis Carlos, Fernando, Monica, Dag, Fredy, Rodrigo, Diego, Roshan, Clari, Guille, Betta, Javi, Ricardin, Charly, Andresito, Duong, Tyler, Sensei Laurie.

My family for their unconditional support and sacrifices that have allowed me to grow not only as a scientist but as a human being. A mi padres por su amor, dedicación, e incalculables sacrificios que me han permitido seguir adelante en la vida, y porque que pesar de estar lejos, siempre han estado conmigo. A mi madre por su entusiasmo y ternura hacia sus hijos. A mi padre por ser ejemplo de abnegación y tenacidad. My hermanito, for being my best buddy and for always being there to share adventures and to talk, talk, and talk. To my family in Canada, mom and dad, Cris, Dan, Rob and Primo for all the love and warmth you have always given me, especially mom Ferrari for her care and genuine interest in science. A mis abuelitos por su cariño y por ser ejemplos de vida, y a todos mis tíos, tías, primos y primas, por tantos momentos felices compartidos. Los llevo a todos en mi corazon.

My lovely wife, Cati, for being my tower of strength during the difficult times in this journey, for her incredible understanding and care, for her patience in keeping up with all the traveling and crazy hours, for her immeasurable love, for being the chief editor of this work, and for being my inspiration in life.

Table of Contents

List of Tables

List of Figures

Images in this dissertation are presented in color.

Chapter 1

Introduction

The Standard Model of elementary particles has been successful at describing the building blocks of nature and their interactions. The top quark is the currently heaviest component of the Standard Model. With a mass close to that of a gold atom, the top quark was theoretically predicted in 1973 [26], but it was not until 1995 that it was discovered at the Tevatron collider at Fermilab. Fermilab is the only place in the world where top quark physics studies can be made, and where the production of top quarks, by means of the electroweak interaction, was recently announced [27, 28].

Electroweak top quark production is also known as "Single Top" because only one top quark is produced in the final state. Single Top serves as an important validation tool for the Standard Model as well as a window to new physics. In addition, Single Top is one of the backgrounds for many reactions including the missing particle of the Standard Model, the Higgs boson. There are various computational challenges related to Single Top searches, including advanced techniques to separate small signals from difficult-to-discriminate backgrounds. This will be a common task during future analyses in the experiments at the Large Hadron Collider (LHC). To properly "observe" the interactions that take place at Fermilab, a complex detection system is required. Fermilab has two main detector systems, CDF and DØ. The analysis

presented in this dissertation accounts for the seach for Single Top with the latter.

In the past five years at DØ, Single Top has been the subject of many doctoral dissertations [29, 30, 31, 32, 33, 34, 35, 36] and more recently [37, 38, 39]. This dissertation continues from this previous work and presents the results of the research I conducted, together with DØ collaborators at Fermilab, that led to the ground-breaking discovery of Single Top production. For Single Top, the signal-over-background ratio is of the order of 10^{-3}, thereby requiring that all the possible information from known well-modelled variables be obtained. In this study, I use the multivariate technique known as Boosted Decision Trees (BDT) to analyze Single Top signal. A decision tree (DT) is an algorithm that can be used to classify events as signal or background, and is built by recursively splitting a sample into two disjointed subsets. Each split is based on a selection cut that maximizes the signal-to-background ratio of the resulting subsets. The separation generated by the DT is then enlarged by a technique called Boosting, for which a series of trees is generated that increasingly gives more importance to events that are difficult to classify.

The Single Top signal and its backgrounds are modeled using Monte Carlo techniques. This modeling is based on the current particle physics theory, which also includes a complete simulation of the particles interaction with the detector. All of the BDT training is performed using the Monte Carlo samples, while the collected data in the detector is only used in the final measurements.

This dissertation is organized as follows: Chapter 2 gives the theoretical grounds for Single Top quark production; Chapter 3 presents some of the work I completed, together with the theory group at Michigan State University, where the influence of NLO correction to the Single Top kinematical distributions and cross section are explored; Chapter 4 introduces the experimental facilities at Fermilab and the DØ detector; Chapter 5 presents a discussion on particle identification using the available experimental tools; Chapter 6 contains a description of the data and the Monte Carlo

samples used in the Single Top analysis together with the corrections applied to them; Chapter 7 describes the selection cuts applied to the Single Top samples and illustrates the agreement between the simulations and the data; Chapter 8 provides an explanation on Decision Tress, Boosting, and BDT optimization studies; Chapter 9 presents the uncertainties taken into consideration in the analysis, the measurements of the Single Top cross section, the V_{tb} matrix element, as well as the significance of the cross section measurement and Chapter 10 summarizes the results of the analysis and provides a future outlook for Single Top.

Both the Data and the Monte Carlo go through a very intricate processing procedure before they are used in any multivariate technique (such procedure is outlined in the flow chart in Figure 1.1). The flow chart allows us to visualize where in the processing of the samples all the corrections have relevance, the selection cuts are applied, and what samples are modified by some procedures and not by others. There are four main stages in the processing of the data and Monte Carlo. stage 1 is the processing of the samples into the Common Analysis Framework (CAF) format; stage 2 contains the general selection of the DØ V+jets group; stage 3 is the DØ Top group selection criteria; and the stage 4 consists of the corrections, reweightings, selections, and scale factors directly related to the DØ Single Top group.

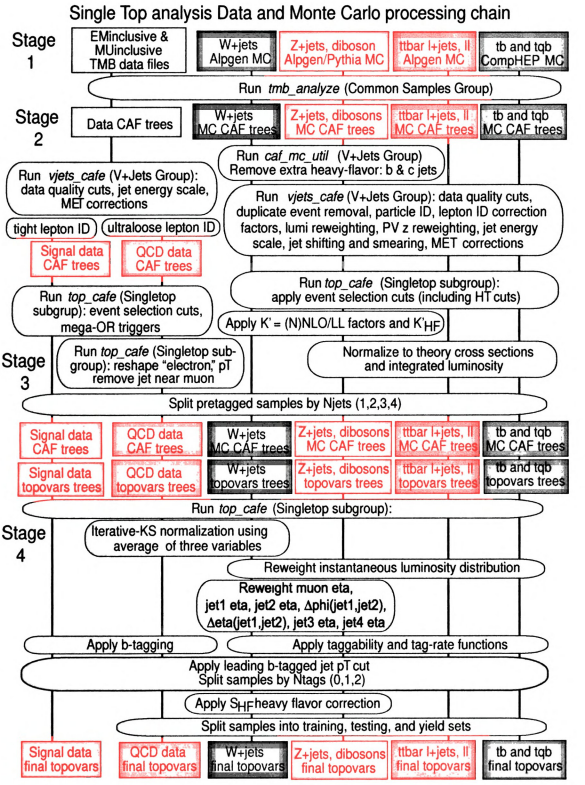

Figure 1.1: Flow chart of the stages of processing for data and MC files in the Single Top analysis.

Chapter 2

Theory

The particles we know today, and their interactions, have been successfully described by the Standard Model of Elementary Particles [40, 10, 41, 42]. For many years, scientists have conducted experiments to understand, confirm or contradict the Standard Model's predictions.

In 1995, the heaviest particle in the Standard Model was discovered at the Tevatron collider at Fermilab. This particle has a mass of approximately 173.1 ± 1.3 GeV/c^2 [43] and is now known as the "top quark" [44, 45].

C.P- Yuan et al [46] and S. Willenbrock [47] predicted a particular production mode of the top quark by means of the electro-weak interaction. This production mode has been recently observed at the Tevatron [27, 28] and is also known as Single Top quark production; the name derives from the fact that the top quark is produced singly rather than in pairs (quark-antiquark). The production of the Single Top quark is the topic of this dissertation.

2.1 Standard Model

The Standard Model is a non-abelian gauge theory that characterizes the building blocks of nature and their interaction. The Standard Model is built from the symme-

try group SU(3) × SU(2) × U(1), from which the electroweak and strong forces can be derived; the gravitational force is not part of the model.

The components of the Standard Model can be grouped into "particles of matter" and "mediators": 24 particles of matter, and four mediators. The particles of matter can be classified into 6 leptons and 6 quarks together with their respective antimatter partners. All of the matter particles have spin 1/2 while the mediators have spin 1. Figure 2.1 shows a cartoon representation of all particles and their mediators.

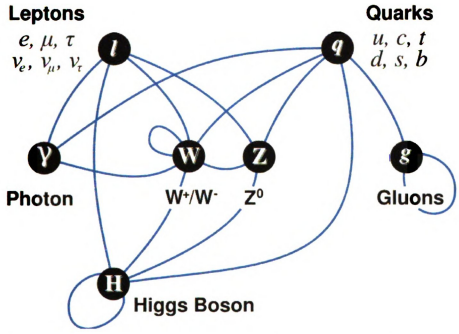

Figure 2.1: Summary of the particles and their interactions [8].

All the Standard Model particles are summarized in Table 2.1. The quarks and the leptons can be grouped into three generations. The first generation contains the lightest components. In addition, quarks form baryons (3-quark composites, i.e. protons and neutrons) and mesons (quark-antiquark composites).

The Standard Model explains the interaction of particles by means of the mediators which are exchanged when the interaction occurs. The electromagnetic inter-

	Quark			Lepton		
Generation	Flavor	Charge	Mass [MeV/c^2]	Flavor	Charge	Mass [MeV/c^2]
I	Up (u)	$+2/3e$	1.5 to 3.0	Electron (e)	$-e$	0.511
	Down (d)	$-1/3e$	3.0 to 7.0	Neutrino (ν_e)	0	$< 2.0 \times 10^{-6}$
II	Charm (c)	$+2/3e$	1.25×10^3	Muon (μ)	$-e$	0.511
	Strange (s)	$-1/3e$	80-130	neutrino (ν_μ)	0	$< 1.7 \times 10^{-4}$
III	Top (t)	$+2/3e$	171.4×10^3	Tau (τ)	$-e$	1777
	Bottom (b)	$-1/3e$	4.7×10^3	Neutrino (ν_τ)	0	< 15.5

Table 2.1: Elementary Particles and their properties, all particles have spin 1/2. Where, $e = 1.602 \times 10^{-19}\ C$ is the magnitude of the electron charge [1].

action mediator is the photon, the weak interaction mediators are the W^+, W^- and Z gauge bosons, and the gluons mediate the strong interactions. See Table 2.2 for a summary of the gauge bosons properties.

Force	Mediator boson	Charge	Mass [GeV/c^2]
Strong	Gluon (g)	0	0
Weak	$W^\pm$	$\pm\ e$	80.398 ± 0.025
Weak	Z	0	91.1876 ± 0.0021
ElectroMagnetic	Photon (γ)	0	0

Table 2.2: Gauge bosons properties [1].

There are a total of 19 free parameters in the SM, most of which have been established experimentally, Table 2.3.

Parameter	Value
Electron mass (m_e)	$0.510998910 \pm 0.000000013$ MeV/c^2
Muon mass (m_μ)	105.658367 ± 0.000004 MeV/c^2
Tau mass (m_τ)	1776.84 ± 0.17 MeV/c^2
Up quark mass (m_u)	1.5 to 3.3 MeV/c^2
Down quark mass (m_d)	3.5 to 6.0 MeV/c^2
Strange quark mass (m_s)	105^{+25}_{-35} MeV/c^2
Charm quark mass (m_c)	$1.27^{+0.07}_{-0.11}$ GeV/c^2
Bottom quark mass (m_b)	$4.20^{+0.17}_{-0.07}$ GeV/c^2
Top quark mass (m_t)	173.1 ± 1.3 GeV/c^2
CKM element V_{us}	0.2257 ± 0.0010
CKM element V_{cb}	$0.0415^{+0.0010}_{-0.0011}$
CKM element V_{ub}	0.00359 ± 0.00016
CKM CP-Violating Phase (δ)	$57^\circ \pm 8.7^\circ$
U(1) gauge coupling $\alpha^{-1}(M_Z)$	98.70 ± 0.21
SU(2) gauge coupling $\alpha'^{-1}(M_Z)$	30.10 ± 0.23
SU(3) gauge coupling $\alpha_S^{-1}(M_Z)$	9.25 ± 0.43
QCD Vacuum Angle (θ_{QCD})	0
Higgs quadratic coupling (μ)	Unknown
Higgs self-coupling strength (λ)	Unknown

Table 2.3: Free parameters of Standard Model [1, 2, 3, 4, 5]. The gauge couplings α_i are related to g_i used later in the text by $\alpha_i = \frac{g_i^2}{4\pi}$

.

2.1.1 Standard Model Lagrangian

2.1.1.1 Quantum Electrodynamics (QED)

The Lagrangian $\mathcal{L}$ for a massless electromagnetic field A_μ interacting with a spin-1/2 field ψ of mass m is given by:

$$\mathcal{L} = -\frac{1}{4}F_{\mu\nu}F^{\mu\nu} + \bar{\psi}(i\gamma^\mu D_\mu - m)\psi, \tag{2.1}$$

where $F^{\mu\nu}$ is the electromagnetic field tensor,

$$F_{\mu\nu} = \partial_\mu A_\nu - \partial_\nu A_\mu, \tag{2.2}$$

and D_μ is the covariant derivative,

$$D_\mu = \partial_\mu + ieA_\mu Q; \tag{2.3}$$

where Q is the charge operator and e is the electron charge.

This Lagrangian is invariant under local gauge transformations:

$$\psi(x) \rightarrow U(x)\psi(x), \qquad A_\mu \rightarrow A_\mu(x) + \partial_\mu\alpha(x), \tag{2.4}$$

with $U(x) = \exp(-ieQ\alpha(x))$, which for infinitesimal $\alpha(x)$:

$$\psi(x) \rightarrow (1 - ieQ\alpha(x)). \tag{2.5}$$

The invariance implies the conservation of the electric current J^μ_{em} and electric charge q[10]:

$$\partial_\mu J^\mu_{em} \qquad q = \int J^0_{em} d^3x \tag{2.6}$$

2.1.1.2 SU(2) symmetry

The Lagrangian of an internal symmetry group SU(2), such as the isospin, for spin-1/2 fields ψ is given by [10]:

$$\mathcal{L} = \bar{\psi}(i\gamma^{\mu}\partial_{\mu} - m)\psi, \tag{2.7}$$

where ψ transforms as a doublet in the isospin space, and it is required to be invariant under infinitesimal local gauge transformations:

$$\psi(x) \rightarrow [1 - ig\ \boldsymbol{\alpha}(x) \cdot \boldsymbol{T}]\psi(u), \tag{2.8}$$

where $\boldsymbol{\alpha}(x)$ is a vector in isospin space, and $\boldsymbol{T}$ [1] is the isospin operator, with the SU(2) generators as components.

The ψ-field part of the Lagrangian can be made invariant by introducing the covariant derivative D_{μ} :

$$D_{\mu} = \partial_{\mu} + ig\boldsymbol{W}_{\mu} \cdot \boldsymbol{T}, \tag{2.9}$$

given a gauge field ${\boldsymbol{W}_{i\mu}}^2$, which transforms as:

$$\boldsymbol{W}_{\mu}(x) \rightarrow \boldsymbol{W}_{\mu}(x) + \partial_{\mu}\boldsymbol{\alpha}(x) + g\boldsymbol{\alpha}(x) \times \boldsymbol{W}_{\mu}(x). \tag{2.10}$$

The $\boldsymbol{W}$-field part of the Lagrangian can be written as:

$$\mathcal{L}_{W} = -\frac{1}{4}\boldsymbol{W}_{\mu\nu} \cdot \boldsymbol{W}^{\mu\nu}, \tag{2.11}$$

with

$$\mathcal{W}_{\mu\nu} = \partial_{\nu}\boldsymbol{W}_{\nu} - \partial_{\nu}\boldsymbol{W}_{\nu} - g\boldsymbol{W}_{\mu} \times \boldsymbol{W}_{\nu}. \tag{2.12}$$

[1] $T_i = 1/2\tau_i$ where τ_i are the Pauli matrices.
[2] $i = 1, 2, 3$

For each independent generator T_i there is a corresponding gauge field $W_{i\mu}$ with the Lagrangian defined as:

$$\mathcal{L} = -\frac{1}{4} W_{i\mu\nu} W_i^{\mu\nu} + \bar{\psi}(i\gamma^\mu D_\mu - m)\psi \tag{2.13}$$

which by requiring invariance under infinitesimal gauge transformations result in the conservation of the current:

$$\boldsymbol{J^\mu} = \bar{\psi}\gamma^\mu \boldsymbol{T}\psi + \boldsymbol{W^{\mu\nu}} \times \boldsymbol{W_\nu} \tag{2.14}$$

is conserved. Although the SU(2) gauge model is a candidate model to explain the weak interaction, it does not explain the gauge boson masses nor the left-handed nature of charged currents. Further, the SU(2) model does not unify the weak and electromagnetic forces. However, it would serve as a building block for the $SU(2)_L \times U(1)_Y$ model explained below.

2.1.1.3 $SU(2)_L \times U(1)_Y$

The electromagnetic and weak interactions are unified in the gauge group $SU(2)_L \times U(1)_Y$. The generators for this group are the weak hypercharge Y and the weak isospin T, related to the electric charge Q by $Q = T_3 + Y/2$. The electromagnetic force is characterized by a one-dimensional unitary transformation and the weak force is described by SU(2). The weak force transforms particles according to their helicity, such that left-handed components transform as doublets, and right-handed components as weak isosinglets. See Table 2.4.

The fermion mass term $m\bar{\psi}\psi$ is not invariant under $SU(2)_L$, for this reason the fermions in this model are consider massless. Therefore the $SU(2)_L \times U(1)_Y$ Lagrangian is given by:

Field				$SU(3)$ C	$SU(2)$ L	$U(1)$ Y	T	T_3	Q
Q_L^i	$\begin{pmatrix} u_L \\ d_L \end{pmatrix}$	$\begin{pmatrix} c_L \\ s_L \end{pmatrix}$	$\begin{pmatrix} t_L \\ b_L \end{pmatrix}$	3	2	1/6	1/2	$\begin{matrix} +1/2 \\ -1/2 \end{matrix}$	$\begin{matrix} +2/3 \\ -1/3 \end{matrix}$
u_R^i	u_R	c_R	t_R	3	1	2/3	0	0	+2/3
d_R^i	d_R	s_R	b_R	3	1	-1/3	0	0	-1/3
L_L^i	$\begin{pmatrix} \nu_{eL} \\ e_L \end{pmatrix}$	$\begin{pmatrix} \nu_{\mu L} \\ \mu_L \end{pmatrix}$	$\begin{pmatrix} \nu_{\tau L} \\ \tau_L \end{pmatrix}$	1	2	-1/2	1/2	$\begin{matrix} +1/2 \\ -1/2 \end{matrix}$	$\begin{matrix} 0 \\ -1 \end{matrix}$
e_R^i	e_R	μ_R	τ_R	1	1	-1	0	0	-1
ν_R^i	${\nu^e}_R$	${\nu^\mu}_R$	${\nu^\tau}_R$	0	0	0	0	0	0

Table 2.4: Standard Model fermion fields and their gauge quantum numbers. T is the total weak isospin and T_3 its third component, and Q the electric charge.

$$\mathcal{L}_{EW} = -\frac{1}{4}\boldsymbol{W}^{\mu\nu} \cdot \boldsymbol{W}_{\mu\nu} - \frac{1}{4}B^{\mu\nu}B_{\mu\nu} + \bar{\psi}i\gamma^\mu D_\mu \psi \tag{2.15}$$

with a separate term for right and left handed fields. The fields ψ involved in the Lagrangian are shown in Table 2.4. The massless gauge fields are model as an isotriplet $\boldsymbol{W}^\mu$ for $\mathrm{SU}(2)_L$ and a singlet B_μ for $\mathrm{U}(1)_Y$. With the field tensor $\boldsymbol{W}^{\mu\nu}$ defined as in Equation 2.12, $B_{\mu\nu} = \partial_\mu B_\nu - \partial_\nu B_\mu$, and the covariant derivative as

$$D_\mu = \partial_\mu + ig'\boldsymbol{W}_\mu \cdot \boldsymbol{T} + ig\frac{1}{2}B_\mu Y. \tag{2.16}$$

The Lagrangian is invariant under infinitesimal local gauge transformations for each $\mathrm{SU}(2)_L$ and $\mathrm{U}(1)_Y$ independently. One must note, however, this electroweak model does not include the masses of the $W^\pm$ and Z bosons nor the masses of fermions. The mass problem is solved by the spontaneous symmetry breaking mechanism know as the Higgs mechanism, which consists of the introduction of an SU(2) doublet of scalar fields Φ:

$$\Phi = \begin{pmatrix} \phi^+ \\ \phi^0 \end{pmatrix}, \tag{2.17}$$

which results in two additional Lagrangian terms: $\mathcal{L}_{Higgs}$ and $\mathcal{L}_{Yukawa}$. The Higgs Lagrangian incorporates the kinetic energy of the Higgs field, its gauge interactions, and the Higgs potential:

$$\mathcal{L}_{Higgs} = (D^{\mu}\phi)^{\dagger} D_{\mu}\phi - V(\Phi) \tag{2.18}$$

$$V(\Phi) = -\mu^2 \phi^{\dagger}\phi + \lambda(\phi^{\dagger}\phi)^2, \tag{2.19}$$

where μ is a parameter of the Standard Model, the sign of the term is chosen such that the vacuum expectation value is non-zero, $< \Phi^{\dagger}\Phi >_0 = v^2/2$ with $v = \mu/\sqrt{\lambda}$. Which results in the generation of the gauge bosons masses. The Higgs potential is shown in Figure 2.2.

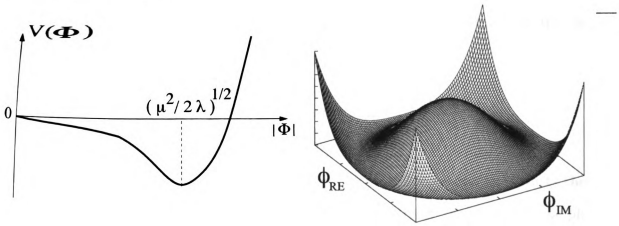

Figure 2.2: Higgs potential. The vacuum expectation value is non-zero, spontaneously breaking the symmetry. This mechanism is in charge of giving the masses to the Standard Model particles [9, 10].

Without losing generality, one can choose the vacuum state to be:

$$< \Phi >_0 = \begin{pmatrix} 0 \\ v/\sqrt{(2)} \end{pmatrix}, \tag{2.20}$$

and parametrize Φ as

$$\Phi(x) = \begin{pmatrix} 0 \\ (v + H(x))/\sqrt{(2)} \end{pmatrix}, \tag{2.21}$$

where $H(x)$ is a real field with zero vacuum expectation value. The $\mathcal{L}_{Higgs}$ can then be rewritten as:

$$\mathcal{L}_{Higgs} = \frac{1}{2}(\partial H)^2 + \frac{1}{4}g'^2 W^+ W^- (v+H)^2 + \frac{1}{8}g_Z^2 Z Z (v+H)^2 - V[\frac{1}{2}(v+H)^2] \tag{2.22}$$

where the terms in v^2 correspond to the mass terms for the W and Z bosons.

To unify the electromagnetic and weak interactions, the term $ieQA$ must be contained in the neutral term $i(g'W_{3\mu}T_3 + g\frac{1}{2}B_\mu Y)$ of the covariant derivative. This implies that the W_3 and B fields are a linear combination of A and another neutral field Z [42]:

$$\begin{pmatrix} W_3 \\ B \end{pmatrix} = \begin{pmatrix} \cos\theta_w & \sin\theta_w \\ -\sin\theta_w & \cos\theta_w \end{pmatrix} \begin{pmatrix} Z \\ A \end{pmatrix} \tag{2.23}$$

where θ_w is the electroweak mixing angle. The electroweak model predicts the existence of four carriers: W_1, W_2, W_3 and B. These carriers are related to the physical gauge bosons in Table 2.2 by:

$$W^\pm = (W_1 \mp W_2)/\sqrt{2} \tag{2.24}$$

$$Z = W_3 \cos\theta_W - B \sin\theta_W \tag{2.25}$$

$$\gamma = W_3 \cos\theta_W - B \sin\theta_W \tag{2.26}$$

with corresponding masses:

$$M_W = \frac{1}{2}gv, \quad \text{and} \quad M_Z = \frac{1}{2}g_Z v = \frac{M_W}{\cos\theta_w}, \quad \text{and} \quad M_\gamma = 0 \tag{2.27}$$

where $g_Z = \frac{e}{\sin\theta_w \cos\theta_w}$.

The $\mathcal{L}_{Yukawa}$ Lagrangian represents the interactions of the Higgs field with the fermions, from which the fermion masses can be obtained:

$$\mathcal{L}_{Yukawa} = \Gamma_u^{ij} \bar{Q}_L^i \sigma_2 \phi^* u_R^j - \Gamma_d^{ij} \bar{Q}_L^i \phi d_j^R - \Gamma_e^{ij} \bar{L}_L^i \phi e_R^j + h.c., \tag{2.28}$$

where σ_2 is the second Pauli matrix, and the coefficients Γ_u, Γ_d and Γ_e are 3×3 matrices in the generation space.

2.1.2 Cabibbo-Kobayashi-Maskawa Matrix

The Cabibbo-Kobayashi-Maskawa Matrix or CKM matrix, is a unitary matrix that relates the physical quark states (mass eigenstates) to the weak interaction generations (weak force eigenstates), and describes the probability of a transition from one quark state to another.

$$\begin{pmatrix} d' \\ s' \\ b' \end{pmatrix}_L = V_{CKM} \begin{pmatrix} d \\ s \\ b \end{pmatrix}_L = \begin{pmatrix} V_{ud} & V_{us} & V_{ub} \\ V_{cd} & V_{cs} & V_{cb} \\ V_{td} & V_{ts} & V_{tb} \end{pmatrix} \begin{pmatrix} d \\ s \\ b \end{pmatrix}_L \tag{2.29}$$

The magnitudes of the matrix elements are obtained experimentally as decribed in [1]. The current values of these magnitudes are:

$$|V_{CMK}| = \begin{pmatrix} 0.97419 \pm 0.00022 & 0.2257 \pm 0.0010 & 0.00359 \pm 0.00016 \\ 0.2256 \pm 0.0010 & 0.97334 \pm 0.00023 & 0.0415 \, {}^{+\,0.0010}_{-\,0.0011} \\ 0.00874 \, {}^{+\,0.00026}_{-\,0.00037} & 0.0407 \pm 0.0010 & 0.999133 \, {}^{+\,0.000044}_{-\,0.000043} \end{pmatrix} \tag{2.30}$$

The V_{tb} matrix element is particularly of great interest in the Single Top studies.

Because a direct measurement of $|V_{tb}|$ can only be performed through the observation of the Single Top quark. The measurement is carried out based on the Single Top cross section measurement which is proportional to $|Vtb|^2$ [48].

The $|V_{tb}|$ value presented in Equation 2.30 above is obtained by requiring the unitarity of the CKM matrix as well the assumption of the existence of three quark generations and not the direct measurement. The measurement results are shown in Section 9.7.

2.1.3 Quantum Chromodynamics

Quantum Chromodynamics (QCD) is constructed from the SU(3) symmetry group and describes the strong interaction of quarks mediated by gluon exchange. The strong interaction is responsible for binding quarks to form hadrons, and binding protons and neutrons to form nuclei. The quantum number associated with the strong interaction is known as "color charge," [10]. Quarks have one unit of color, while gluons have one unit of color and one unit of anticolor.

The QCD Lagrangian can be written as:

$$\mathcal{L} = -\frac{1}{4}F_{\alpha}^{\mu\nu}F^{\alpha\mu\nu} + \bar{\psi}_j(i\gamma_\mu D_{jk}^{\mu} - M_j\delta_{jk})\psi_k \tag{2.31}$$

where the indices a, j and k refer to the color charge, and D to the covariant derivative:

$$D_{jk}^{\mu} = \delta_{jk}\partial^{\mu} + ig_s(T_a)_{jk}G_a^{\mu}, \tag{2.32}$$

where G_a^{μ} are the gluon fields, T_a are the SU(3) generators, g_s is the strong coupling constant, M_{jk} the quark mass matrix, and $F_a^{\mu\nu}$ the gluon field tensor:

$$F_a^{\mu\nu} = \partial^{\mu}G_a^{\nu} - \partial^{\nu}G_a^{\mu} - g_s f_{abc}G_b^{\mu}G_c^{\nu} \tag{2.33}$$

f_{abc} is defined by the permutation of the SU(3) generators, $[T_a, T_b] = i f_{abc} T_c$.

The strong coupling parameter α_s which sets the strength of the interaction, has the following energy dependence:

$$\alpha_s(E) = \frac{g_s^2(E)}{4\pi} = \frac{12\pi}{33 - 2n_f \ln\left[\left(\frac{E}{\Lambda}\right)^2\right]}, \tag{2.34}$$

where n_f is the number of quark flavors, and Λ is a scale parameter which is determined experimentally ($\Lambda \sim 200$ GeV). This results in a coupling constant that goes to zero as $E \to \infty$, the strength of the interaction decreases with the energy of the process. At very high energies (short distances), quarks and gluons interact weakly, whereas at large distances, the interaction increases in strength.

The coupling parameter energy dependence has some implications when a quark receives a large amount of energy as a result of a high energy collision. As the quark moves away from the quarks to which it is color-bounded, the color field grows until it is energetically favorable to produce a quark-antiquark pair. This process is repeated many times producing a cascade of hadrons that are later reconstructed as jets in the detector.

2.2 Top Quark

The top quark is a spin-1/2 fermion with electric charge +2/3. The DØ and CDF experiments have measured the top quark mass to be $m_t = 173.1 \pm 0.6(stat) \pm 1.1(syst)$ GeV/c^2 [43].

From its discovery in 1995, until the recent Single Top quark production discovery, all studies and measurements of the top quark have taken place at the Fermilab Tevatron collider. At the Tevatron, the top quark is produced dominantly in pairs $t\bar{t}$ by means of the strong interaction. Top quarks may be produced through two different strong interaction processes: the quark-antiquark annihilation (Figure 2.3)

and the gluon fusion processes (Figure 2.4). At 1.96 TeV, the $t\bar{t}$ production cross section is of approximately 7 pb, mainly from contributions from the quark-antiquark annhilation process: $q\bar{q} \rightarrow t\bar{t}$ [49, 50, 51].

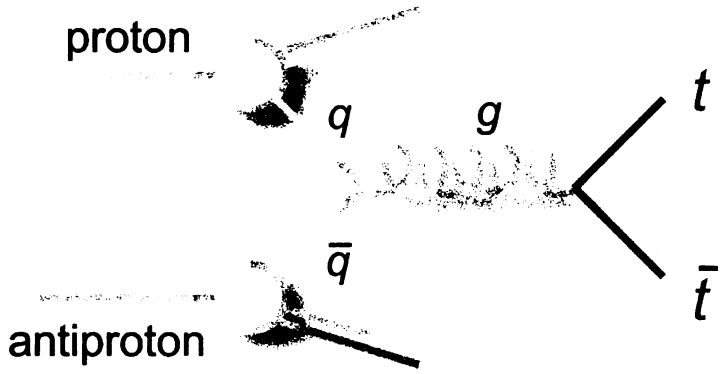

Figure 2.3: Leading Order Feynman for the quark-antiquark annihilation process in the production of top quark pairs [11].

The Standard Model predicts the top quark to decay in one of the down-type quarks (u, s or b). The branching fractions are proportional to the diagonal elements of the CKM matrix [52], Section 2.1.2:

- $B(t \rightarrow W + d) \approx 0.006\%$,
- $B(t \rightarrow W + s) \approx 0.17\%$,
- $B(t \rightarrow W + b) \approx 99.8\%$;

therefore, the top quark decay is expected to be dominated by $t \rightarrow Wb$. Then, the W boson produced by the top quark decays with the following branching ratios:

- $BR(W^+ \rightarrow e^+\nu_e) = 1/9$,
- $BR(W^+ \rightarrow \mu^+\nu_\mu) = 1/9$,
- $BR(W^+ \rightarrow \tau^+\nu_\tau) = 1/9$,

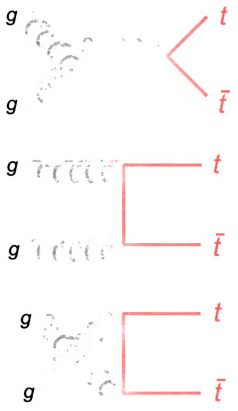

Figure **2.4:** Leading Order Feynman for the gluon fusion processes in the production of top **quark** pairs [11].

- **BR**$(W^+ \to u\bar{d}) = 3/9$, and
- **BR**$(W^+ \to c\bar{s}) = 3/9$.

In the $t\bar{t}$ case, the possible final products are summarized in the pie chart shown in Figure **2.5**.

At **next**-to-leading-order (NLO), the Standard Model prediction of the top quark decay **width** is [1]:

$$\Gamma_t \approx \frac{G_F\, m_t^3}{8\pi\sqrt{2}} \left(1 - \frac{M_W^2}{m_t^2}\right)^2 \left(1 + 2\frac{M_W^2}{m_t^2}\right) \left[1 - \frac{2\alpha_s}{3\pi}\left(\frac{2\pi^2}{3} - \frac{5}{2}\right)\right], \qquad (2.35)$$

where m_t is the quark top mass. The corresponding lifetime is roughly $1 \times 10^{-25} s$,

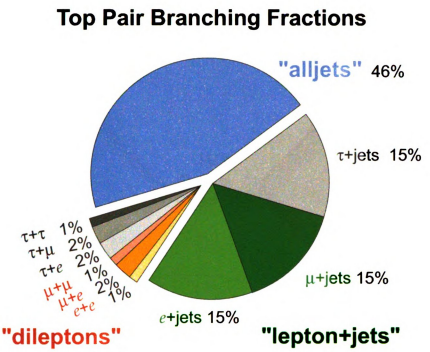

Figure 2.5: Final states for the top quark pair production, the slide size is proportional to the branching ratio of each process. The final states can be divided into three classes: dileptons, leptons+jets, and alljets [11].

which is approximately 20 times smaller than the timescale of strong interactions. As a consequence, the top quark decays before it has a chance to hadronize, resulting in a unique opportunity to study a bare quark.

2.3 Single Top

The top quark can also be produced by means of the electroweak interaction, which in contrast with the strong interaction production, results in one single top quark rather than a pair. At the Tevatron collider, to Leading Order (LO) there are two dominant Single Top channels:

- s-channel: produced by a virtual, time-like W boson from a $q\bar{q}$ annihilation, which then decays into a top and bottom quarks, as shown in Figure 2.6. At

NLO, the predicted s-channel cross section is 1.12 ± 0.05 pb [53]. The s-channel is sometimes referred as "tb" production, where tb includes both $t\bar{b}$ and $\bar{t}b$ states.

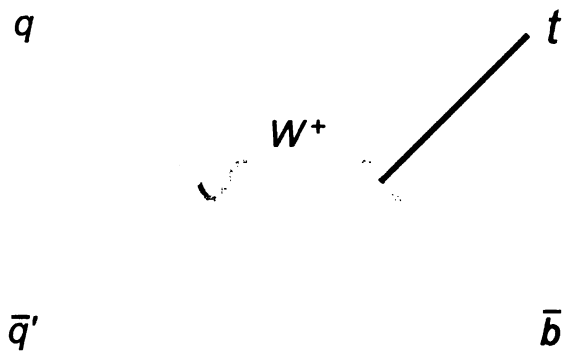

Figure 2.6: Leading Order Feynman diagram of the Single Top s-channel production mode [11].

- **t-channel**: produced by a vitual, space-like W boson from light and bottom quark and resulting in a forward scattered light quark and a top quark, as shown in Figure 2.7. At NLO, the predicted t-channel cross section is 2.34 ± 0.13 pb [53]. The t-channel is sometimes referred as "tqb" production, where tqb includes both $tq\bar{b}$ and $\bar{t}qb$ states.

There is an additional production mode in which the Single Top created in association with an on-shell W boson. However, this channel has too small of a cross section at the Tevatron energies to be observed.

As mentioned in Section 2.2 above, the top quark decays in W-boson plus a b-quark. In cases where the W decays hadronically, the Single Top signal will be very difficult to separate from the overwhelming QCD background. For this reason the studies presented in this dissertation are limited to the electron and muon leptonic final states of Single Top. The Feynman diagrams for the Single Top muon final states are shown in Figure 2.8 for both the s and t channels.

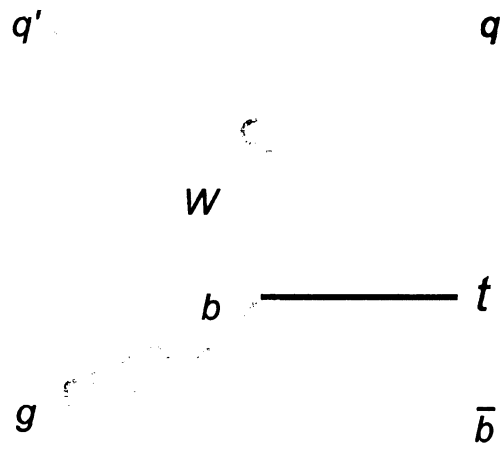

Figure 2.7: Leading Order Feynman diagram of the Single Top t-channel production mode [11].

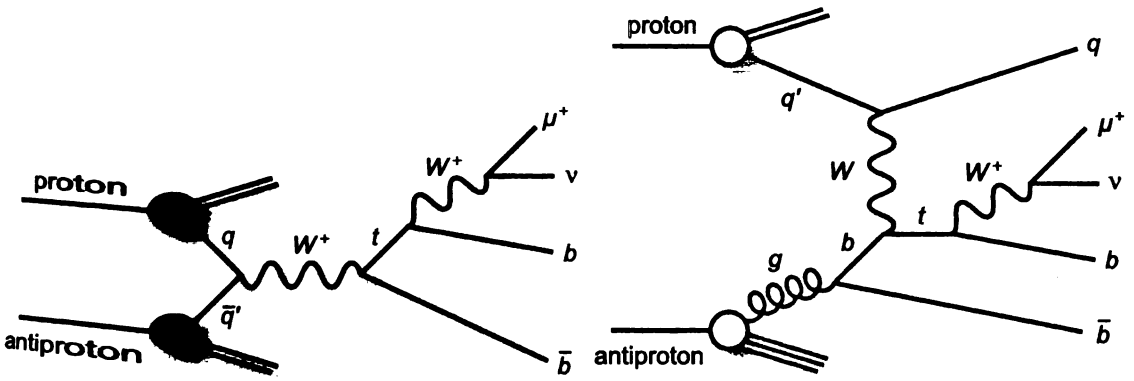

Figure 2.8: Single Top quark production and decay. In these diagrams the W-boson decays leptonically into a muon and a neutrino [11]. The final state for the s-channel has a b-quark created along with the t-quark, a charged lepton from the W-boson decay and its respective neutrino. In the t-channel case, the main components are the spectator light quark, the lepton and the neutrino from the W decay, and the b-quark from the top quark decay.

2.3.1 Background Processes

The Single Top background processes have the same final state as the Single Top signal. These backgrounds are characterized to be enormous compared to the signal. In this analysis, the main backgrounds considered are:

- W bosons produced with multiple jets (some of which could be fragmented $b\bar{b}$ quark pairs and therefore lead to legitimate heavy flavor tags), referred as W+jets,
- radiatively produced jets which either produce $b\bar{b}$ quark pairs or lead to fake vertex tags (called "QCD" backgrounds), and
- the production of conventional $t\bar{t}$ quark pairs.

The Leading Order Feynman diagrams for these processes are presented in Figure 2.9.

2.3.2 Motivation to study Single Top

2.3.2.1 Measurement of the CKM matrix element V_{tb}

Single Top offers a unique and direct way to measure the element $|V_{tb}|$ of the CKM matrix, Section 2.1.2. The measurement presented in this analysis does not assume the unitarity of the CKM matrix nor the number of quark families. There are three main assumptions on the direct measurement of V_{tb}. First, the Single Top production is assumed to include only the electroweak interaction, thereby not considering scenarios beyond the Standard Model. Second, it is assumed that $|V_{tb}|^2 >> |V_{td}|^2 + |V_{ts}|^2$. This is experimentally supported by the measurements [54, 55] of the ratio:

$$R = \frac{\mathcal{B}(t \to W\ b)}{\mathcal{B}(t \to W\ q)} = \frac{|V_{tb}|^2}{|V_{td}|^2 + |V_{ts}|^2 + |V_{tb}|^2}. \tag{2.36}$$

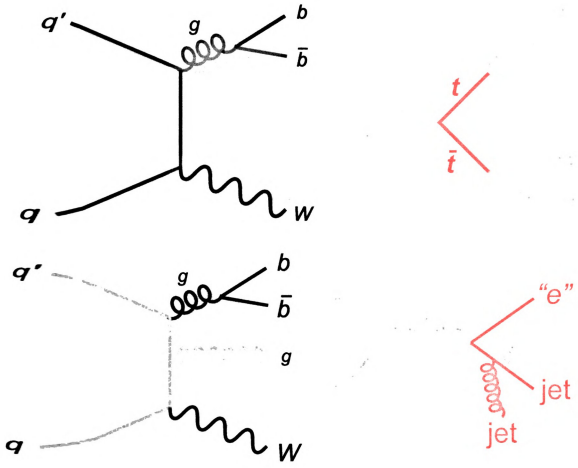

Figure 2.9: Feynman diagrams for the Single Top background processes. W+jets (top-left), $t\bar{t}$ (top-right), and multijets (bottom).

Third, although it is further assumed that the Wtb vertex is CP-conserving and of the $V - A$ type, it is allowed to have anomalous strength. The most general Wtb vertex in the Standard Model is given by:

$$\Gamma^{\mu}_{Wtb} = -\frac{g'}{\sqrt{2}} V_{tb}\, u(p_T) \left[\gamma^{\mu} f_1^L P_L\right] u(p_T), \tag{2.37}$$

where f_1^L is the left-handed Wtb coupling, and P_L is the left-handed projection operator, $P_L = (1 - \gamma_5)/2$. The Single Top cross section is directly proportional to the square of the effective Wtb coupling, from where a measurement of V_{tb} can be inferred. References [56, 48, 57] present the results of the V_{tb} measurement and a

more in depth discussion. Section 9.7 contains the results of the V_{tb} measurement with 2.3 fb^{-}1 of DØ data.

2.3.2.2 Top quark spin polarization

The Single Top quarks are produced by means of the left-handed electroweak interaction, resulting in highly polarized top quarks [58, 59, 60]. Since the the top quark decays before it has a chance to hadronize, the top quark spin polarization can be studied in the top quark rest frame through its decay products: $t \rightarrow W^{+}b \rightarrow l\ \nu_l\ b$, [12, 61, 7, 6].

When the W is polarized longitudinally: the b-quark moves in the direction opposite to the top quark spin and the W prefers to move in the direction of the top quark spin. The W decay products prefer to align along the W polarization, and since the W is boosted in the direction of the spin polarization, the charged lepton prefers to move along the top quark spin axis, as illustrated in Figure 2.10.

For the case of left-handed W, the b quark moves in the direction of the top quark spin, and the W in the opposite direction. The right-handed lepton then prefers to move against the W direction, which corresponds to the same direction as the top quark polarization, also shown in Figure 2.10.

The angular decay distribution for the charged lepton follows the angular distribution [12]:

$$\frac{1}{\Gamma}\frac{d\Gamma}{d\cos\theta} = \frac{1}{2}(1+\theta) \tag{2.38}$$

where θ is the angle between the direction of the charged lepton and the top quark polarization. These angular correlations play an important role when separating the Single Top signal from the overwhelming background.

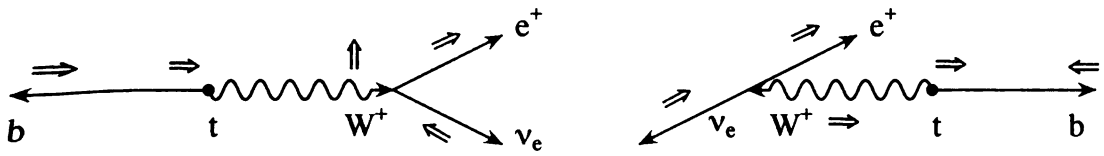

Figure 2.10: Top quark decay and correlation between the charged lepton and the top quark spin on the top quark rest frame. The large arrows are the preferred direction of the polarization [12].

2.3.2.3 Physics Beyond the Standard Model

Some of the possible extensions of the Standard Model include: existence of more than three quark families, additional gauge bosons, extra scalar bosons, and modified top quark interactions. Each extension affects the structure of the Single Top quark production, the final state kinematics, and thus the Single Top quark cross section [12].

In the event of a fourth quark generation, the direct production of such quarks can be observed through Single Top production $q\bar{q}' \rightarrow W^* \rightarrow t\bar{b}'$, where b' is the b-like quark of the fourth generation and W^* is the mediator gauge boson. This process is illustrated in Figure 2.11. The associated production cross section will depend on the magnitude of the W^* t b' coupling and the mass of the b'.

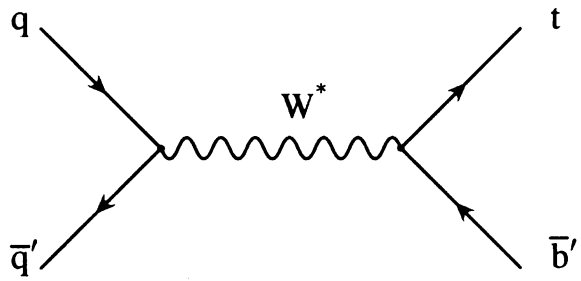

Figure 2.11: Single Top production and a fourth generation quark b' [12].

Models like the topflavor [62] predict the existence of additional weak bosons $W'^{\pm}$ and Z'. In this model Single Top is produced by the exchange of a W'^{-} boson

having the same finals states as the Standard Model Single Top production, as shown in Figure 2.12. The $W'^{\pm}$ can be study by searching for resonances in the invariant mass distribution of the $W'^{\pm}$ t b system at the $M_{W'^{\pm}}$.

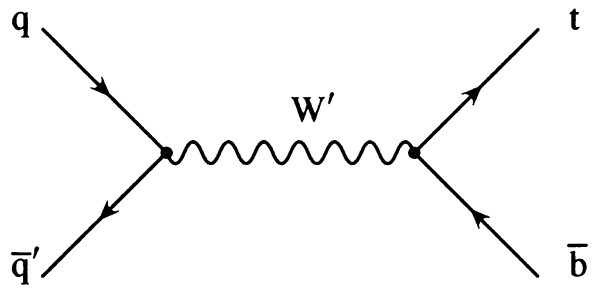

Figure 2.12: Single Top production by means of the $W'^{\pm}$ gauge boson.[12].

The Single Top production can also be affected by flavor-changing neutral currents (FCNC), which are forbidden in the Standard Model. These currents allow the top quark to have anomalous couplings such as those in Figure 2.13, where the top quark decays into a gauge boson and a c-quark. The resulting FCNC Single Top production diagrams are shown in 2.14.

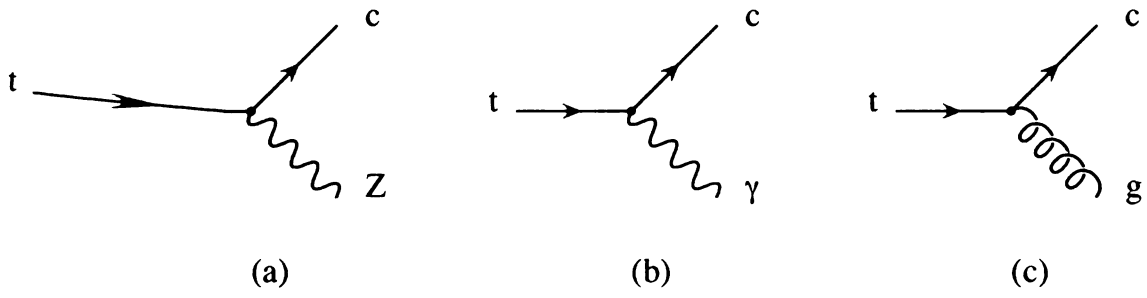

Figure 2.13: FCNC couplings for the top quark decaying into a c-quark plus a gauge boson. Similar diagrams are also permitted by FCNC currents for the top quark decaying into a u-quark.[12].

Summarizing, the Single Top quark production can be used as tool to test Beyond the Standard Model theories. These theories will permit the understanding of new

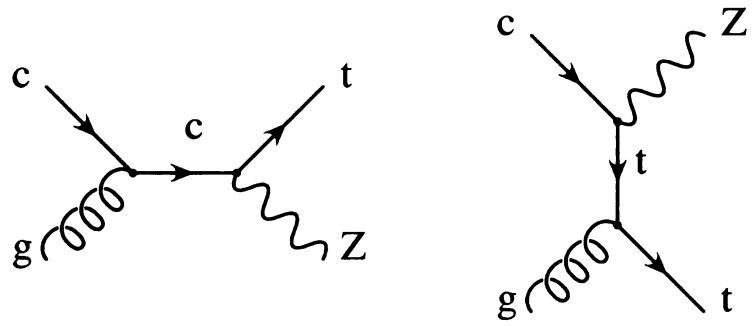

Figure 2.14: LO Feynman diagrams for the Single Top production by means of FCNC, $g\,c \longrightarrow t\;Z$.[12].

physics phenomena, and also help in the search of new particles such as the Higgs boson.

Chapter 3

NLO Studies of Single Top Quark Production

The Single Top quark production is predicted by the well-confirmed Standard Model. Which can be considered not only as a tool to test the Standard Model, but also as a window to physics beyond it. Consequently, accurate calculations are required which include higher order QCD corrections to make the Single Top distinguishable from other processes. Such calculations, should not only include effects on the production cross section, but should also include the event topology of both the production and decay of the top quark. Therefore, the theoretical calculation can be directly compared to the experimental findings in the Tevatron collider at Fermilab.

This Chapter presents the NLO corrections effects on the Single Top quark production, and the work I conducted, together with the Michigan State University theory group.

3.1 Event topology

The Single Top s and t channels have common elements in their event signatures as well as differential features. They both have at least one b-jet, missing transverse

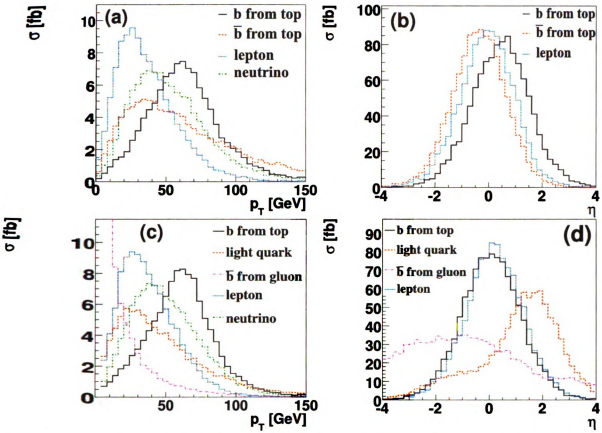

Figure 3.1: Parton level kinematical distributions for the transverse momentum p_T (a,c) and pseudorapidity η (c,d) for final state partons in the s-channel (upper row) and t-channel (lower row) Single Top quark events. The histograms only include the final state of t, not $\bar{t}$.

energy, and a lepton, but their kinematical distributions have different shapes. More specifically at the parton level:

- s-channel: there are two b quark jets, one from the top quark decay and one produced with the top quark itself. As well, there are one high-p_T lepton and a neutrino. In the detector, the neutrino is represented by missing transverse energy (MET) coming from the W boson decay. Illustrated in Figure 2.8.

- t-channel: there is one b quark jet from the top quark decay, one light quark jet recoiling against the top quark, one high-p_T lepton, and a neutrino coming from the W boson decay. In addition, there is a target fragment b quark that tends to be relatively soft at high rapidity, and collinear to the initial gluon.

This results in a b-jet that is difficult to observe in the detector. Illustrated in Figure 2.8.

Figure 3.1 shows some of the parton level distributions for the Single Top final products. Although experimentally is it not possible to determine whether a b jet comes from the top quark or not, the jet distributions are shown separately for each b jet for illustrative purposes. The b quark coming from the top quark decay tends to be central and to have a hard p_T spectrum. The lepton from the W decay prefers to move in the direction of the top quark polarization (see Section 2.3.2.2) which results in a softer lepton spectrum compared to the neutrino. Also, note the asymmetry on the light quark η distribution for the t channel, which comes from the nature of the $p\bar{p}$ collider.

3.2 NLO calculations

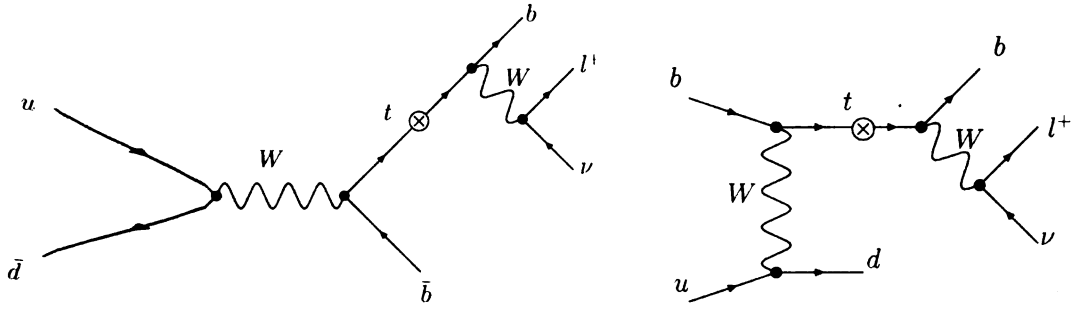

Figure 3.2: Single Top LO Feynman diagrams for the s and t channels. The symbol $\otimes$ represents the separation used in the NWA method between the production and decay of the Single Top.

A complete NLO calculation should include the contributions from top quark production and decay including the angular correlations of the final state particles to study the top quark polarization. References [61, 7, 6] present such corrections, at the order of $\alpha(s)$, using the one scale, space-slicing method together with the Narrow Width Approximation (NWA).

The NWA is used to separate the study of Single Top into two stages: production, and decay, as depicted in Figure 3.2. The two parts can then be related using the polarization information of the top quark. In the NLO corrections, there are mainly two kind of divergences: ultraviolet (UV) and infrared (IR). The ultraviolet divergences are removed by renormalizating the wave functions. The IR divergences are handled by considering virtual and real corrections. The Phase Space Slicing (PSS) method uses the cut off scale parameter s_{min} to separate the phase space into two regions: the resolved and the unresolved region. The amplitude in the resolved region has no divergence and can be integrated using Monte Carlo methods. The amplitude in the unresolved region contains all the soft and colinear divergences and can be integrated analytically [61].

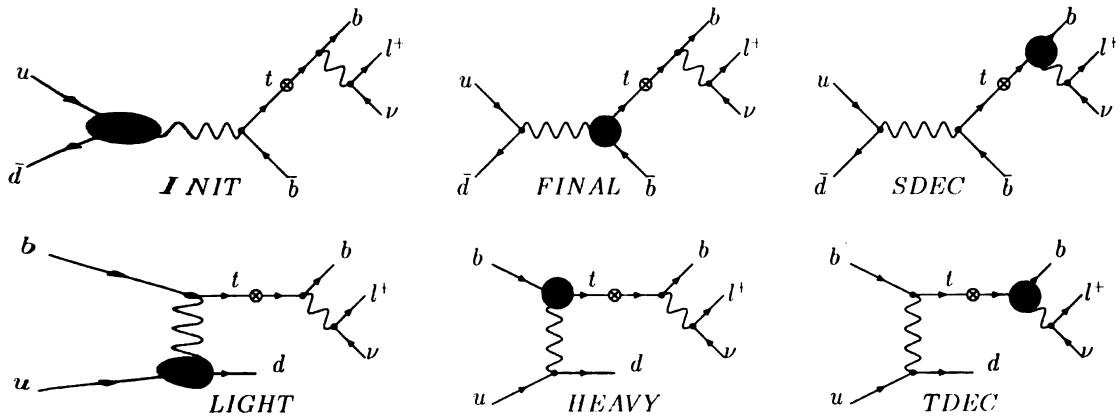

Figure 3.3: Different contributions to the Single Top NLO corrections, s-channel (upper row) t-channel (lower row). The black dots indicate the higher order QCD corrections, both for virtual and real emissions.

The process involved in the NLO calculation can be separated into categories, as shown in Figure 3.3. For the s-channel:

- INIT: corrections to the initial state of the single top production.
- FINAL: corrections to the final state of the single top production.
- SDEC: corrections to the decay of the top quark.

For the t-channel:

- LIGHT: corrections in which the gluon is connected to the light quark.
- HEAVY: correction in which the gluon is connected to the heavy quark.
- TDEC: corrections to the top quark decay process.

The contributions to the total cross sections are presented in Table 3.1, the NLO corrections effect on particular distributions is shown in Section 3.3 below.

	s-channel			t-channel	
	Cross Section (fb)	NLO Fraction (%)		Cross Section (fb)	NLO Fraction (%)
LO	31.2	65.0	LO	99.2	94.6
INIT	10.7	22.3	LIGHT	5.56	5.31
FINAL	5.5	11.5	HEAVY	1.03	0.98
SDEC	0.57	1.19	TDEC	-0.81	-0.77
$O(\alpha_s)$ sum	16.8	35.0	$O(\alpha_s)$ sum	5.54	5.28
NLO	47.9	100	NLO	104.8	100

Table 3.1: NLO corrections contributions for both s- and t-channels for the Single Top production [6, 7].

3.3 Single Top distributions at NLO

When studying Single Top experimentally, it is necessary to apply selection cuts to the collected samples to remove unwanted backgrounds. Although no detector simulations are included in this study, there are some selection criteria applied to the generated samples that allow comparison of the NLO corrections results with the

experimental counterparts. In particular, it is required that the events contain one lepton, MET, two to four jets, and the following cuts:

- Lepton: $p_T > 15$ GeV, $|\eta| < 2.5$.
- MET: > 15 GeV.
- All jets: $p_T > 15$ GeV, $|\eta| < 3.0$.
- jet conesize: $\Delta R = 0.5$.

Plots in Figures 3.4 and 3.5 show NLO effect on selected Single Top distributions. The size of the NLO effect is larger in the s-channel compared to the t-channel. However, in general, the NLO effect has a very similar shape as LO for both channels. More specifically, the NLO QCD corrections:

- for the lepton and $\not{E}_T$ (first row of Figures 3.4 and 3.5), have very similar shapes to the LO distributions. This is explained by the fact that they are not quark distributions.
- for the b-jets, shift and widen the p_T distributions. The peak value moves to lower values. The $\bar{b}$-jet η distribution for the s-channel becomes more central, while the shape for the b-jet η remains almost unchanged. The H_T distributions are broadened as a consequence of the NLO corrections.
- for the t-channel spectator (light) jet, move the pseudorapidity distribution slightly forward, due to the additional gluon radiation.

3.4 "Lonely Top"

There have been many studies regarding the separation of the Single Top signal from its overwhelming background. One of these studies, which is referred as "Lonely

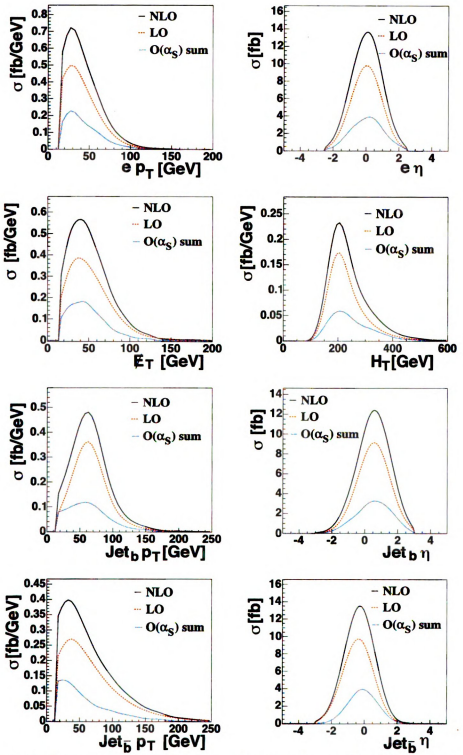

Figure 3.4: NLO corrections effect in distributions for the Single Top s-channel [6]. The dotted red line represents the LO calculation, the blue line the sum of NLO contributions, and the black line the sum of LO plus NLO. Top row: electron p_T and electron η. Second row: $\not{E}$ and total transverse energy H_T. Third row: b-jet p_T and b-jet η. Bottom row: $\bar{b}$-jet p_T and $\bar{b}$-jet η. Figures from Reference [7]

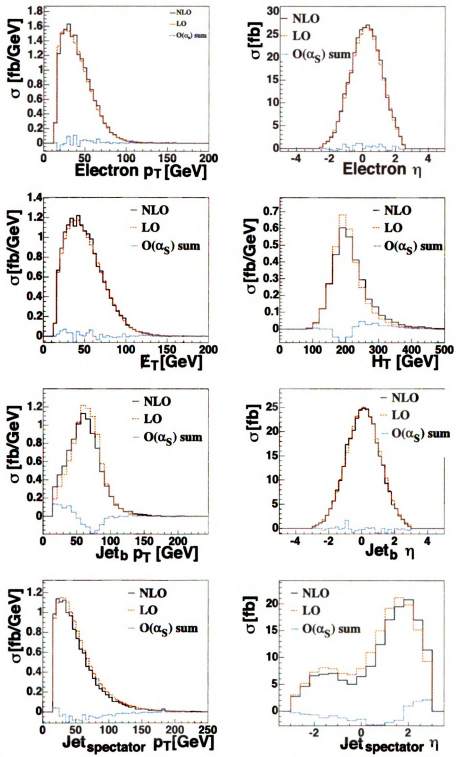

Figure 3.5: NLO effect in distributions for the Single Top t-channel [6]. The dotted red line represents the LO calculation, the blue line the sum of NLO contributions, and the black line the sum of LO plus NLO. Top row: electron p_T and electron η. Second row: $\not{E}$ and total transverse energy H_T. Third row: b-jet p_T and b-jet η. Bottom row: light quark jet p_T and light quark jet η. Figures from Reference [6].

Top" [63, 64], is based on the usage of correlation functions between pseudorapidity distributions of the final lepton and the untagged jet. The "Lonely Top" calculations were performed at LO. However, as shown in the previous section, the NLO corrections affect the kinematics in Single Top quark production. With that consideration, this Section explores the NLO effects on the "Lonely Top" correlation functions.

In order to have a similar sample to the one used in Reference [63], the following additional selection criteria are required:

- Lepton: $p_T > 15$ GeV, $\mid \eta \mid < 2.0$.
- MET: > 15 GeV.
- All jets: $p_T > 30$ GeV, $\mid \eta \mid < 2.5$.
- Leading jet (Jet in the event with the highest p_T): $p_T > 40$ GeV, $\mid \eta \mid < 2.0$.
- H_T (total event transverse energy): < 300 GeV.
- Reconstructed top mass: 155 GeV $< m_T <$ 200 GeV.
- jet conesize: $\Delta R = 0.5$.

The b-tagging effect on the sample is included by using a probability distribution, which determines whether each jet would be b-tagged or misstagged [63]. For a b-jet, the probability to be b-tagged is given by

$$p_{tagged,bjet}(p_T) = 0.5 \tanh(p_T/36GeV),$$

while for any other jet, the misstagged probability is given by

$$p_{misstagged,jet}(p_T) = 0.01 \tanh(p_T/80GeV).$$

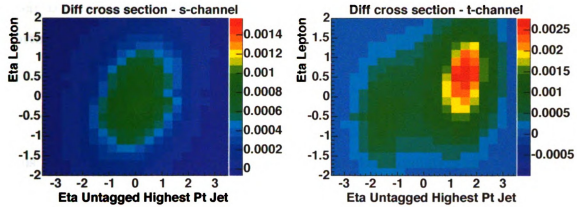

Figure 3.6: Double differential cross section for s-channel and t-channel. Only LO contributions are shown. The x-axis corresponds to the untagged-jet η and the y-axis to the lepton η.

The asymmetry functions presented in Reference [63] are based on the CP invariance of initial $p\bar{p}$ state of the at the Tevatron collider. The Single Top differential cross sections shown in Figure 3.6 exhibits some asymmetrical behavior in both s- and t-channels. This motivates writing the differential cross section as the sum of three orthogonal functions:

$$\frac{d^2\sigma}{d\hat{\eta_j}d\hat{\eta_l}}(\hat{\eta_j},\hat{\eta_l}) = \overline{F}(\hat{\eta_j},\hat{\eta_l}) + F_+(\hat{\eta_j},\hat{\eta_l}) + F_-(\hat{\eta_j},\hat{\eta_l})$$

where, each one of asymmetry functions (F) is defined as:

$$\overline{F}(\hat{\eta_j},\hat{\eta_l}) = \frac{1}{4}[\frac{d^2\sigma}{d\hat{\eta_j}d\hat{\eta_l}}(\hat{\eta_j},\hat{\eta_l}) + \frac{d^2\sigma}{d\hat{\eta_j}d\hat{\eta_l}}(-\hat{\eta_j},-\hat{\eta_l}) + \frac{d^2\sigma}{d\hat{\eta_j}d\hat{\eta_l}}(\hat{\eta_j},-\hat{\eta_l}) + \frac{d^2\sigma}{d\hat{\eta_j}d\hat{\eta_l}}(-\hat{\eta_j},\hat{\eta_l})]$$

$$F_+(\hat{\eta_j},\hat{\eta_l}) = \frac{1}{4}[\frac{d^2\sigma}{d\hat{\eta_j}d\hat{\eta_l}}(\hat{\eta_j},\hat{\eta_l}) + \frac{d^2\sigma}{d\hat{\eta_j}d\hat{\eta_l}}(-\hat{\eta_j},-\hat{\eta_l}) - \frac{d^2\sigma}{d\hat{\eta_j}d\hat{\eta_l}}(\hat{\eta_j},-\hat{\eta_l}) - \frac{d^2\sigma}{d\hat{\eta_j}d\hat{\eta_l}}(-\hat{\eta_j},\hat{\eta_l})]$$

$$F_-(\hat{\eta_j},\hat{\eta_l}) = \frac{1}{2}[\frac{d^2\sigma}{d\hat{\eta_j}d\hat{\eta_l}}(\hat{\eta_j},\hat{\eta_l}) - \frac{d^2\sigma}{d\hat{\eta_j}d\hat{\eta_l}}(-\hat{\eta_j},-\hat{\eta_l})]$$

where by construction, the $\overline{F}$and F_- functions have even parity while the F_+ has odd parity. If the four quadrants of the $(\hat{\eta_j},\hat{\eta_l})$ plane are label as A, B, C and D,

where B corresponds to first quadrant, A to the second, C to the third, and D to the fourth,

$$\begin{matrix} A & B \\ C & D \end{matrix}.$$

Thus the definition of these variables, implies that the information on:

$$\overline{F}(A) = \overline{F}(B) = \overline{F}(C) = \overline{F}(D),$$

$$F_+(A) = F_+(D) \ , \ F_+(B) = F_+(C) \ , \ F_+(A) = -F_+(B),$$

and

$$F_-(A) \neq F_-(B) \ , \ F_-(A) = F_-(D) \ , \ F_-(B) = F_-(C)$$

The above indicates that all the information in $\overline{F}$ and F_+ is contained in one quadrant, and in two quadrants for F_-. These asymmetry functions are shown in in Figure 3.7, including only the LO contributions. Based on the description of these functions, it is expected that the NLO corrections contributions would result in changes on the function shapes. Such changes are related to those encountered in the Single Top kinematical distributions. These NLO effects are shown in Figures 3.8 to 3.11, and reviewed in the next Section below.

3.4.1 "Lonely Top" at NLO

The asymmetry functions at NLO for the Single Top s- and t-channels are presented in Figures 3.8 to 3.11. The NLO contributions are shown in the middle column and the final distribution, including LO and NLO corrections, is shown in the third column. The unique features of these functions can be used to separate the Single Top signal

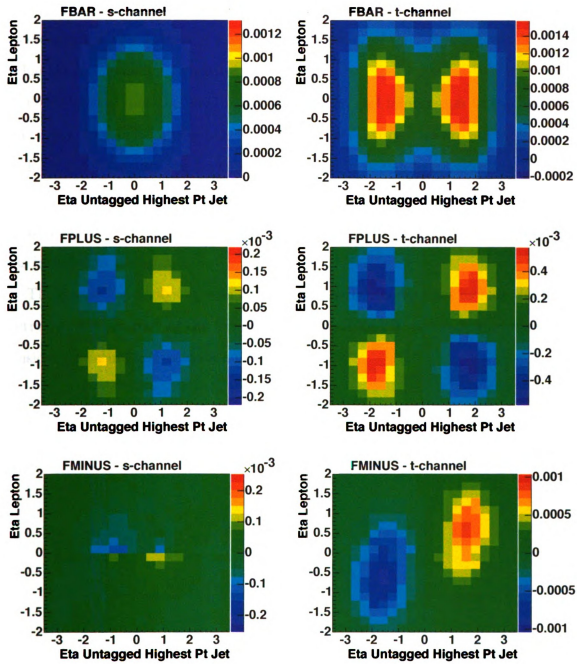

Figure 3.7: FBAR ($\overline{F}$), FPLUS (F_+), and FMINUS (F_-) asymmetry functions, for the s-channel (left) and t-channel (right). Only LO contributions are included in these plots.

from the background, and to differentiate the s-channel from the t-channel. The difference between the two channels arises from the angular distribution asymmetry on the spectator jet on the t-channel, as shown in Section 3.1. This asymmetry also causes the two distinct peaks on the $\overline{F}$ function of the t-channel, which for the s-channel corresponds to a central distribution.

One observes that the NLO corrections indeed add information to the functions that was not available at the LO. Although, these contributions are not so dissimilar to dramatically modify the asymmetry functions, it is safe to consider that the new features that appear as a result of the NLO corrections would contribute to the differentiation of the Single Top signal. This is also despite the fact that no background was included in the study.

The Single Top analysis presented in this dissertation does not include the asymmetry function as part of the Decision Tree variables list; however, they should be consider for future multivariate analyses.

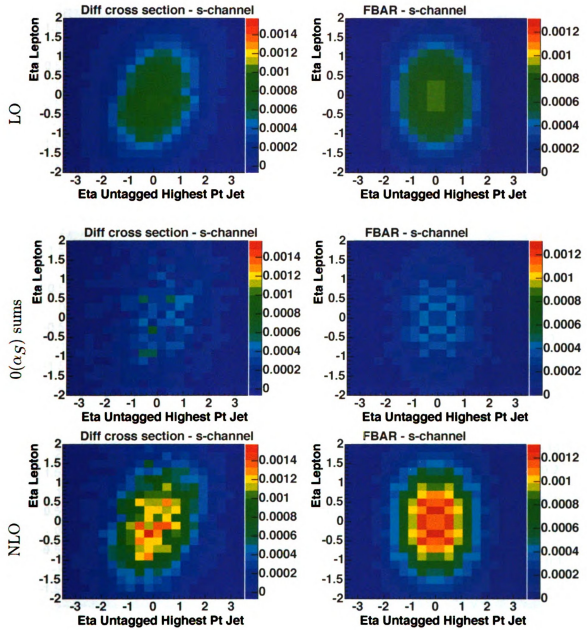

Figure 3.8: NLO corrections in the s-channel for the differential cross section (left column), $\overline{F}$ (right column). The LO contribution is show in the first row, the sum of all NLO corrections contributions on the middle row, and the LO plus NLO corrections is show in the last row.

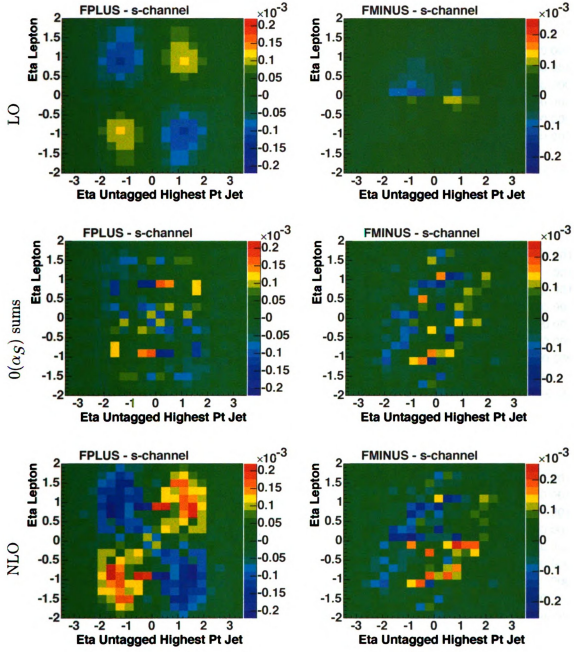

Figure 3.9: NLO corrections in the s-channel for F_+ (left column), and F_- (right column). The LO contribution is show in the first row, the sum of all NLO corrections contributions on the middle row, and the LO plus NLO corrections is show in the last row.

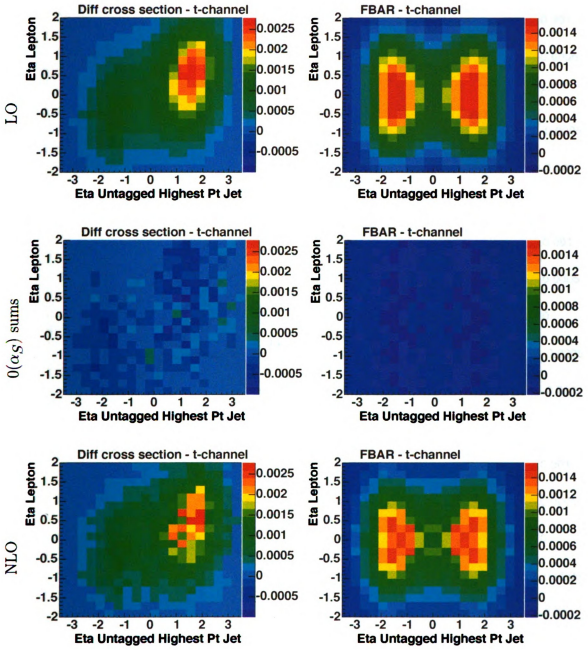

Figure 3.10: NLO corrections in the t-channel for the differential cross section (left column), $\overline{F}$ (right column). The LO contribution is show in the first row, the sum of all NLO corrections contributions on the middle row, and the LO plus NLO corrections is show in the last row.

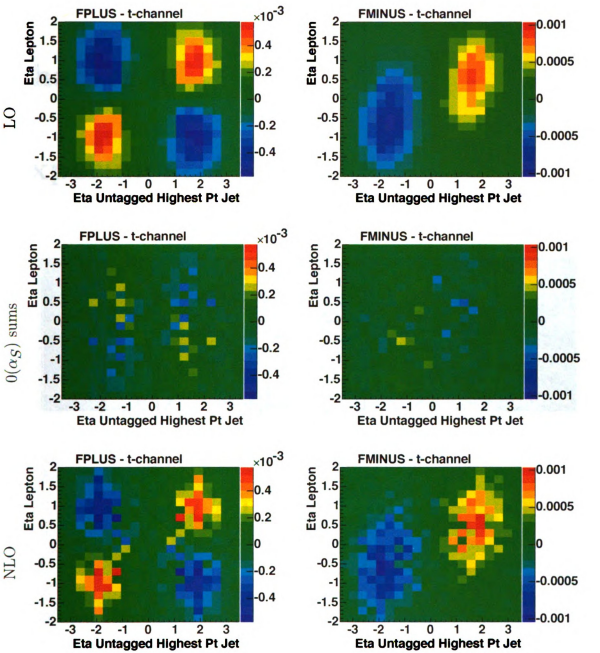

Figure 3.11: NLO corrections in the t-channel for F_+ (left column), and F_- (right column). The LO contribution is show in the first row, the sum of all NLO corrections contributions on the middle row, and the LO plus NLO corrections is show in the last row.

Chapter 4

Experimental Setup

Figure 4.1: Aerial view of the Fermilab National Accelerator Laboratory.

The Fermi National Accelerator Laboratory (Fermilab) [65, 13] is located near Chicago, Illinois in the USA. Currently, Fermilab is the only facility in the world where the high energy collisions of protons and anti-protons are possible at a center-of-mass energy of $s = \sqrt{1.96}$ TeV [13, 66]. It all begins from a bottle of hydrogen

and culminates with the collision of protons and anti-protons traveling very close to the speed of light. To properly study the interactions that take place at Fermilab, a complex detection system is required which would allow one to "observe" the details of these energetic collisions, and study interesting physics processes such as the Single Top. The two main detectors at Fermilab are known as DØ and CDF. This chapter presents a description of the accelerator complex and the DØ detector at Fermilab.

4.1 Accelerator complex

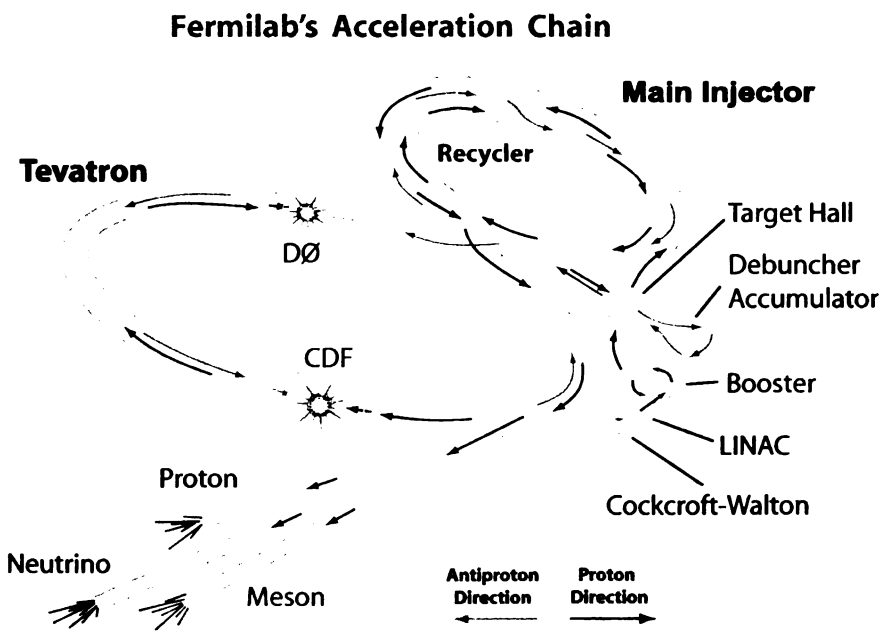

Figure 4.2: Fermilab accelerators chain, there are 2 interaction points, CDF, and DØ [13].

The Fermilab accelerator complex is composed of seven chained machines that have, as their ultimate purpose, the generation of protons and anti-protons at $E_{beam} = \sqrt{980}$ GeV each [16]. These machines are known as: a Cockcroft-Walton pre-accelerator, linear accelerator (LINAC), booster synchrotron, main injector, antiproton source, antiproton recycler, and the Tevatron [14]. In the following sections a description of

each segment of the acceleration chain is presented. Figure 4.2 is an schematic view of the full chain.

4.1.1 Cockcroft-Walton pre-accelerator

The acceleration process starts by using hydrogen H_2 and turning it into H^- ions. The charged hydrogen is accelerated by an electric field produced by a potential difference of 750 kV. Such high voltage is achieved by charging in parallel capacitors from an AC source, and by using diodes to discharge them in series. The H^- ions are accelerated to 750 keV.

4.1.2 LINAC

The energy of the H^- ions coming from the Cockcroft-Walton accelerator is increased further by using a linear accelerator, which augments the ions' energy from 750 keV to 400 MeV [14]. The LINAC uses a series of RF cavities to accelerate the particles by alternating the electric field in the cavity and giving a small boost to the ions when they pass the gaps between cavities. Since the acceleration of the ion occurs only at specific conditions of location (gap) and electric field, the ions are confined in bunches. Before the ions continue to the next acceleration step they pass through a carbon foil to remove the electrons. A schematic view of the LINAC is shown in Figure 4.3.

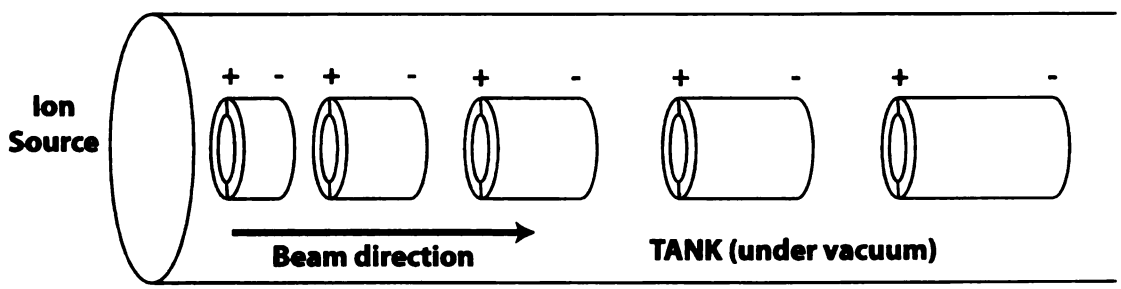

Figure 4.3: LINAC alternating series of gaps and drift tubes [14].

4.1.3 Booster Synchrotron

The booster is the first synchrotron of the accelerator chain with a diameter of approximately 150 m. It uses RF cavities for the acceleration of the particles. The charged particles travel in a circular path due to magnetic fields and receive an acceleration due to electric fields during each revolution. The particles' energy after the Booster is 8 GeV.

4.1.4 Main Injector

The Main Injector is a synchrotron that serves several purposes. The most relevant task of the Main Injector is to accelerate both protons and antiprotons to energies of 150 GeV which is the initial energy of the particles in the Tevatron. In addition, the Main Injector also accelerates the protons coming from the Booster to 120 GeV and sends them to the antiproton production chain.

4.1.5 Antiproton Source and Recycler

The antiprotons are selected from the particles produced from the collision of 120 GeV protons coming from the Main Injectors into a fixed, nickel target. A lithium lens is used to focus the secondary particles produced after the collision, from which only the 8 GeV antiprotons are selected by a dipole magnet. A cartoon schematic of this procedure is presented in Figure 4.4.

Once the antiprotons are produced they are sent to the Debuncher, which is a triangular shaped synchrotron that reduces the spread on the antiprotons' momenta. After the Debuncher, the protons are stored in the Accumulator until they are ready to go back to the Main Injector for further acceleration or into the Recycler for later usage.

The antiproton production efficiency is very low taking about 12 hours to produce

enough antiprotons to start the $p\bar{p}$ collisions. Due to this fact, there is an additional component in the Fermilab complex, the Recycler whose main purpose is to temporarily store remaining antiprotons from Tevatron or those coming from the Accumulator.

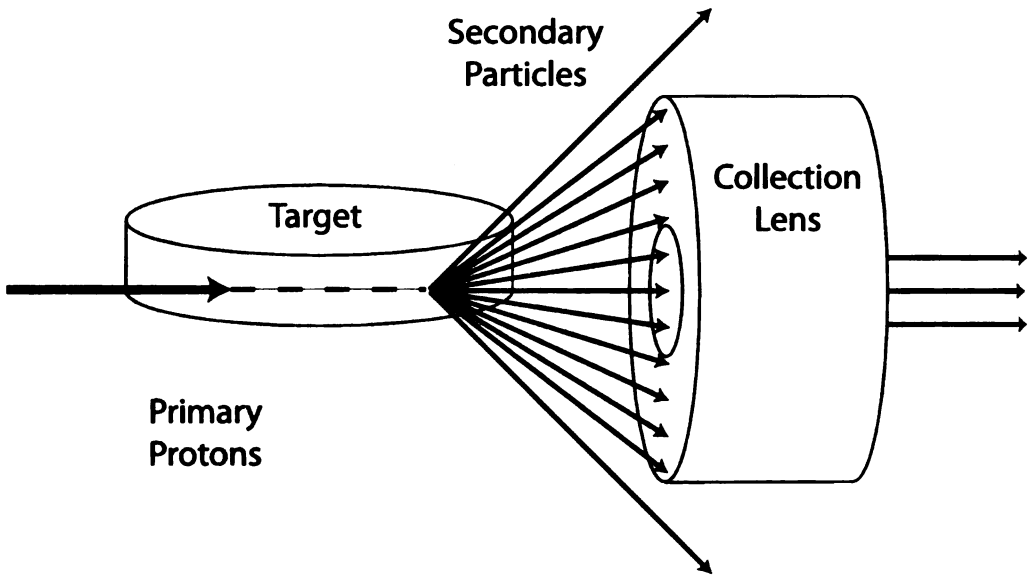

Figure 4.4: Schematic diagram of the $\bar{p}$ production [14].

4.1.6 Tevatron

The Tevatron [67] is the final stage in the acceleration chain (The circumference of the Tevatron is about 6.3 km). It uses RF cavities to bring the energy of the protons and the antiprotons to 980 GeV, which is equivalent to a center-of-mass energy of 1.96 TeV. While sharing the same beam pipe, the protons rotate clockwise while the antiprotons travel in the opposite direction..

The Main Injector sends 36 bunches of protons and 36 bunches of antiprotons to the Tevatron. These sets of bunches constitute a "store". The spacing between bunches is 396 ns with a gap of 2.64 μs every 12 bunches. The beams are magnetically squeezed and forced to interact with each other at two points, DØ and CDF.

4.2 The DØ Detector

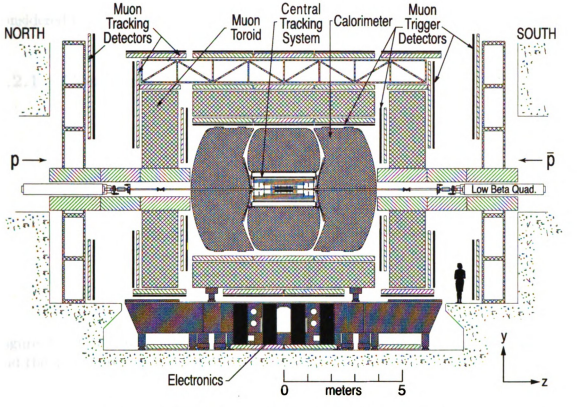

Figure 4.5: Schematic view of the DØ detector [15].

The DØ detector was designed to study collisions of protons and anti-protons at a center of mass energy of 1.96 TeV [15] [68] , and optimized to study high mass states and large p_T phenomena. The DØ detector consists of four major subsystems: central tracking, calorimeter, muon spectrometer, and trigger systems, as shown Figure 4.5. The central tracker allows precise measurement of particles near the collision point; it is composed of a silicon micro-strip tracker (SMT), a central fiber tracker (CFT), and a 2 T solenoid. Between the solenoid and the calorimeter there are preshower detectors used for the electron identification. The calorimeter is divided into three sections: one in the central region and two end caps. The purpose of the calorimeter is to identify and measure energy depositions of electromagnetic and hadronic particles.

The outer-most layer of DØ is used to detect muons. DØ also incorporates a trigger system that receives the signals from all the sub-detectors and selects events that are considered to be interesting enough to be analyzed.

4.2.1 Coordinate system

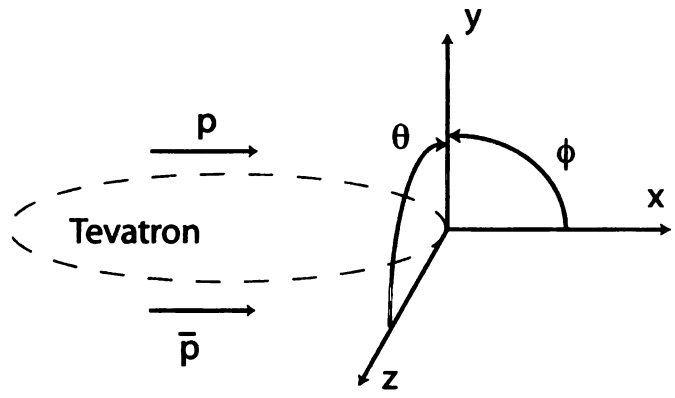

Figure 4.6: Coordinate system used at DØ, the z-axis is along the proton direction and the y-axis upward.

DØ uses a right-handed coordinate system with the z-axis along the proton direction, and the y-axis pointing upward. The angles ϕ and θ are the azimuthal and polar angles, as shown in Figure 4.6. The polar angle is commonly described by the pseudo-rapidity η, defined as:

$$\eta = -\ln\left[\tan\left(\frac{\theta}{2}\right)\right] \tag{4.1}$$

in the limit of $m << E$, the pseudo-rapidity approximates the true rapidity y, defined as:

$$y = -\frac{1}{2}\log\left[\frac{E+p_z}{E-p_z}\right] \tag{4.2}$$

which is an invariant quantity under Lorentz boosts along the z-axis. This quantity is zero for particles with $\theta = 90°$, and high values for $\theta \to 0°$.

4.2.2 Luminosity Monitor

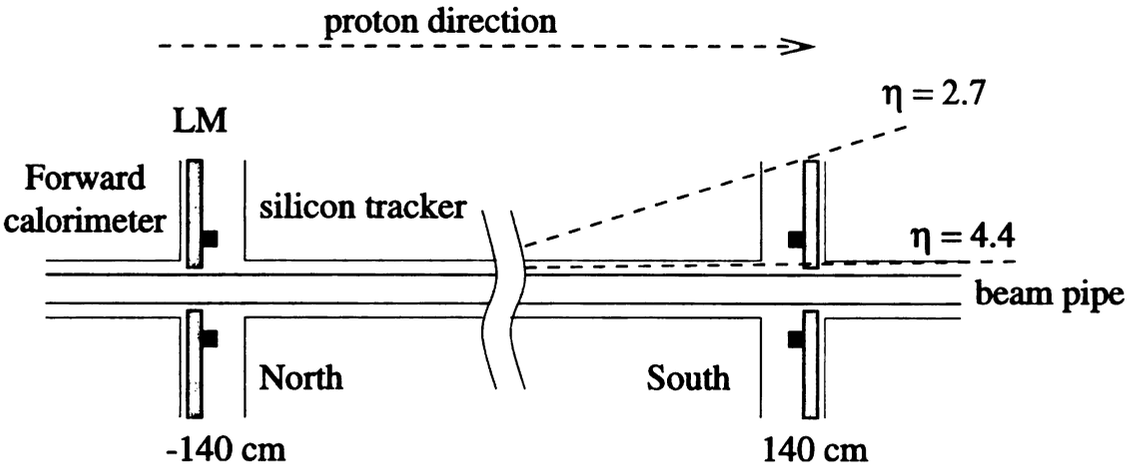

Figure 4.7: Schematic view of the DØ Luminosity monitors [15].

Luminosity is a quantity that represents the number of particles per unit of area per unit time, and is related to the rate of a given process as follows:

$$Rate = \frac{dN}{dt} = \sigma \times \mathcal{L} \tag{4.3}$$

where σ is the total cross section. DØ uses the Luminosity Monitor (LM) described in detail the in [69] to collect information about inelastic $p\bar{p}$ collisions for each bunch crossing. The LM consists of two arrays of 24 plastic scintillator wedges located at $z = \pm 140$ cm, and covering the pseudo-rapidity region of $2.5 < |\eta| < 4.4$, see Figure 4.7. In addition to determining the Luminosity, the LM also measures the beam halo rates and the z-coordinate of the interaction vertex.

The instantaneous Luminosity is measured as:

$$\mathcal{L} = \frac{f\tilde{N}_{LM}}{\sigma_{LM}} \tag{4.4}$$

where f is the beam crossing frequency $\sim$ 2.53 MHz, $\tilde{N}_{LM}$ is the average number of $p\bar{p}$

inelastic collisions, and σ_{LM} is the effective cross section. The integrated luminosity [1] delivered at DØ is presented in Figure 4.8. The z-vertex can be measured using the time of flight from North and South detectors: $z_{vtx} = \frac{c}{2}(T_S - T_N)$. The approximate resolution of z_{vtx} is about 6 cm.

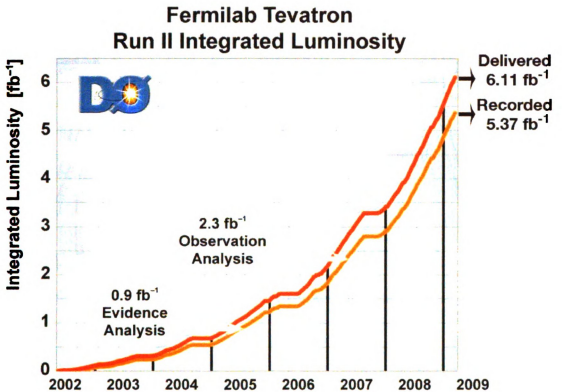

Figure 4.8: Integrated Luminosity delivered at DØ [16].

4.2.3 Central Tracking

There are two central tracking detectors: the Silicon Microstrip Tracker (SMT) and the Central Fiber Tracker (CFT), which are contained in a 2 T magnetic field. The purpose of the SMT is to measure the momenta of charged particles and the location of the primary vertex. The resolution of the central tracking system is 35 μm. Figure 4.9

[1] The integrated luminosity L, is defined as the instantaneous luminosity $\mathcal{L}$ integrated over time, $\int \mathcal{L} dt$

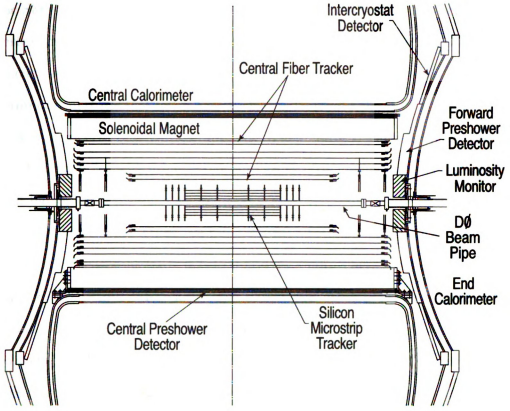

Figure 4.9: Schematic view of the central tracking system and the preshower detectors [15].

shows the location of the system within the DØ detector.

4.2.3.1 Silicon Microstrip Tracker

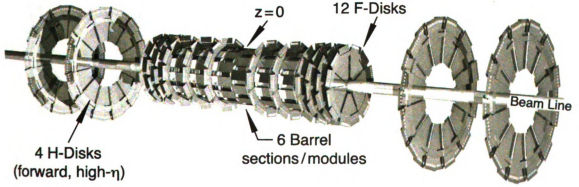

Figure 4.10: 3D Schematic of the Silicon Microstrip Tracker [15].

The SMT is located near the collision point at DØ and provides information about the vertex and tracks of the interactions. It contains an array of silicon barrels and disks positioned to maximize the η coverage. The barrel detectors measure the r and ϕ coordinates, and the disks r, z and ϕ. The barrels and the disk are made of doped silicon with a reverse bias voltage applied. When charged particles pass through the silicon, electron-hole pairs are created, and an electric current can then be measured.

Each barrel has 4 layers. Layers 1 and 2 have 12 ladders each; and layers 3 and 4 have 24, see Figure 4.11. There are 6 barrels for a total of 432 ladders. The centers of the barrels are located at $|z| = 6.2, 19.0$ and 31.8 cm. There are two types of known as disks "F-disks" and "H-disks". One F-disk has 12 double-sided wedges, and an H-disk has 24 full wedges. The F-disks are located at $|z| = 12.5, 25.3, 38.2, 43.1, 48.1$ and 53.1 cm, the H-disks $|z| = 100.4$ and 121 cm. The SMT has total of 932 readout modules, for a total of 792,576 channels. Figure 4.10 is a 3D view of the full SMT detector.

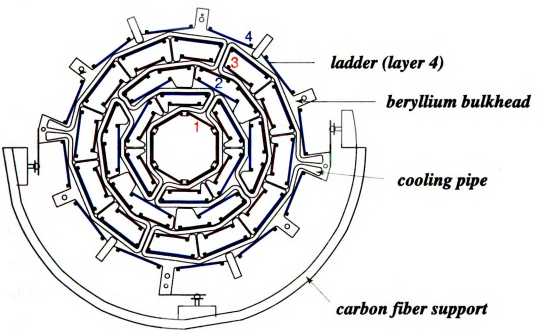

Figure 4.11: Side view of a barrel for the SMT detector [15].

4.2.3.2 Central Fiber Tracker

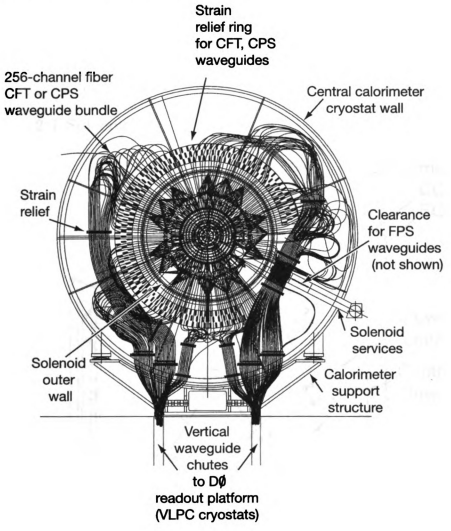

Figure 4.12: Schematic view of Central Fiber Tracker and the clear wave guides fibers [15].

The CFT surrounds the SMT and consists of scintillating fibers positioned in 8 concentric cylinders covering the region $r = 20$ cm to $r = 52$ cm, and $|\eta| < 1.7$. Each cylinder has two doublet layers, one layer parallel to the z-axis, and the second layer aligned at a stereo angle $\phi = \pm 3°$.

When charged particles travel through the fibers, the atoms of the scintillating fiber get excited and emit light with a wavelength of 340 nm. The fibers have a dye which absorbs the 340 nm light which is then emitted at 530 nm. The light is

extracted from the fiber using a waveguide and finally, it is collected by a visible light photon counter (VLPC). The position of a particle is determined by the crossing of the fibers. The CFT resolution is approximately 100 μm. Figure 4.12 shows the south face of the CFT and the waveguides.

4.2.3.3 2 T Solenoid

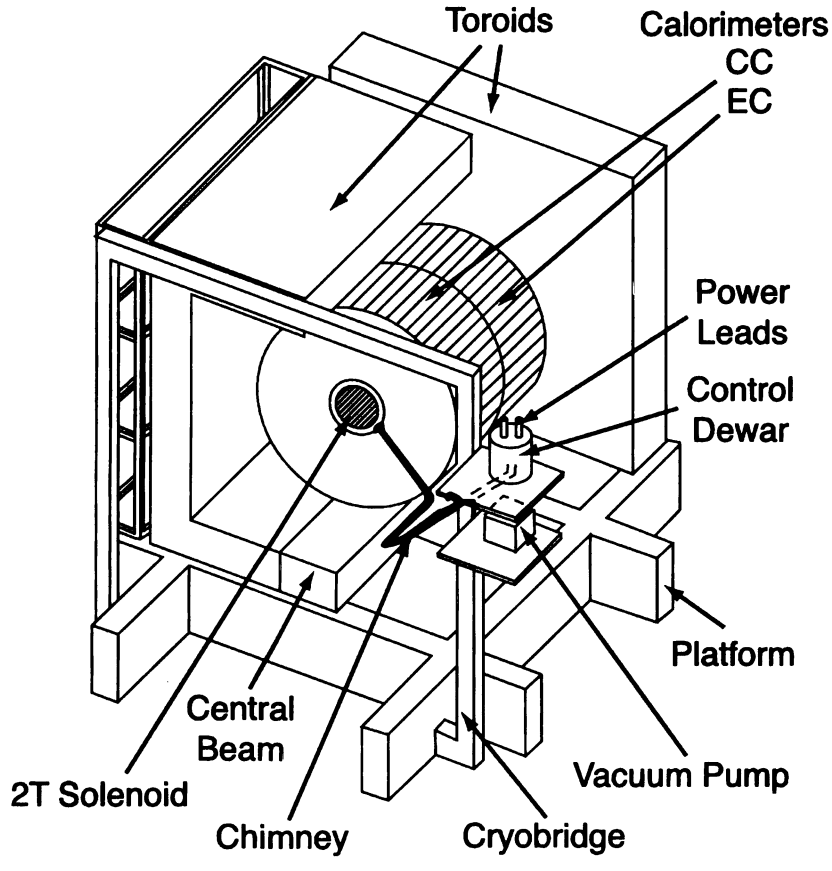

Figure 4.13: Location of the solenoid with respect to the other component of the DØ detector [15].

The 2 T superconducting solenoid, containing both the CFT and the SMT, was designed to optimize the momentum resolution. The size of the magnet is 2.73 m in length by 1.42 cm in diameter. Figure 4.13 shows the location of the solenoid with

respect to the other parts of DØ.

The magnet has two layers of superconducting conductors made of Cu:NbTi. The cooling system uses liquid helium to maintain its superconducting state. The operating current of the solenoid is 4749 A. In Figure 4.14 the magnetic field for both the solenoid and the toroid is shown.

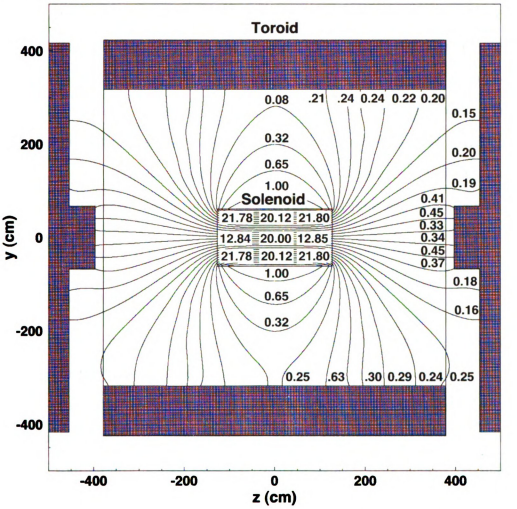

Figure 4.14: Side view ($y - z$) of magnetic field for the solenoid and the toroids [15].

4.2.4 Preshower detectors

The preshower detector assists in the reconstruction of electrons, photon identification and background rejection. It is composed of three parts: the Central Preshower

(CPS) covering the region $|\eta| < 1.3$ and located between the solenoid and the Central Calorimeter at $r = 72$ cm, and two Forward Preshower (FPS) covering the region $1.5 < |\eta| < 2.5$ located next to the faces of the end calorimeters. The preshower detectors can be seen in Figure 4.9.

The CPS has three layers of scintillating fibers, one parallel to the z-axis and the other two at an stereo angle of $\phi = +23.8°$ and $\phi = -24.0°$, respectively. There are a total of 1280 strips in the CPS. The FPS has four double layers of triangular-shaped scintillating strips; the first two layers are at an angle of 22.5° relative to each other, a radiator 11 cm thick follows and finally two more scintillating layers. Charged particles appear in the first two layers or minimum ionizing particle (MIP) layers. The radiator causes both electrons and muons to start showering, and the final two layers are used to detect the showering of electrons and photons, and separate them from hadrons.

4.2.5 Calorimeter

The calorimeter is composed of one central calorimeter (CC) and two end caps (EC) - north and south. It provides energy measurements for photons, electrons and jets. The three parts of the calorimeter are illustrated in Figures 4.15 and 4.16. The calorimeter intercepts most of the particles energy, causing them to interact within the detector volume producing "showers" of increasingly lower-energy particles. A cartoon diagram of the showering process is shown in Figure 4.17. The CC covers $|\eta| \lessapprox 1.0$, and the two end calorimeters extend the coverage to $\eta \approx 4.0$.

Each calorimeter is built similarly with an electromagnetic region, a fine hadronic section and a coarse hadronic section. The EM section uses plates of depleted uranium as absorbing material and liquid argon as the active medium. The fine hadronic section uses uranium-niobium plates as absorbing material, and the coarse hadronic section uses copper and stainless steel plates. Both of the hadronic sections use liquid

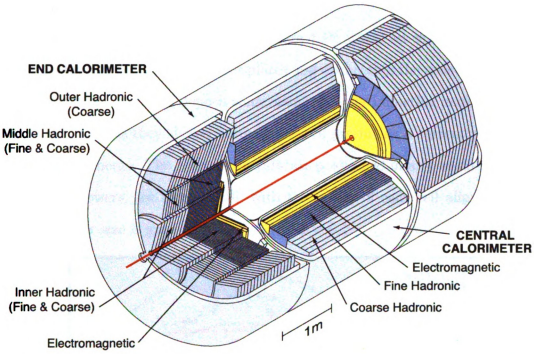

Figure 4.15: 3D view of the DØ calorimeters, central and end caps [15].

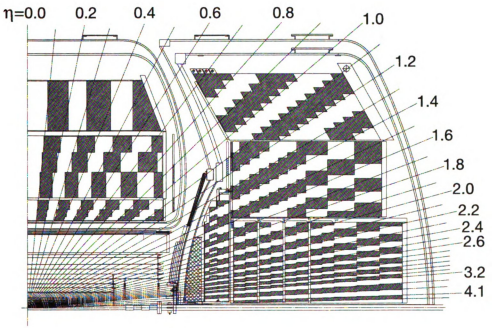

Figure 4.16: Schematic view of the transverse cut of one of the octants of the DØ calorimeter. The shading pattern indicates cells for signal readout. The η coordinates are represented by the radial lines [15].

argon as the active medium.

A typical calorimeter cell is shown in Figure 4.18, where an electric field is established by grounding the metal absorber plates and connecting the resistive surfaces to a 2 kV high voltage. Particles deposit some energy into the inducting material and ionize the liquid argon as they shower through the cell producing a current proportional to the particle's energy. The calorimeter cells are positioned in a "pseudo-projective" set of readout towers, see Figure 4.16, with the center of each cell aligned for each tower. The tower size is generally $\Delta\eta = 0.1$, $\Delta\phi = 0.1$.

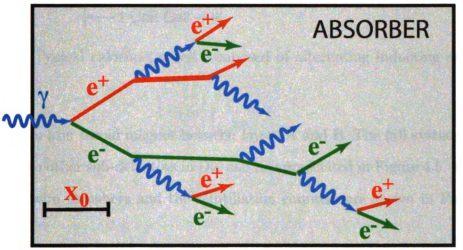

Figure 4.17: Example of an electromagnetic shower, when a photon interacts with the absorber material. X_0 is the radiation length.

4.2.6 Muon System

Muons do not deposit much energy in the tracker or the calorimeter, therefore a special sub-detector is needed to confirm the muon's detection. The DØ muon measuring system consists of toroidal magnets, proportional drift tubes (PDT), central scintillation counters, and mini drift tubes (MDT). The central system covers the region of $\eta \lessapprox 1.0$, and the forward system extends the coverage up to $\eta \approx 2.0$. The muon detector has three layers: A, B and C, with layer A located closer to the interaction point,

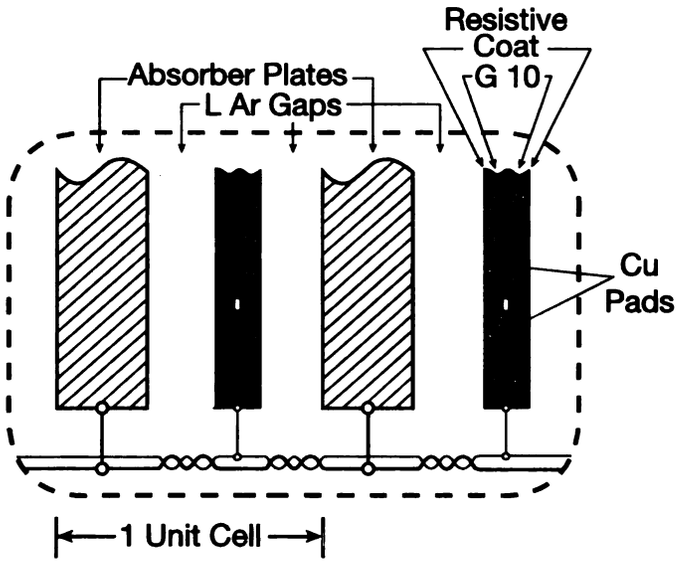

Figure 4.18: Typical calorimeter cell composed of alternating inducting and active material [15].

and within the iron toroid magnet between layers A and B. The full system location with respect to other sub-detectors in DØ can be appreciated in Figure 4.5. Exploded views of the wire chambers and the scintillation counters are shown in Figure 4.20 and 4.21.

The drift chambers are used to measure the muon position and momentum. Each chamber consist of two walls held at a negative voltage, and a central wire with a positive voltage. Both walls and the central wire are surrounded by an inert gas that is ionized when the muons travel through the chamber. The scintillators provide precise timing measurements which are used by the triggering system. When the muons pass through the scintillator counters, light is produced, which is then collected by a photomultiplier. The photomultiplier sends the signal to the read out system. The outer most scintillator counters are used to reject cosmic rays muons signals, by associating a muon in a PDT with the appropriate bunch crossing. The toroid improves the measuring capabilities of the muon momentum by bending the muons as they enter the 1.8 T magnetic field.

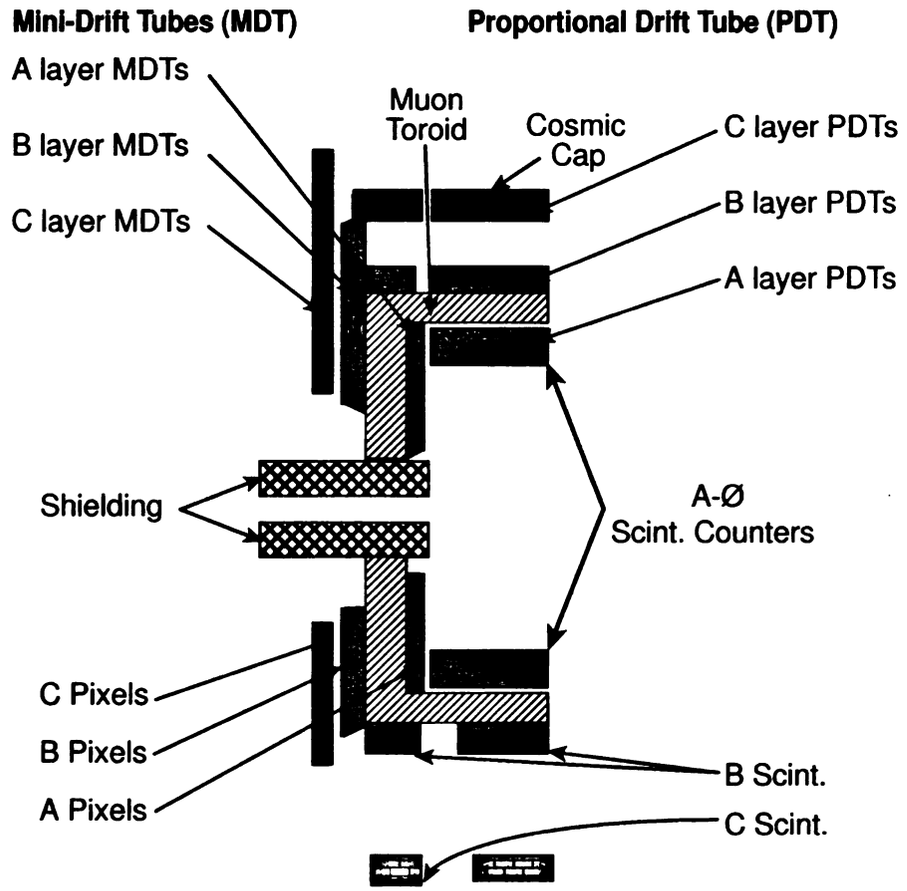

Figure 4.19: Schematic view of the full muon detector system [15].

4.2.7 Triggering

The trigger system uses the information provided by each of the sub-detectors to select interesting physics events to be stored to tape. There are three levels of triggering, each one reducing the number of events, but with an increasing complexity in the processing. The first level (Level 1 – L1) handles all the processing by a collection of hardware elements and reduces the event rate from 1.7 MHz to 2 KHz. The second level (Level 2 – L2) incorporates more sophisticated hardware computing engines and delivers a trigger decision based not only on individual detector elements, but also correlations among them; the acceptance rate for L2 is 1 kHz. Finally, events passing L1 and L2 are sent to a processing farm of microprocessors, Level 3 – L3. At

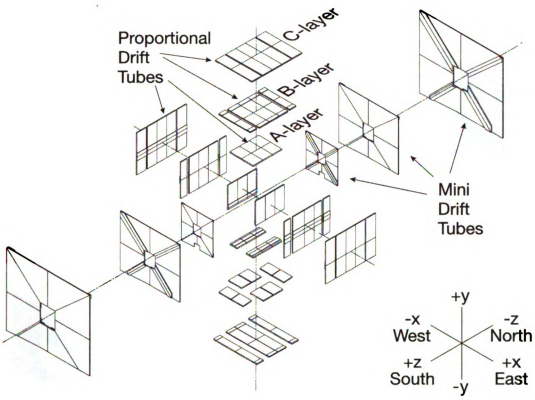

Figure 4.20: Muon wires [15].

L3, complex algorithms reduce the acceptance rate to about 50 Hz, which is the rate the events are stored for offline reconstruction. The overall operation of the trigger is controlled by the COOR package, which interacts with the trigger framework (TFW) and the data acquisition system (DAQ). A block diagram of the DØ trigger system is shown in Figure 4.22.

Due to the fact that all Level 1 decisions should be made quickly, the tools available are limited compared to the other triggering levels where more complex operations are done. At L1, only the calorimeter trigger tower information, the muon detector signals and the transverse momentum of charged particles tracks in the CFT are available. At Level 2, the correlations among different sub-detectors use global physics objects such jets and electrons to based the decision made at this stage (L2Global). Figure 4.23 shows a flow diagram for both L1 and L2 triggering.

The final portion of the triggering system is the L3 computer farm, which consists

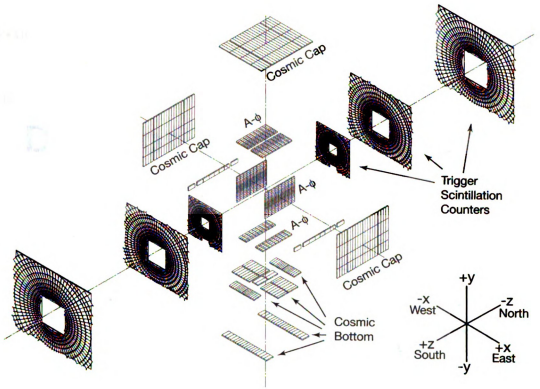

Figure 4.21: Muon scintillators [15].

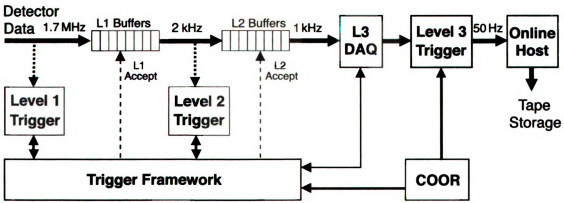

Figure 4.22: Trigger overview block diagram [15].

of approximately 100 nodes. The Level 3 trigger collects the information from all the sub-detectors for events that passed the Level 1 and Level 2 requirements. The selection done at this level is complex where some partial reconstruction of events occurs and more elaborate cuts can be applied. The reconstruction algorithms are similar to those encountered in the offline processing.

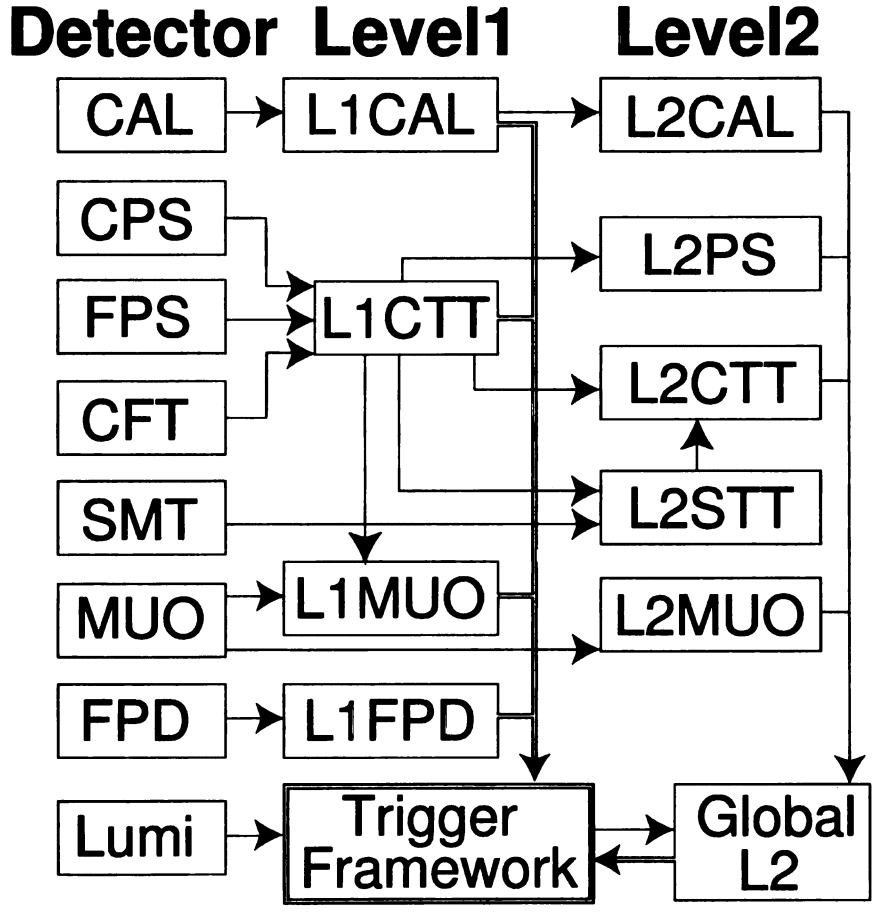

Figure 4.23: Block diagram of the L1 and L2 trigger systems [15].

Chapter 5

Event Reconstruction and Object Identification

To fully represent the interactions that occur at the DØ detector one must refer to the results of reconstruction algorithm known as d0reco [70], rather than the subdetectors. These algorithms process the raw data and produce final physics objects such as electrons, muons or jets. The aim of this chapter is to describe these reconstruction algorithms and the requirements used to define physics objects.

5.1 Reconstruction

5.1.1 Tracks

When charged particles travel through the Central Tracking System (see Figure 4.5) energy is deposited in the silicon strips of the SMT and in the fibers of the CFT. These energy deposits are known as "hits." The tracking system uses the information from sequences of hits to defined tracks to determine the trajectories of the particles immersed in the 2 T magnetic field present in the solenoid.

DØ uses two algorithms to find tracks: Histograming Track Finding (HFT), and the Alternative Algorithm (AA). Both are combined using a Kalman filter by a Global

Track Reconstruction (GTR) algorithm, defining the final set of tracks in the event.

Histogramming Track Finding (HTF)

The HTF [71] algorithm uses a Hough Transformation to map points from the (x, y) space into the (ρ, ϕ) space. This algorithm uses the principle that if a hit occurs in the point (x, y) then there must be a track coming from the origin with curvature ρ and direction ϕ. When all the hits are mapped to the ρ and ϕ plane, they will populate a peak rather than being uniformly distributed in the plane which is the case for random hits. A histogram is populated with the information of the (ρ, ϕ) plane and passed by a Kalman filter for further cleaning and fitting tracks. The passing tracks go through a second, similar histogramming procedure that uses the hits locations (r, z) to form lines in the (z_0, C) plane, with z_0 defined as the starting position of the track along the z-axis and $C = dz/dr$, the track inclination. The tracks are then formed by passing the histograms through another Kalman filter and finally by extrapolating the points to tracks.

Alternate Algorithm (AA)

The AA [17] constructs tracks by progressively adding layers from both the SMT and the CFT to the track definition starting from hits in the SMT detector. The first step in the reconstruction consists of pattern recognition of possible tracks with hits in at least three layers of the SMT detectors. The first hit must come from one of the F-Disks of the SMT detector, the next hit must be within $\Delta\phi < 0.18$ with respect to the first point, and the last hit is chosen where the track hypothesis has a circle radius of at least 30 cm (corresponding to having a track with at least 180 GeV) and an axial impact parameter of less than 2.5 cm with respect to the beam spot. The reconstruction algorithm is illustrated in Figure 5.1.

The hypothesis track is then extrapolated to subsequent layers and hits are added

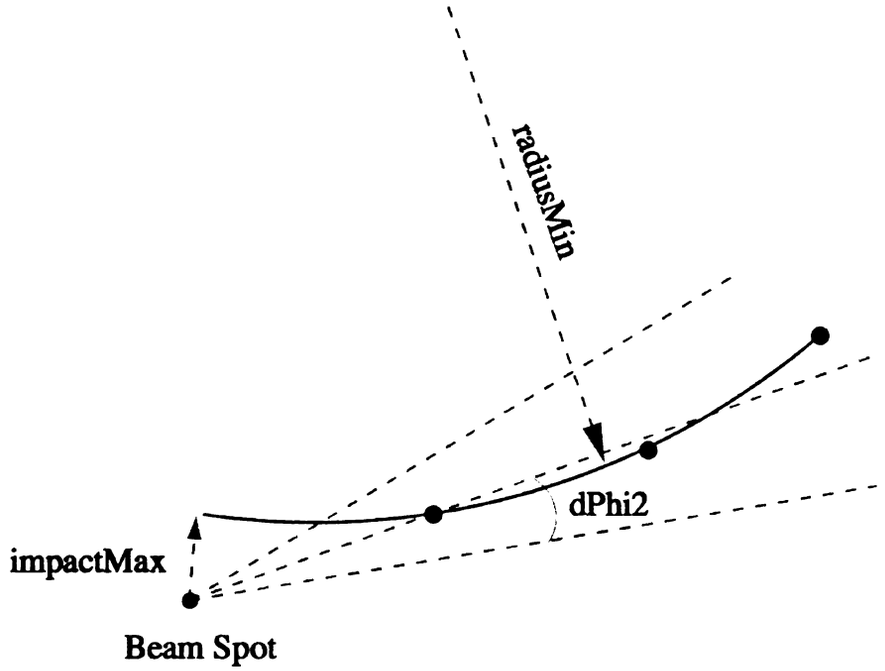

Figure 5.1: Illustration of the AA algorithm for track reconstruction [17].

to the hypothesis if the $\chi^2 < 16$; if there multiple hits in a layer, a new hypothesis is then created. The fitting continues until there are three consecutively missed layers or the end of the detector is reached. The quality of a hypothesis is measured by the number of missed layers, number of hits, the χ^2 associated to it, and some other goodness measurements. The pool of available hypothesis is then ranked. Similarly, tracks can be reconstructed with the CFT-only information, but the quality of these tracks is not as good as those defined using the SMT.

5.1.2 Primary Vertices

The primary vertices (PV) correspond to the location of the hard scatter interaction point. Their proper identification is important for the correct reconstruction of physics object. The PV are reconstructed by the usage of an adaptive primary vertex algorithm [24], which consists of three steps: vertex finding, vertex fitting and vertex

selection.

The vertex finding is performed by clustering tracks according to their z-position. The selected tracks must have $p_T > 0.5$ GeV and more than two SMT hits. The clustered tracks are fitted to a common vertex using a Kalman filter, whereby iteratively removing tracks with the highest contribution to the χ^2 until the total vertex χ^2 per degree of freedom is reduced to less than 10. The tracks are then preselected according to the cluster distance to the closest approach to the beam spot (DCA), requiring the selected tracks to have a DCA significance ($|DCA|/\sigma_{DCA}$) < 5.0. After the preselection, the tracks are fitted using the adaptive vertex fitter algorithm, where each track receives a weight given by:

$$w_i = \frac{1}{1 + e^{(\chi^2 - \chi^2_{cutoff})/(2T)}} \tag{5.1}$$

where χ^2_i is the contribution of the i^{th} track to the χ^2 and χ^2_{cutoff} and T are fixed parameters that control the function. The reweighting procedure is repeated until the change in the weight with respect to the previous iteration is less than 0.1. Finally, the vertex is chosen as that with the lowest probability of being one which came from a minimum bias interaction [72].

5.1.3 Electrons

Electrons are defined as clusters of energy depositions in the calorimeter, together with a track confirmation from the Central Tracking System [73, 23]. The shower produced by an electron candidate must be consistent with the shower of an electromagnetic object.

The electrons are reconstructed mostly using the EM section of the calorimeter. Possible electron candidates are formed by clustering EM towers in a cone of $\Delta R < 0.4$ near a seed tower with $E_T > 0.5$ GeV. It is also required that at least 90% of the

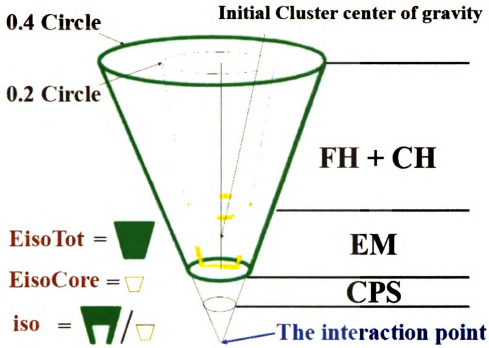

Figure 5.2: Illustration of the isolation parameter. EisoTot is the energy in a cone of radius 0.4. EisoCore is the energy in a cone of radius 0.2 (using EM layers). The numerator of iso subtracts EisoCore from EisoTot.

energy deposited by cluster is located in the EM section of the calorimeter, a quantity known as the Electromagnetic Fraction. The EM objects deposit most of their energy in narrow regions of the EM layers, while hadronic objects have a much wider radius. This measurement is quantified by the isolation, defined as:

$$\text{isolation} = \frac{E_{total}(\Delta R < 0.4) - [E_{EM}(\Delta R < 0.2)]}{E_{EM}(\Delta R < 0.2))} \tag{5.2}$$

where $E_{total}(\Delta R < 0.4)$ is the total energy in both the hadronic and electromagnetic part of the calorimeter within $\Delta R < 0.4$. The isolation definition is illustrated in Figure 5.2. Additionally a covariance matrix is formed from the information of the shower energy fraction, cluster size, total energy shower and primary vertex position. A 7×7 H-matrix is then defined as the inverse of the covariance matrix, $H = M^{-1}$.

Finally, a likelihood discriminant [74] is built in order to differentiate a cluster

coming from an Electromagnetic object from one of a Hadronic object with a large EM fractions:

$$\mathcal{L}_{\text{EM}} = \frac{\mathcal{P}_{\text{sig}}}{\mathcal{P}_{\text{sig}} + \mathcal{P}_{\text{bkg}}} \tag{5.3}$$

where $\mathcal{P}_{\text{sig}}$ and $\mathcal{P}_{\text{bkg}}$ are the probabilities of an EM object to be signal or background repectively.

For the results presented in this dissertation the electrons must be within $|\eta^{\text{det}}| < 1.1$ (Only CC electrons), and they can be one of the following types:

- **Loose, isolated electron**

  A loose, isolated electron is defined by:

  - Electron ID=10, ±11;
  - EM fraction at least 90%;
  - The χ^2 from the H-matrix must be less than 50;
  - The energy deposition in the calorimeter must be matched to a charged particle track from the tracking detectors with $p_T > 5$ GeV and z(track, primary vertex) < 1 cm;
  - The isolation must be greater than 0.15; and
  - The transverse momentum $p_T(e) > 15$ GeV.

- **Tight, isolated electron**

  A tight, isolated electron must pass all the loose, isolated electron requirements and have a value of EM-likelihood $\mathcal{L}_{\text{EM}} > 0.85$.

- **Orthogonal electron**

  An "orthogonal" electron is defined to have EM fraction > 0.9, H-matrix $\chi^2 < 50$, isolation < 0.15, $p_T(e) > 15$ GeV, and $\mathcal{L}_{\text{EM}} \leq 0.85$. There are

no requirements for a matching track. The orthogonal electrons are used to define the multijet background sample.

5.1.4 Muons

Muons are defined by using the hits information of the A, B and C layers of the muon detection system and by matching the tracks from the Central Tracking System to these hits [75, 20, 21].

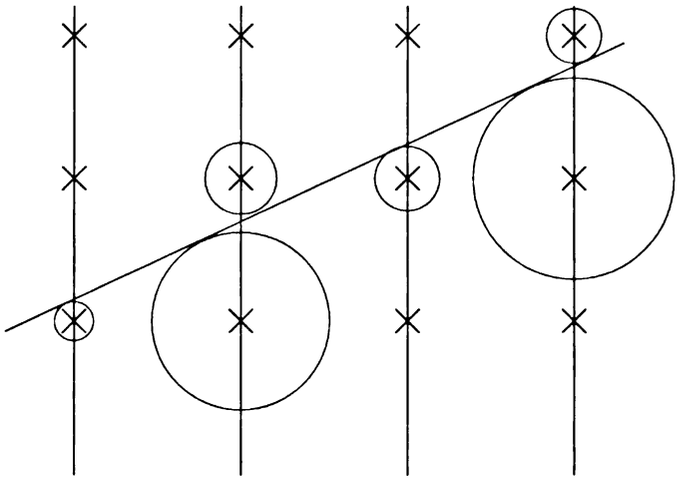

Figure 5.3: Cartoon representation of the muon track segment algorithm. The wire's are represented by the black x's, the MC track by the blue line, and the drift circles are red.

The first step in the muon identification corresponds to the pattern study of the hits in the muons chambers [76]. A straight line called "segment" is fitted through the hits, followed by a fit of the segment to the scintillators hits consistent with the segment trajectory. Using the Toroid magnet, the p_T of the muon can be measured by fitting the trajectories of the hits' curvature. A muon defined with only the track from the muon system is known as "local" muon. The resolution of a local muon can be improved by matching the segment to a track in the Central Tracking System.

Muons are described in terms of *type* and *quality*. The *type* is represented by *nseg*: A muon with segments in the A-layer has $nseg = 1$; one with segments in the

B and C layers, $nseg = 2$; and with segments in all layers has $nseg = 3$. $nseg$ is positive for muons with central track matching and negative for no matching. The *quality* is described by the location and types of hits in the muon system and can be *Loose*, *Medium* or *Tight*.

- Tight muons

  A Tight muon must satisfy: $|nseg| = 3$, at least two A layer wire hits, at least one A layer scintillator hit, at least three BC layer wire hits, at least one BC scintillator hit and a converged, local fit.

- $|nseg| = 3$ Medium/Loose muons

  A Medium $|nseg| = 3$ muon satisfies: $|nseg| = 3$, at least two A layer wire hits, at least one A layer scintillator hit, at least two BC layer wire hits, at least one BC scintillator. If one of the tests fails, the muon is considered Loose.

- $nseg + 2$ Medium/Loose muons

  A Loose $nseg+2$ muon satisfies: $nseg+2$, at least one BC layer wire hit, at least one BC scintillator. If the muon is located in $|\eta_{detector}| < 1.6$ it is considered Muon $nseg + 3$.

- $nseg + 1$ Medium/Loose muons

  A Loose $nseg + 1$ muon satisfies: $nseg + 2$, at least two A layer wire hits, and at least one scintillator hit. If the muon is located in $|\eta_{detector}| < 1.6$ it is considered Muon $nseg + 1$.

The quality of the muon track can be one of the following:

- *Loose track:* $|dca| < 0.2$ cm, or $|dca| < 0.02$ cm for muons with a SMT hit.

- *Medium track:* fulfills loose track requirements and $\chi^2/d.o.f. < 4$.

- *Tight track:* fulfills medium track requirements and has SMT hits.

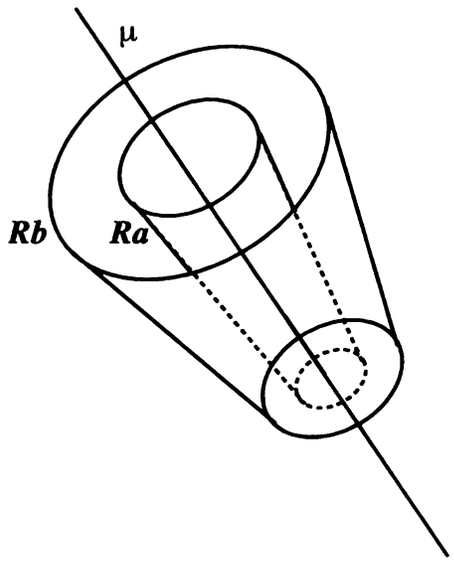

Figure 5.4: A hollow cone in R, with the inner edge R_a and the outer edge R_b surrounding the muon. The transverse energy of the cells contained in the cone are added defining the cone Halo.

The muon isolation variables are designed to separate $W \rightarrow \mu\nu$ signal from heavy flavor background ($B \rightarrow \mu$). Based on the fact that muons from heavy flavor decays are usually inside the jet, these variables are:

- TrackHalo: $|\sum^{tracks} p_T|$ in $\Delta R(track, muon\ track) < 0.5$.
- CalorimeterHalo, see Figure 5.4: $|\sum^{cells} E_T|$ in $0.1 < \Delta R(cal-cells, muon\ cal-track) < 0.4$.
- $\Delta R(\mu, jet)$: Distance to closest jet in $\eta - \phi$ space.
- ScaledTrackHalo: $|\sum^{tracks} p_T/p_T(\mu)|$ in $\Delta R(track, muon\ track) < 0.5$.
- ScaledCalorimeterHalo: $|\sum^{cells} E_T/p_t(\mu)|$ in $0.1 < \Delta R(cal-cells, muon\ cal-track) < 0.4$.

In order to discriminate muons coming from the collisions from cosmic rays, the muons candidates are to be registered within 10 ns from the bunch crossing. This criteria is known as the "loose cosmic ray rejection".

In this analysis, the following muon definitions are used:

- **Loose, isolated muon**

  A Loose muon is defined by:

  - The quality of the muon must be *medium* |nseg| = 3;
  - the muon must pass the loose cosmic ray rejection timing requirements;
  - the muon track quality must be "medium" and match to a track in the central tracker;
  - the $p_T(\mu)$ of the muon must be greater than 15 GeV; and
  - $\Delta R(\mu, jet) > 0.5$.

- **Tight, isolated muon**

  Tight isolated muons are loose muons that must pass the additional isolation criterion called "TopScaledLoose," which means the $ScaledTrackHalo < 0.2$ and $ScaledCalorimeterHalo < 0.2$.

5.1.5 Jets

Jets are cone-like objects that represent the traces that strongly interacting particles, such as gluons and quarks, leave in the detector [18]. These traces are present in both electromagnetic and hadronic sections of the DØ calorimenter. It is important that the jet definitions comply with the following requirements [18]:

- Fully specified: selection process, jet variables and corrections must be uniquely defined.

- Theoretically well-behaved: Infrared singularities should not appear in the perturbative calculations. As well, the jet definition should not be sensitive to soft radiation in the event as seen in Figure 5.6. The algorithm should also be

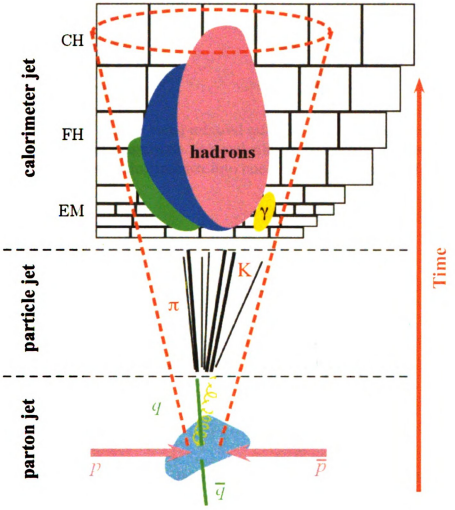

Figure 5.5: Illustration of the evolution of hard-scatter parton in to a jet in the calorimeter.

insensitive to collinear radiation which is illustrated in Figure 5.7. Jets should be also invariant under boosts, computationally easy to implement, and order independent, that is to say that the same jets should be found at either parton, particle or detector level.

- Experimentally specified: jets must be detector independent, not sensitive to angle or resolution smearing, stable with respect to the luminosity, easy to calibrate, and computing resource efficient.

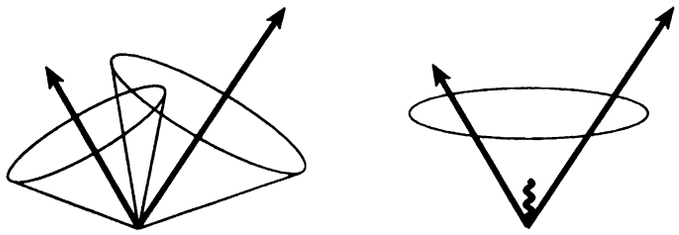

Figure 5.6: Illustration of a jet being infrared safe, the jet clustering occurs near seeds represented by arrows of magnitude proportional to the energy. In the figure on the right, the case of two jets being merged into one due to the presence of soft radiation between them [18].

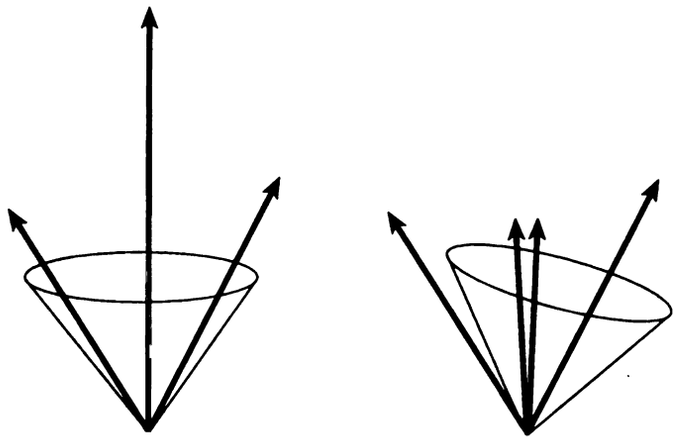

Figure 5.7: Illustration of problems due to collinear radiation on jet algorithms [18].

Before the jet reconstruction starts at DØ, the T42 algorithm [77] is run to remove isolated small energy deposits that are likely due to noise. In order for a calorimeter cell to be considered as a signal cell it is required that the energy deposit on the cell must be at least 4σ, or 2.5σ if the neighbor cell has 4σ energy deposited on it. Here, σ is defined as the RMS fluctuation on the signal in the cell.

The next step in the jet reconstruction is to form energy pre-clusters from the calorimeter towers [1] by first selecting seed towers that have energy deposits greater than X GeV [18]. The seed towers are sorted by p_T, then pre-clustered by adding those with $p_T > 1$ MeV and within $\Delta R < 0.3$. Pre-clusters with $p_T > 1$ GeV are

[1] A calorimeter tower is defined as the sum of all cells with common pseudo-rapidity and azimuthal angle

then added by an iterative process forming objects with $\Delta R < 0.5$ and centroids calculated by using a weighted midpoint cone algorithm [18]. The last step in the jet definition is the splitting and merging of jets. Jets sharing a fraction of energy greater than 50% are merged otherwise they are split into two jets.

In addition to the jet reconstruction, there is a set of criteria used to remove fake jets. These criteria follow the Jet-ID Algorithm Group's recommendations [78] and [79]:

- To remove electromagnetic particles from the list of jets, the jet electromagnetic fraction is required to be $0.05 < EMF < 0.95$.
- To remove jets generated by calorimeter noise, at least 60% of the jet energy must be deposited in the fine hadronic part of the calorimeter since the noise level is higher in the coarse section.
- To remove jets clusters from problematic cells, known as "hot cells", the ratio of the highest to the next-to-highest energetic towers must be less than 10.
- To remove jets coming from a single hot tower, jets for which one calorimeter tower contains more than 90% of the energy are removed.
- To remove residual noise from readout, the jet p_T is compared to the energy found by the level 1 trigger system.

In addition to the previous requirements, this analysis requires that jets have $p_T > 15$ GeV and be within $|\eta| < 3.4$. (The jet p_T cut is made after all corrections have been applied).

5.1.5.1 Jet Energy Scale

The energy in the calorimeter cells differs from the energy of stable particle jets before interacting with the detector. The jet energy scale purpose is to correct for these discrepancies [80]:

$$E_{jet}^{corr} = \frac{E_{jet}^{uncorrected} - O}{F_\eta \times R \times S} \tag{5.4}$$

where $E_{jet}^{uncorrected}$ is the jet energy determined by the reconstruction algorithm, O is the energy offset due to electronic noise, multiple interactions, underlying event, energy pile-up and noise from the Uranium absorber. F_η is the relative response correction to account for the calorimeter different η regions. R is the absolute response correction which represents non-instrumented and lower energy response regions of the calorimeter. S is the showering correction for the energy radiated outside the cone.

5.1.6 Missing E_T

Neutrinos cannot directly be detected at DØ, rather their presence is only inferred from the imbalance of the energy in the transverse plane [81, 82]. The sum of the transverse momenta of undetected neutrinos is therefore equal to the negative sum of the transverse momenta of all particles observed in the detector. In practice, the MET is defined as the vector sum of the electromagnetic and fine hadronic calorimeter cell energies, the cells in the coarse hadronic calorimeter are only added if they are part of a good jet. Finally, additional corrections are applied to the MET calculation to account for corrections applied to reconstructed objects and for the presence of muons.

5.1.7 b-tagging

In the Single Top analysis, it is important to identify jets that come from the decay of a b-quark, since the final state of the Single Top final involves at least one b-jet. After the b-quark hadronizes into a b-hadron, it will decay throughout the DØ detector. These b-hadrons have a longer lifetime than lighter hadrons resulting in a displaced decay vertex from the primary interaction point; this displacement is typically a few

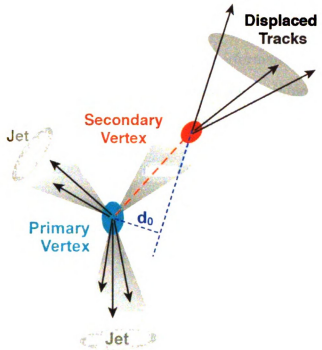

Figure 5.8: Illustration of the secondary vertex formed by the decay of a b-hadron. [17].

millimeters. The b-jets are identified by using this displacement, together with the the jet kinematical variables.

A neural network b-jet tagger developed by the DØ B-ID group is used to identify b-jets. First, the jets are required to be "taggable" and then the jets are "tagged." For data, the tagging is done directly while for the simulated samples, a parameterization called *tag-rate function* (TRF) is used. The TRFs are derived on data to realistically estimate the b-tagging efficiency in the simulation because the simulated samples have a higher b-tag efficiency than data.

Some quality requirements on the jet to be b-tagged are first imposed to reject different tracking efficiencies, badly reconstructed jets and detector effects in general. This quality selection is called "taggability" and it consists of requiring that the jets have at least two good quality tracks with SMT hits pointing to a common origin.

The details of the taggability calculation are found in the Appendix 6 of the Single Top selection note [19].

The "neural network (NN) tagger" and its performance in data are described in detail in [83]. The NN tagger uses the following variables, ranked in order of separation power, to discriminate b jets from other jets:

- decay length significance of the Secondary Vertex Tagger (SVT);
- weighted combination of the tracks' IP significances;
- Jet LIfetime Probability (JLIP) (probability that the jet originates from the PV);
- χ^2 per degree of freedom of the SVT secondary vertex;
- number of tracks used to reconstruct the secondary vertex;
- mass of the reconstructed secondary vertex; and
- number of secondary vertices found inside the jet.

There are 12 different operating points provided by b-tagger, each defined by a cut on the output of the NN tagger. For the analysis presented in this dissertation the following operating points were used:

- *one tag:* Exactly one jet passes the TIGHT (NNoutput > 0.775) b-tagging cut and no other jet passes the OLDLOOSE cut (NNoutput > 0.5); and
- *two tags:* Two jets pass the OLDLOOSE b-tagging cut.

The veto of a second OLDLOOSE candidate in the one-tag definition ensures that there is no overlap between the one tag and two tags samples.

Chapter 6

Data and Simulation Samples

In this Chapter, the data sample used for the analysis is presented, as well as the simulation samples and their corrections.

6.1 Data Sample

The data sample in this analysis corresponds to the data collected by the DØ detector between April 2002 and August 2007. The events collected during this period of time are known as "RunII" as they correspond to the second phase of the Tevatron physics program. During the RunII there are two periods Run IIa and Run IIb which are differentiated by the upgrade made during the three month shutdown in 2006. Among the upgrades are the SMT, CFT, solenoidal magnet preshower detectors, forward muon detector and forward proton detector [15], which include the associated electronics, triggering [84] and data acquisition systems.

The run numbers for the data collected range from 151,817 to 215,670 inclusive for the Run IIa, and sometimes labeled as *p17*, and from 222,028 to 234,913 sometimes labeled as *p20*. The data used have been reconstructed with production code versions p17.09.03 (refixed), p17.09.06 (unfixed, cable-swap), and p17.09.06 (unfixed, non-cable-swap) for Run IIa data, and p20.07.01 and p20.08.xx for Run IIb data; they

have been obtained from the DØ Common Samples Group [85, 86].

There is a total of 2.3 fb^{-1} of good quality data in each of the electron and muon channels, as shown in Table 6.1 [87].

		Integrated Luminosity [pb^{-1}]		
Channel	Trigger Version	Delivered	Recorded	Good Quality
Run IIa electron	v8.00 - v14.93	1,312	1,206	1,043
Run IIa muon	v8.00 - v14.93	1,349	1,240	1,055
Run IIb e and mu	v15.00 - v15.80	1,497	1,343	1,216
Total Run II Integrated Luminosity				**2.3 fb^{-1}**

Table 6.1: Integrated luminosities for the datasets used in this analysis.

All the data are required to pass any "reasonable" trigger. See Section 6.5 for the definition of "reasonable" trigger and for the efficiencies obtained with it.

6.2 Simulation Samples

In order to extract the final cross section measurement, one must properly model both the signal and background for Single Top such that the sum of the background plus the signal simulated samples are equal to the data samples. All of the processes are simulated using Monte Carlo techniques, with the exception of multijet events, which are obtained directly from the data.

6.2.1 Signal Modeling

The Single Top events sample were generated with the COMPHEP-SINGLETOP [88] Monte Carlo event generator which includes all the details of the current understanding of Single Top quark production. The kinematical distribution of events produced by SINGLETOP match those from NLO calculations [7, 6, 89]. The top quark mass used

for the event generation corresponds to 170 GeV/c^2 [1], the parton distribution functions CTEQ6M are used [91] and the scales are m_t^2 for the s-channel and $(m_t/2)^2$ for the t-channel. The top quarks and the W bosons are decayed in COMPHEP-SINGLETOP to ensure the spins are properly treated. PYTHIA [92] version 6.409 was used to add the underlying event and initial- and final-state radiation. TAUOLA [93] was used to decay tau leptons, and EVTGEN [94] to decay B hadrons.

6.2.2 Background Modeling

The backgrounds for Single Top are W+jets, multijets, Z+jets, $t\bar{t}$, and dibosons. The W+jets, Z+jets and $t\bar{t}$ were generated using ALPGEN [95] which is a leading order matrix element Monte Carlo generator similar to the COMPHEP used for the signal generation. Version 2.11 of ALPGEN was used, which is comprised of a jet-matching algorithm following the MLM prescription [96] to match parton showers with the matrix elements. The matching algorithm ensures that each jet is generated by ALPGEN at the parton level and not filled in by PYTHIA, thus avoiding regions of ΔR and transverse momentum space for the radiated jets that used to be generated twice. For these samples, the parton-matching cluster threshold was set to 8 GeV, and the parton-matching cluster radius size was set to $R = 0.4$.

For the $t\bar{t}$ samples, the top quark mass is set to 170 GeV/c^2, the scale $m_t^2 + \sum p_T^2$(jets) used was along with the CTEQ6L1 pdf set. For the W+jets events, the pdf was the same as for the $t\bar{t}$ events, but the scale was $m_W^2 + \sum m_T^2$, where m_T is the transverse mass defined as $m_T^2 = m^2 + p_T^2$ and the sum $\sum m_T^2$ extends to all final state partons (including the heavy quarks, excluding the W decay products) [95].

The W+light-parton (lp) jets samples must have parton-level cuts on the light partons to avoid divergences in the cross section. These cuts were p_T(lp) > 8 GeV

[1] At the moment of the event generation, the top quark mass average was close to 170 GeV/c^2. Although this mass differs from the the current top quark mass average, the effect on the final result is negligible as shown in References [19, 90].

and $\Delta R(\text{lp, lp}) > 0.4$ for all massless partons (including the charm partons in these samples). For the W +heavy-flavor samples, there are no p_T or ΔR cuts on the b or c partons, but additional light partons have the $p_T(\text{lp}) > 8$ GeV and $\Delta R(\text{lp, lp}) > 0.4$ applied.

In addition, the dibosons WW, WZ, and ZZ which represent only a small fraction of the total background are also included in the analysis. These diboson samples were generated using PYTHIA with inclusive decays.

6.2.3 Additional Monte Carlo Treatments

In all Monte Carlo event sets the duplicate events are removed. For the W+jets and Z+jets the events with heavy flavor jets added by PYTHIA are also removed to prevent duplication of the phase space of those generated already by ALPGEN [97]. The Wcj subprocesses are included in the Wjj sample with massless charm.

All the Monte Carlo events have DØ's version of Tune A for the underlying event[2]. The Single Top and Z+jets samples have the decays into electrons, muons, and taus as separate samples, whereas the W+jets and $t\bar{t}$ samples have them generated together in combined samples with approximately one third of each present (according to the branching fractions).

The Monte Carlo event samples are processed through the the DØ detector simulator "DØgstar" [98] which is based on GEANT [99]. Next, all the events go through the same reconstruction process as the data. Table 6.2 shows the cross sections, branching fractions, and initial numbers of events of the Monte Carlo samples. The central values of the cross sections for Single Top [100] and $t\bar{t}$ pairs [101] are for 170 GeV top mass. The W+jets and Z+jets cross sections are from ALPGEN. The diboson cross sections were calculated using the NLO event generator MCFM [102].

[2] The "underlying event" corresponds to the partons (of the interacting protons and anti-protons) that did not participate in the hard interaction, and the resulting particles and measurements.

	The Monte Carlo Event Sets			
Event Type	Cross Section [pb]	Branching Fraction	No. of p17 Events	No. of p20 Events
Signals				
$tb \to \ell$+jets	$1.12^{+0.05}_{-0.12}$	0.3240 ± 0.0032	0.6M	0.8M
$tqb \to \ell$+jets	$2.34^{+0.13}_{-0.17}$	0.3240 ± 0.0032	0.5M	0.8M
Signal total	$\mathbf{3.46^{+0.18}_{-0.29}}$	$\mathbf{0.3240 \pm 0.0032}$	**1.1M**	**1.6M**
Backgrounds				
$t\bar{t} \to \ell$+jets	$7.91^{+0.61}_{-1.01}$	0.4380 ± 0.0044	2.6M	1.3M
$t\bar{t} \to \ell\ell$	$7.91^{+0.61}_{-1.01}$	0.1050 ± 0.0010	1.3M	0.9M
Top pairs total	$\mathbf{7.91^{+0.61}_{-1.01}}$	$\mathbf{0.5430 \pm 0.0054}$	**3.9M**	**2.2M**
$Wb\bar{b} \to \ell\nu bb$	93.8	0.3240 ± 0.0032	2.3M	2.5M
$Wc\bar{c} \to \ell\nu cc$	266	0.3240 ± 0.0032	2.3M	3.0M
$Wjj \to \ell\nu jj$	24,844	0.3240 ± 0.0032	21.0M	18.3M
W+jets total	**25,205**	$\mathbf{0.3240 \pm 0.0032}$	**25.6M**	**23.8M**
$Zb\bar{b} \to \ell\ell bb$	43.0	0.10098 ± 0.00006	1.0M	1.0M
$Zc\bar{c} \to \ell\ell cc$	114	0.10098 ± 0.00006	0.2M	1.0M
$Zjj \to \ell\ell jj$	7,466	0.10098 ± 0.00006	3.9M	7.0M
Z+jets total	**7,624**	$\mathbf{0.03366 \pm 0.00002}$	**5.1M**	**9.0M**
$WW \to$ anything	12.0 ± 0.7	1.0 ± 0.0	2.9M	0.7M
$WZ \to$ anything	3.68 ± 0.25	1.0 ± 0.0	0.9M	0.6M
$ZZ \to$ anything	1.42 ± 0.08	1.0 ± 0.0	0.9M	0.5M
Diboson total	$\mathbf{17.1 \pm 1.0}$	$\mathbf{1.0 \pm 0.0}$	**4.7M**	**1.8M**

Table 6.2: The cross sections, branching fractions, and initial numbers of events in the Monte Carlo event samples. The symbol ℓ stands for electron plus muon plus tau decays.

6.3 Multijets Background Modeling

The multijet background is modeled using the data events that pass all the selection criteria, excluding the likelihood requirement for electrons and the isolation requirement in the case of muons (see Chapter 7). Below is a more detailed explanation of the procedure to obtain the Multijets background for both muon and electron channels.

6.3.1 Electron Channel

The electron multijets background is modeled using the "orthogonal" dataset. The orthogonal dataset corresponds to the events that pass all selection cuts (before b tagging) but where the EM object fails the electron likelihood cut and is not required to have a matching track. The kinematical distributions of this sample do not completely correspond to those of a multijet background mainly due to the "not track match" requirement. This is solved by reweighting the distributions using the procedure explained below.

The fake-electron probability comes from the "matrix method" of normalization [103, 104]. In this method, the tight data sample (events with a "tight" electron) is a subset of the ultraloose data sample (events with an "ultraloose" electron). The ultraloose sample contains $N_{\text{uloose}}^{\text{real}-e}$ events with a real electron and $N_{\text{uloose}}^{\text{fake}-e}$ fake-electron events. The efficiency for a real ultraloose electron to pass the tight electron selection is $\varepsilon_{\text{real}-e}$, and the efficiency for a fake ultraloose electron to pass the tight electron criteria is $\varepsilon_{\text{fake}-e}$. Thereby N_{uloose} and N_{tight} are given by:

$$N_{\text{uloose}} = N_{\text{uloose}}^{\text{fake}-e} + N_{\text{uloose}}^{\text{real}-e} \tag{6.1}$$

$$N_{\text{tight}} = N_{\text{tight}}^{\text{fake}-e} + N_{\text{tight}}^{\text{real}-e} = \varepsilon_{\text{fake}-e}\, N_{\text{uloose}}^{\text{fake}-e} + \varepsilon_{\text{real}-e}\, N_{\text{uloose}}^{\text{real}-e} \tag{6.2}$$

and $N_{\text{tight}}^{\text{fake}-e}$ can be expressed as:

$$N_{\text{tight}}^{\text{fake}-e} = \frac{\varepsilon_{\text{fake}-e}}{1-\varepsilon_{\text{fake}-e}} N_{\text{uloose}-\text{tight}} - \frac{\varepsilon_{\text{fake}-e}}{1-\varepsilon_{\text{fake}-e}} \frac{1-\varepsilon_{\text{real}-e}}{\varepsilon_{\text{real}-e}} N_{\text{tight}}^{\text{real}-e} \quad (6.3)$$

but the second term is small compared to the first term, which allows it to be rewritten as,

$$N_{\text{tight}}^{\text{fake}-e} = \frac{\varepsilon_{\text{fake}-e}}{1-\varepsilon_{\text{fake}-e}} N_{\text{uloose}-\text{tight}} \quad (6.4)$$

which represents the factor use for the re-weighting of the orthogonal data set. The $\varepsilon_{\text{fake}-e}$ can be parametrized as a function of p_T of the electron as shown in Figure 6.1. The electron p_T distributions before and after the re-weight is applied are shown in Figure 6.2, where the multijet background is shown in brown.

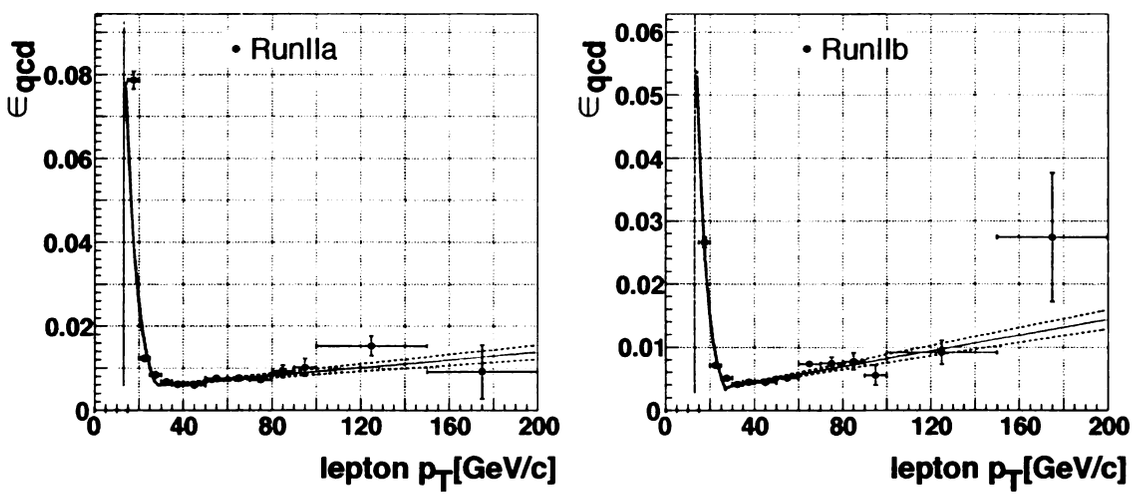

Figure 6.1: $\varepsilon_{\text{fake}-e}$ as a function of electron p_T for Run IIa (p17) (left) and Run IIb (p20) data (right) [19].

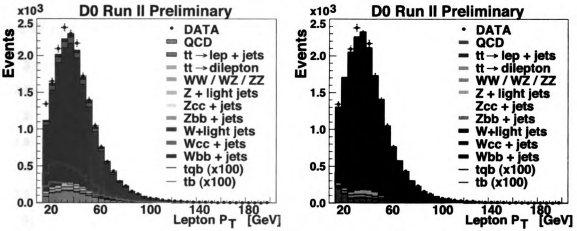

Figure 6.2: Electron transverse momentum distribution before (left) and after (right) multijet background reshaping [19].

6.3.2 Muon Channel

The muon multijets background is modeled using an orthogonal sample, whereby the events pass all selection cuts (before b tagging) however no isolation requirements are imposed to the muon. Events passing the muon channel requirement are also removed to ensure the orthogonality of the samples. In past Single Top analysis [105], an isolation requirement of $\Delta R(\text{muon, jet}) > 0.5$ was required, which led to a statistically limited sample. Removing the ΔR cut the sample size increased the sample size by a factor of ten. In order to make the jets in these events match those in the signal data, any jets close to the muon are removed from the event and $\not\!\!E_T$ is recalculated to regain momentum balance.

A comparison of kinematical distributions for the old and new multijets background models is shown in Fig. 6.3. When looking at these plots one has to keep in mind that both the old sample (labeled "Reverse isolation"), and the new sample (labeled "Large QCD") are only models of the true multijets background present in the signal sample, and do not precisely represent the background. The uncertainties on the multijets background normalization are of the order of (∼30%), and the size

of the background is small compared to other more dominant backgrounds such as in the W+jets background.

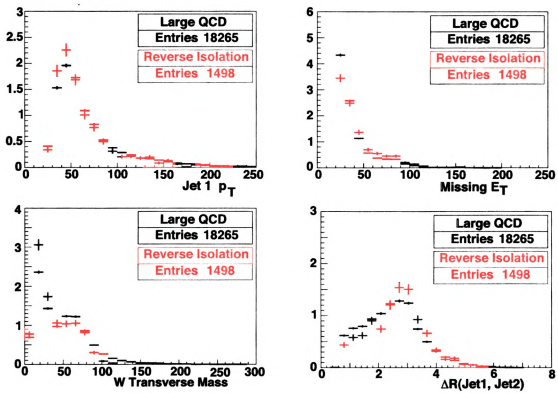

Figure 6.3: Kinematic distributions comparing the old (red points) and new (black points) multijets background models. Upper row, p_T(jet1) and $\not\!\!E_T$, lower row, $M_T(W)$ and ΔR(jet1, jet2) [19].

6.4 Corrections

The description of the data by the simulated samples is not perfect. To rectify these differences, it is necessary to apply corrections to the Monte Carlo. One of the common mismodeling issues is the higher resolutions of the Monte Carlo simulation compared to data, which is corrected by the "smearing" of the event in one variable to better reproduce the data events.

The number of events coming from the simulated samples is obtained by scaling

the Monte Carlo such that the reconstruction and selection efficiencies match those found in data, and by normalizing:

- the $t\bar{t}$, Z+jets, dibosons and Single Top samples to the integrated luminosity of the data-set using the cross sections and branching fractions listed in Table 6.2; and
- the W+jets and multijet samples to data using an Iterative Kolmogorov-Smirnov (IKS) method explained in detail in Section 7.2).

All of the corrections applied to the different objects in Monte Carlo are described in the following pages.

6.4.1 Muons

To study the muon corrections, events from the decay of a Z boson into a pair of muons is used, $Z \rightarrow \mu\mu$. This procedure is known as the "tag-and-probe" method which uses the correlation between the two muons to measure efficiencies. The muon momentum resolution is estimated from the width and shape of the Z peak. The smeared variable is q/p_T, which is proportional to the radius of curvature and where q is the muon charge and p_T, the muon transverse momentum. The smearing can be expressed as:

$$\frac{q}{p_T} \rightarrow \frac{q}{p_T} + (A + \frac{B}{p_T}) \times Rnd \tag{6.5}$$

where *Rnd* is a Gaussian-distributed number centered at zero with width 1, and A and B are measured parameters determined from the $Z \rightarrow \mu\mu$ sample (See Refence [20] for more detail).

In addition to the smearing, the muons are corrected by the following three factors: the muon ID efficiency, the track match, and the isolation. The ID scale factor is parametrized in η_{det} and ϕ, as shown in Figure 6.4; the track match is parametrized in track-z and η_{CFT}, Figure 6.5; and the isolation in η, as shown in Figure 6.6. All

the corrections applied follow the recommendation of the DØ Muon ID Group which are described in Ref. [20, 21]:

$$\varepsilon_{\mu-\mathrm{ID}} = \frac{\varepsilon^{\mathrm{Data}}_{\mathrm{MediumID}}}{\varepsilon^{\mathrm{MC}}_{\mathrm{MediumID}}} \times \frac{\varepsilon^{\mathrm{Data}}_{\mathrm{TrackMatch}}}{\varepsilon^{\mathrm{MC}}_{\mathrm{TrackMatch}}} \times \frac{\varepsilon^{\mathrm{Data}}_{\mathrm{TightIsol}}}{\varepsilon^{\mathrm{MC}}_{\mathrm{TightIsol}}} \tag{6.6}$$

6.4.2 Electrons

The electron corrections are derived by using $Z \rightarrow ee$ data and Monte Carlo samples. The scale factor applied to the Monte Carlo accounts for the differences in electron cluster-finding and identification efficiency. This scale factor is divided into two parts: "preselection" and "post-selection." Preselection refers to the basic electron criteria that are common among many electron quality definitions: ID, electromagnetic fraction, and isolation. The preselection scale factor is parametrized in η_{det} as shown in Figure 6.7. The post-preselection criteria, which are unique for our particular electron quality definition, consist of the H-matrix cut, the track-matching requirements, and the likelihood cut. The post-preselection scale factor is parameterized in $(\eta_{\mathrm{det}},\phi)$. These follow the recommendations by the DØ EM ID Group's certifications [22, 23]:

$$\varepsilon_{e-\mathrm{ID}} = \frac{\varepsilon^{\mathrm{Data}}_{\mathrm{Presel}}}{\varepsilon^{\mathrm{MC}}_{\mathrm{Presel}}} \times \frac{\varepsilon^{\mathrm{Data}}_{\mathrm{PostPresel}}}{\varepsilon^{\mathrm{MC}}_{\mathrm{PostPresel}}} \tag{6.7}$$

6.4.3 Jets

The standard jet shifting, smearing and removal (JSSR) procedures are used to recalibrate and possibly discard simulated jets in a consistent way to force the simulated events to match the data jets. The JSSR determination is completed by studying photon+jet events in both Monte Carlo and data. The main quantity used in this determination is the p_T imbalance, defined as:

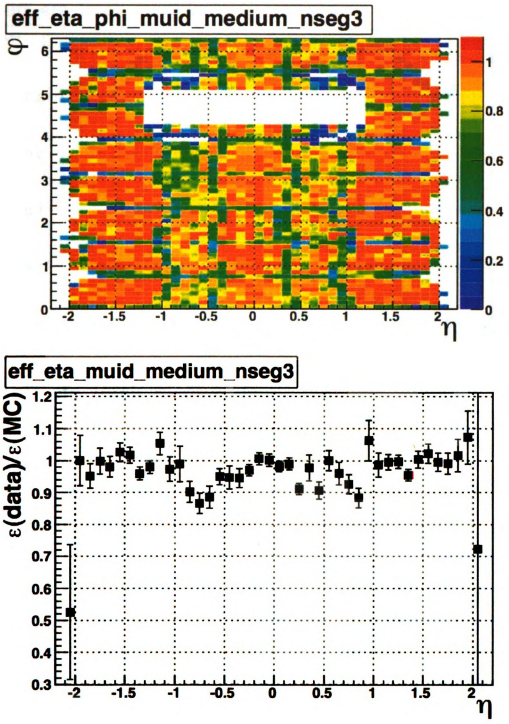

Figure 6.4: Muon reconstruction efficiencies as a function of η_{det} and ϕ for the data in Run IIa (*left*) and ratios of data and MC efficiencies (*right*). The muons in the hole region (bottom part of the detector) are not considered. Similar efficiencies are found for the Run IIb data. [20, 21].

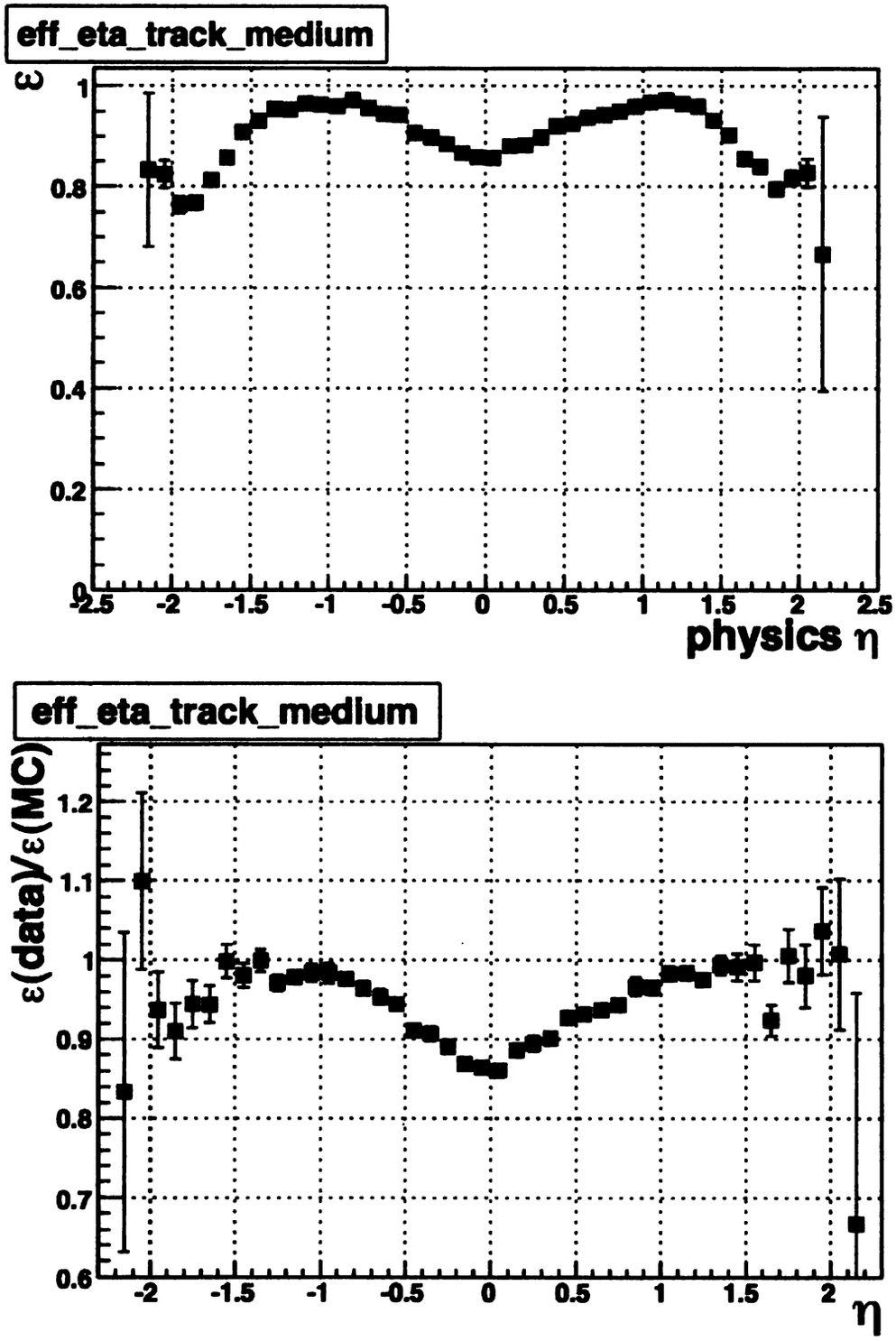

Figure 6.5: Muon track match efficiencies as a function of η_{CFT} for the data in Run IIa (*left*) and ratios of data and MC efficiencies (*right*). Similar efficiencies are found for the Run IIb data. [20, 21].

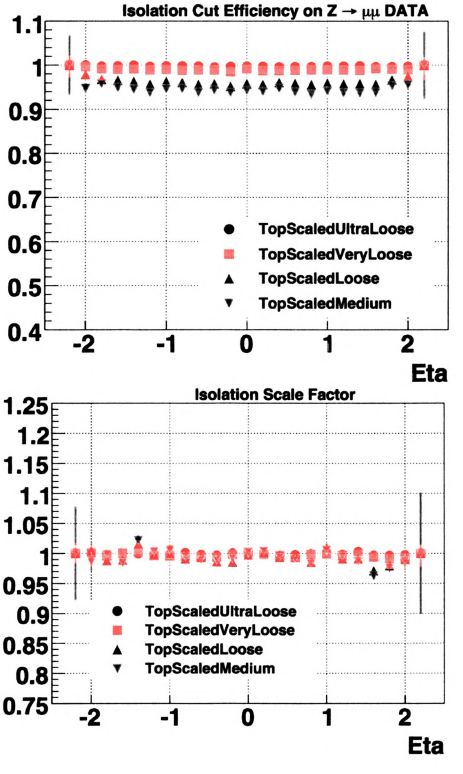

Figure 6.6: Muon isolation efficiencies as a function of η for the data in Run IIa (*left*), ratios of data and MC efficiencies (*right*). Similar efficiencies are found for the Run IIb data. [20, 21].

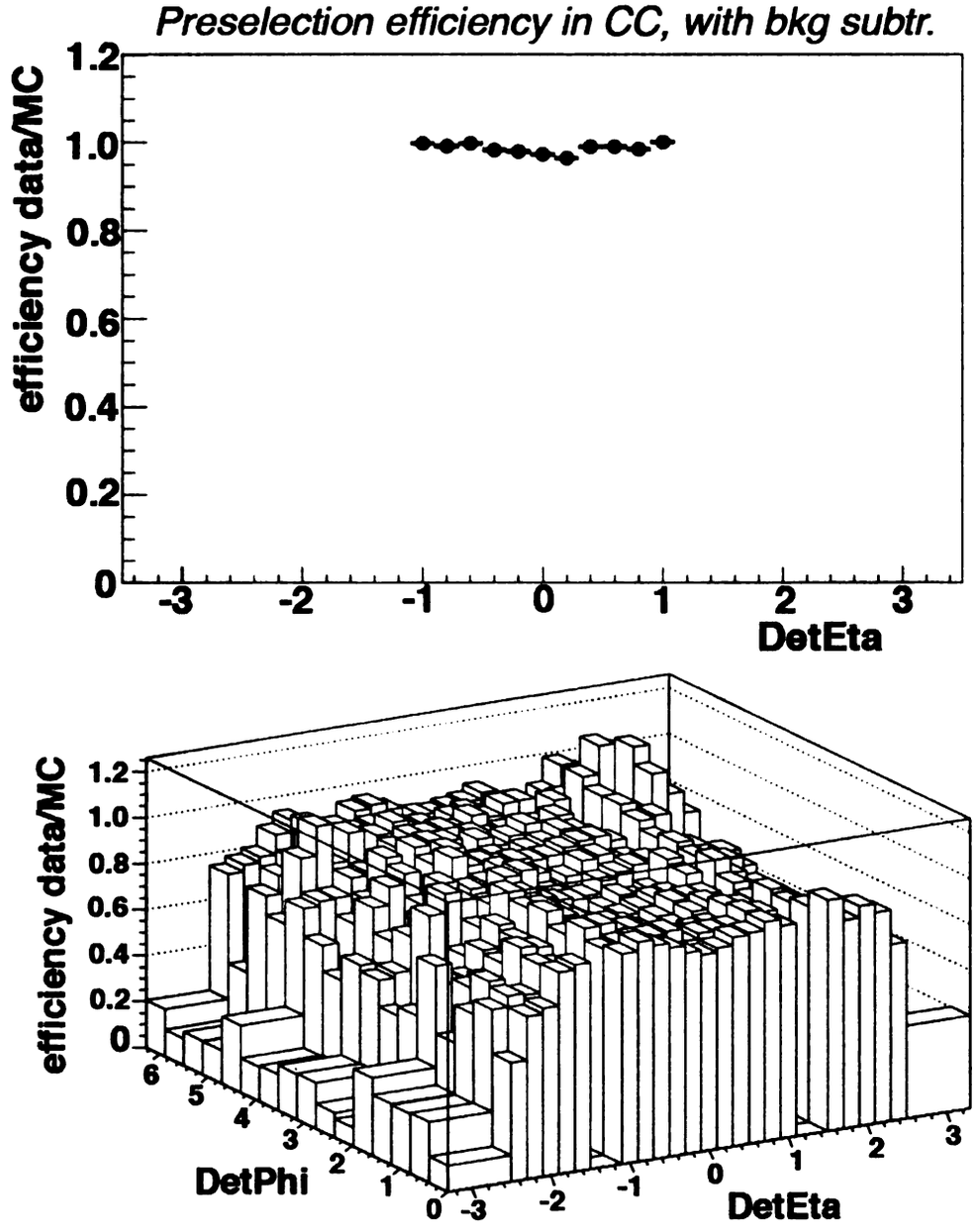

Figure 6.7: Electron efficiencies for preselection and postselection corrections for Run IIa samples.[22, 23].

$$\Delta S = \frac{p_T^{jet} - p_T^{\gamma}}{p_T^{\gamma}} \tag{6.8}$$

the details of this procedure are described in [106]. For this analysis, the standard JSSR processor is used with smearing and threshold removal set to **TRUE**, and shifting set to **FALSE**.

6.4.4 Primary Interaction vertex

Using the V+Jets Group's vjets_cafe package [107, 108], the position of the primary vertices along the beamline in z are reweighted to make the distribution in MC events match data. The correction factor defined as the ratio of MC to data is measured using $Z \rightarrow \mu\mu$ samples.

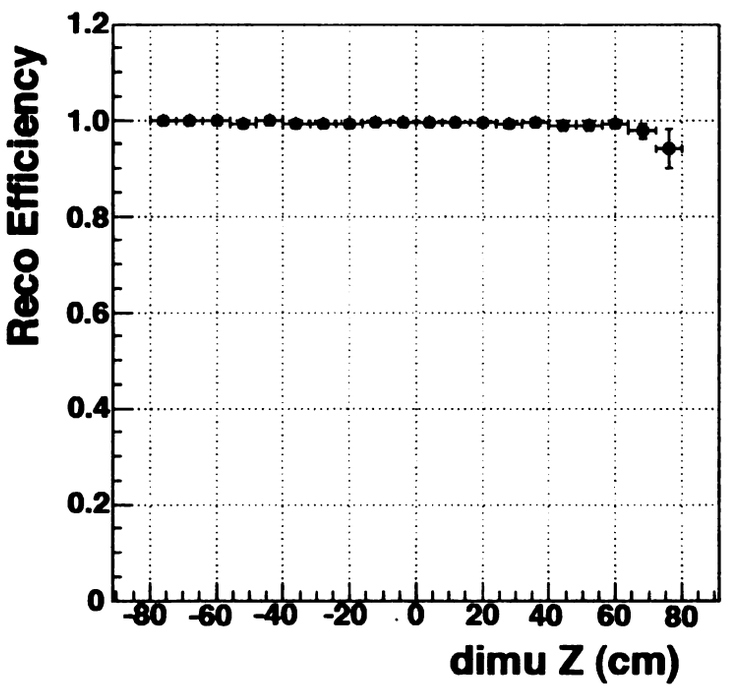

Figure 6.8: Primary vertex reconstruction efficiency in data as a function of z[24].

6.4.5 Luminosity Reweighting

Since the luminosity distributions change over time, the MC events are reweighted using the vjets_cafe package to match the luminosity of Run IIa and Run IIb data.

6.4.6 Beam Position Reweighting

The vertex-finding algorithms and reconstruction efficiencies depend on the z position of the vertex. The beam position reweighting corrects for the efficiencies, as a function of z, by fitting the primary vertex distribution in zero bias events to a convolution of two Gaussian beams and the beam beta function. If then parametrizes the scale factor as a function of z for different instantaneous luminosities (See [109, 110] for more detail).

6.4.7 Z-p_T Reweighting

Since the Z boson spectrum is not properly reproduced by the Monte Carlo [111], it is required to reweight the MC such that the Z p_T spectrum matches the theory [112].

6.4.8 Taggability

"Taggability" is defined as the probability of a jet to be taggable. A taggable jet is a calorimeter jet matched within $\Delta R < 0.5$ of a track jet which consists of at least two tracks, with $\Delta R < 0.5$ between them. Here, each track used to form the track jet must have at least one SMT hit and at least one of the tracks must have $p_T > 1$ GeV.

Since the tagger and tracking reconstruction are not perfectly modeled, the Monte Carlo can not be tagged directly. The TRFs must be applied to the MC in order to compensate for differences. The TRFs are parametrized in jet p_T, jet η, and primary vertex z zones. The details for the Single Top taggability measurements can be found in reference [19]. The results for the electrons channels for the Run IIb data can

be seen in Figure 6.9. The observed taggability and the predicted taggability are compatible within uncertainties.

b-tagging Event Weights and b-Jet Assignment Combinations

The probability to tag a jet of flavor α can be expressed as the product of the taggability and the tagging efficiency:

$$\mathcal{P}_\alpha(p_T, \eta) = P^{\text{taggable}}(p_T, \eta) \times \varepsilon_\alpha(p_T, \eta),$$

which can be used to predict that an event contains exactly a given number of tags. The probability equations for the b-tag definitions on page 83 herein are the following:

$$P_{\text{event}}(1 \text{ tag}) = \sum_{j=1}^{N_{\text{jets}}} \mathcal{P}_{\alpha_j}^{\text{TIGHT}}(p_{Tj}, \eta_j) \prod_{i \neq j} (1 - \mathcal{P}_{\alpha_i}^{\text{OLDLOOSE}}(p_{Ti}, \eta_i)) \tag{6.9}$$

$$P_{\text{event}}(2 \text{ tags}) = \sum_{j=1}^{N_{\text{jets}}} \mathcal{P}_{\alpha_j}^{\text{OLDLOOSE}}(p_{Tj}, \eta_j) \prod_{i \neq j} \mathcal{P}_{\alpha_i}^{\text{OLDLOOSE}}(p_{Ti}, \eta_i) \prod_{k \neq j \neq i} (1 - \mathcal{P}_{\alpha_k}^{\text{OLDLOOSE}}(p_{Tk}, \eta_k)) \tag{6.10}$$

Using the TRFs, the number of tagged jets per event can be estimated. However, individual jets cannot be tagged because the TRF returns a weight. This is solved by creating permutations of the same event for different scenarios of different number of b-tagged or non-b-tagged jets with a corresponding weight. Therefore, each event is taken into account several times, and the sum of weights for all possible combinations in each event returns the original probability for the event to be not-tagged, tagged once or tagged twice. This method allows the use of kinematic variables that rely the b-tagging information of the jets.

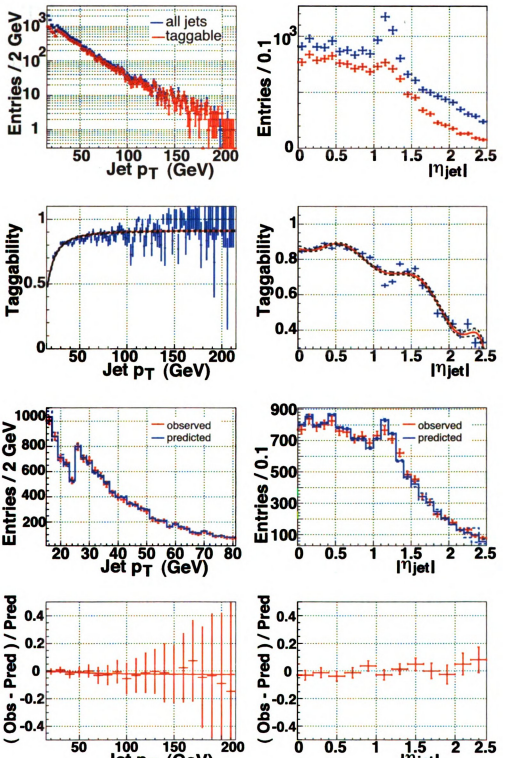

Figure 6.9: The upper four plots show the fits for the derivation of the taggability. The lower four plots show the ratio of the predicted taggability rate function over the observed taggability. These plots are all for the electron channel in the Run IIb period in the *central plus* primary vertex zone. Results for other channels are found in [19].

6.5 Trigger Efficiencies

The data used in this analysis are selected using a so-called "Mega-OR" of triggers, which have a trigger efficiency close to 100% and thus no trigger MC efficiency correction factors are needed.

In the trigger Mega-OR, an event is said to have passed the trigger requirement if it was collected with any "reasonable" trigger in the DØ trigger list. Reasonable triggers are generally defined to be all triggers except b tagging, gap, and forward proton triggers, as well as EM triggers in the case of the muon channel, and muon triggers in the case of the EM channel. The total number of triggers used was: 788 triggers for the Run IIa electron channel, 358 triggers for the Run IIa muon channel, 492 triggers for the Run IIb electron channel, and 303 triggers for the Run IIb muon channel.

Since the Mega-OR uses a large number of triggers, events that might have failed a certain requirement will be collected by another trigger. To show that the efficiency of the Mega-OR is 100%, the ratio of Single-Lepton-OR selected data, to Mega-OR selected data is compared with the ratio of MC simulation that has had the known Single-Lepton-OR turn-on curves applied to 100% efficient MC simulation. A ratio of these two ratios is then taken to represent the efficiency of the Mega-OR selection.

Assuming that the Single-Lepton-OR is modeled correctly, then the ratio of ratios corresponds to the Mega-OR efficiency in data divided by the Mega-OR efficiency in Monte Carlo (100%). This ratio should be around 1.0 as long as the assumption of 100% trigger efficiency in the Mega-OR is correct. The ratio will be less than 1.0 if the trigger efficiency of the Mega-OR is less than 100%. Any value larger than 1.0 indicates imperfect modeling of the multijet background or the Single-Lepton-OR trigger. These ratios are shown in Figure 6.10 with respect to the topological variables that are likely to be most sensitive to the trigger selection. In these plots, the vertical lines delineate the relevant region containing 90% of the data (with 5%

of the data on either side). A horizontal line is drawn at 100% efficiency (red), and at ±5% (blue). Figure 6.10 shows that there is no indication of efficiency loss for the Mega-OR trigger set. For more detail on this study refer to [19].

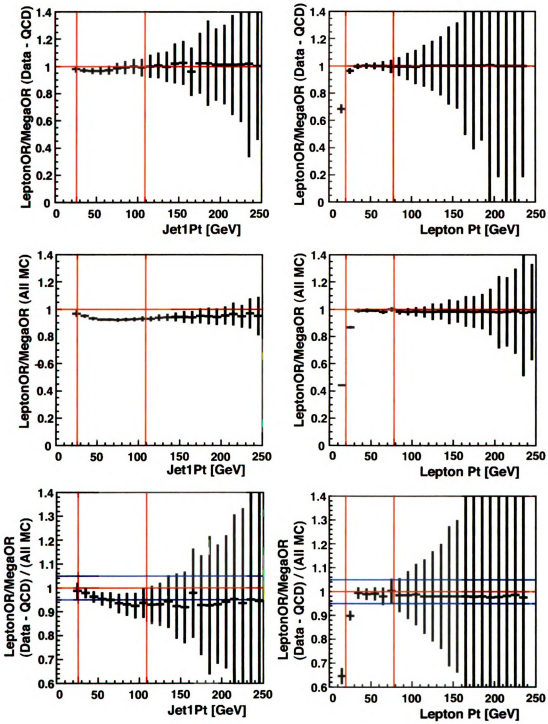

Figure 6.10: Run IIa (p17) electron channel: Ratio of Single-Lepton-OR to Mega-OR in data-minus-multijets (top row); ratio of Single-Lepton-OR to 100% in the sum of MC backgrounds (middle row); ratio of these "efficiencies" in data to MC (bottom row). The ratio is calculated for the leading jet p_T (left) and electron p_T (right) distributions. The corresponding plots for Run IIb, muon channel, and additional variables dependance can be found in Reference [19].

Ch

Ev

7.1

Chapter 7

Event Selection

This Chapter presents the selection cuts applied to the data and Monte Carlo samples and the plots demonstrating the agreement between the model and the data. The purpose of the selection cuts is to reject events that have a similar final state signature with respect to the Single Top signal. Due to the complexity of this analysis and the overwhelming background, it is not possible to consider a cut-based-only study. Some other tools such as multi-variate techniques are required to accomplish the goal of separating the signal from the background.

A brief presentation of the selection will be shown in this Chapter, for further details see [19].

7.1 Event Selection Cuts

The purpose of selections cuts is to find W-like events containing an isolated lepton, missing transverse energy, and two to four jets with high transverse momentum. Most selection cuts are common to both muons and electron channels and are listed in the following pages. In addition to all the quality and kinematical selections, there are also additional selection requirements related to the number of b-tagged jets per event. The b-tagging algorithm is applied after all the other selections and corrections are

performed. The events before the b-tagging stage are known as "pre-tagged" events.

The pretagged samples are dominated by W+jets events, with some $t\bar{t}$ contribution that becomes more significant for higher jet multiplicities, and smaller contributions from multijets, Z+jets and diboson events.

Common selection for both electron and muon channels:

- Good quality (for data);
- Instantaneous luminosity > 0;
- Remove duplicate events;
- Pass trigger requirement: at least one of the selected triggers has to fire;
- Good primary vertex: $|z_{\mathrm{PV}}| < 60$ cm with at least three tracks attached;
- Two, three, or four good jets with $p_T > 15$ GeV and $|\eta^{\mathrm{det}}| < 3.4$;
- The leading jet is required to have $p_T > 25$ GeV;
- Jet triangle cut $|\Delta\phi(\text{leading jet}, \not\!\!E_{\mathrm{T}})|$ vs. $\not\!\!E_T$:
  - $|\Delta\phi|$ from 1.5 to π rad when $\not\!\!E_T = 0$ GeV;
  - and $\not\!\!E_T$ from 0 to 35 GeV when $|\Delta\phi| = \pi$ rad;
- Missing transverse energy
  - $20 < \not\!\!E_T < 200$ GeV in events with exactly two good jets and
  - $25 < \not\!\!E_T < 200$ GeV in events with three or more good jets.

Electron channel selection

- Only one tight electron with $|\eta^{\mathrm{det}}| < 1.1$ and $p_T > 15$ (20) GeV in events with 2 (3 or more) good jets;
- No additional loose electron with $p_T > 15$ GeV;

- No tight isolated muon with $p_T > 15$ GeV and within $|\eta^{\text{det}}| < 2.0$;
- Electron coming from the primary vertex: $|\Delta z(e, \text{PV})| < 1$ cm;
- Electron triangle cuts $|\Delta\phi(e, \not\!\!E_T)|$ vs. $\not\!\!E_T$:
  - $|\Delta\phi|$ from 2 to 0 rad when $\not\!\!E_T = 0$ GeV, and $\not\!\!E_T$ from 0 to 40 GeV when $|\Delta\phi| = 0$ rad;
  - $|\Delta\phi|$ from 1.5 to 0 rad when $\not\!\!E_T = 0$ GeV, and $\not\!\!E_T$ from 0 to 50 GeV when $|\Delta\phi| = 0$ rad;
  - $|\Delta\phi|$ from 2 to π rad when $\not\!\!E_T = 0$ GeV, and $\not\!\!E_T$ from 0 to 24 GeV when $|\Delta\phi| = \pi$ rad;
- Scalar sum of the transverse energies of all good jets and the electron transverse momentum and the missing transverse energy:
  - $H_T(\text{alljets}, e, \not\!\!E_T) > 120$ GeV in events with exactly two good jets;
  - $H_T(\text{alljets}, e, \not\!\!E_T) > 140$ GeV in events with exactly three good jets and
  - $H_T(\text{alljets}, e, \not\!\!E_T) > 160$ GeV in events with exactly four good jets;

Muon channel selection

- Only one tight muon with $p_T > 15$ GeV and $|\eta^{\text{det}}| < 2.0$;
- No additional loose muons with $p_T > 4$ GeV;
- No loose electron with $p_T > 15$ GeV and within $|\eta^{\text{det}}| < 2.5$;
- Muon coming from the primary vertex: $|\Delta z(\mu, \text{PV})| < 1$ cm;
- Muon triangle cuts $|\Delta\phi(\mu, \not\!\!E_{\text{T}})|$ vs. $\not\!\!E_T$:
  - $|\Delta\phi|$ from 1.2 to 0 rad when $\not\!\!E_T = 0$ GeV, and $\not\!\!E_T$ from 0 to 85 GeV when $|\Delta\phi| = 0$ rad;

- $|\Delta\phi|$ from 2.5 to π rad when $\not\!\!E_T$ = 0 GeV, and $\not\!\!E_T$ from 0 to 30 GeV when $|\Delta\phi| = \pi$ rad;

- Muon track curvature significance cuts |TrackCurvSig| vs. $|\Delta\phi(\mu, \not\!\!E_T)|$, where |TrackCurvSig| = $|\frac{q/p_T}{\sigma(1/p_T)}|$, and q and p_T are the charge and transverse momentum of the charged track associated with the muon:

  - $|\Delta\phi|$ from 0.875π to π rad when |TrackCurvSig| = 0, and |TrackCurvSig| from 0 to 4 (6) when $|\Delta\phi| = \pi$ rad for Run IIa (Run IIb) period;

  - $|\Delta\phi|$ from 2 to π rad when |TrackCurvSig| = 0, and |TrackCurvSig| from 0 to 2 (3) when $|\Delta\phi| = \pi$ rad for Run IIa (Run IIb) period;

  These cuts are needed to reject events with poorly measured muons that cause an excess in data over background model in the $\Delta\phi$ distributions (See Section 7.1.1).

- Transverse momentum of the leading jet within the ICD region of the detector: leading jet $p_T > 30$ GeV when $1.0 <$ |leading jet $\eta^{\text{det}}| < 1.5$;

- Scalar sum of the transverse energies of all good jets, the electron transverse momentum, and the missing transverse energy:

  - $H_T(\text{alljets}, \mu, \not\!\!E_T) > 110$ GeV in events with exactly two good jets;

  - $H_T(\text{alljets}, \mu, \not\!\!E_T) > 130$ GeV in events with exactly three good jets and

  - $H_T(\text{alljets}, \mu, \not\!\!E_T) > 160$ GeV in events with exactly four good jets;

Tables 7.1 and 7.3 show the number of events for data and MC signal samples as they pass through the selection chain of cuts as mentioned above.

Selection cut - Electron Channel	Run IIa Data	(%)	Run IIb Data	(%)
Initial	335,220,569	(100)	207,299,315	(100)
ZeroLumi, duplicate, DQ	266,288,632	(79)	178,635,715	(86)
Trigger	239,165,711	(71)	169,252,679	(82)
Tight lepton with $p_T > 15$ GeV	2,536,008	(0.76)	2,082,467	(1.0)
Second-lepton veto	2,483,784	(0.74)	2,039,680	(0.98)
Jet selection	1,266,682	(0.38)	1,024,900	(0.49)
Leading jet $p_T > 25$ GeV	568,856	(0.17)	468,752	(0.23)
Veto opposite lepton type	568,619	(0.17)	468,488	(0.23)
Vertex selection	536,645	(0.16)	429,777	(0.22)
15 GeV$< \not\!\!E_T <$ 200 GeV	200,025	(0.059)	169,597	(0.081)
First lepton triangle cut	119,261	(0.035)	107,602	(0.051)
Second lepton triangle cut	116,993	(0.034)	105,635	(0.050)
Third lepton triangle cut	113,133	(0.033)	101,961	(0.049)
Jet triangle cut	100,936	(0.030)	92,973	(0.044)
Number of good jets cut	41,785	(0.012)	39,642	(0.019)
Instantaneous luminosity > 0	41,600	(0.012)	39,640	(0.019)
H_T(alljets, e, $\not\!\!E_T$) cut	30,310	(0.0090)	29,070	(0.014)
$\not\!\!E_T > 20/25/25$ GeV	27,567	(0.0082)	26,291	(0.013)
Lepton $p_T > 15/20/20$ GeV	26,847	(0.0080)	25,595	(0.012)
Additional duplicate removal	24,662	(0.0074)	25,595	(0.012)
Selection cut - Electron Channel	**Run IIa Data**	**(%)**	**Run IIb Data**	**(%)**
Initial	330,306,915	(100)	352,185,449	(100)
ZeroLumi, duplicate, DQ	270,187,161	(82)	303,612,626	(86)
Trigger	247,589,750	(75)	265,892,437	(76)
Jet selection	170,537,062	(52)	187,509,219	(53)
Tight lepton with $p_T > 15$ GeV	919,420	(0.28)	774,158	(0.22)
Second-lepton veto	906,444	(0.27)	761,494	(0.22)
Veto opposite lepton type	903,054	(0.27)	758,603	(0.22)
Leading jet $p_T > 25$ GeV	386,770	(0.13)	339,038	(0.096)
Vertex selection	357,389	(0.12)	300,569	(0.085)
15 GeV$< \not\!\!E_T <$ 200 GeV	192,933	(0.058)	169,964	(0.048)
First lepton triangle cut (loose)	142,940	(0.043)	131,555	(0.037)
Second lepton triangle cut	138,612	(0.041)	127,700	(0.036)
Jet triangle cut	118,931	(0.036)	112,164	(0.031)
Number of good jets cut	49,649	(0.015)	48,963	(0.015)
Instantaneous luminosity > 0	49,479	(0.015)	48,682	(0.015)
H_T(alljets, μ, $\not\!\!E_T$) cut	41,219	(0.013)	41,027	(0.012)
$\not\!\!E_T > 20/25/25$ GeV	38,291	(0.012)	38,176	(0.012)
Leading jet $p_T > 30$ GeV if in ICD	36,962	(0.011)	36,960	(0.011)
First lepton triangle cut	34,297	(0.010)	34,357	(0.010)
Track curvature significance cut	31,957	(0.0097)	32,939	(0.010)
Additional duplicate removal	31,581	(0.0096)	32,939	(0.010)

Table 7.1: Numbers of data events after each selection cut is applied.

Selection cut - Electron Channel	**Run IIa tb**	**(%)**	**Run IIb tb**	**(%)**
Initial	400,000	(100)	600,000	(100)
ZeroLumi, duplicate, DQ	376,482	(94.1)	538,312	(89.7)
Jet selection	371,476	(92.9)	534,079	(89.0)
Leading jet $p_T > 25$ GeV	360,830	(90.2)	519,723	(86.6)
Tight lepton with $p_T > 15$ GeV	96,728	(24.2)	119,434	(19.9)
Second-lepton veto	96,352	(24.1)	119,031	(19.8)
Veto opposite lepton type	96,315	(24.1)	118,985	(19.8)
Vertex selection	95,093	(23.8)	118,028	(19.7)
15 GeV$< \not\!\!E_T <$ 200 GeV	89,039	(22.3)	110,229	(18.4)
First lepton triangle cut	85,463	(21.4)	105,926	(17.7)
Second lepton triangle cut	84,617	(21.2)	104,905	(17.5)
Third lepton triangle cut	83,892	(21.0)	103,910	(17.3)
Jet triangle cut	81,906	(20.5)	101,291	(16.9)
Number of good jets cut	66,412	(16.6)	81,330	(13.6)
H_T(alljets, e, $\not\!\!E_T$) cut	65,276	(16.3)	79,997	(13.3)
$\not\!\!E_T > 20/25/25$ GeV	62,425	(15.6)	76,371	(12.7)
Lepton $p_T > 15/20/20$ GeV	60,439	(15.1)	73,914	(12.3)
Selection cut - Muon Channel	**Run IIa tb**	**(%)**	**Run IIb tb**	**(%)**
Initial	400,000	(100)	600,000	(100)
ZeroLumi, duplicate, DQ	374,407	(93.6)	535,883	(89.3)
Jet selection	370,388	(92.6)	531,898	(88.7)
Tight lepton with $p_T > 15$ GeV	103,850	(26.0)	142,162	(23.7)
Second-lepton veto	102,579	(25.6)	140,502	(23.4)
Veto opposite lepton type	101,835	(25.5)	139,890	(23.3)
Leading jet $p_T > 25$ GeV	98,410	(24.6)	135,491	(22.6)
Vertex selection	96,858	(24.2)	133,046	(22.2)
15 GeV$< \not\!\!E_T <$ 200 GeV	91,124	(22.8)	124,976	(20.8)
First lepton triangle cut (loose)	88,967	(22.2)	121,997	(20.3)
Second lepton triangle cut	87,994	(22.0)	120,668	(20.1)
Jet triangle cut	85,024	(21.3)	116,697	(19.5)
Number of good jets cut	70,870	(17.7)	97,375	(16.2)
H_T(alljets, e, $\not\!\!E_T$) cut	70,342	(17.6)	96,713	(16.1)
$\not\!\!E_T > 20/25/25$ GeV	67,365	(16.8)	92,553	(15.4)
Leading jet $p_T > 30$ GeV if in ICD	67,036	(16.8)	92,095	(15.4)
First lepton triangle cut	63,592	(15.9)	87,395	(14.6)
Track curvature significance cut	62,466	(15.6)	86,426	(14.4)

Table 7.2: Numbers of MC tb channel signal events after each selection cut is applied

Selection cut - Electron Channel	**Run IIa tqb**	**(%)**	**Run IIb tqb**	**(%)**
Initial	375,000	(100)	600,000	(100)
ZeroLumi, duplicate, DQ	351,768	(93.8)	539,371	(89.9)
Jet selection	345,854	(92.2)	534,328	(89.1)
Leading jet $p_T > 25$ GeV	332,850	(88.8)	516,360	(86.1)
Tight lepton with $p_T > 15$ GeV	88,776	(23.7)	113,510	(18.9)
Second-lepton veto	88,468	(23.6)	113,153	(18.9)
Veto opposite lepton type	88,439	(23.6)	113,119	(18.9)
Vertex selection	87,274	(23.3)	112,246	(18.7)
15 GeV$< \not\!\!E_T <$ 200 GeV	81,709	(21.8)	104,923	(17.5)
First lepton triangle cut	78,791	(21.0)	101,204	(16.9)
Second lepton triangle cut	78,230	(20.9)	100,441	(16.7)
Third lepton triangle cut	77,485	(20.7)	99,439	(16.6)
Jet triangle cut	75,669	(20.2)	97,002	(16.2)
Number of good jets cut	61,491	(16.4)	78,709	(13.1)
H_T(alljets, e, $\not\!\!E_T$) cut	60,162	(16.0)	77,086	(12.9)
$\not\!\!E_T > 20/25/25$ GeV	57,284	(15.3)	73,163	(12.2)
Lepton $p_T > 15/20/20$ GeV	55,325	(14.8)	70,511	(11.8)
Selection cut - Muon Channel	**Run IIa tqb**	**(%)**	**Run IIb tqb**	**(%)**
Initial	350,000	(100)	599,250	(100)
ZeroLumi, duplicate, DQ	327,973	(93.7)	540,256	(90.2)
Jet selection	323,583	(92.5)	535,067	(89.3)
Tight lepton with $p_T > 15$ GeV	89,649	(25.6)	141,100	(23.6)
Second-lepton veto	88,757	(25.4)	139,636	(23.3)
Veto opposite lepton type	88,129	(25.2)	138,793	(23.2)
Leading jet $p_T > 25$ GeV	84,270	(24.1)	132,962	(22.2)
Vertex selection	83,019	(23.7)	130,531	(21.8)
15 GeV$< \not\!\!E_T <$ 200 GeV	77,994	(22.3)	122,623	(20.5)
First lepton triangle cut (loose)	76,268	(21.8)	119,893	(20.0)
Second lepton triangle cut	75,467	(21.6)	118,504	(19.8)
Jet triangle cut	72,972	(20.9)	114,569	(19.1)
Number of good jets cut	59,778	(17.1)	93,745	(15.6)
H_T(alljets, e, $\not\!\!E_T$) cut	59,146	(16.9)	92,903	(15.5)
$\not\!\!E_T > 20/25/25$ GeV	56,428	(16.1)	88,522	(14.8)
Leading jet $p_T > 30$ GeV if in ICD	56,049	(16.0)	87,923	(14.7)
First lepton triangle cut	53,573	(15.3)	84,103	(14.0)
Track curvature significance cut	52,637	(15.0)	83,411	(13.9)

Table 7.3: Numbers of MC tqb channel signal events after each selection cut is applied

7.1.1 Triangular Cuts

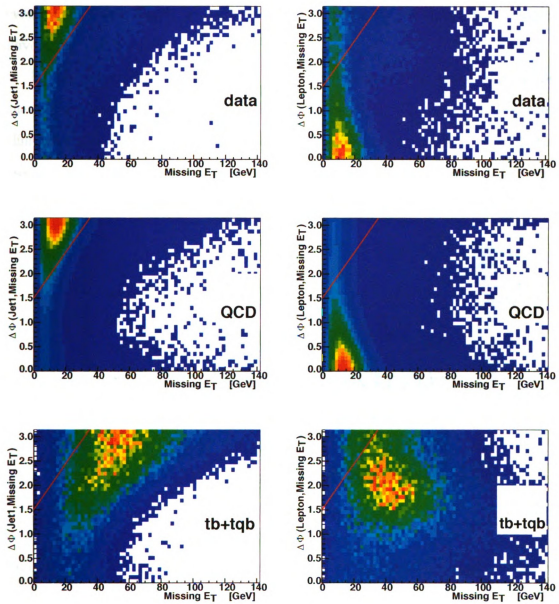

Figure 7.1: $\Delta\phi$(jet1,$\not\!\!E_T$) versus $\not\!\!E_T$ (left) and $\Delta\phi$(lepton,$\not\!\!E_T$) versus $\not\!\!E_T$ (right) two-dimensional distributions for data (top), multijets (middle) and tb+tqb signal (bottom), in the electron channel in Run IIb data. Similar distributions for the Run IIa and muon channels can be found in [19].

The goal of the triangle cuts is to reduce the multijets background. Figure 7.1 shows the distributions of data, multijets and MC signal events in the two-dimensional planes of $\Delta\phi$(jet1,$\not\!\!E_T$) versus $\not\!\!E_T$ and $\Delta\phi$(lepton,$\not\!\!E_T$) versus $\not\!\!E_T$. This is before any

triangular or $\not\!\!E_T$ cut is applied. The red lines illustrate the events removed by the triangular cuts; events inside the triangles fail the selection criteria. These rejected events correspond mostly to multijet events, however for the signal, the triangle cuts have a very little impact.

For the muon channel, there is an additional triangular cut aimed to reject poorly measured muons in data that are not well modeled in MC. This cut uses the two-dimensional plane: "absolute value of the track curvature significance" vs. "$\Delta\phi(\mu, \not\!\!E_T)$," (see Figure 7.2). The need for this special cut can be seen in Figure 7.3 where the distribution $\Delta\phi(\mu, \not\!\!E_T)$ is plotted before and after the cut is applied.

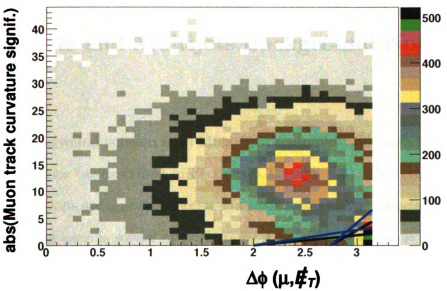

Figure 7.2: Absolute value of the muon track curvature significance versus $\Delta\phi(\mu, \not\!\!E_T)$. The cuts are shown as heavy black (blue) lines for Run IIa (Run IIb).

7.1.2 Total Transverse Energy (H_T) cut

The purpose of the H_T cut is to control the multijet background to levels below ~5% in the final selection. Figure 7.4 shows the H_T distribution together with the $M_T(W)$ distribution before and after the cut is applied illustrating the motivation and use of this cut.

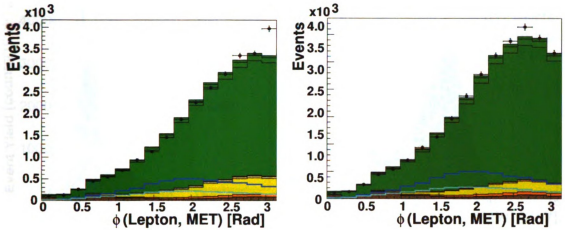

Figure 7.3: $\Delta\phi(\mu, \not\!\!E_T)$ distribution for the Run IIa before(after) the muon track curvature significance triangle cut – left(right).

7.2 W+jets and Multijets Background Normalization

The W+jets background is taken from Monte Carlo samples and corrected for reconstruction efficiencies (as described in Sections 6.2.3 and 6.4). Unfortunately, some additional corrections are necessary because of some mismodeling associated ALPGEN. This mismodelling issue is solved by performing a reweighting of the W+jets sample to reproduce the jet η distributions in data (more in Section 7.2.1). The modeling of the multijets background is base on the data as explained in Section 6.3.

The normalization of the multijets and the W+jets backgrounds is obtained using an iterative KS-test normalization method (IKS) that calculates two anti-correlated scale factors which are applied to the each one of the backgrounds guaranteeing the proper normalization to data. The two normalization scale factors $S_{W+\text{jets}}$ and $S_{\text{multijets}}$ are calculated during the pre b-tagging stage.

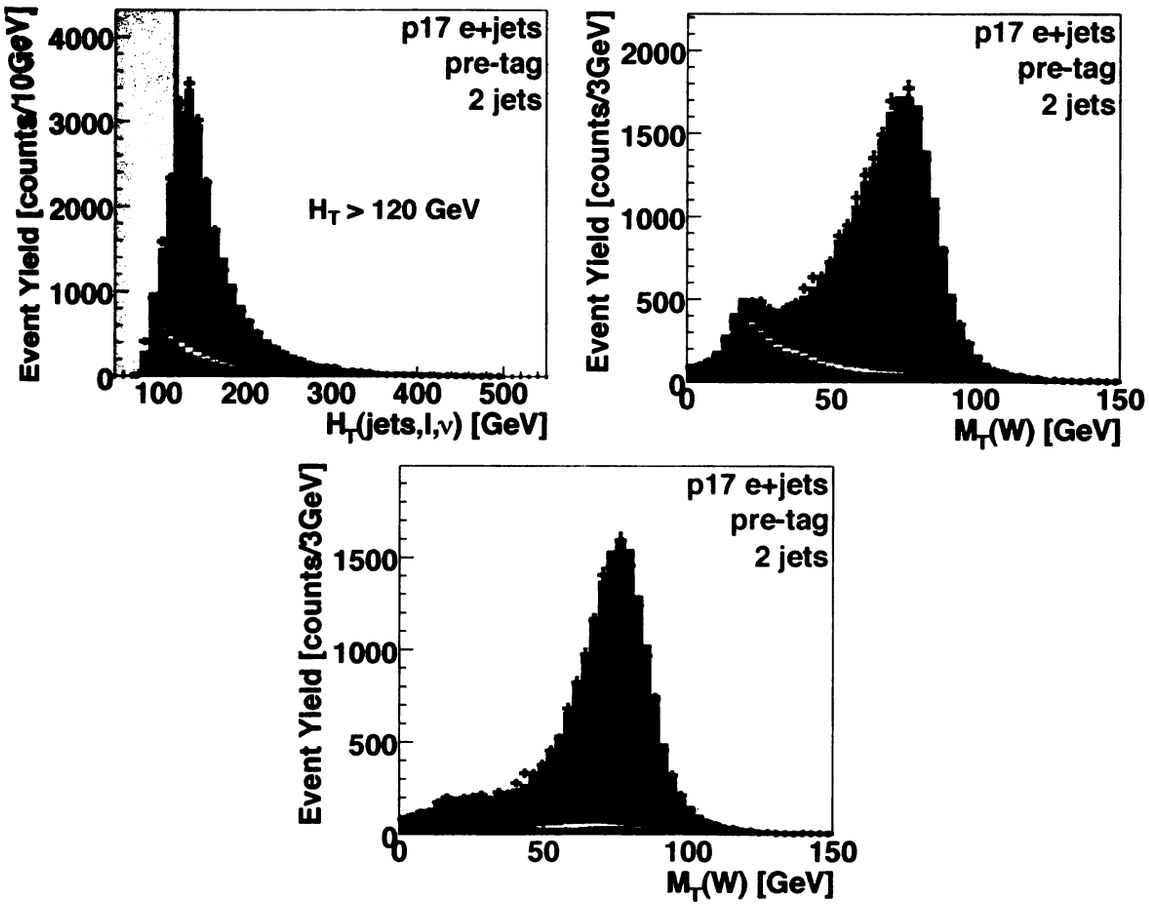

Figure 7.4: Pretagged distributions for Run IIa events with 2-jet in the electron channel for for H_T(lepton, $\not\!\!E_T$, alljets) (left) and the W boson transverse mass before(after) the H_T cuts is applied - middle(bottom). Similar distributions for other jet multiplicity channel, leptons and reconstruction version can be found in [19]

The total amount of data (yield of data) can be expressed as:

$$Y_{\text{pretagged data}} = S_{W+\text{jets}} * Y_{W+\text{jets}}^{\text{before-IKS}} + Y_{\text{all other MC}} + S_{\text{multijets}} * Y_{\text{multijets}}^{\text{before-IKS}}, \tag{7.1}$$

where Y_{sample} is the event yield of a sample (sample = pretagged data, W+jets, all other MC, and multijets) after all the selection cuts and corrections have been applied. The $S_{W+\text{jets}}$ and $S_{\text{multijets}}$ are determined simultaneously using an iterative KS-test normalization (IKS) method:

1. Select a kinematic variable (var1) that has noticeable differences on the distributions for W+jets and multijets backgrounds;

2. Initialize $S_{W+\text{jets}} = 1.0$, $\text{KS}_{\text{max}} = 0.0$ and calculate a corresponding $S_{\text{multijets}}$ from Equation 7.1;

3. For var1 execute a Kolomogorov-Smirnov test (KS-test) between data and background distributions;

4. If the new KS value is greater than KS_{max}, assign the new KS value to KS_{max};

5. Increase $S_{W+\text{jets}}$ by 0.001;

6. Repeat the steps 3-5 until $S_{W+\text{jets}}$ is equal to 4.0 or when $S_{\text{multijets}}$ becomes negative; and

7. Repeat the procedure for a group of varN kinematic variables.

The final $S_{W+\text{jets}}$ and $S_{\text{multijets}}$ are determined by doing a weighted average:

$$S_{W+\text{jets}} = \frac{\sum_{i=\text{var1}}^{\text{varN}} S^i_{W+\text{jets}} * \text{KS}^i_{\text{max}}}{\sum_{i=\text{var1}}^{\text{varN}} \text{KS}^i_{\text{max}}}$$

$$S_{\text{multijets}} = \frac{\sum_{i=\text{var1}}^{\text{varN}} S^i_{\text{multijets}} * \text{KS}^i_{\text{max}}}{\sum_{i=\text{var1}}^{\text{varN}} \text{KS}^i_{\text{max}}}$$

For this analysis there were 3 variables chosen to calculate the normalization factors: $p_T(\ell)$, $\not\!\!E_T$, and $M_T(W)$. The weighted averages were calculated for each channel corresponding to a different jet multiplicity, lepton and reconstruction version. The results are summarized in Table 7.4.

IKS Normalization Scale Factors

	$S_{W+\text{jets}}$				$S_{\text{multijets}}$			
	Run IIa (p17)		Run IIb (p20)		Run IIa (p17)		Run IIb (p20)	
	e	μ	e	μ	e	μ	e	μ
2 jets	1.51	1.30	1.41	1.23	0.348	0.0490	0.388	0.0639
3 jets	1.92	1.79	1.75	1.57	0.291	0.0291	0.308	0.0410
4 jets	2.29	2.06	1.81	1.92	0.189	0.0244	0.424	0.0333

Table 7.4: W+jets and multijets scale factors calculated using the iterative KS-test normalization method.

7.2.1 Reweighting for the W+Jets Sample

The W+jets sample must be reweighted before the b-tagging is applied. The purpose of this reweighting is to obtain a better data-background agreement by correcting the ALPGEN modeling discrepancies in the Monte Carlo. The distributions that need to be reweighted are (in order): $\eta(\text{jet1}), \eta(\text{jet2}), \Delta\phi(\text{jet1}, \text{jet2}), \Delta\eta(\text{jet1}, \text{jet2}), \eta(\text{jet3})$, and $\eta(\text{jet4})$.

For a given distribution, the reweighting function is calculated by obtaining the ratio:

$$\text{reweight function} = \frac{data - All\ Backgrounds_{except\ W+\text{jets}}}{W + \text{jets}}, \tag{7.2}$$

Figure 7.5 shows the derivation of the reweighting function for $\eta(\text{jet2})$ in the Run IIa sample set. The same procedure is followed to obtain the reweighting function for all other distributions, each reweighting is calculated after the previous reweighting is applied to the W+jets sample.

The reweighting functions are combined in a bin-by-bin basis for the electrons and muons and for all jets multiplicity. The leptons combination is consistent with the motivation of the reweighting which is to correct jet quantities, and the jet combina-

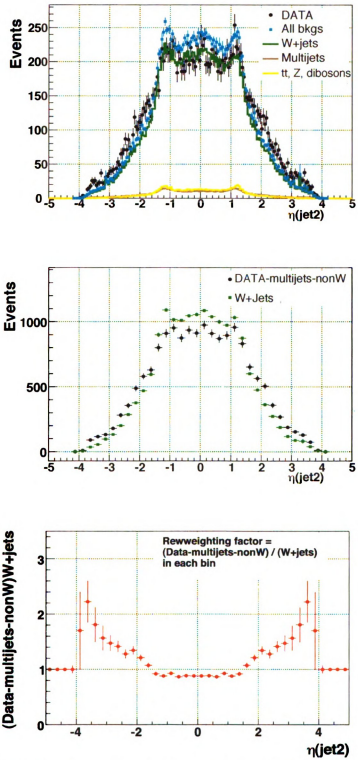

Figure 7.5: ALPGEN W+jets reweighting factor derivation for η(jet2). The first plot shows the disagreement between data and all backgrounds, the middle plot illustrates the numerator and denominator of Equation 7.2 and the plot to the right presents the reweighting function.

tion is because there was no noticeable difference between the reweighting functions for different jet bins. The final reweighting functions for the Run IIa and Run IIb are presented in Figure 7.6.

Figure 7.7 shows the distributions of four jet-related parameters before and after the reweightings for Run IIb, muon and jets combined. Additional distributions can be found in [19].

To achieve a good background-data agreement the W+jets sample needs to be reweighted: the muon detector pseudorapidity $\eta^{\text{det}}(\mu)$. Figure 7.8 shows the distributions before and after the reweighting is applied. Although all of the reweights presented in this subsections are small, they are necessary to ensure the final data-background agreement.

7.2.2 W+Jets Heavy-Flavor Fraction

The ALPGEN leading-log cross section for $Wb\bar{b}$, $Wc\bar{c}$, and Wjj are required to be scaled by the theoretical factors K' and K'_{HF} in order to account for the NLO effect. The DØ V+Jets Group [113] calculated them by using comparisons of the LL and NLO calculations, and are presented in Table 7.5.

NLO/LL K' and K'_{HF} Factors for V+Jets Cross Sections

	Wjj	Wcj	$Wc\bar{c}$	$Wb\bar{b}$	Zjj	$Zc\bar{c}$	$Zb\bar{b}$
Run IIa	1.30	1.80	1.30 × 1.47	1.30 × 1.47	1.346	1.346 × 1.25	1.346 × 1.25
Run IIb	1.30	1.80	1.30 × 1.47	1.30 × 1.47	1.30	1.30 × 1.67	1.30 × 1.52

Table 7.5: NLO/LL K' and K'_{HF} Theoretical Factors for V+Jets Cross Sections.

In order to achieve better data-background agreement, an extra scale correction factor S_{HF} for the heavy flavor W+jets samples is required. The procedure to

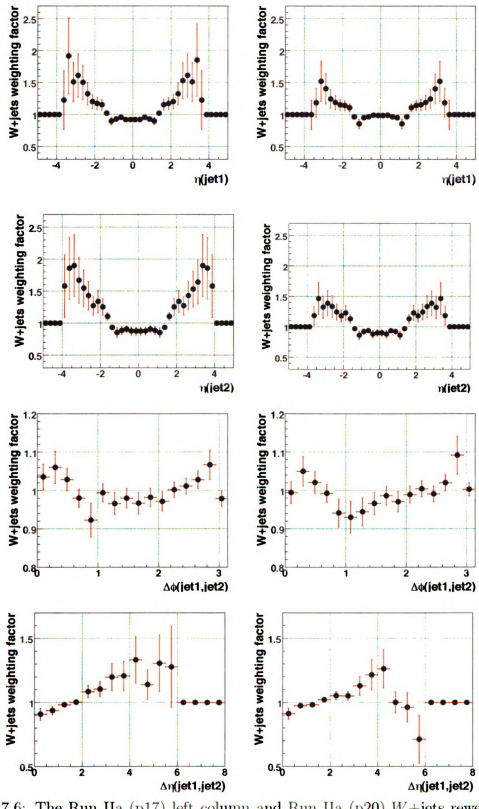

Figure 7.6: The Run IIa (p17) left column and Run IIa (p20) W+jets reweighting factors for $\eta(\text{jet1}), \eta(\text{jet2}), \Delta\phi(\text{jet1}, \text{jet2})$, and $\Delta\eta(\text{jet1}, \text{jet2})$ ALPGEN.

Event Yield

Event Yield (equation 4)

Event Yield

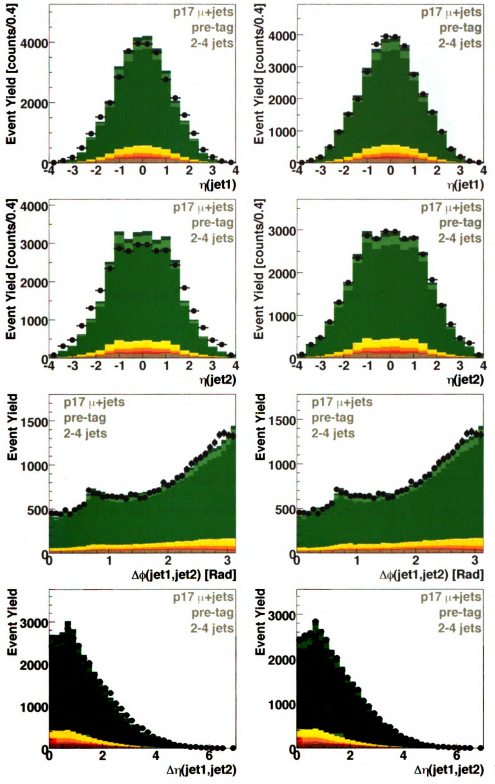

Figure 7.7: Distributions before (left) and after the reweighting (right) for the muon, Run IIb channels. η(jet1), η(jet2), $\Delta\phi$(jet1,jet2) and $\Delta\eta$(jet1,jet2).

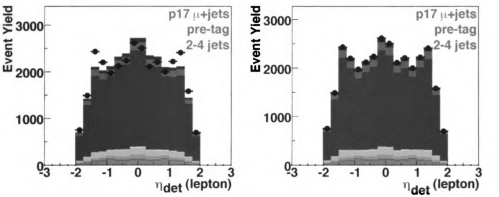

Figure 7.8: Muon pseudorapidity for Run IIa before and after the reweightings are applied left and right, respectively.

calculate S_{HF} is explained in detail in [114]. Let us consider:

$$D' = X' + S \times (W' + S_{HF} \times B') \tag{7.3}$$

$$D'' = X'' + S \times (W'' + S_{HF} \times B'') \tag{7.4}$$

where D, W, B and X are the yields for the samples data, W+light-jets, W+heavy-flavor and the rest of the background plus signal respectively. The method uses two ortogonal samples: one that passes the b-tagging requirements ($'$) and one orthogonal to it ($''$), thereby ensuring that the data-background agreement holds in both samples. Solving for S_{HF}:

$$S_{HF} = \frac{W'(D'' - X'') - W'' * (D' - X')}{B''(D' - X') - B' * (D'' - X'')}. \tag{7.5}$$

The final S_{HF} applied to all channels is:

$$S_{HF} = 0.946 \pm 0.082 \text{ (stat)}$$

which corresponds to a weighted average of all S_{HF} presented in Table 7.6.

Heavy-Flavor Scale Factor Corrections S_{HF} for W+Jets Events

	Run IIa		Run IIb		
	e	μ	e	μ	
1 tag	1.04 ± 0.19	1.15 ± 0.20	0.95 ± 0.20	0.65 ± 0.18	
2 tags	0.84 ± 0.30	0.70 ± 0.29	1.23 ± 0.40	1.17 ± 0.40	
	Run IIa+b		$e + \mu$		Run IIa+b
	e	μ	Run IIa	Run IIb	$e + \mu$
1 tag	1.00 ± 0.14	0.90 ± 0.13	1.10 ± 0.14	0.79 ± 0.13	0.95 ± 0.10
2 tags	1.02 ± 0.25	0.91 ± 0.17	0.77 ± 0.21	1.20 ± 0.28	0.97 ± 0.17

Table 7.6: Heavy-flavor scale factor corrections for the two run periods and lepton types and combinations of each, calculated using two-jet events.

7.3

7.3 Number of Events After Selection

Tables 7.7 and 7.8 show the number of events for each sample after the selection criteria, discussed previously, have been applied. These numbers are important as they represent the statistics available for training a Decision Tree and are also used to calculate statistical uncertainty of the measurement.

Number of p17 Events after Selection

	Electron Channel			Muon Channel		
	2 jets	3 jets	4 jets	2 jets	3 jets	4 jets
Signal MC						
tb	42,407	14,339	3,693	42,295	16,181	3,990
tqb	36,568	14,273	4,484	33,744	14,563	4,330
tb+tqb	78,975	28,612	8,177	76,039	30,744	8,320
Background MC						
$t\bar{t}\rightarrow ll$	105,957	67,291	22,008	88,999	66,241	21,622
$t\bar{t}\rightarrow l$+jets	34,183	110,291	128,273	23,066	103,952	140,513
$Wb\bar{b}$	33,958	11,589	3,439	38,522	14,757	4,362
$Wc\bar{c}$	29,781	11,165	3,202	34,861	14,112	3,925
Wcj	15,518	5,427	1,252	17,462	6,346	1,509
Wjj	214,395	74,244	18,417	260,622	98,177	24,348
$Zb\bar{b}$	2,827	1,202	432	7,371	2,077	591
$Zc\bar{c}$	722	348	125	3,406	1,280	364
Zjj	9,192	3,516	1,353	35,374	11,060	2,729
Dibosons	92,882	25,726	5,897	113,327	33,989	7,637
PreTag data						
Multijets	241,173	105,002	46,458	18,281	8,083	2,827
Data	18,582	4,834	1,246	23,243	6,675	1,663
OneTag data						
Multijets	6,938	3,773	1,845	1,050	591	300
Signal data	508	202	103	627	259	131
TwoTags data						
Multijets	451	417	285	67	68	38
Signal data	67	61	37	71	62	56

Table 7.7: Number of events for the electron and muon channels after selection in the p17 sample.

Number of p20 Events after Selection

	Electron Channel			Muon Channel		
	2 jets	3 jets	4 jets	2 jets	3 jets	4 jets
Signal MC						
tb	51,228	17,890	4,796	55,557	24,016	6.853
tqb	44,863	19,223	6,425	50,861	24,416	8,134
tb+tqb	96,091	37,113	11,221	106,418	48,432	14,987
Background MC						
$t\bar{t}\rightarrow ll$	61,642	47,435	15,473	57,435	51,705	17,168
$t\bar{t}\rightarrow l$+jets	15,461	49,628	57,644	11,787	51,564	69,033
$Wb\bar{b}$	50,850	19,131	5,572	63,506	26,499	7,736
$Wc\bar{c}$	37,524	13,860	4,061	48,043	20,081	5,588
Wcj	6,596	2,298	567	8,016	3,082	724
Wjj	91,261	32,106	8,335	120,751	47,562	11,711
$Zb\bar{b}$	3,266	1,418	609	12,124	4,499	1,280
$Zc\bar{c}$	2,185	883	347	9,454	3,308	864
Zjj	9,193	3,516	1,353	35,387	11,067	2,730
Diboson	25,373	7,642	2,001	36,486	11,865	3,001
PreTag data						
Multijets	229,208	101,466	47,660	21,416	9,188	3,233
Data	19,048	5,087	1,460	23,972	7,040	1,927
OneTag data						
Multijets	6,838	3,417	1,773	1,150	689	271
Signal data	547	207	124	595	290	142
TwoTags data						
Multijets	505	444	287	77	76	29
Signal data	79	56	51	85	79	80

Table 7.8: Number of events for the electron and muon channels after selection in the p20 sample.

7.4 Event Yields

In this section, the number of events after the event selection on the 2.3 fb^{-1} of data analyzed in this dissertation are presented. Tables 7.9 and 7.10 show these yields for all signals and backgrounds before the b tagging is applied. They are separated by data-taking period, lepton flavor and jet multiplicity within each table. Similarly Tables 7.11 and 7.12 show the yields after b-tagging algorithm is applied and the resulting selected events have one two b-tagged jets respectively. Figure 7.9 is a graphical representation of the or all yield tables for easy comparing the yields among the different backgrounds and the signal.

Tables 7.13 and 7.14 summarize the signals, summed backgrounds, and data from each channel, showing the uncertainties on the signals and backgrounds, and the signal:background ratios. Table 7.15 presents the differences between the data and the background model plus SM signal prediction for each analysis channel as a factor times the background+signal model uncertainty These numbers demonstrate the consistency of the background model with the data.

Pretagged Event Yields

	Run IIa						Run IIb					
	Electron Channel			Muon Channel			Electron Channel			Muon Channel		
	2 jets	3 jets	4 jets	2 jets	3 jets	4 jets	2 jets	3 jets	4 jets	2 jets	3 jets	4 jets
Signals												
tb	23	8.2	2.2	27	11	2.8	24	8.4	2.3	26	11	3.3
tqb	43	17	5.8	51	23	7.0	43	19	6.3	49	24	7.9
tb+tqb	67	26	8.0	77	33	10	67	27	8.6	75	35	11
Backgrounds												
$t\bar{t}\rightarrow ll$	60	37	12	57	41	13	65	42	13	61	46	14
$t\bar{t}\rightarrow l$+jets	41	136	158	32	143	196	43	141	168	33	145	198
$Wb\bar{b}$	479	160	45	530	211	57	458	161	42	499	200	61
$Wc\bar{c}$	1,041	356	101	1,196	485	125	1,006	351	94	1,126	453	137
Wcj	1,338	315	65	1,514	389	81	1,327	316	70	1,442	377	96
Wjj	13,847	3,309	722	17,028	4,612	984	14,166	3,489	795	16.941	4,710	1,137
$Zb\bar{b}$	18	7.1	3.5	70	22	6.6	19	8.2	3.4	70	26	7.4
$Zc\bar{c}$	33	12	4.2	151	46	13	35	15	5.9	152	54	14
Zjj	461	125	40	1,309	348	84	596	167	55	1,833	507	118
Dibosons	339	98	24	457	142	34	343	103	26	445	145	37
Multijets	923	278	74	896	235	69	987	294	188	1,369	377	108
Background Sum	18,582	4,834	1,246	23,243	6,675	1,663	19,048	5,087	1,460	23,972	7,040	1,927
Data	18,582	4,834	1,246	23,243	6,675	1,663	19,048	5,087	1,460	23,972	7,040	1,927

Table 7.9: Yields after selection and before b tagging.

Pretagged Event Yields for Combined Signals and Backgrounds

	Electron+Muon, Run IIa+Run IIb							
	2 jets		3 jets		4 jets		All Channels	
Signal								
tb+tqb	286		121		37		444	
Backgrounds								
$t\bar{t}$	392	(0.5%)	731	(3%)	772	(12%)	1,895	(2%)
W+jets	73,938	(87%)	19,894	(84%)	4,612	(73%)	98,444	(86%)
Z+jets & dibosons	6,331	(7%)	1,825	(8%)	475	(8%)	8,631	(8%)
Multijets	4,175	(5%)	1,184	(5%)	439	(7%)	5,798	(5%)
Background Sum	84,845		23,636		6,296		114,777	
Data	84,845		23,636		6,296		114,777	
$S:B$	1:297		1:195		1:170		1:259	

Table 7.10: Yields after selection but before b tagging for the analysis channels and backgrounds combined. The percentages are of the total background for each component.

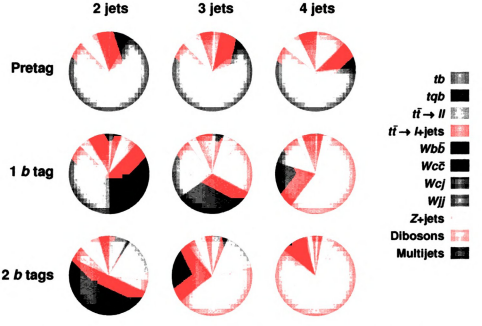

Figure 7.9: Illustration of the composition of the datasets as a function of number of jets and number of b tags.

Single-Tagged Event Yields

	Run IIa						Run IIb					
	Electron Channel			Muon Channel			Electron Channel			Muon Channel		
	2 jets	3 jets	4 jets	2 jets	3 jets	4 jets	2 jets	3 jets	4 jets	2 jets	3 jets	4 jets
Signals												
tb	9.1	3.1	0.82	10.2	3.9	1.0	9.5	3.3	0.91	9.9	4.3	1.2
tqb	17.4	6.6	2.1	20.5	8.6	3.6	16.9	7.2	2.5	18.5	8.7	3.0
tb+tqb	26.4	9.7	3.0	30.7	12.5	3.6	26.4	10.5	3.4	28.4	13.0	4.2
Backgrounds												
$t\bar{t}\rightarrow ll$	23.6	14.2	4.3	22.1	15.6	4.8	25.6	16.1	4.9	23.5	17.0	5.0
$t\bar{t}\rightarrow l$+jets	16.3	52.0	57.0	12.5	54.3	69.8	16.4	53.8	61.5	12.2	53.6	70.6
$W b\bar{b}$	135.4	44.2	12.0	146.4	57.1	16.0	129.5	44.3	11.6	136.0	53.4	16.8
$Wc\bar{c}$	66.0	24.8	8.1	73.9	33.4	9.9	68.6	26.2	7.6	72.4	32.6	10.9
Wcj	98.3	24.0	5.0	112.1	30.2	6.3	106.1	25.8	5.4	111.9	29.7	6.6
Wjj	73.6	21.9	6.1	87.0	30.1	8.1	114.4	35.4	9.6	128.3	46.5	14.5
$Zb\bar{b}$	6.5	2.8	0.89	26.8	7.9	2.5	5.0	2.4	1.0	20.1	7.7	2.2
$Zc\bar{c}$	2.7	1.2	0.55	13.3	4.6	1.5	2.1	1.1	0.57	10.7	4.3	1.2
Zjj	5.4	1.8	0.63	12.7	4.3	1.1	6.0	2.1	0.79	13.9	5.0	1.3
Dibosons	16.2	5.3	1.4	22.3	7.8	2.1	17.4	5.8	1.7	22.7	8.4	2.4
Multijets	28.0	10.3	3.0	51.5	17.2	7.3	31.0	10.1	7.1	73.5	28.2	9.0
Background Sum	472.1	202.4	99.0	580.6	262.5	129.4	522.1	223.2	111.6	625.3	286.5	140.5
Bkgds+Signals	498.5	212.2	101.8	611.3	275.0	134.6	548.5	233.6	115.2	653.6	299.4	144.7
Data	508	202	103	627	259	131	547	207	124	595	290	142

Table 7.11: Yields after selection for events with exactly one b-tagged jet.

Double-Tagged Event Yields

	Run IIa						Run IIb					
	Electron Channel			Muon Channel			Electron Channel			Muon Channel		
	2 jets	3 jets	4 jets	2 jets	3 jets	4 jets	2 jets	3 jets	4 jets	2 jets	3 jets	4 jets
Signals												
tb	5.69	2.12	0.58	6.66	2.75	0.75	5.26	2.00	0.58	5.61	2.59	0.78
tqb	0.81	1.61	0.90	0.92	2.15	1.07	0.94	1.89	1.01	0.99	2.22	1.21
tb+tqb	6.50	3.72	1.49	7.59	4.90	1.82	6.20	3.89	1.58	6.60	4.80	1.99
Backgrounds												
$t\bar{t}\rightarrow ll$	13.91	9.70	3.12	14.09	11.22	3.58	13.58	9.99	3.17	12.95	10.79	3.33
$t\bar{t}\rightarrow l$+jets	4.32	28.63	43.16	3.51	32.18	55.38	4.07	27.71	43.44	3.11	29.00	51.06
$Wb\bar{b}$	33.96	12.34	3.69	35.64	15.71	4.77	30.54	12.19	3.43	30.84	14.42	5.07
$Wc\bar{c}$	5.12	2.75	1.28	5.62	3.56	1.50	5.55	3.15	1.17	5.60	3.72	1.67
Wcj	1.44	0.68	0.19	1.62	0.83	0.26	2.04	0.96	0.28	2.07	1.04	0.33
Wjj	1.45	0.86	0.34	1.70	1.20	0.46	2.81	1.66	0.64	3.21	2.20	0.98
$Zb\bar{b}$	0.88	0.74	0.31	6.14	2.60	0.91	0.69	0.60	0.34	4.34	2.07	0.70
$Zc\bar{c}$	0.15	0.13	0.10	1.05	0.54	0.25	0.14	0.14	0.10	0.86	0.53	0.19
Zjj	0.14	0.09	0.05	0.31	0.20	0.07	0.16	0.11	0.06	0.34	0.24	0.09
Dibosons	2.05	0.85	0.28	3.06	1.37	0.46	1.96	0.91	0.30	2.98	1.38	0.46
Multijets	1.90	1.10	0.48	3.28	1.98	0.93	2.25	1.37	1.13	4.92	3.12	0.97
Background Sum	65.33	57.88	53.00	76.03	71.40	68.57	63.78	58.80	54.06	71.22	68.50	64.85
Bkgds+Signals	71.82	61.59	54.48	83.60	76.29	70.40	69.99	62.68	55.64	77.81	73.31	66.85
Data	67	61	37	71	62	56	79	56	51	85	79	80

Table 7.12: Yields after selection for events with exactly two b-tagged jets.

Tagged Event Yields for Each Channel and Signal:Background Ratios

	Single-Tagged			Double-Tagged		
	2 jets	3 jets	4 jets	2 jets	3 jets	4 jets
Electron Channel for Run IIa Data (p17)						
Signal Sum	26.4 ± 2.8	9.7 ± 1.3	3.0 ± 0.6	6.5 ± 1.0	3.7 ± 0.6	1.5 ± 0.3
Background Sum	472.1 ± 38.4	202.4 ± 16.9	99.0 ± 10.0	65.3 ± 9.5	57.9 ± 8.6	53.0 ± 8.5
Data	508	202	103	67	61	37
$S:B$	1:18	1:21	1:33	1:10	1:16	1:36
Electron Channel for Run IIb Data (p20)						
Signal Sum	26.4 ± 2.8	10.5 ± 1.4	3.4 ± 0.7	6.2 ± 0.9	3.9 ± 0.6	1.6 ± 0.3
Background Sum	522.1 ± 44.8	223.2 ± 19.0	111.6 ± 11.0	63.8 ± 9.4	58.8 ± 8.7	54.1 ± 8.5
Data	547	207	124	79	56	51
$S:B$	1:20	1:21	1:33	1:10	1:15	1:34
Muon Channel for Run IIa Data (p17)						
Signal Sum	30.7 ± 3.2	12.5 ± 1.6	3.6 ± 0.8	7.6 ± 1.1	4.9 ± 0.8	1.8 ± 0.4
Background Sum	580.6 ± 47.2	262.5 ± 21.0	129.5 ± 12.6	76.0 ± 10.6	71.4 ± 10.2	68.6 ± 10.8
Data	627	259	131	71	62	56
$S:B$	1:19	1:21	1:36	1:10	1:14	1:37
Muon Channel for Run IIb Data (p20)						
Signal Sum	28.4 ± 3.4	13.0 ± 1.8	4.2 ± 0.9	6.6 ± 1.0	4.8 ± 0.8	2.0 ± 0.4
Background Sum	625.3 ± 59.4	286.5 ± 25.8	140.5 ± 14.1	71.2 ± 10.2	68.5 ± 10.1	64.9 ± 10.4
Data	595	290	142	85	79	80
$S:B$	1:22	1:22	1:33	1:11	1:14	1:32

Table 7.13: Summed signal and background yields after selection with total uncertainties, the number of data events, and the signal:background ratio in each analysis channel.

Tagged Event Yields for Each Channel and Signal:Background Ratios

Electron and Muon Channels for Runs IIa+IIb

	2 jets	3 jets	4 jets
		Single-Tagged	
Signal Sum	112.0 ± 14.5	45.7 ± 7.0	14.2 ± 3.2
Background Sum	$2,200.1 \pm 153,4$	974.5 ± 72.3	480.6 ± 45.4
Data	2,277	958	500
$S:B$	1:20	1:21	1:34
		Double-Tagged	
Signal Sum	26.9 ± 4.0	17.3 ± 2.8	6.9 ± 1.5
Background Sum	276.4 ± 32.8	256.6 ± 32.3	240.5 ± 34.1
Data	302	258	224
$S:B$	1:10	1:15	1:34

Table 7.14: Summed signal and background yields after selection with total uncertainties, the number of data events, and the signal:background ratio for electron and muon Run IIa and Run IIb channels combined.

Data Excess (+) or Deficit (−) Over SM-Signal+Background Model

	Run IIa (p17)					
	Electron Channel			Muon Channel		
	2 jets	3 jets	4 jets	2 jets	3 jets	4 jets
1 tag	0.26σ	-0.60σ	0.10σ	0.35σ	-0.78σ	-0.16σ
2 tags	-0.51σ	-0.07σ	-2.04σ	-1.18σ	-1.35σ	-1.33σ

	Run IIb (p20)					
	Electron Channel			Muon Channel		
	2 jets	3 jets	4 jets	2 jets	3 jets	4 jets
1 tag	-0.03σ	-1.39σ	0.79σ	-1.11σ	-0.40σ	-0.20σ
2 tags	0.94σ	-0.74σ	-0.53σ	0.70σ	0.56σ	1.29σ

e,μ, 2,3,4jets, 1,2tags		p17,p20, 2,3,4jets, 1,2tags		p17,p20, e,μ, 1,2tags			All
p17	p20	e	μ	2 jets	3 jets	4 jets	channels
-0.37σ	-0.31σ	-0.25σ	-0.42σ	-0.17σ	-0.67σ	-0.22σ	-0.34σ

Table 7.15: Differences between the data and the predicted background (including SM signals) shown as a factor times the uncertainty on the signal+background predictions.

7.5 Cross-Check Samples

In order to ensure that the background model reproduces the data in regions were the biggest backgrounds dominate ("W+jets" and "$t\bar{t}$"), two cross-check samples of events for both the electron and the muon channels were prepared. The selection criteria for these samples are the same as for the all other samples (see Section 7.1), plus the following additional requirements:

"W+jets" sample

- Exactly two jets
- H_T(lepton,$\not\!\!E_T$,alljets) < 175 GeV
- One b-tagged jet

"$t\bar{t}$" sample

- Exactly four jets
- H_T(lepton,$\not\!\!E_T$,alljets) > 300 GeV
- One or two b-tagged jets

Table 7.16 shows the yields with backgrounds and channels combined for the cross-check samples. The agreement between the data and and background is shown in Figure 7.10, where the W transverse mass distribution is plotted for all channels combined (electron and muon, Run IIa and Run IIb). Plots for the individual channels together with other 12 significant variables can be found in in Appendix E. For the W+jets samples, W+jets events form 84% (electron channel) and 74% (muon channel) of the samples, and the $t\bar{t}$ component forms only 1% of the samples. For the $t\bar{t}$ samples, $t\bar{t}$ events form 85% (electron) and 82% (muon) of the samples, and the W+jets events form only 10% (electron) and 11% (muon) of the samples.

Event Yield [counts/10GeV]

Yields for the Cross-Check Samples

	W+Jets Samples		$t\bar{t}$ Samples	
Signal				
tb+tqb	38	(3%)	8	(2%)
Backgrounds				
$t\bar{t}$	16	(1%)	311	(83%)
W+jets	999	(78%)	40	(11%)
Z+jets & dibosons	109	(9%)	7	(2%)
Multijets	113	(9%)	7	(2%)
Backgrounds+Signals	1,275		373	
Data	1,311		368	

Table 7.16: Yields after selection in the cross-check samples, for channels and backgrounds combined. The numbers in parentheses are the percentages of the total background+signal for each source.

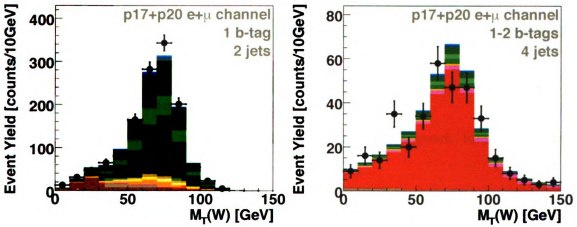

Figure 7.10: The W transverse mass distribution for the "W+jets" and "$t\bar{t}$" cross-check samples, for all channels combined.

7.6 Variables Definition

Table 7.17 lists the discriminating variables used in this analysis. The distributions of the variables are shown in Figs. 7.12 to 7.20 for all analysis channels combined. Jets are sorted in p_T where index 1 refers to the leading jet in a jet category. The jet categories are as follows: "jet$n$" (n=1,2,3,4) corresponds to each jet in the event, "tag$n$" refers to b-tagged jets, "untag$n$" signifies non-b-tagged jets, "best$n$" relates to the best jet, and "notbest$n$" pertains to all but the best jet. The best jet is defined as the one for which the invariant mass $M(W, \text{jet})$ is closest to $m_{\text{top}} = 170$ GeV/c^2.

The variables are separated into the following categories:

- **Object kinematics**

  These are individual object transverse energy (E_T) or momentum (p_T) or pseudorapidity (η) variables.

- **Event kinematics**

  These are total transverse energy or invariant mass variables.

- **Angular correlations**

  These are either ΔR, $\Delta\phi$ angles between jets and leptons or top quark spin correlation variables.

- **Top quark reconstruction**

  These are variables relating to reconstructing the top quark, identifying which jet to use, and which neutrino solution to pick.

  Neutrino p_z solutions In order to estimate the neutrino's p_z the W boson mass is used, which results in a quadratic equation with two solutions for p_z^ν. The smaller solution is denoted by the index "S1" and the other solution by "S2".

Top mass difference The top quark mass is reconstructed as:

$$M_{\rm top} = \sqrt{(E_{\rm lep} + E_\nu + E_{\rm jet})^2 - (\vec{p}_{\rm lep} + \vec{p}_\nu + \vec{p}_{\rm jet})^2}$$

using all possible conbinations of lepton, neutrino and jet. $M_{\rm top}$ is then compared with 170 GeV defining the difference of these two quantities as $\Delta M_{\rm top}$. The combination that gives the smallest difference in each event is called $\Delta M_{\rm top}^{\Delta M^{\rm min}}$, and the corresponding mass difference $\Delta M_{\rm top}^{\rm min}$.

Significance of top quark candidate. Assuming the top quark mass resolution function is a Gaussian distribution, the significance is calculated as:

$$\text{Significance}_{\rm min}(M_{\rm top}) = \ln \frac{g^{\rm Reco}(M_{\rm top} = M_{\rm top}^{\rm Reco})}{g^{\rm Reco}(M_{\rm top} = 170\ \text{GeV})},$$

where $g^{\rm Reco}$ is a Gaussian distribution centered at the reconstructed top quark mass with width $\delta M_{\rm top}$, given by:

$$\begin{aligned}
\delta M_{\rm top} &= \sqrt{c_1^2\ \delta^2 E_{\rm jet} + c_2^2\ \delta^2 \not{E}_T}\,, \text{ where} \\
c_1 &= \frac{1}{M_{\rm top}}(E_{\rm sum} - k_x^{\rm jet} p_x^{\rm sum} - k_y^{\rm jet} p_y^{\rm sum} - k_z^{\rm jet} p_z^{\rm sum})\,, \\
c_2 &= \frac{1}{M_{top}}(k_{E_\nu} E_{\rm sum} - \frac{1}{\cos\phi_{\not{E}_T}} p_x^{\rm sum} - \frac{1}{\sin\phi_{\not{E}_T}} p_x^{\rm sum} - k_\nu p_z^{\rm sum})\,, \\
E_{\rm sum} &= E_{\rm lep} + E_\nu + E_{\rm jet}\,, \text{ and} \\
p_i^{\rm sum} &= p_i^{\rm lep} + p_i^\nu + p_i^{\rm jet}\,, (i = x,\ y,\ \text{and}\ z)\,.
\end{aligned}$$

where

$$k_x^{\rm jet} = \frac{E_T^{\rm jet}\cos\phi}{p_T^{\rm jet}\cosh y}\,,\quad k_y^{\rm jet} = \frac{E_T^{\rm jet}\sin\phi}{p_T^{\rm jet}\cosh y}\,,\quad \text{and}\quad k_z^{\rm jet} = \frac{\sinh y}{\cosh y}\,,$$

y is the jet rapidity, and ϕ is its azimuthal angle.

The reconstructed top quark mass that gives the smallest significance in each event is called $M_{\text{top}}^{\text{sig}}$, and the corresponding significance is called $\text{Significance}_{\text{min}}(M_{\text{top}})$.

- **Jet reconstruction**

  These variables include the jet width in η and ϕ, the jet mass, and the relative p_T with respect to the the leading jet.

7.7 Data and Monte Carlo Agreement

Figure 7.11 shows the color scheme used in the plots in this analysis.

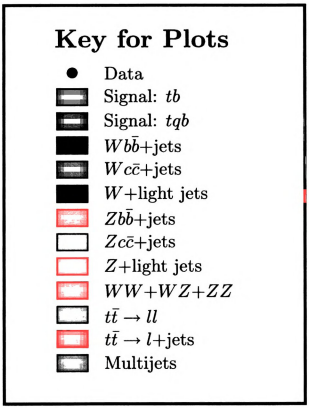

Figure 7.11: Illustration of the color scheme used in plots of signals and backgrounds in the Single Top analyses.

Figures 7.12 to 7.20 demonstrate the agreement between data and Monte Carlo

Decision Tree Input Variables

Object kinematics
- p_T(jet2)
- p_T(jet3)
- p_T(jet4)
- p_T(tag1)
- p_T(light2)
- p_T(notbest2)
- p_T(lepton)
- $\not\!\!E_T$
- Q(lepton)$\times\eta$(jet1)
- Q(lepton)$\times\eta$(jet2)
- Q(lepton)$\times\eta$(best)
- Q(lepton)$\times\eta$(light1)
- Q(lepton)$\times\eta$(light2)

Jet Widths
- Width$_\eta$(jet2)
- Width$_\eta$(jet4)
- Width$_\phi$(jet4)
- Width$_\eta$(tag1)
- Width$_\eta$(light2)
- Width$_\phi$(light2)

Angular Correlations
- ΔR(jet1,jet2)
- ΔR(jet1,lepton)
- ΔR(tag1,lepton)
- ΔR(light1,lepton)
- $\Delta\phi$(lepton,$\not\!\!E_T$)
- cos(best,lepton)$_{\text{besttop}}$
- cos(best,notbest)$_{\text{besttop}}$
- cos(jet1,lepton)$_{\text{btaggedtop}}$
- cos(lepton$_{\text{besttop}}$,besttop$_{\text{CMframe}}$)
- cos(lepton$_{\text{btaggedtop}}$,btaggedtop$_{\text{CMframe}}$)
- cos(tag1,lepton)$_{\text{btaggedtop}}$
- cos(lepton,Q(lepton)$\times z$)$_{\text{besttop}}$

Event kinematics
- Centrality(alljets)
- H_T(alljets)
- H_T(alljets−tag1)
- H_T(alljets−best)
- H_T(jet1,jet2)
- H_T(jet1,jet2,lepton,$\not\!\!E_T$)
- H_T(alljets,lepton,$\not\!\!E_T$)
- H_T($\not\!\!E_T$,lepton)
- H(alljets−tag1)
- M(alljets)
- M(alljets−best)
- M(alljets−tag1)
- M(jet1,jet2)
- M(jet1,jet2,W)
- M(jet3,jet4)
- M_T(jet1,jet2)
- p_T(jet1,jet2)
- $\sqrt{\hat{s}}$
- $M_T(W)$

Top quark reconstruction
- $M(W,\text{best1})$ ("best" top mass)
- $M(W,\text{tag1})$ ("b-tagged" top mass)
- $M(W,\text{tag1},S2)$
- (with second neutrino solution)
- $M(W,\text{jet1})$
- $M(W,\text{jet1},S2)$
- $M(W,\text{jet2})$
- $M(W,\text{jet2},S2)$
- $M(W,\text{notbest2})$
- $M(W,\text{notbest2},S2)$
- $M_{\text{top}}^{\Delta M^{\text{min}}}$
- $M_{\text{top}}^{\text{sig}}$
- $\Delta M_{\text{top}}^{\text{min}}$
- Significance$_{\text{min}}(M_{\text{top}})$

Table 7.17: Variables used with the decision trees in five categories: object kinematics, jet reconstruction, angular correlations, event kinematics, and top quark reconstruction. For the angular variables, the subscript indicates the reference frame. Plots for these variables are shown in Figures 7.12 to 7.20.

for the variables in Table 7.17 for all the 24-channels combined. Figures 7.22 to 7.27 show the distribution of W transverse mass for data and the background model. The plots are separated by number of jets (2, 3, 4), number of b tags (1, 2), lepton type (e, μ), and run period (Run IIa (p17) and Run IIb (p20)). Figure 7.28 shows the W transverse mass distribution with electron and muon and p17 and p20 combined. Additional plots can be found in Appendix B.

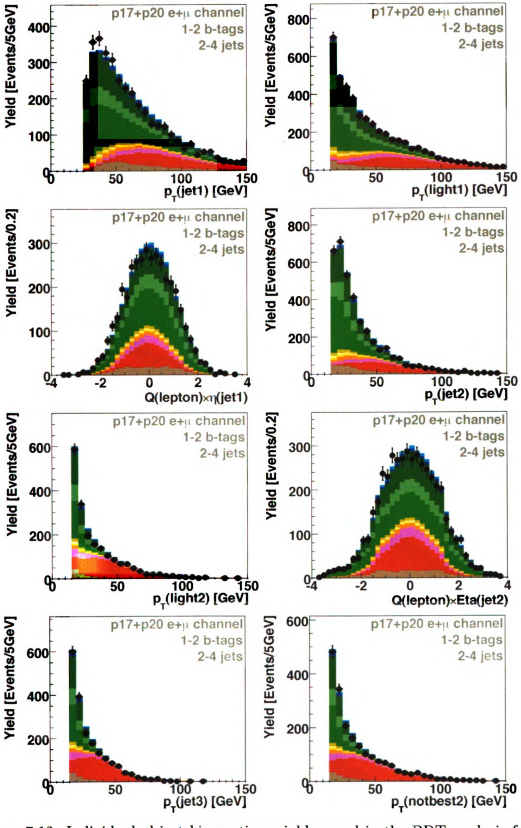

Figure 7.12: Individual object kinematic variables used in the BDT analysis for all channels combined (Part I).

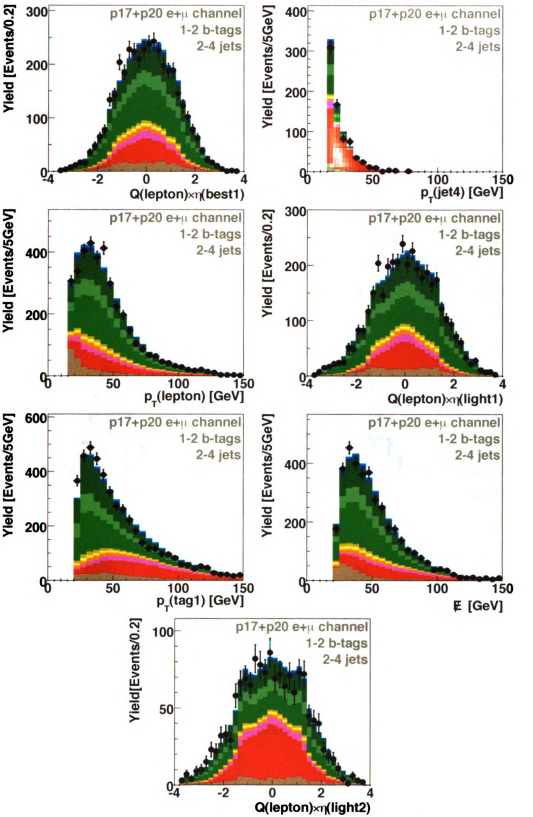

Figure 7.13: Individual object kinematic variables used in the BDT analysis for all channels combined (Part II).

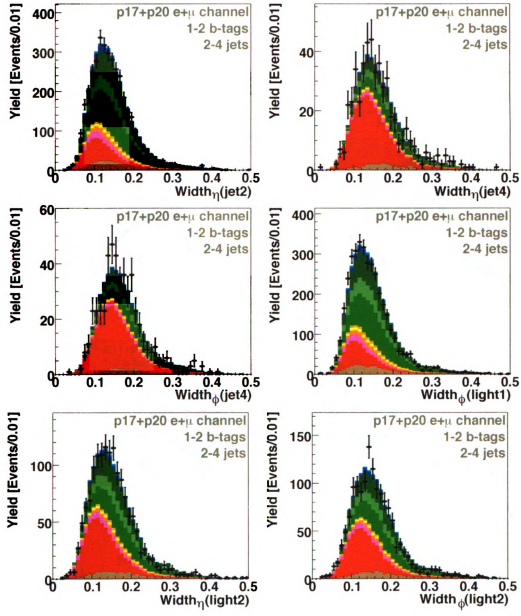

Figure 7.14: Jet reconstruction variables used in the BDT analysis for all channels combined.

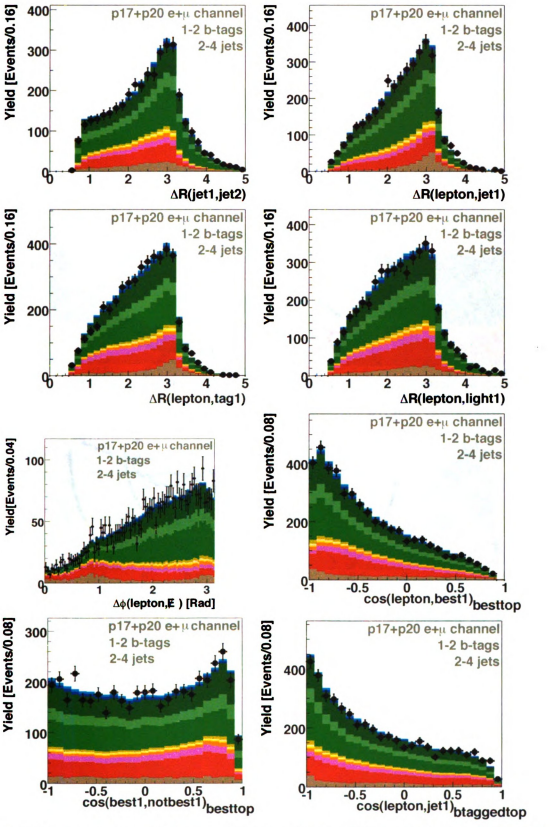

Figure 7.15: Angular correlation variables used in the BDT analysis for all channels combined (Part I).

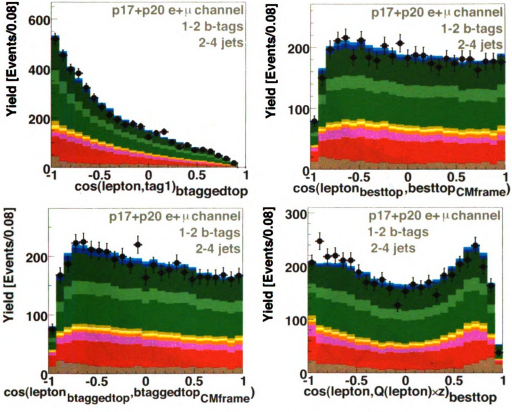

Figure 7.16: Angular correlation variables used in the BDT analysis for all channels combined (Part II).

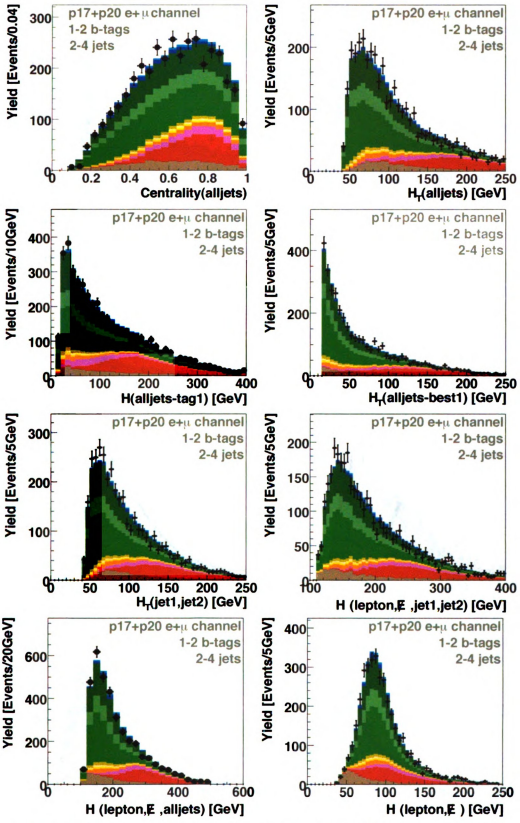

Figure 7.17: Event kinematic variables used in the BDT analysis for all channels combined (Part I).

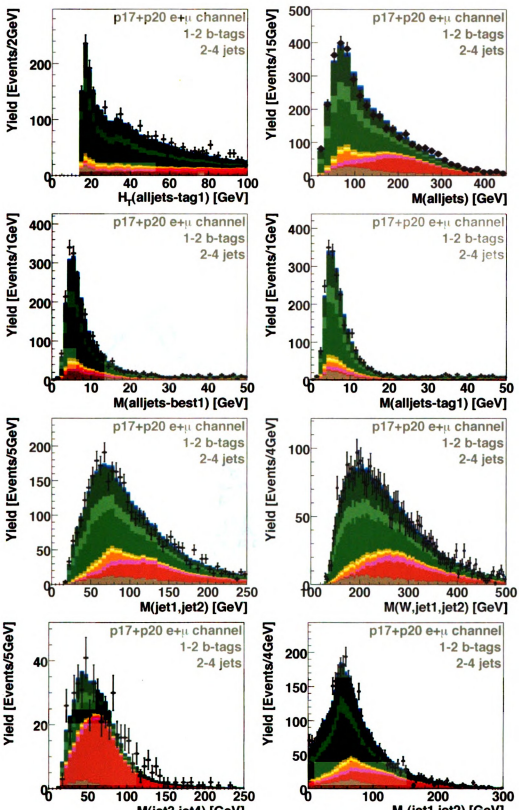

Figure 7.18: Event kinematic variables used in the BDT analysis for all channels combined (Part II).

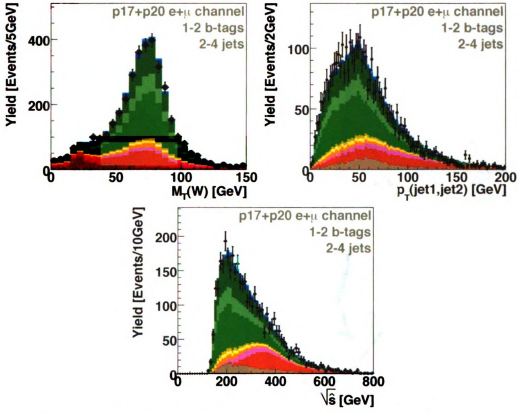

Figure 7.19: Event kinematic variables used in the BDT analysis for all channels combined (Part III).

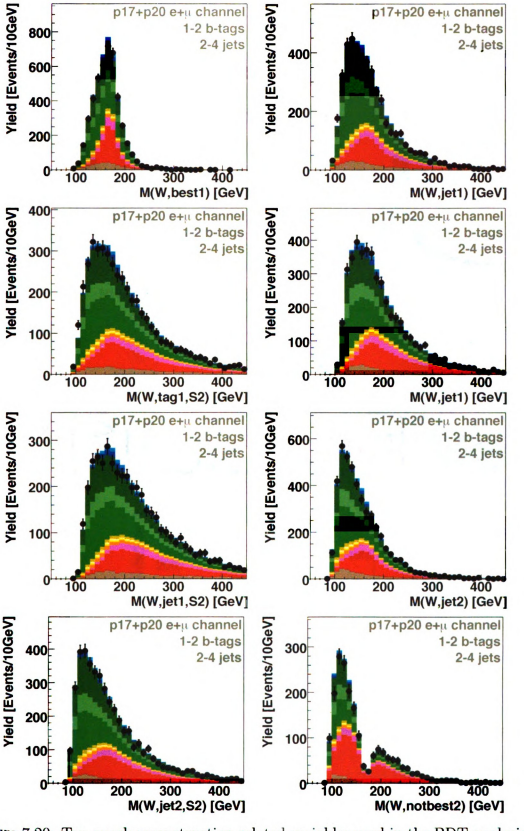

Figure 7.20: Top quark reconstruction related variables used in the BDT analysis for all channels combined.

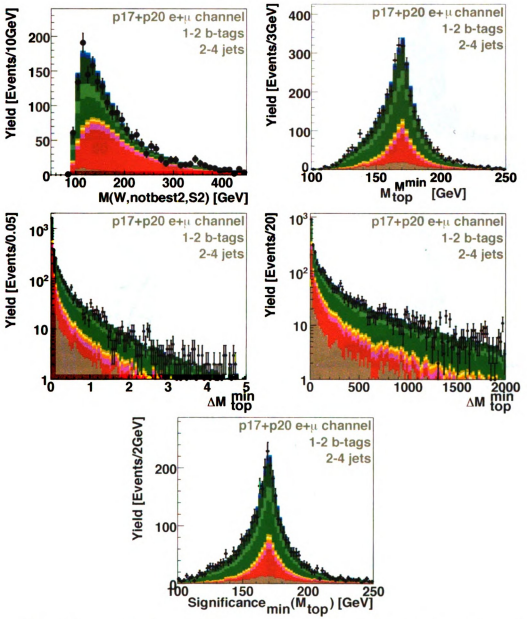

Figure 7.21: Top quark reconstruction related variables used in the BDT analysis for all channels combined.

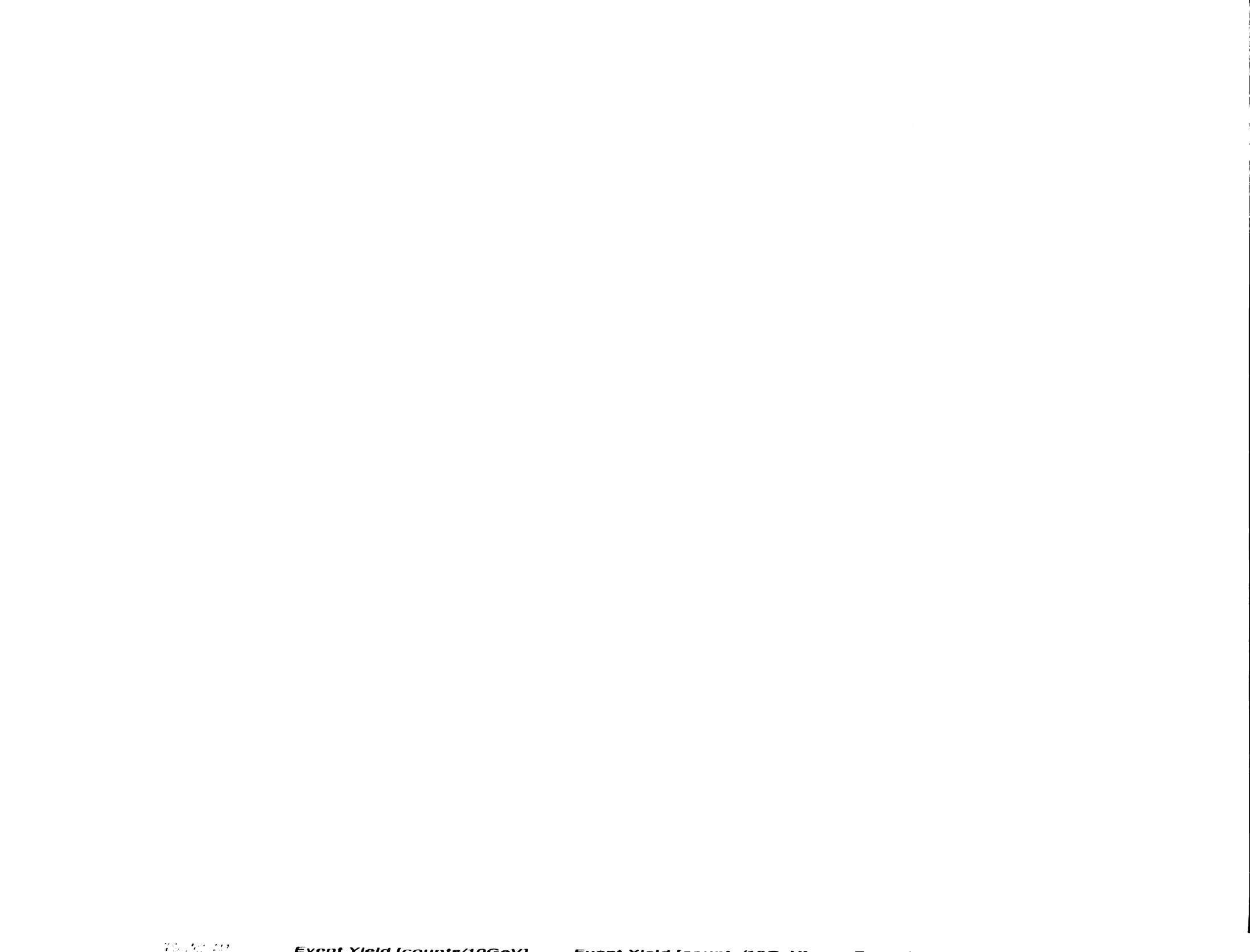

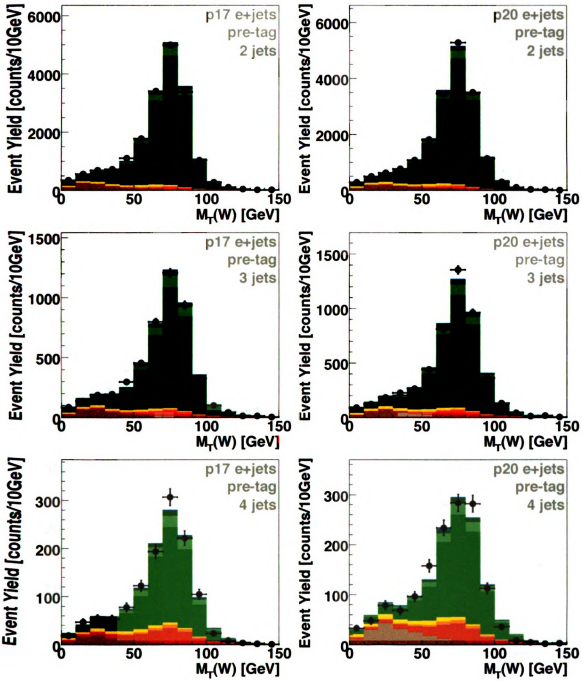

Figure 7.22: The W boson transverse mass distributions in the electron channel for **2-jet** (top row), 3-jet (middle row), and 4-jet events (bottom row), for p17 (left) and **p20** (right) for events before the b-tagging is applied.

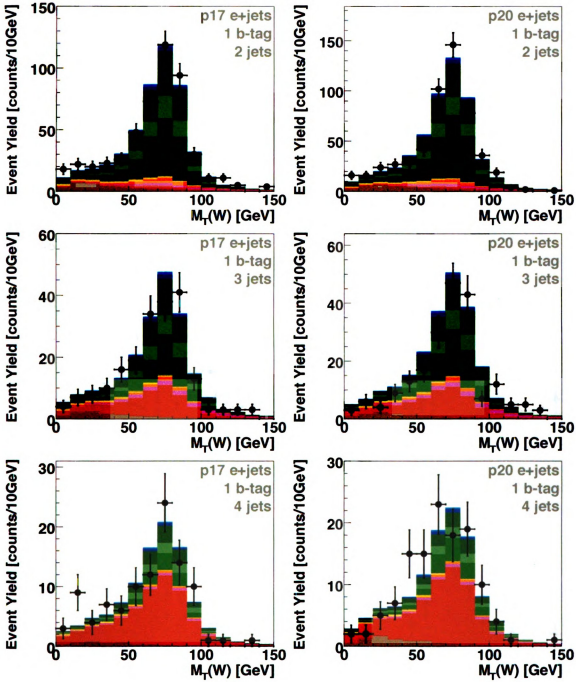

Figure 7.23: The W boson transverse mass distributions in the electron channel for 2-jet (top row), 3-jet (middle row), and 4-jet events (bottom row), for p17 (left) and p20 (right) for events with one b-tagged jet.

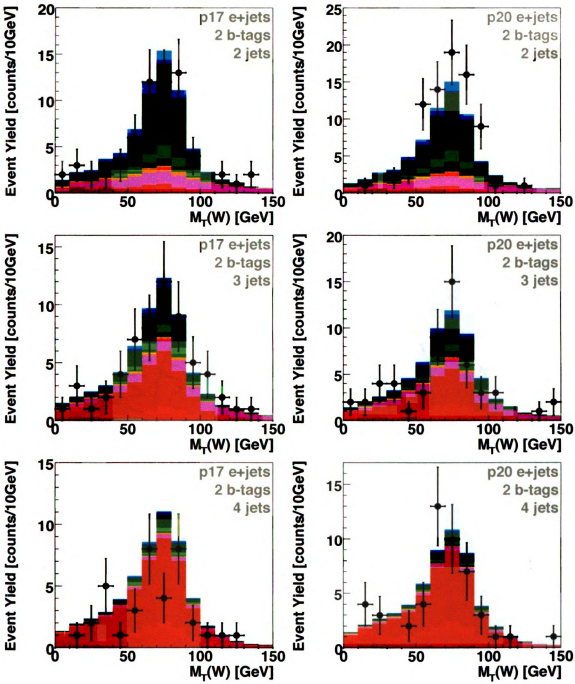

Figure 7.24: The W boson transverse mass distributions in the electron channel for 2-jet (top row), 3-jet (middle row), and 4-jet events (bottom row), for p17 (left) and p20 (right) for events with two b-tagged jets.

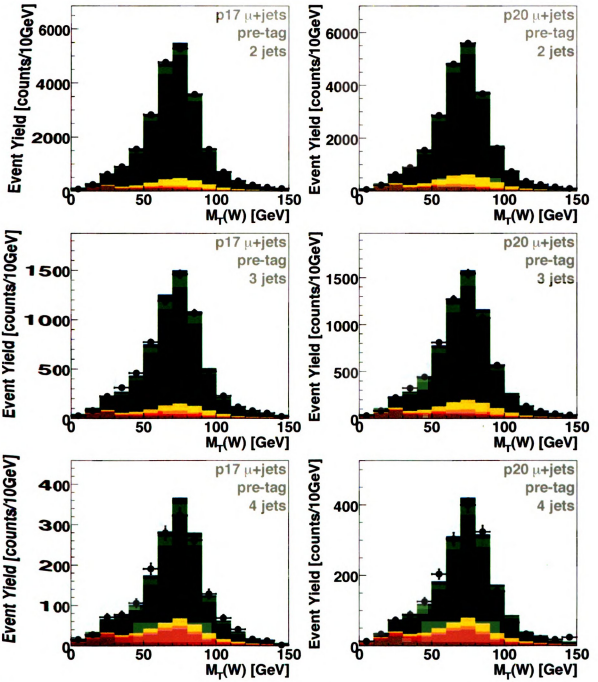

Figure 7.25: The W boson transverse mass distributions in the electron channel for **2-jet** (top row), 3-jet (middle row), and 4-jet events (bottom row), for p17 (left) and **p20** (right) for events before the b-tagging is applied.

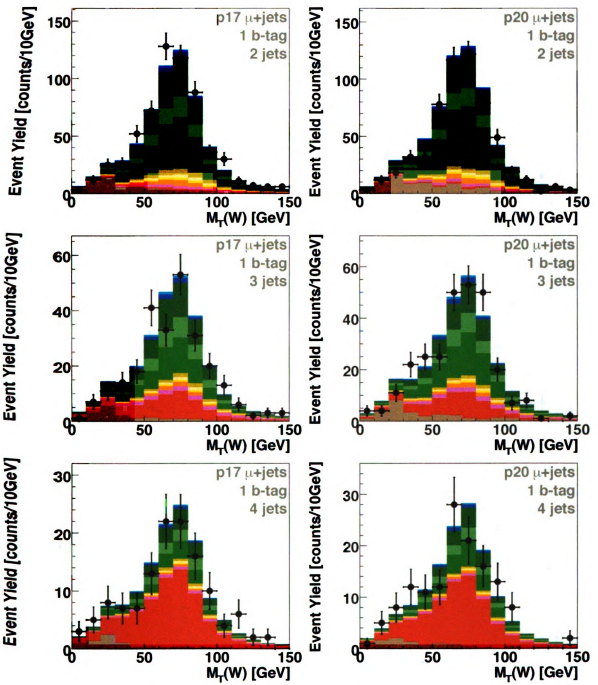

Figure 7.26: The W boson transverse mass distributions in the electron channel for **2-jet** (top row), 3-jet (middle row), and 4-jet events (bottom row), for p17 (left) and **p20** (right) for events with one b-tagged jet.

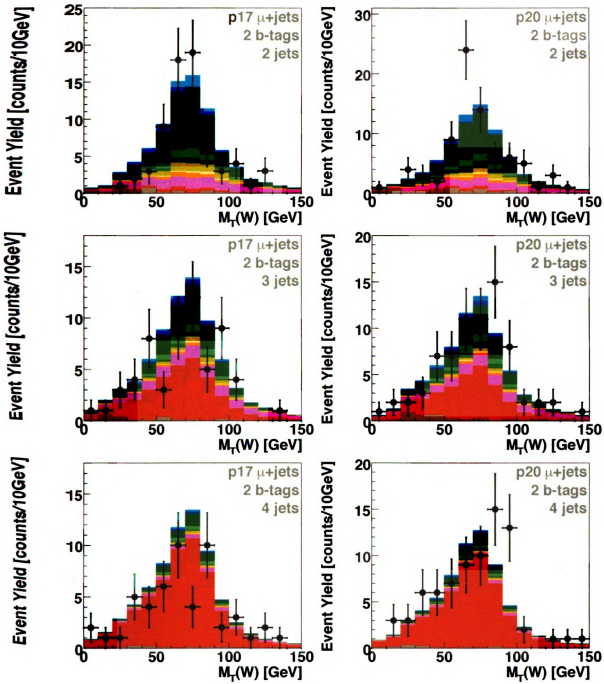

Figure 7.27: The W boson transverse mass distributions in the electron channel for **2-jet** (top row), 3-jet (middle row), and 4-jet events (bottom row), for p17 (left) and **p20** (right) for events with two b-tagged jets.

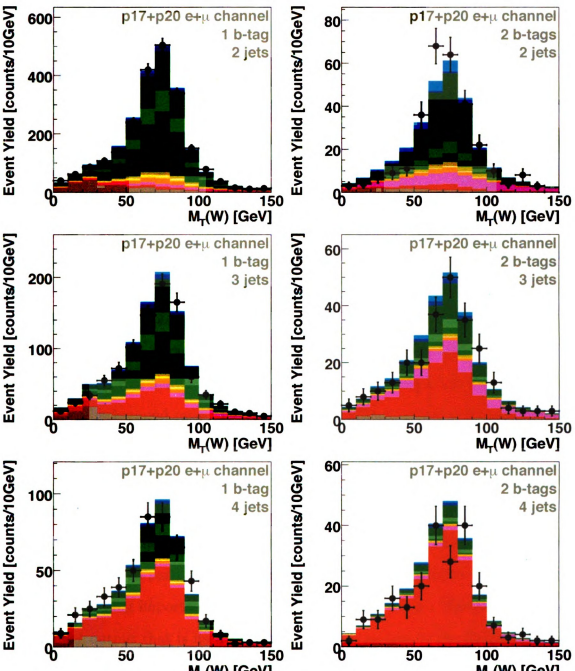

Figure 7.28: The W boson transverse mass distributions in the electron and muon channels and Run IIa and Run IIb datasets combined, for 2-jet (top row), 3-jet (middle row), and 4-jet events. Single-tagged (left), and double-tagged (right) events.

Chapter 8

Decision Trees

A Decision Tree (DT) [115, 116, 117] is an algorithm that can be used to classify events as signal or background. The structure of a DT resembles a tree, hence the name. It is built by splitting a sample recursively into two disjointed subsets until the ratio of signal-to-background reaches a predefined threshold or the number of events reaches a minimum. Each split is based on a selection cut that maximizes the signal-to-background ratio. The result is many subsets of the main sample based on the principle "divide and conquer." However, one Decision Tree is not enough to separate the Single Top signal from the background, rather some additional tools are required such as Boosting.

Boosting is a technique that increases the separation performance for a multivariate technique. In particular, Boosting for Decision Trees creates a series of trees that give increasing importance to the harder to classify events. The final result is a discriminant output that is used to perform a measurement of the Single Top cross section. This chapter presents an overview of Decision Trees and Boosting.

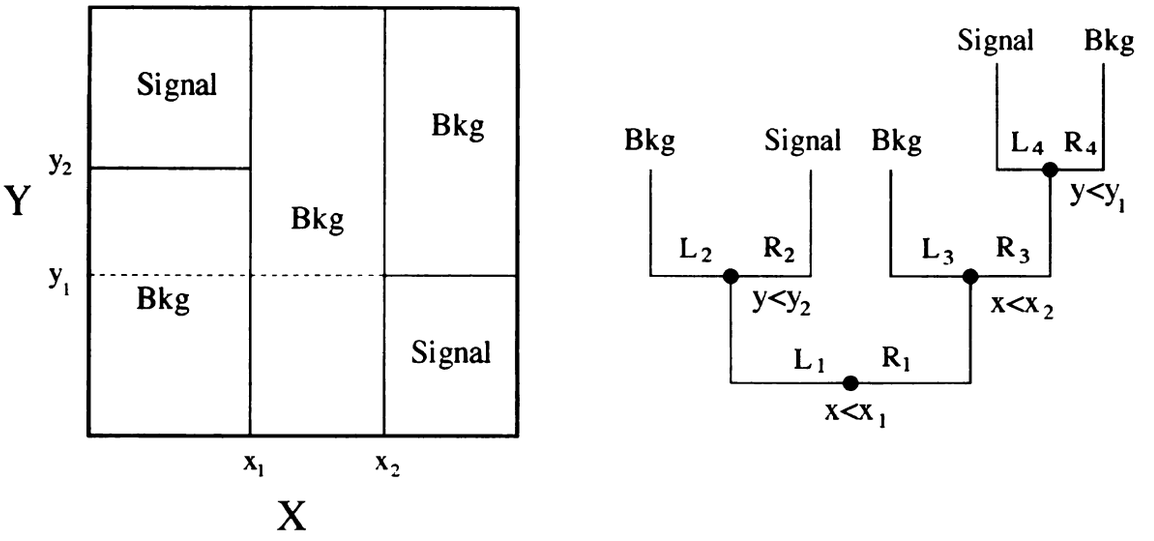

Figure 8.1: 2D plane of a simple classification problem, and a Decision Tree solving the classification problem of signal and background.

8.1 Overview

Consider the following two dimensional classification problem: in the plane (X,Y) there are five regions that need to be separated, two of these regions are considered signal and three are background (see Figure 8.1). The solution to this problem can be seen as a simple binary tree which, by performing a series of disjoint cuts, the plane is separated into five non-overlaping regions. Starting with a cut on the x-axis for values of $X < x_1$, the full sample is split in two subsets: right (R_1) and left (L_1). Next, the L_1 subset is divided into L_2 and R_2 by the cut $Y < y1$, similarly the R_1 subset is split twice more until all five regions are defined. This procedure can be scaled to more complex problems where the number of dimensions is much greater than two, and the cuts criteria are more difficult to determine.

More generally, a Decision Tree is built by repeatedly splitting an initial set of signal and background into two *nodes*. The criteria for a split is known as *cut*, where each cut is selected to maximize the signal-to-background ratio on the node to be split. The final nodes are know as *leaves*. A node is determined to be a leaf if the

number of elements in the node is less than a defined *leaf size*, or if the node is composed of all signal or all background. Each node has a *purity* value assigned to it defined by:

$$p = \frac{\sum_i s_i}{\sum_i s_i + b_i} = \frac{s}{s+b} \tag{8.1}$$

where s_i and b_i are the weights of each signal and background event.

An event defined by the variables $\vec{x_i}$ will follow a unique path through the DT and will end up in one and only one leaf. The purity p of this leaf is the DT discriminant output for that event: $D(\vec{x_i}) = p$. A simple Decision Tree is illustrated in Figure 8.2: for an event with $H_T < 242$ GeV and $m_{\text{top}} > 162$ GeV, the final discriminant output will be $D(\vec{x_i}) = 0.82$, progressing along one path until it reaches the final leaf. Similarly other events with different $\vec{x_i}$ will follow unique paths.

The Decision Trees have many advantages compared to other multivariate techniques. If an event fails one of the node cuts, the event is still considered in subsequent nodes and, in principle, it may pass the classification criteria; this is in contrast to a purely cut-based analysis. In addition, DTs are also easy to understand as they have a human-readable structure making it possible to follow a particular event through the full tree. Lastly, any final result can be explained by Boolean logic.

The process in which a Decision Tree is built is known as *training*, which is explained in the following Section. The training of a Decision Tree is fast compared to other multivariate techniques such as Neural Networks, that is to say large amounts of data can be processed in much shorter amount of time. For this analysis, all the training is done using the background models, and the data is used only at the end when performing the measurements.

Also adding more variables to the DT does not affect the DT performance as long as the variables are well-modelled, an extra variable can only do good to the classification problem. Neither is it necessary to preprocess the input files as in other

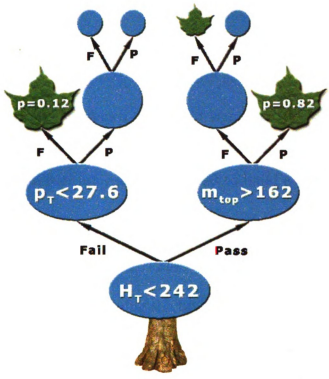

Figure 8.2: Graphical representation of a DT. Nodes with their associated splitting test are shown as (blue) circles and terminal nodes with their purity values are shown as (green) leaves. All nodes continue to be split until they become leaves. Note that if one event fails a cut, it does not necessarily follow that the event will fail to pass as that event can be recuperated and pass later down the tree chain [25].

multivariate techniques. Any monotonic transformation to the input variables will yield the exact same tree, which is due to the principle used to split nodes (explained in the next Section). Lastly, another implication is that discrete variables can be directly used in the list of variables.

Some of the draw-backs of a DT are the intrinsic instability of the tree structure with respect to the training sample composition. This means that any small changes are propagated to the whole tree due to the hierarchical nature of the process, and in some occasions producing very different trees but still with similar separation power. One additional issue with DTs is that the final output has a discrete nature, this is because the discriminant output is defined based on the purity of the leaves but the

number of leaves is finite.

8.2 Training Algorithm

Let us consider a sample of known content of signal and background events where each event is defined by an event weight and a set of variables $\vec{x_i}$. Using this "traning" sample, the following algorithm can be employed to build a Decision Tree:

1. Normalize the signal training sample and the background training sample to the same value, such that $\sum s_i = \sum b_i$ $(s = b)$;

2. Create the first node, containing the full training sample $s + b$;

3. For each variable: order the events by the value of the variable and select the variable value (cut value) that gives the best signal-background separation. More about this in Section 8.2.1;

4. From the list of variables and cuts from the previous step, choose the one that gives the best signal-background separation. If no further improvement in the separation is possible, the node becomes a leaf;

5. Using the selected variable and cut value, split the node into two subsamples one passing the selection cut and one failing it. The two subsamples are now child nodes of the original node;

6. If the number of events on the node reaches a minimum, the node becomes a leaf. This minimum is one of the DT parameters (see Section 8.2.3); and

7. Apply the algorithm recursively from Step 3 until all nodes are leaves.

8.2.1 Splitting a Node

The most critical part in the Decision Tree training process is the splitting of a node, as the structure of the tree can be dramatically changed if the splitting criterion is modified. The determination of the splitting of a node is based on the quantity *degradation*, D, which is constructed from the weight of the events in the node, including both signal and background events. For any split, the change in the degradation can be expressed as, ΔD:

$$\Delta D = D - D_L - D_R = D(s,b) - D(s_L,b_L) - D(s_R,b_R) \tag{8.2}$$

where L and R are indices corresponding to the right and left daughter nodes, and by construction $s = s_L + s_R$ and $b = b_L + b_R$. This quantity ΔD sometimes is referred as the "goodness of the split." The goal with each split is to find the one that best separates signal from background. This can be accomplished by finding the cut that reduces the most of the degradation or equivalently the split that gives the maximum ΔD. As such, finding the optimal split can be seen as a minimization problem. The part of the algorithm that split the node can be expressed as the following steps:

1. For each variable:
   - Sort all the events in the node according to the current variable;
   - Go through the events in order and calculate ΔD for the split corresponding to cutting between the current and the next event; and
   - Select the cut value for which ΔD is maximum.
2. Out of all combinations (variable, cut value), select the one that gives the maximum separation.

There are many possible degradation measures that have been used in the past. For example, the Misclassification Error, the Gini Index [118] and the Cross En-

tropy [116]. Each degradation measurement is defined in terms of the node purity p as follows:

$$\begin{aligned} \text{Misclassification Error}: &\quad D = 1 - max(p, 1-p) \\ \text{Gini Index}: &\quad D = 2p(1-p) \\ \text{Cross Entropy}: &\quad D = -p\log p - (1-p)\log(1-p). \end{aligned}$$

where p is defined as in Equation 8.1.

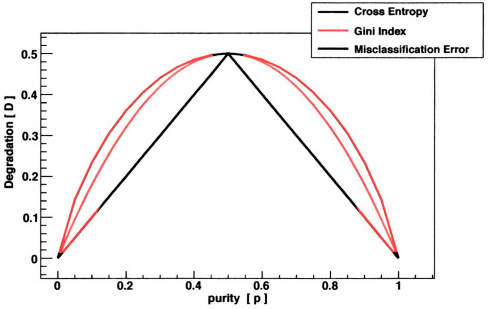

Figure 8.3: Degradation measures comparison as a function of the purity p. The Cross Entropy has been scaled down to compare the 3 cases.

Figure 8.3 shows a comparison of these three degradation measures. The measures are similar as they are maximal for equal amounts of signal and background ($p = 0.5$), symmetric and concave. The exception to the similarity ais that the Misclassification Error is not differentiable with respect to p. Alternately, these measures are often defined in terms of the sum of weights of signal and background in the node, s and b

as:

$$\text{Missclassification Error}: \quad D = max(s,b) \tag{8.3}$$

$$\text{Gini Index}: \quad D = \frac{sb}{s+b} \tag{8.4}$$

$$\text{Cross Entropy}: \quad D = -s\log\frac{s}{s+b} - b\log\frac{b}{s+b}. \tag{8.5}$$

A preference among the definitions is a matter of taste, but they do differ from each other by a factor of $(s+b)$. The second set of quantities is easier to handle as they are additive. From this point on, the definition of degradation measure will correspond to Equations 8.3, 8.4, and 8.5, which is also used in [119].

For the analysis presented in this dissertation, the degradation measure used is the Gini Index (Equation 8.4). It was found that for the set of samples used (see chapter 6) it had better performance when classifying Single Top events. Detail on the degradation measure selection can be found in Section 8.3.

8.2.2 Boosting

Boosting was introduced into machine learning over ten years ago [120] and is a powerful technique to improve the performance of any weak classifier [1]. Boosting has been widely used in several scientific fields including high energy physics: the MiniBooNE experiment used it together with Decision Trees [119, 121] and similarly the Single Top group at DØ [56, 105]. The DØ work on Boosting led to the evidence of Single Top in 2006.

In the case of Decision Trees, the Boosting technique is based on three principles. First, creating a initial tree, second, calculating an associated error function, and third, generating a second tree with a smaller error function. The third step is done by re-weighting the events on the first tree such that the misclassified events will have

[1] Weak classifier: A classifier that performs just above random classification.

a higher weight than properly classified events.

There are many Boosting algorithms available. For the results presented in this dissertation, the AdaBoost algorithm was chosen. Formulated by Y. Freund, and R. Schapire [122, 123, 124] (AdaBoost is short for Adaptive Boosting). Adaptative refers to subsequent decision tress that are tweaked in favor of the misclassified events by previous trees.

The Boosting algorithm consist of the following steps for the n^{th} tree in the Boosting chain:

1. Train the n^{th} Decision Tree;

2. Calculate the error ϵ_n associated the the tree. ϵ_n is equal to the weighted fraction of *misclassified* [2] events;

3. Calculate the tree weight according to:

$$\alpha_n = \beta \times \ln \frac{1 - \epsilon_n}{\epsilon_n} \tag{8.6}$$

   where β is parameter of the algorithm known as the Boosting parameter; and

4. Modify the weight of each event by:

$$\text{Boosted Decision Tree} \quad w_i \rightarrow w_i \times \exp(\alpha_n) \tag{8.7}$$

   thus the $(n+1)^{th}$ tree will be one that better identifies the events that the previous tree failed to properly classify.

The above procedure is repeated N times, where N is the number of Boosting cycles, to be defined by the user. The final N^{th} Boosted Decision Tree discriminant

[2] An event is consider misclassified if $|D_n(\vec{x_i}) - y_i| > 0.5$ where $D_n(\vec{x_i})$ is the discriminant associated with the n^{th} tree, and y is 1 for a signal and 0 for background.

output for the event i is

$$D(\vec{x_i}) = \frac{1}{\sum_{n=0}^{N} \alpha_n} \sum_{n=0}^{N} \alpha_n D_n(\vec{x_i}). \tag{8.8}$$

During the process of training, it was found that Decision Trees always improve their performance with the number of Boosting cycles. This overall improvement is about 20% with respect to the no-Boosting case. In addition, the Boosting produces a smoother discriminant output $D(\vec{x_i})$. The increase in the performance reaches a plateau at approximately 30 Boosting cycles, and does not degrade after that. In Figure 8.4, some quantities are plotted as a function of the number of Boosting cycles: the tree weight with respect to the first tree, Cross Section Significance [3] and the number of leaves.

8.2.3 Boosted Decision Tree (BDT) Parameters

There are several parameters that can influence the final result of a Boosting Decision Tree, some have been explicitly defined in previous sections:

- *Initial normalization.* Step 1 in Sec. 8.2. In this analysis, both the signal and the background are normalized to $s = \sum s_i = b = \sum b_i = 0.5$.

- *Criteria for deciding when a node becomes a leaf.* This parameter is known as minimum leaf size and represents the minimum number of events allowed in a leaf. (Step 6 in Sec. 8.2). This value was set to 100.

- *Degradation function used to find the best split.* Sec. 8.2.1. The Gini Index was used as degradation measure.

- *Number of Boosting cycles.* 50 Boosting cycles provided the best separation.

[3] Cross Section Significance (CSS) is defined as $\sqrt{(\sum (s_i/(s_i + b_i)))}$

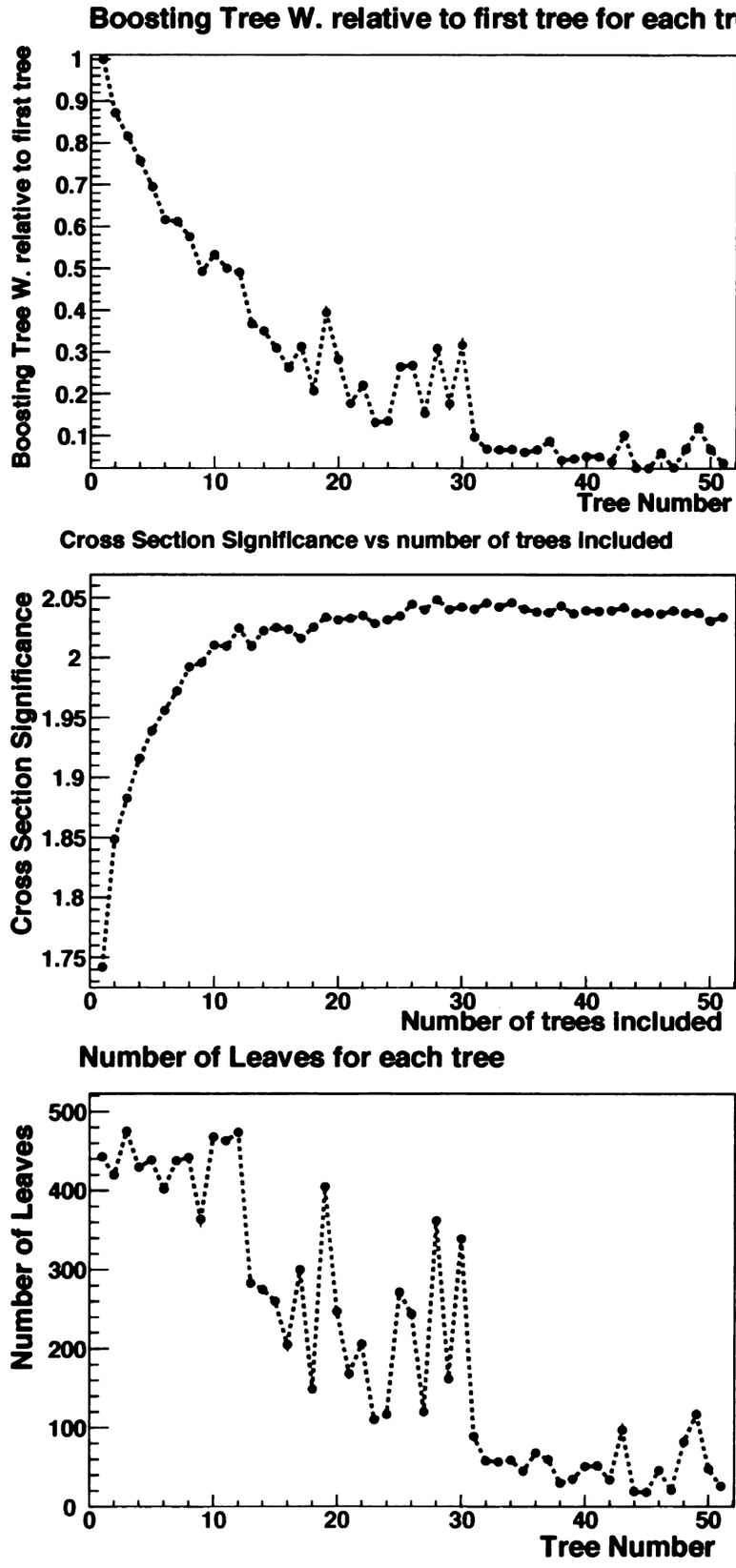

Figure 8.4: Relative weight, Cross Section Significance; and number of leaves as a function of the number of Boosting cycles for one of the 24-channels in the analysis.

- *Value of the Boosting parameter* β. $\beta = 2$ gave the best performance.

A more detailed discussion on the choice of values for these parameters is in Section 8.3.

8.2.4 Decision Tree Implementation

To build and evaluate the decision trees we use the code package `classifier` which is in the DØ CVS code repository [4]. This code has been used before by the Single Top group at DØ, and corresponds with the code used for the Single Top evidence publication [56, 105]. There are some differences with the code currently used, but these are mainly improvements and additional options which were implemented.

8.3 BDT optimization

It is very important to have good list of well-modelled variables when training a BDT. In addition, an appropriate fine tuning of the BDT paramenters (8.2.3) can guarantee an optimal BDT.

8.3.1 Variable Selection

A list of sensitive variables has been derived based on an analysis of the signal and background Feynman diagrams [125, 126] and on a study of Single Top quark production at next-to-leading order [6, 7]. The variables fall into five categories: individual object kinematics, jet widths (RMS width of the jet energy cluster), global event kinematics, top quark reconstruction variables, and variables based on angular correlations.

The number of initial variables is about 600, but not all are used as those with unsatisfactory data-background agreement are directly removed. Each variable is

[4] http://cdcvs0.fnal.gov/cgi-bin/public-cvs/cvsweb-public.cgi/

required to have a Kolmogorov-Smirnov test value of at least 0.1 calculated from comparing the variable distribution for data with the sum of backgrounds. The KS implementation in ROOT [172] is used, together with histograms with many bins [$O(1000)$] in order to get an accurate estimate.

The addition of well-modelled variables in Decision Tree training does not degrade the performance. Indeed, if new variables have even some discriminating power, they will improve the performance of the tree even by a small quantity. If they are not discriminating enough, they will be ignored and the tree unchanged. However, having more variables also increases the computation power required to train a BDT, therefore all the variables that have no or little discriminating power have been removed from the list.

The variable selection process is done by following the subsequent procedure of:

- train several decision trees with the full list of well modeled variables;
- using the decision tree variable ranking[5] to judge which variables were more important during the decision tree training;
- next, out of the 24-channels available: the 50 highest (best) ranked variables are selected from the {2-jets,1-b-tag} channels, the 30 best from the {3-jets,1-b-tag} channels, the 20 best from the {2-jets,2-b-tag} channels, and the 10 best from each of the other three jets/tags combinations;
- All the sublists are combined and then reduced by removing duplicated variables.

The number of variables selected for each channel varies according to the importance of the channel in the whole analysis. For channels with a smaller signal-background, a larger number of variables are taken to be part of the common list of

[5] The decision tree variable ranking for a variable is the sum of degradation improvement ΔD for each split in which the variable is used.

variables, such as the 2-jet,1-b-tag. The final number of variables after all the variable selection is performed is 64 (see Table 7.17).

8.3.2 Parameters Optimization

As described in Section 8.2.3, there are many parameters that can impact the performance of a Decision Tree. In order to study their impact in the final result, several Decision Trees were trained (using the first subset of events) and figure of merit was used to compare each case performance in a second (independent) subset. The figure of merit used to determine which parameters to choose was the *expected Cross Section Significance* calculated in the second subset.

The Cross Section Significance is defined as:

$$\mathrm{CSS} = \sqrt{\sum_i s_i^2/(s_i + b_i)} \tag{8.9}$$

where s_i and b_i are the signal and background yields in bin i of a histogram of the decision tree output with 100 equal-sized bins.

To choose the optimal set of decision tree parameters, an initial value for each parameter is chosen based on previous results from the Decision Tree analysis in the Single Top evidence paper [56]. Ideally, one could give each parameter a range of values and then with all possible combinations of parameters settings, perform a scan of the parameters phase-space and select the optimal selection of parameters. However, this procedure would require too much computation due to the many possible combinations and high probability of introducing human error. Instead, the strategy used for the optimization was to "smarten up" the possible values given to each parameter still covering its full range, and concentrating on near zones, where the fine tuning of a parameter can make a significant impact on the final result. Finally, one parameter is varied at a time combining the setting of a few well-performing points and then

run all possible combinations for this reduced set.

Out of the 24-channels available in the analysis, only the most significant channels were included in the parameter optimization. Such events have exactly two jets, of which one of them b-tagged. There were also additional cross checks performed in other channels to ensure there was no bias by only considering few channels in the optimization.

The BDT parameter phase-space is complex to interpret because there are several nonlinearities and several dimensions which could cause some difficulties at the moment of interpreting the final result. It is often the case that the trends observed in the optimizations do not follow a particular pattern as one moves along the parameter range.

The initial set of parameters for all the scans is:

- AdaBoost Parameter: 0.20
- Minimal Leaf Size: 100
- degradation Measure: Gini

The BDT parameter with the biggest impact in the final optimization is the number of Boosting cycles. There is a clear improvement when going from zero to twenty Boosting cycles. For each one of the parameters to be scanned, the following Boosting cycles are used: 20, 30, 50 and 70.

Next, the results of the study are summarized in a plot of the figure of merit as a function of number of Boosting cycles and different parameter values.

8.3.3 The AdaBoost Parameter

The following values were given to the AdaBoost parameter:

- 0.05, 0.15, 0.18, 0.20, 0.22, 0.25, 0.30 and 0.50.

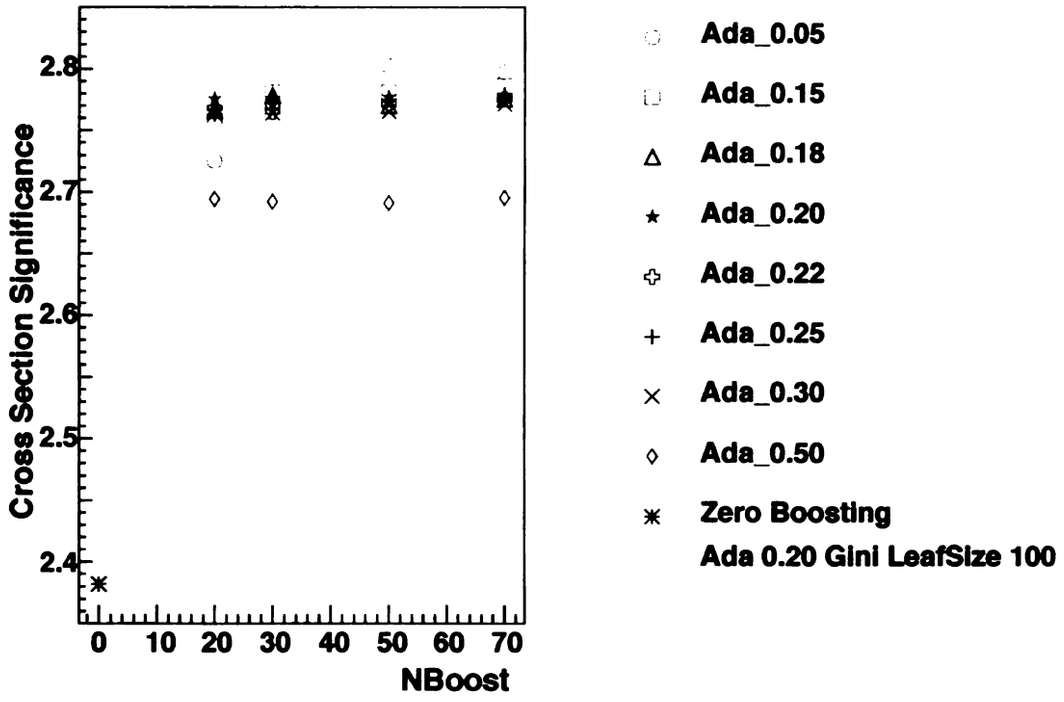

Figure 8.5: Cross section Significance as a function of the number of Boosting cycles for different values of the AdaBoost parameter. The uncertainty on the points is estimated to be ± 0.05. As a reference, the zero Boosts point is added to the plot to show the importance of Boosting. Note the zero suppressed vertical scale.

Note that most points are close to the previous analysis [56] value 0.2. In Figure 8.5, one can see that for most AdaBoost values a plateau is reached after 50 Boosting cycles. In most cases, the improvement can be seen up to approximately 30 cycles, after which the performance fluctuates up and down, demonstrating that no real improvement occurs when going beyond 50. In addition, the AdaBoost values near 0.2 perform similarly, giving us no reason why to change this paramenter value from 0.2, thereby confirming the previous analysis optimization studies.

8.3.4 Degradation Measures

The following degradation measures were contemplated in the study:

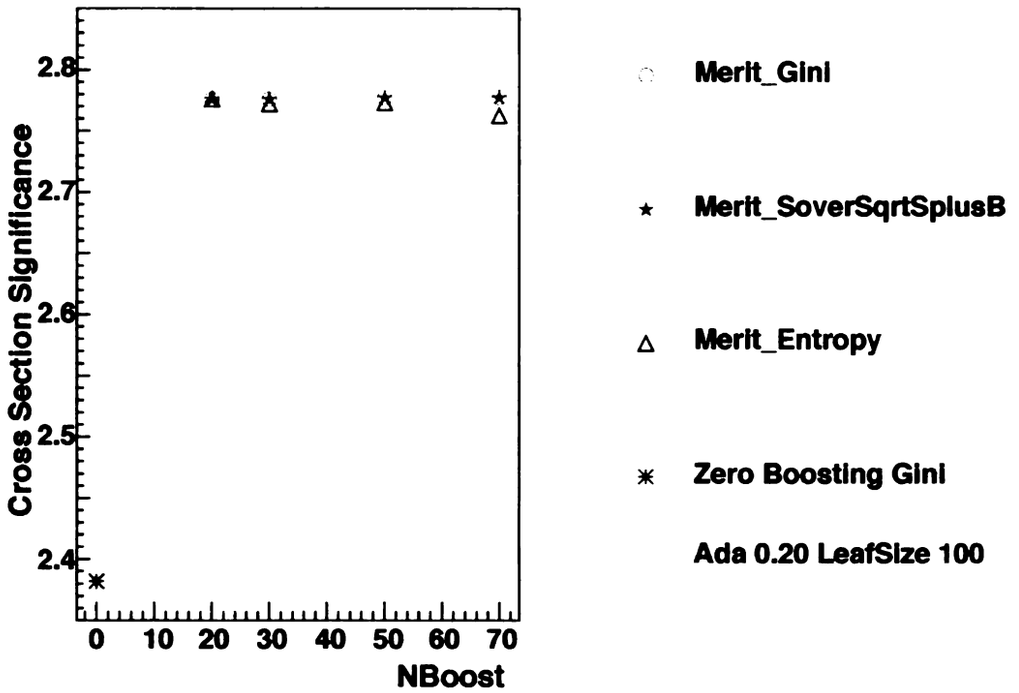

Figure 8.6: Excess significance as a function of the number of Boosting cycles for different purity measures. The uncertainty on the points is estimated to be ± 0.05. As a reference, the zero Boosts point is added to the plot to show the importance of Boosting.

- Gini, Entropy, $s/\sqrt{s+b}$ and $s/\sqrt{b}$.

The result from the scan is presented in Figure 8.6. $s/\sqrt{b}$ is not shown since it performed significantly worse than the other measures. The Gini Index was chosen as optimal point for this parameter.

8.3.5 Minimal Leaf Size

The following values for minimal leaf sizes were used in this scan:

- 50, 75, 90, 100, 110, 125, 150, 200 and 500.

In Figure 8.7 there is no clear trend when varying the minimal leaf size parameter, and again, it is clear that after 50 Boosting cycles, there is no improvement in the

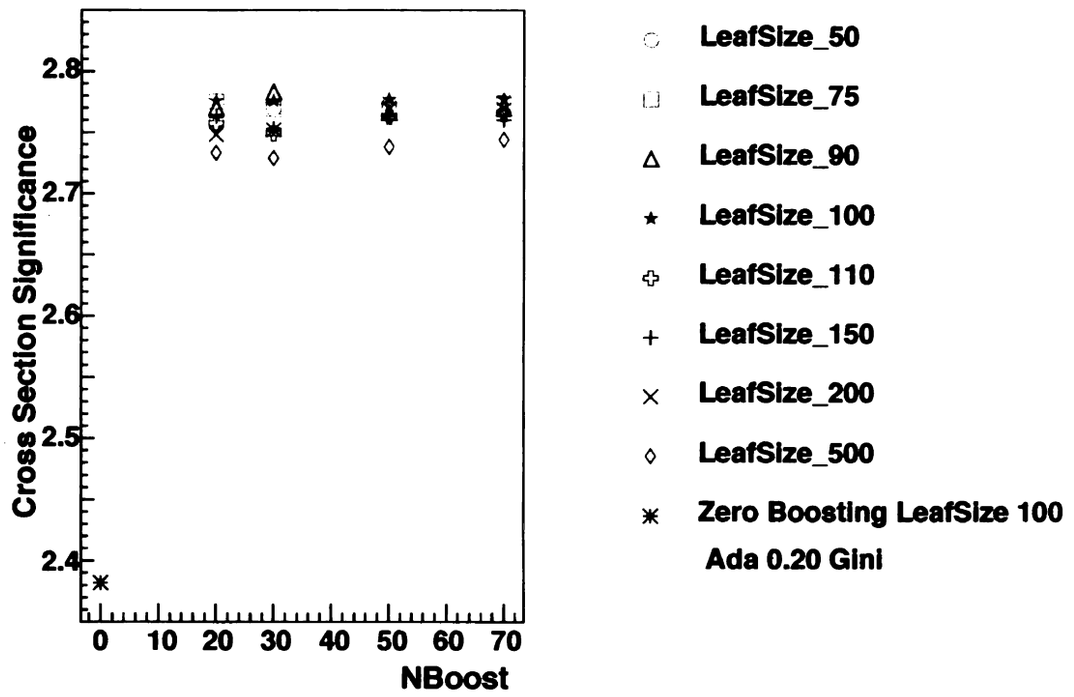

Figure 8.7: Excess significance as a function of the number of Boosting cycles for different Minimum leaf size. The uncertainty on the points is estimated to be ± 0.05. As a reference, the zero Boosts point is added to the plot to show the importance of Boosting.

performance. The value of this parameter is very important because a leaf size too small will create overly large trees which then degrades the tree performance. The final value for the leaf size is 100.

8.3.6 Parameters Summary

After scanning the parameter phase space and performing many studies using different parameter combinations, we arrive at the following optimal set of parameters:

- Number of Boosting cycles: 50
- AdaBoost parameter: 0.20
- Minimal leaf size: 100

- Degradation measure: Gini

This list of parameter settings gives the best separation for the studied channels (e+2jets/1tag, μ+2jets/1tag). In addition, the same set of values can be used in other analysis channels since the other channels have less impact on the final measurement; therefore, no further optimization is critical.

As an additional cross check, the AdaBoost parameter scan was also performed for the following channels: events with exactly three jets, where one jet is b-tagged, and events with exactly two jets, two of them b-tagged. In Figures 8.8 and 8.9, the selected point (0.2) lies right in the middle of a small spread in the CSS for both cases, confirming the results of the optimization. It is also reassuring that the dependance with the number of Boosting cycles remains the same and that after 50 Boosting cycles no clear improvement occurs.

8.4 Discriminant Output Transformation

A Boosted decision tree output given by the Equation 8.8, the possible values for $D(\vec{x_i})$ range from 0 to 1. As the number of Boosting cycles increases the average BDT output gets more central for both signal and background distributions, as shown in Figure 8.10 before the transformation. This effect produces an output distribution that is scarcely populated in the high (low) discriminant output regions. When performing the final measurements this behavior can cause irregularities, as some bins can contain signal but no background or vice-versa producing undefined results. In order to solve this problem, a monotonic transformation is applied to the BDT output:

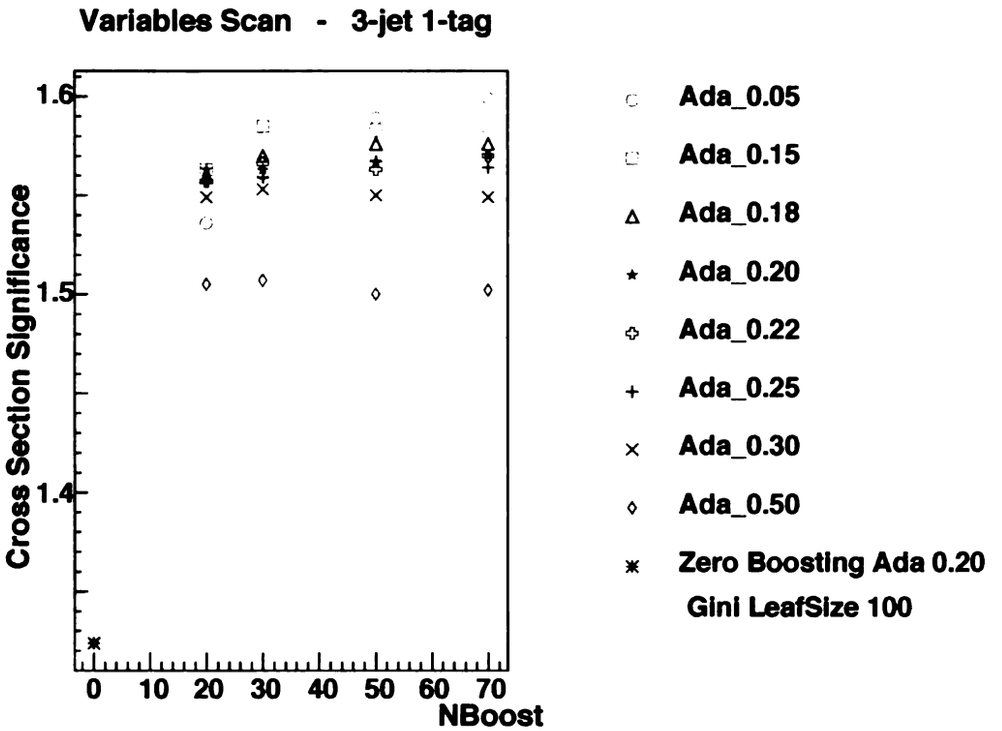

Figure 8.8: CSS as a function of the number of Boosting cycles for different values of the AdaBoost parameter for the 3-jet 1-tag case. The uncertainty on the points is estimated to be ± 0.05. As a reference, the zero Boosts point is added to the plot to show the importance of Boosting.

$$y = \begin{cases} \frac{k}{x}, & x \leq 0.8 \\ M - Kx, & 0.8 < x < 0.95 \\ 1, & x \geq 0.95 \end{cases} \tag{8.10}$$

where the constants are determined such that the total normalization of the BDT output is the same after and before the transformation is applied and by ensuring continuity of $f(x)$ in the full range 0 to 1. The constants are determined to be: $k = 0.346$, $K = 2.88$ and $M = 0.2.74$. In addition to the function $f(x)$, it is also required that at least 40 background events are present in each bin of width 0.02, in

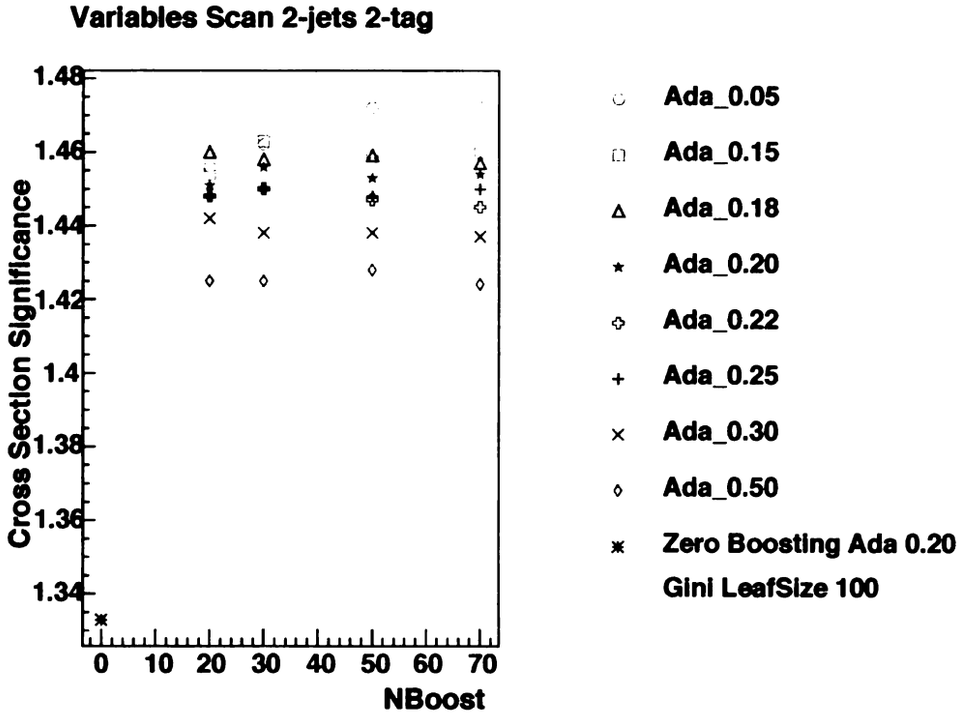

Figure 8.9: CSS as a function of the number of Boosting cycles for different values of the AdaBoost parameter for the 2-jet 2-tag case. The uncertainty on the points is estimated to be ± 0.05. As a reference, the zero Boosts point is added to the plot to show the importance of Boosting.

order ensure that there are no empty bins when measuring the cross section (more in Section 9.3). The transformation is applied from the high discriminant region down to zero. Figure 8.10 shows the BDT discriminant output before and after the transformation.

8.5 Removal Of One Variable From The Training

One additional study was performed to confirm that the right variables were used while training the BDTs. The performance of the BDTs were evaluated after one variable from the initial list of 64 variables is removed from the training. The figure of merit used for this study is the same used when selecting the BDT parameters CSS.

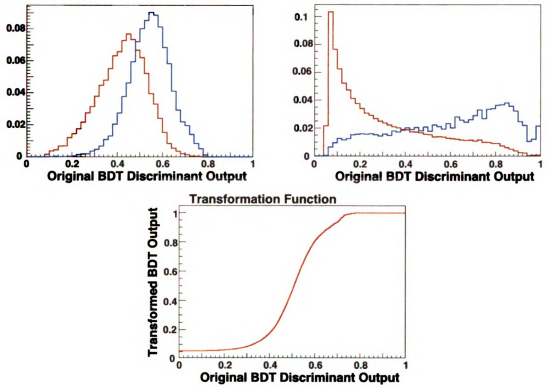

Figure 8.10: BDT discriminant output before (top left) and after (top right) the transformation, for both signal (blue) and background (red). The monotone transformation $f(x)$ is shown in the bottom. The plots correspond to one of the 24-channels in the analysis, similar results are obtained for other channels. The total number of bins is 50.

A summary of the results is presented in Figure 8.11, where the ratio of the CSS for the decision tree trained with one variable less than the nominal case (all variables). The statistical uncertainty associated with the calculation of the CSS is the cause of any fluctuation above 1.

It is found that no single variable alone can cause an abrupt change in the final performance, as there is no CSS change greater 0.7%. This derives from the nature of the DTs, for which the full set of variables gives the classification power rather than individual contributions.

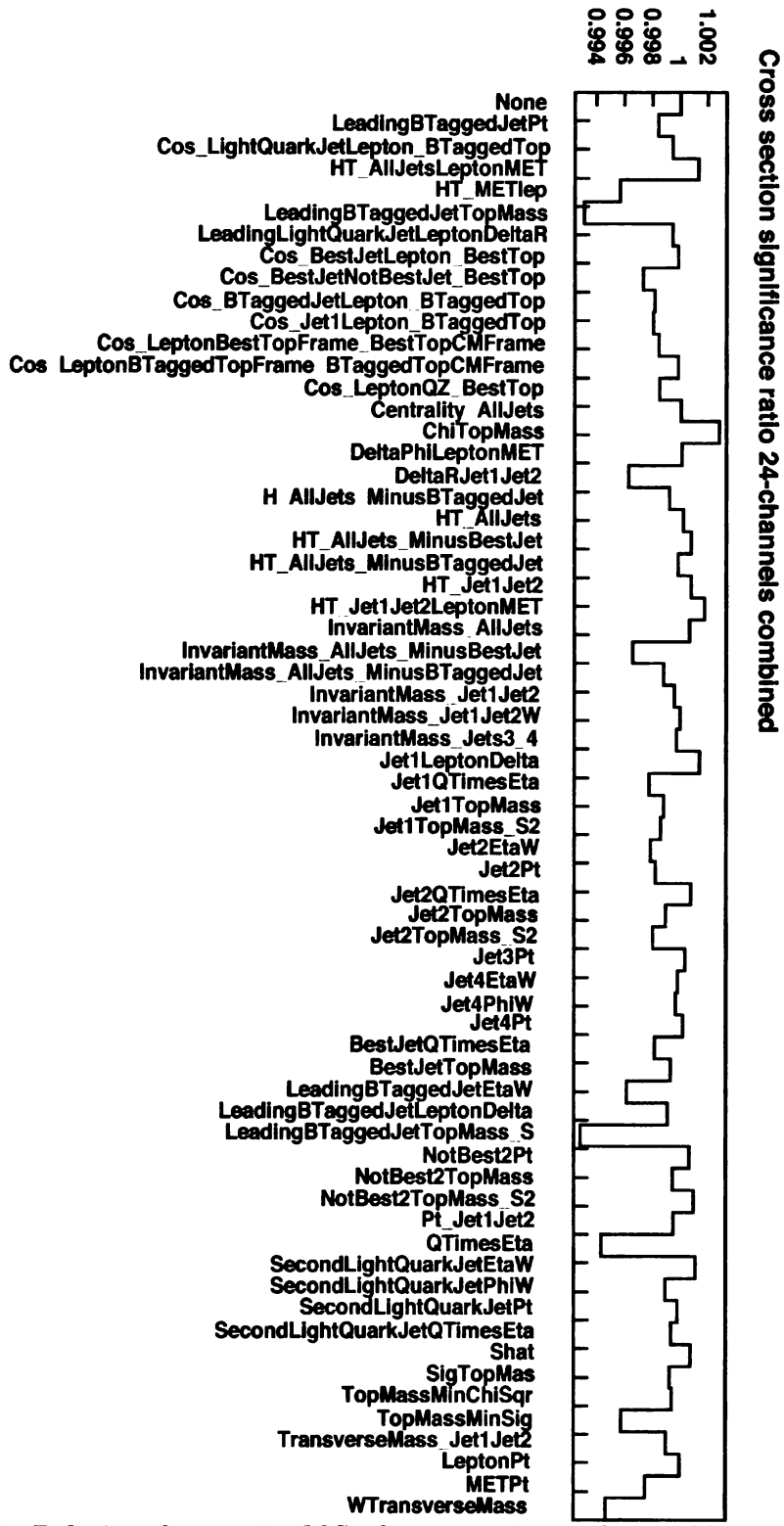

Figure 8.11: Relative changes in CSS after removing each variable compared to the all variables included case (first bin). The CSS for the all variable case is 5.465. The statistical uncertainty is estimated to be 1-2%.

Chapter 9

Analysis

In this Chapter, the full Single Top analysis is outlined. Starting from the systematics used in the analysis, followed by the process used to split the samples, and finally presenting the final measurements and their significances.

9.1 Systematic Uncertainties

There are two types of systematic uncertainties included in this analysis: uncertainties on the normalization of the signal and background samples, and those related to distributions shape-changing systematics (summarized in Tables 9.1 and 9.2). The uncertainties for each of the 24 channels is presented in Appendix C.

Below are listed all of the uncertainties contributions in the analysis:

- **Integrated luminosity**

  Corresponds to the $\pm 6.1\%$ uncertainty on the luminosity estimate, and affects the signal, $t\bar{t}$, Z+jets, and diboson yields. This systematic has an impact on the normalization only.

- **Theory cross sections**

  The uncertainties on the Single Top and $t\bar{t}$ cross sections have the following

contributions: scale, PDF, kinematics, and top quark mass choice [53, 128]. The mass uncertainty is taken as the difference between the cross section at 170 GeV and the current quark top mass world average (172.4 GeV [43]). The uncertainties values are $+4.3\%, -11.2\%$ for s-channel tb, $+5.5\%, -7.4\%$ for t-channel tqb, and $+7.7\%, -12.7\%$ for $t\bar{t}$. For tb+tqb combined, the uncertainty is $+5.2\%, -8.4\%$.

The diboson cross section uncertainties were calculated using the NLO MCFM generator [102]: the uncertainty for WW is $\pm 5.6\%$, for WZ it is $\pm 6.8\%$, and for ZZ it is $\pm 5.5\%$, and on the sum of the three processes it is $\pm 5.8\%$. This average value is used as uncertainty for the Z+jets background.

- **Branching fractions**

  The branching fractions for a W boson to decay to an electron, muon, or tau lepton, have an average uncertainty of $\pm 1.5\%$ [1].

- **Parton distribution functions**

  The effect of changing the parton distribution functions is evaluated by reweighting signal events according to the 40 CTEQ error PDFs and by measuring the signal acceptance in each case. This evaluation corresponds to a systematic uncertainty of $\pm 3\%$.

- **Trigger efficiency**

  The trigger used for the Single Top analysis corresponds to the OR of many trigger conditions which gives a trigger efficiency close to 100% (see Section 6.5). The corresponding uncertainty is $\pm 10\%$ for all the p20 muon channels and $\pm 5\%$ for others. The uncertainties for muons and electrons and Run IIa and Run IIb are treated as uncorrelated.

- **Instantaneous luminosity reweighting**

  All the MC luminosity distributions are reweighted to match the Run IIa or

Run IIb data distributions. The uncertainty on this reweighting is ±1.0%.

- **Primary vertex modeling and selection**

  The MC primary vertex distributions along the z-axis are reweighted to match the data distributions [129, 130]. The uncertainty on this reweighting is ±0.05%, and the uncertainty on the difference in primary vertex selection efficiency between data and MC is ±1.4%.

- **Electron reconstruction and identification efficiency**

  The electron scale factor uncertainty includes the dependence of the electron ID scale factor on the variables not included in the parameterization: jet multiplicity dependence, track match and likelihood scale factor. The dependences on ϕ and p_T of the electron are included in the systematic error as well as the limited statistics in each bin of the parametrization. The assigned total uncertainty ±is 2.5%.

- **Muon reconstruction and identification efficiency**

  The MC scale factor uncertainties for muon reconstruction and identification, including isolation requirements, are estimated by the muon ID group. The assigned total uncertainty is ±2.5%.

- **Jet fragmentation**

  The Jet fragmentation sytematic uncertainty is measured by comparing the acceptance of $t\bar{t}$ events generated with ALPGEN+PYTHIA with the ones generated by ALPGEN+HERWIG. The resulting uncertainty is about 1% to 8%, and is applied to all MC samples in the analysis.

- **Initial-state and final-state radiation**

  This uncertainty is evaluated using $t\bar{t}$ samples with the generation of these effects varied within expectations [75]. The uncertainty ranges from 0.6% to 12.6%.

- **b-jet fragmentation**

  The b-jet fragmentation uncertainty comes from the difference between the fragmentation parametrizations preferred by SLD (SLAC Large Detector) vs. LEP (Large Electron Positrion collider) data, and it is evaluated in the $t\bar{t}$ pairs cross section [131]. The uncertainty is measured to be $\pm 2.0\%$.

- **Jet reconstruction and identification**

  The efficiency to reconstruct and identify jets has an uncertainty of $\pm 1\%$. This uncertainty is related to the fact that jets reconstructed in MC have a higher efficiency than those in data.

- **Jet energy resolution**

  It was found that the shape changing variations due to JES are smaller than 4% for all signals and backgrounds, therefore it was safe to assign a flat JES uncertainty of $\pm 4\%$.

- **W+jets and multijets normalization**

  The W+jets and multijets backgrounds are normalized to the data using a fit as described in Section 7.2. The uncertainties related to this normalization vary from channel to channel (see Appendix C), and range from 30% to 54% for the multijets backgrounds and from 1.8% to 5.0% for the W+jets backgrounds.

- **W+jets heavy-flavor scale factor correction**

  The heavy-flavor scale factor correction, S_{HF}, for $Wb\bar{b}$ and $Wc\bar{c}$ is measured in data in several channels, as shown in Section 7.2.2. The Monte Carlo TRF uncertainty induces fluctuations in the effective scale factor that are at least as large as the channel-to-channel variations in the measurement. Therefore, any additional systematic can be considered as double-counting. However, a $\pm 13.7\%$ uncertainty on the scale factor is assigned.

- **Z+jets heavy-flavor scale factor correction**

  The heavy-flavor scale factor K'_{HF} for $Zb\bar{b}$ and $Zc\bar{c}$ is determined from NLO calculations, with an uncertainty of $\pm 13.7\%$ taken from the S_{HF} of W+jets events.

- **Sample statistics**

  This uncertainty is due to the finite size of the samples. Tables 7.7 and 7.8 show the number of events on each sample. All of the samples statistics are taken into account for each bin of the final discriminant distribution.

- **Jet energy scale**

  The JES uncertainty is evaluated by increasing/decreasing the JES correction by one standard deviation on each MC sample and then repeating the whole analysis with the shifted samples. The result is a shape-changing uncertainty, and an overall normalization uncertainty, see Appendix D. The normalization part ranges from 1.1% to 13.1% on the signal acceptance and from 0.1% to 2.1% on the combined background.

- **Taggability and tag-rate functions for MC events**

  The uncertainty associated with b-tagging in MC events is evaluated by adding the taggability and the tag rate components of the uncertainty in quadrature. The TRF values are raised and lowered by one standard deviation on each MC sample. The entire analysis is then repeated. This raising and lowering is done simultaneously for heavy flavor and light jets which causes the uncertainties for heavy flavor TRFs and light jets TRFs to be correlated. The result is an overestimation of the total TRF uncertainties. These uncertainties affect both shape and normalization of the MC samples. The normalization of the uncertainty is shown for each analysis channel in Appendix C and the shape changing systematics part is shown in Appendix D. The values range from 2.3%

to 11.4%.

- ALPGEN **reweighting** Some W+jets background distributions are reweighted based on several pretagged data distributions (see Section 7.2.1). The uncertainty from these reweightings affects the shapes of the W+jets background components but not its normalization (more detail can be found in Appendix D).

Relative Systematic Uncertainties

Components for Normalization and Shape	
Jet energy scale for signal	(1.1–13.1)%
Jet energy scale for total background	(0.1–2.1)%
(not shape for Z+jets or dibosons)	
b tagging, single-tagged	(2.1–7.0)%
b tagging, double-tagged	(9.0–11.4)%
Component for Shape Only	
ALPGEN reweighting	—

Table 9.1: A summary of the relative systematic uncertainties for each of the correction factors or normalizations. The uncertainty shown is the error on the correction or the efficiency, before it has been applied to the MC or data samples.

Relative Systematic Uncertainties	
Components for Normalization	
Integrated luminosity	6.1%
$t\bar{t}$ cross section	12.7%
Z+jets cross section	5.8%
Diboson cross sections	5.8%
Branching fractions	1.5%
Parton distribution functions	3.0%
(signal acceptances only)	
Triggers	5.0%
Instantaneous luminosity reweighting	1.0%
Primary vertex selection	1.4%
Lepton identification	2.5%
Jet fragmentation	(0.7-4.0)%
Initial-and final-state radiation	(0.6-12.6)%
b-jet fragmentation	2.0%
Jet reconstruction and identification	1.0%
Jet energy resolution	4.0%
W+jets heavy-flavor correction	13.7%
Z+jets heavy-flavor correction	13.7%
W+jets normalization to data	(1.8-5.0)%
Multijets normalization to data	(30-54)%
MC and multijets statistics	(0.5-16)%

Table 9.2: A summary of the relative systematic uncertainties for each of the correction factors or normalizations. The uncertainty shown is the error on the correction or the efficiency, before it has been applied to the MC or data samples (Part II).

9.2 Sample Preparation

The signal and background model samples are split into three independent and non-overlaping subsets. The first subset is used for the training of the BDTs; the second subset is used for the combination of the BDTs with other multivariate analyses [132, 133]; and the third subset is used to perform all the final measurements. It is important to note that only the Monte Carlo samples are split and that the data remains unaltered. The data is only used at the point where the final cross section measurement is performed.

The procedure to split the samples is based on the EventNumber, where the EventNumber is a unique identifier for each MC event. The motivation for its usage is to have all of the b-tagged permuted events in the same subset, which avoids possible correlations among the sets. The splitting criteria are outlined in Table 9.3. All the subsets are normalized such that each subset has the same sum-of-weights as the original sample.

Sample Subset Splitting Procedure

Subset	Splitting Criterion
Training subset, "first third"	EventNumber `mod 3 = 0`
Testing subset, "second third"	EventNumber `mod 3 = 1`
Yield subset, "third third"	EventNumber `mod 3 = 2`

Table 9.3: Splitting procedure of the samples. The event number is given to a MC event during generation and is the same for all permutations of an event.

9.3 Measuring a Cross Section

The Single Top cross section is determined by using signal and background binned distributions (BDT discriminant outputs). The cross section calculations are performed

employing Bayesian statistics with the `top_statistics` [135, 136] package.

9.3.1 Bayesian Approach

For a given histogram bin, the number of expected events d, is determined by:

$$d = \alpha\ L\ \sigma + \sum_{k=1}^{N} b_i = a\sigma + \sum_{k=1}^{N} b_i \tag{9.1}$$

where α is the signal acceptance, $L = \int \mathcal{L} dt$ is the integrated luminosity, σ is the signal cross section, b_i is the yield for the background i, and $a \equiv \alpha\mathcal{L}$ is the effective luminosity for the signal. In that bin, the likelihood to observe a data count D, given the number of expected events d, is determined by the Poisson distribution:

$$p(D|d) = \frac{e^{-d} d^D}{\Gamma(D+1)}. \tag{9.2}$$

Furthermore, since the probability to observe a count is independent on the counts in other bins, the combined likelihood for M bins corresponds to the product of all of bins' likelihoods:

$$\mathrm{L}(\boldsymbol{D}|\boldsymbol{d}) \equiv \mathrm{L}(\boldsymbol{D}|\sigma, \boldsymbol{a}, \boldsymbol{b}) = \prod_{j=1}^{M} \mathrm{L}(D_j|d_j) \tag{9.3}$$

where $\boldsymbol{D}$ and $\boldsymbol{d}$ represent vectors of the observed and expected counts, and $\boldsymbol{a}$ and $\boldsymbol{b}$ are the corresponding vectors of effective luminosity and background yields.

From Bayes' theorem, the posterior probability $p(\sigma, \boldsymbol{a}, \boldsymbol{b}|\boldsymbol{D})$ [137] can be written as:

$$p(\sigma|\boldsymbol{D}) = \frac{1}{\mathcal{N}} \int\int \mathrm{L}(\boldsymbol{D}|\sigma, \boldsymbol{a}, \boldsymbol{b}) \pi(\sigma, \boldsymbol{a}, \boldsymbol{b})\ d\boldsymbol{a} d\boldsymbol{b} \tag{9.4}$$

where $\pi(\sigma, \boldsymbol{a}, \boldsymbol{b})$ is the prior probability density, $\mathcal{N}$ the overall normalization, and the the posterior density integration over $\boldsymbol{a}$ and $\boldsymbol{b}$ is to remove the dependence on the

nuisance parameters. The prior density contains the knowledge of all parameters, including all systematic uncertainties and their correlations. In addition, the prior can be factorized as [135]:

$$\pi(\sigma, \boldsymbol{a}, \boldsymbol{b}) = \pi(\boldsymbol{a}, \boldsymbol{b})\pi(\sigma), \tag{9.5}$$

where the cross section prior can be assumed to be flat in σ:

$$\pi(\sigma) = 1/\sigma_{max}, \qquad 0 < \sigma < \sigma_{max} \tag{9.6}$$

$$= 0, \qquad \text{otherwise.} \tag{9.7}$$

Hence, the posterior probability for the signal cross section is:

$$p(\sigma|\boldsymbol{D}) = \frac{1}{\mathcal{N}\sigma_{max}} \int\int \mathrm{L}(\boldsymbol{D}|\sigma, \boldsymbol{a}, \boldsymbol{b})\pi(\boldsymbol{a}, \boldsymbol{b})\ d\boldsymbol{a}d\boldsymbol{b} \tag{9.8}$$

where the integral can be estimated numerically by sampling the prior density $\pi(\boldsymbol{a}, \boldsymbol{b})$ by a large number K of points $(\boldsymbol{a}_k, \boldsymbol{b}_k)$

$$\int\int \mathrm{L}(\boldsymbol{D}|\sigma, \boldsymbol{a}, \boldsymbol{b})\pi(\boldsymbol{a}, \boldsymbol{b})\ d\boldsymbol{a}d\boldsymbol{b} \sim \frac{1}{K}\sum_{k=1}^{K} \mathrm{L}(\boldsymbol{D}|\sigma, \boldsymbol{a}_k, \boldsymbol{b}_k). \tag{9.9}$$

The cross section central value is determined by the peak of the posterior density distribution and its uncertainty is established by the 68% interval around the peak. Figure 9.1 illustrates the peak of the posterior density distribution and its peak.

9.3.2 Systematic Uncertainties

To determine the effect of the shape-changing systematics, three separate distributions are required namely, the nominal distribution, and the up and down one standard

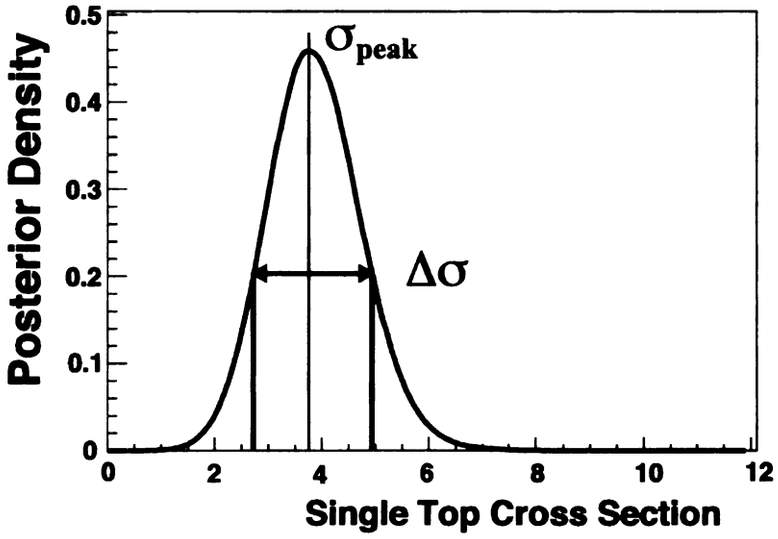

Figure 9.1: Example of a 1D posterior density distribution for the Single Top cross section.

deviation systematic shift distributions (See Figure 9.2). The uncertainty of a given bin is modeled by sampling a Gaussian distribution with mean 0 and width 1, which results a shift for y_{ibin}:

$$\Delta y_{ibin} = s^{\pm}_{tot} \times g(0,1) \times \delta^{\pm}_{ibin} \tag{9.10}$$

where $s^{\pm}_{tot} = \frac{\sum y}{\sum y^{\pm}_{ibin}}$ for shape-only shifts, and 1 otherwise.

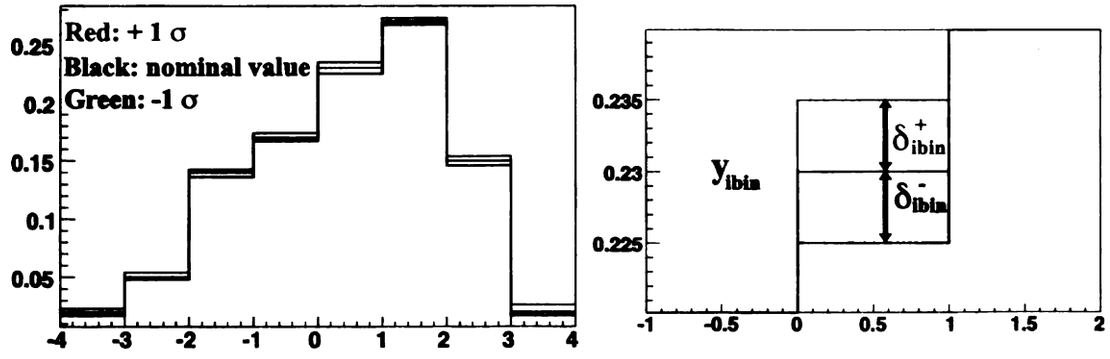

Figure 9.2: Example of a kinematic variable showing the nominal distribution and the up-shifted and down-shifted histograms of the shape-changing systematics. The plot on the right corresponds the the same distribution for only bin only.

The uncertainties that affect only the normalization are computed using a multivariate Gaussian approach in which a correlation matrix encodes all the correlations. Details of this procedure can be found in Reference [135].

9.4 Results

9.4.1 Expected Results

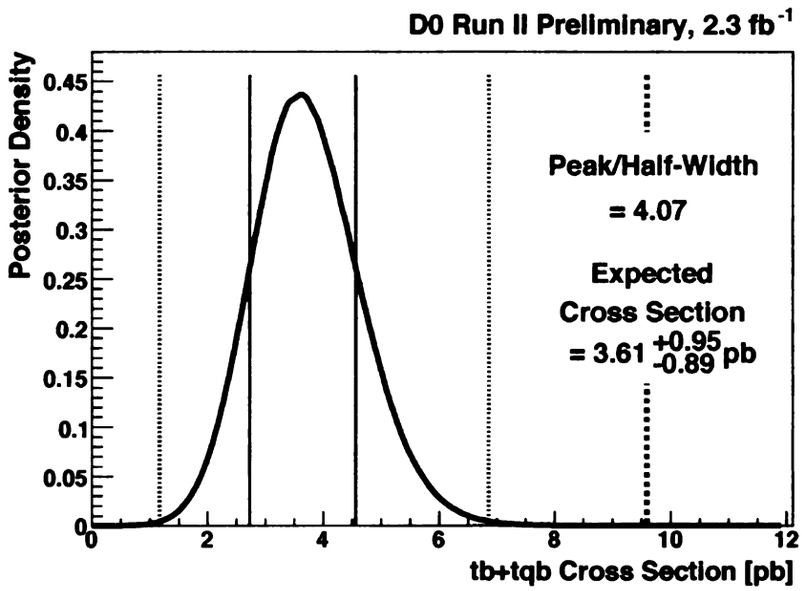

Figure 9.3: Expected posterior density distributions from Decision Tree outputs trained with $s+t$-channel tb+tqb as signal for all 24 channels combined—i.e., Run IIa and Run IIb, e and μ, 2-4 jets and 1 or 2 are b-tagged. All systematic uncertainties are taken into account in this measurement. The theoretical cross section is 3.46 pb.

The Decision Tree discriminants histograms shown in Appendix A were used as input to measured the Single Top cross section. This result is called "expected" because instead of using the data for the measurement, the sum of all backgrounds plus the Standard Model amount of Single Top is used. All of the 24-channels are combined by multiplying the likelihoods. More details of this procedure are given in [135].

The cross section measurements are presented in Table 9.4. The measurements are all consistent with the Standard Model cross section of 3.46 pb which was used during the calculation. As expected, the more channels that are combined, the smaller the uncertainty on the measurement. The Bayesian Posterior for the all-channels-combined cross section is shown in Figure 9.3. The ratio of posterior peak position over the lower 68.3% confidence bound ("peak over half-width") is given in Table 9.5. The purpose of this quantity is to provide a rough estimate of the measurement sensitivity.

Expected Cross Section Measurements

	1,2tags + 2,3,4jets		e,μ + 2,3,4jets	
	e-chan	μ-chan	1 tag	2 tags
Run IIa	$3.60^{+1.90}_{-1.68}$ pb	$3.63^{+1.72}_{-1.53}$ pb	$3.61^{+1.48}_{-1.33}$ pb	$3.53^{+2.59}_{-2.20}$ pb
Run IIb	$3.68^{+1.95}_{-1.71}$ pb	$3.71^{+1.85}_{-1.63}$ pb	$3.74^{+1.58}_{-1.40}$ pb	$3.62^{+2.59}_{-2.30}$ pb
Run IIa+b	$3.64^{+1.41}_{-1.22}$ pb	$3.61^{+1.30}_{-1.12}$ pb	$3.64^{+1.08}_{-0.98}$ pb	$3.61^{+1.94}_{-1.71}$ pb

	e,μ + 1,2tags			All
	2 jets	3 jets	4 jets	channels
Run IIa	$3.69^{+1.55}_{-1.38}$ pb	$3.69^{+2.81}_{-2.45}$ pb	$3.76^{+5.76}_{-3.76}$ pb	$\mathbf{3.60^{+1.32}_{-1.18}}$ **pb**
Run IIb	$3.86^{+1.75}_{-1.54}$ pb	$3.79^{+2.73}_{-2.34}$ pb	$3.73^{+5.28}_{-3.73}$ pb	$\mathbf{3.70^{+1.38}_{-1.23}}$ **pb**
Run IIa+b	$3.78^{+1.19}_{-1.08}$ pb	$3.74^{+2.05}_{-1.84}$ pb	$3.82^{+4.12}_{-3.32}$ pb	$\mathbf{3.61^{+0.95}_{-0.89}}$ **pb**

Table 9.4: Expected cross section measurements for many combinations of analysis channels with all systematic uncertainties taken into account.

In Table 9.5, the Bayes Ratio Significance (BRS) and Bayes Factor Significances (BFS) for the measurements are presented. These quantities are Bayesian measures of the sensitivity. The BFS is calculated according to the procedure described in [138] integrating over the full posterior. And the BRS is an estimate of the same value

calculated using the posterior density at only two points (zero and the peak). For all the channels, BFS and BRS are consistent with each other within 0.5%.

The measurements for all individual channels are presented in Table 9.6.

Expected Posterior Peak Over Half-Width

	1,2tags + 2,3,4jets		e,μ + 2,3,4jets		e,μ + 1,2tags			All
	e-chan	μ-chan	1 tag	2 tags	2 jets	3 jets	4 jets	channels
Run IIa	2.1	2.4	2.7	1.6	2.7	1.5	1.0	**3.1**
Run IIb	2.2	2.3	2.7	1.6	2.5	1.6	1.0	**3.0**
Run IIa+b	3.0	3.2	3.7	2.1	3.5	2.0	1.2	**4.1**

Expected Bayes Ratio Significance

	1,2tags + 2,3,4jets		e,μ + 2,3,4jets		e,μ + 1,2tags			All
	e-chan	μ-chan	1 tag	2 tags	2 jets	3 jets	4 jets	channels
Run IIa	2.3	2.6	3.0	1.6	3.0	1.5	0.7	**3.4**
Run IIb	2.3	2.5	2.9	1.6	2.8	1.7	0.8	**3.3**
Run IIa+b	3.2	3.5	4.2	2.3	4.1	2.2	1.0	**4.7**

Expected Bayes Factor Significance

	1,2tags + 2,3,4jets		e,μ + 2,3,4jets		e,μ + 1,2tags			All
	e-chan	μ-chan	1 tag	2 tags	2 jets	3 jets	4 jets	channels
Run IIa	2.3	2.6	3.0	1.6	3.0	1.5	0.7	**3.4**
Run IIb	2.3	2.5	2.9	1.6	2.8	1.7	0.8	**3.3**
Run IIa+b	3.2	3.5	4.2	2.3	4.1	2.2	1.0	**4.7**

Table 9.5: Expected significance estimators for many combinations of analysis channels: posterior peak over half-width (top Table), Bayes Ratio Significance (middle Table), and Bayes Factor Significance (bottom Table). All systematic uncertainties are taken into account in the calculations. The best values from all channels combined systematics are shown in bold type.

Expected Results in Individual Channels

Channel	$\sigma \pm \Delta\sigma$	P/HW	BFS	BRS
e / p17 / 1tag / 2jets	$3.57^{+2.34}_{-2.02}$ pb	1.8	1.9	1.9
e / p17 / 1tag / 3jets	$4.16^{+4.42}_{-3.87}$ pb	1.1	0.9	0.9
e / p17 / 1tag / 4jets	$3.80^{+11.74}_{-3.80}$ pb	1.0	0.4	0.4
e / p17 / 2tags / 2jets	$3.73^{+4.09}_{-3.38}$ pb	1.1	1.0	1.0
e / p17 / 2tags / 3jets	$3.74^{+6.69}_{-3.74}$ pb	1.0	0.6	0.6
e / p17 / 2tags / 4jets	$3.96^{+14.18}_{-3.96}$ pb	1.0	0.4	0.4
e / p20 / 1tag / 2jets	$3.81^{+2.58}_{-2.22}$ pb	1.7	1.8	1.8
e / p20 / 1tag / 3jets	$3.81^{+4.02}_{-3.36}$ pb	1.1	1.0	1.0
e / p20 / 1tag / 4jets	$4.28^{+10.50}_{-4.28}$ pb	1.0	0.6	0.6
e / p20 / 2tags / 2jets	$3.75^{+4.17}_{-3.43}$ pb	1.1	1.0	1.0
e / p20 / 2tags / 3jets	$3.65^{+6.41}_{-3.65}$ pb	1.0	0.7	0.7
e / p20 / 2tags / 4jets	$3.76^{+14.27}_{-3.76}$ pb	1.0	0.4	0.4
μ / p17 / 1tag / 2jets	$3.71^{+2.20}_{-1.89}$ pb	2.0	2.1	2.1
μ / p17 / 1tag / 3jets	$3.75^{+3.77}_{-3.18}$ pb	1.2	1.0	1.0
μ / p17 / 1tag / 4jets	$4.43^{+11.11}_{-4.43}$ pb	1.0	0.5	0.5
μ / p17 / 2tags / 2jets	$3.85^{+3.88}_{-3.21}$ pb	1.2	1.1	1.1
μ / p17 / 2tags / 3jets	$3.66^{+5.59}_{-3.66}$ pb	1.0	0.7	0.7
μ / p17 / 2tags / 4jets	$3.61^{+13.53}_{-3.61}$ pb	1.0	0.3	0.3
μ / p20 / 1tag / 2jets	$3.82^{+2.52}_{-2.12}$ pb	1.8	1.9	1.9
μ / p20 / 1tag / 3jets	$4.31^{+4.08}_{-3.41}$ pb	1.3	1.2	1.2
μ / p20 / 1tag / 4jets	$4.53^{+10.02}_{-4.53}$ pb	1.0	0.6	0.6
μ / p20 / 2tags / 2jets	$4.19^{+4.43}_{-3.63}$ pb	1.2	1.1	1.1
μ / p20 / 2tags / 3jets	$4.36^{+5.93}_{-4.36}$ pb	1.0	0.8	0.8
μ / p20 / 2tags / 4jets	$3.83^{+13.66}_{-3.83}$ pb	1.0	0.4	0.4

Table 9.6: Expected cross section, peak over half-width, Bayes factor significance and Bayes ratio significance, with all systematic uncertainties taken into account, for the 24 analysis channels.

9.4.2 Observed Results

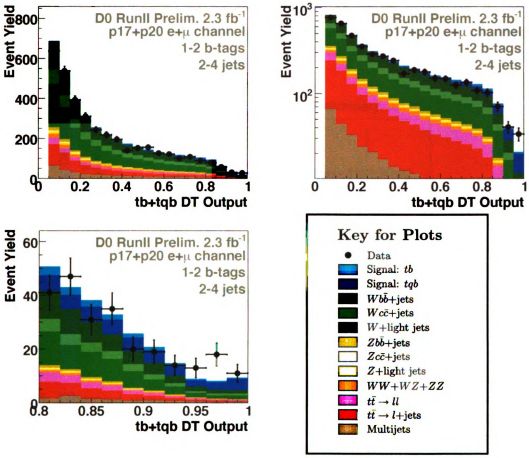

Figure 9.4: Decision tree discriminant outputs for all 24 channels combined. The histograms are obtained by stacking each one of the 24 DT outputs on top of each other. The Single Top contribution in this plot is normalized to the measured cross section. The three plots correspond to the same distribution: linear scale (top left), log scale (top right) and a zoom in the signal region (bottom). The color key is shown in the bottom right-hand corner.

This section contains the decision tree observed Single Top cross section results using the 2.3 fb^{-1} dataset. The decision tree discriminant distributions used for this measurement are shown in Appendix A. The decision tree output for all 24 channels combined [1] is shown in Figure 9.4.

The measured cross sections are presented in Tables 9.7 and 9.8, and the cor-

[1] The histograms are combined by stacking the individual decision tree individual outputs.

responding peak over half-width and BRS are found in Table 9.9. The BFS is not presented as it is not possible to be calculated in real data. Figure 9.5 shows the posterior density for the all combined measurement. The measurements for all of the 24 individual channels are given in Table 9.10.

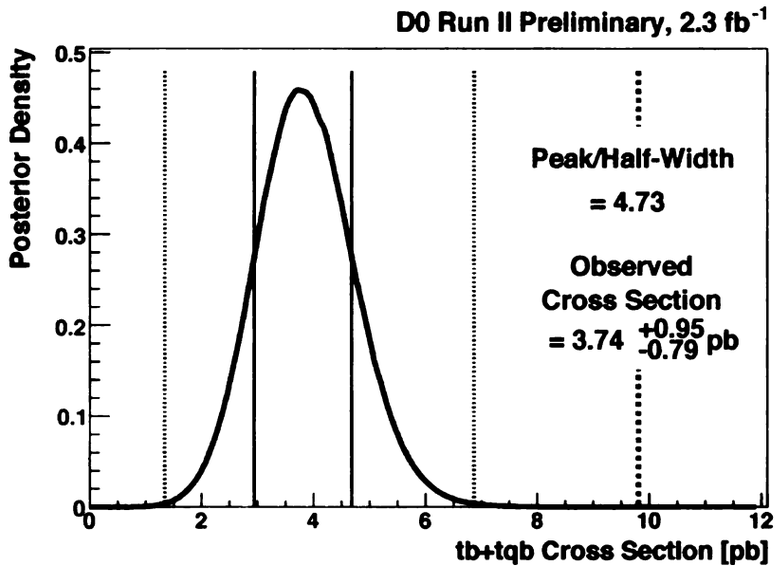

Figure 9.5: Observed posterior density from $s+t$-channel Single Top cross section measurement using boosted Decision Trees. This is for 24 channels combined—*i.e.* Run IIa and Run IIb, e+jets and μ+jets, 2-4 jets and 1 or 2 are b-tagged. All systematic uncertainties are taken into account in this measurement.

Observed Cross Section Measurements

	1,2tags + 2,3,4jets		e,μ + 2,3,4jets	
	e-chan	μ-chan	1 tag	2 tags
Run IIa	$2.32^{+1.70}_{-1.61}$ pb	$2.73^{+1.63}_{-1.45}$ pb	$1.86^{+1.25}_{-1.16}$ pb	$3.65^{+2.60}_{-2.31}$ pb
Run IIb	$6.20^{+2.23}_{-1.94}$ pb	$3.93^{+1.73}_{-1.52}$ pb	$5.80^{+1.63}_{-1.57}$ pb	$3.79^{+2.48}_{-2.22}$ pb
Run IIa+b	$4.40^{+1.47}_{-1.24}$ pb	$3.32^{+1.19}_{-1.02}$ pb	$3.84^{+1.12}_{-0.94}$ pb	$3.72^{+1.90}_{-1.70}$ pb

Table 9.7: Observed cross section measurements for many combinations of analysis channels with all systematic uncertainties taken into account.

Observed Cross Section Measurements

	e,μ + 1,2tags			All
	2 jets	3 jets	4 jets	channels
Run IIa	$1.23^{+1.12}_{-1.03}$ pb	$4.71^{+3.05}_{-2.67}$ pb	$5.82^{+6.66}_{-4.59}$ pb	$\mathbf{2.50^{+1.29}_{-1.16}}$ **pb**
Run IIb	$4.25^{+1.79}_{-1.52}$ pb	$5.57^{+2.90}_{-2.45}$ pb	$9.25^{+6.80}_{-5.19}$ pb	$\mathbf{4.92^{+1.35}_{-1.21}}$ **pb**
Run IIa+b	$2.62^{+1.12}_{-1.00}$ pb	$5.24^{+2.13}_{-1.84}$ pb	$7.00^{+5.26}_{-3.89}$ pb	$\mathbf{3.74^{+0.95}_{-0.79}}$ **pb**

Table 9.8: Observed cross section measurements for many combinations of analysis channels with all systematic uncertainties taken into account.

Observed Posterior Peak Over Half-Width

	1,2tags + 2,3,4jets		e,μ + 2,3,4jets		e,μ + 1,2tags			All
	e-chan	μ-chan	1 tag	2 tags	2 jets	3 jets	4 jets	channels
Run IIa	1.4	1.9	1.6	1.6	1.2	1.8	1.3	**2.2**
Run IIb	3.2	2.6	3.7	1.7	2.8	2.3	1.8	**4.1**
Run IIa+b	3.6	3.2	4.1	2.2	2.6	2.9	1.8	**4.7**

Observed Bayes Ratio Significance

	1,2tags + 2,3,4jets		e,μ + 2,3,4jets		e,μ + 1,2tags			All
	e-chan	μ-chan	1 tag	2 tags	2 jets	3 jets	4 jets	channels
Run IIa	1.3	1.9	1.5	1.6	1.0	1.8	1.3	**2.2**
Run IIb	3.6	2.9	4.4	1.8	3.2	2.6	2.0	**4.6**
Run IIa+b	3.7	3.5	4.4	2.4	2.9	3.2	2.1	**5.0**

Table 9.9: Observed posterior peak over half-width and Bayes ratio significance for many combinations of analysis channels. All systematic uncertainties are taken into account in the calculation. The best values from all channels combined with systematics are shown in bold type.

Observed Results in Individual Channels

Channel	$\sigma \pm \Delta\sigma$	P/HW	BRS
e / p17 / 1tag / 2jets	$0.91^{+1.80}_{-0.91}$ pb	1.0	0.5
e / p17 / 1tag / 3jets	$9.03^{+6.89}_{-5.41}$ pb	1.7	1.8
e / p17 / 1tag / 4jets	$8.15^{+11.22}_{-8.15}$ pb	1.0	0.9
e / p17 / 2tags / 2jets	$0.00^{+3.16}_{-0.00}$ pb	0.0	0.0
e / p17 / 2tags / 3jets	$9.27^{+7.94}_{-6.31}$ pb	1.5	1.5
e / p17 / 2tags / 4jets	$0.00^{+15.51}_{-0.00}$ pb	0.0	0.0
e / p20 / 1tag / 2jets	$0.00^{+0.00}_{-0.00}$ pb	0.0	0.0
e / p20 / 1tag / 3jets	$5.65^{+4.33}_{-3.57}$ pb	1.6	1.7
e / p20 / 1tag / 4jets	$14.15^{+12.53}_{-9.67}$ pb	1.5	1.6
e / p20 / 2tags / 2jets	$4.24^{+4.37}_{-3.62}$ pb	1.2	1.1
e / p20 / 2tags / 3jets	$5.04^{+6.37}_{-4.87}$ pb	1.0	0.9
e / p20 / 2tags / 4jets	$21.37^{+19.44}_{-13.66}$ pb	1.6	1.9
μ / p17 / 1tag / 2jets	$2.53^{+1.96}_{-1.73}$ pb	1.5	1.4
μ / p17 / 1tag / 3jets	$0.81^{+3.42}_{-0.81}$ pb	1.0	0.2
μ / p17 / 1tag / 4jets	$0.00^{+7.05}_{-0.00}$ pb	0.0	0.0
μ / p17 / 2tags / 2jets	$1.56^{+3.99}_{-1.56}$ pb	1.0	0.5
μ / p17 / 2tags / 3jets	$1.00^{+6.35}_{-1.00}$ pb	1.0	0.2
μ / p17 / 2tags / 4jets	$12.65^{+13.95}_{-9.16}$ pb	1.4	1.7
μ / p20 / 1tag / 2jets	$5.05^{+2.58}_{-2.19}$ pb	2.3	2.6
μ / p20 / 1tag / 3jets	$5.19^{+4.50}_{-3.69}$ pb	1.4	1.4
μ / p20 / 1tag / 4jets	$3.62^{+10.38}_{-3.62}$ pb	1.0	0.4
μ / p20 / 2tags / 2jets	$2.02^{+4.19}_{-2.02}$ pb	1.0	0.6
μ / p20 / 2tags / 3jets	$4.38^{+5.17}_{-4.02}$ pb	1.1	1.0
μ / p20 / 2tags / 4jets	$8.68^{+11.18}_{-8.05}$ pb	1.1	1.1

Table 9.10: Observed cross section, peak over half-width and Bayes ratio significance, with all systematic uncertainties taken into account, for the 24 analysis channels.

9.5 Significance

9.5.1 Ensemble Tests

To verify the cross section measurement procedure, several ensembles of pseudo-datasets were generated by using the final discriminant output distributions, The generation is done by randomly drawing a Poissondistributed number in each bin, taking into account all systematic uncertainties. First one set of random systematic shifts is generated for each systematic uncertainty, then the bin contents for all sources in all channels are adjusted accordingly, and finally a Poisson random number is drawn in each bin. The ensemble generation was done using the package `top_statistics` and is described in detail in Reference [134, 135].

There were several ensembles generated, each one with different amounts of Single Top: 2, 3, 3.46 , 4.2, 5, 7, 8 and 10 pb. In each case, the cross section was measured using the same method as with the real data. Figure 9.6 shows the results, where each ensemble has its corresponding cross section measurement as well as a fitted Gaussian around the peak of the distribution.

In addition, a linear fit from the means and their errors can be seen in Figure 9.7. The measured cross sections are consistent with the Single Top cross sections used in the ensemble generation. Furthermore, there was one more ensemble generated which had no Single Top. This ensemble was used to measure the final sensitivity of the analysis, see Section 9.5.2 below.

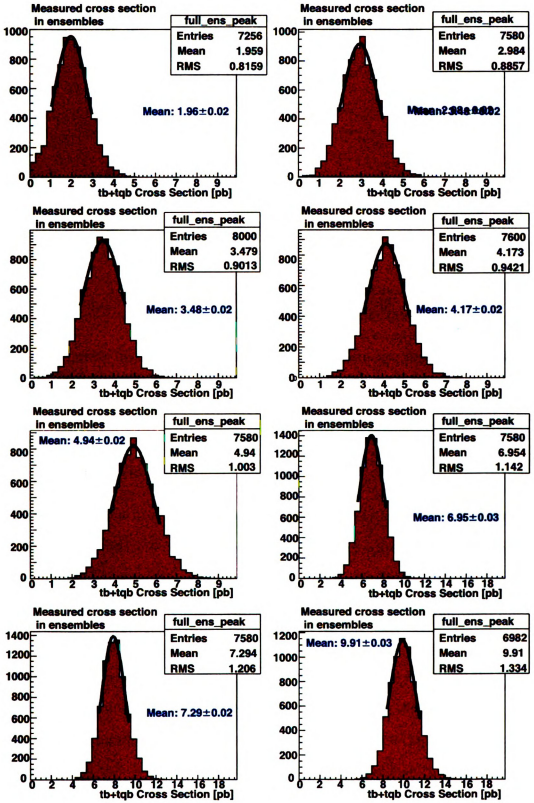

Figure 9.6: Measured Single Top cross sections in ensembles with various amounts of Single Top.

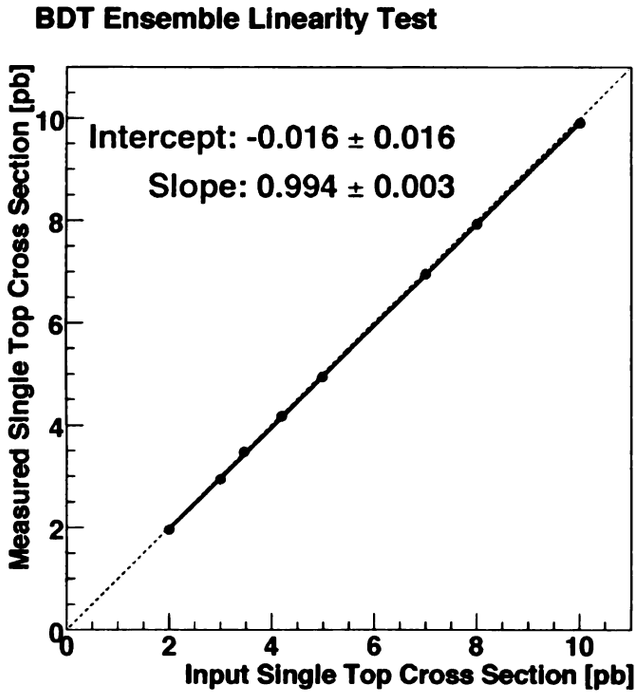

Figure 9.7: Linear fit through the means from the Gaussian fits (Figure 9.6) of the measured cross sections in ensembles

9.5.2 Significance

To measure the Single Top cross section significance, a very large number of zero-signal ensemble pseudo-datasets was used, where each dataset corresponds to 2.3 fb^{-1} data without any Single Top. The measured cross section distribution for the zero-signal ensemble can be seen in Figure 9.8, together with the expected and observed cross sections.

From the measured cross sections in the ensemble, one can calculate the probability that data containing no Single Top quark events could fluctuate enough to produce a cross section measurement of at least the observed cross section. This probability is referred to as the "p-value", and is widely used to estimate the significance of a measurement.

The number of standard deviations equivalence N_σ can be calculated in terms of

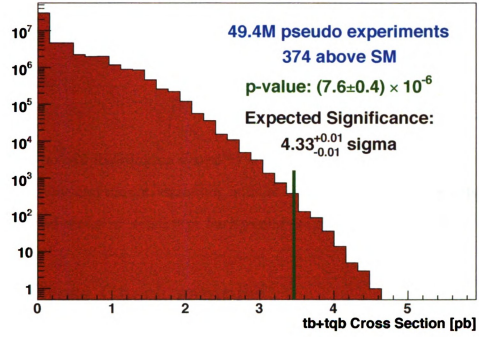

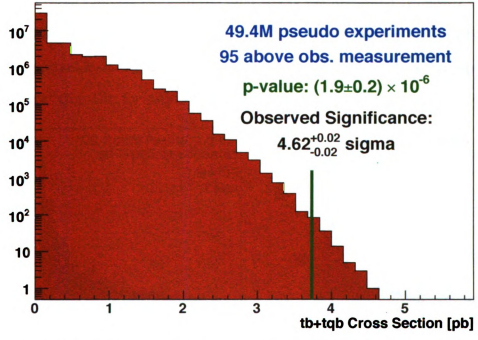

Figure 9.8: Measured cross section from a large ensemble of pseudo-datasets containing no Single Top. The significance of a particular cross section is calculated from the number of pseudo-datasets measuring a cross section higher than the given cross section (green line). The plot above uses the Single Top Standard Model cross section and corresponds to the expected significance. The plot below the bottom uses the measured cross section and therefore corresponds to the observed cross section.

a p-value α as:

$$N_\sigma = \sqrt{2} \cdot \mathrm{erf}^{-1}(1 - 2\alpha) \tag{9.11}$$

which fulfills

$$\int_{-\infty}^{N_\sigma} \mathrm{Gauss}(x)\, dx = 1 - \alpha. \tag{9.12}$$

where the normal distribution Gauss(x) is normalized to unity.

The p-value and the corresponding number of standard deviations for the expected and observed excess of signal over background are shown in Figure 9.8.

9.6 Cross Check samples

The cross check samples are defined in Section 7.5. In this Section, the results from evaluating these samples through the final BDTs are presented. Figure 9.9 shows the Decision Tree output distributions in these cross-check samples for Run IIa-b, e and μ, 1-2 tags combined. In Appendix E all the distributions are shown separately for Run IIa and Run IIb, for e+jets and μ+jets, and for 1 and 2 tags.

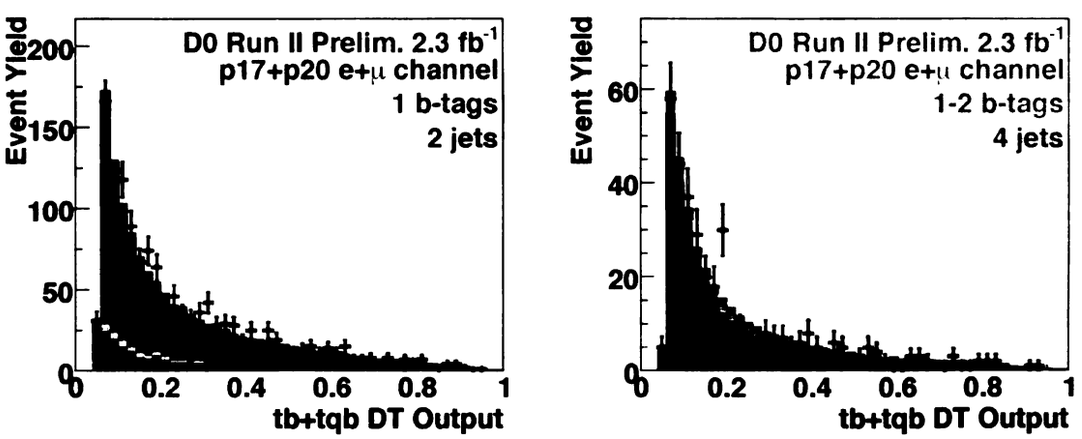

Figure 9.9: Combined Decision Tree outputs for the "W+jets" sample (left) and the "$t\bar{t}$" sample (right) cross-check samples.

From the information in these histograms, one can conclude that there is no

obvious bias in the decision tree measurement from the composition of the different backgrounds components. For these subsamples dominated by W+jets and $t\bar{t}$, the background model describes the data within uncertainties.

9.7 V_{tb} measurement

As outlined in Section 2.3.2.1, the magnitude of the CKM matrix element V_{tb} can be inferred from the Single Top cross section measurement [57]. This is direct measurement that does not assume the unitarity of the CKM matrix nor the existence of three quark families. In addition to the systematics included in the Single Top cross section, there are theoretical uncertainties that must be considered in the V_{tb} measurement. These uncertainties are applied to the s- and t-channels separately, and are summarized in Table 9.11.

	s-channel	t-channel
Top quark mass [%]	5.56	3.48
Factorizatioin scale [%]	3.7	1.74
PDF [%]	3.0	3.0
α_S [%]	1.4	0.01

Table 9.11: Systematic uncertainties in percentage on the cross section factor required in the measurement of V_{tb}.

A Bayesian posterior for $|V_{tb}|^2$ is obtained in the closed interval [0,1]. The resulting limit for the CKM matrix element V_{tb} is:

$$|V_{tb}| > 0.78 \tag{9.13}$$

at 95% C.L. within the Standard Model, ($f_1^L = 1$). When the upper limit constraint on the $|V_{tb}|^2$ posterior is removed, the $V-A$ coupling strength is meassured to be:

$$|V_{tb}\, f_1^L| = 1.05\, {}^{0.13}_{0.12}, \tag{9.14}$$

where f_1^L is the left-handed Wtb coupling. Figure 9.10 shows the posterior probability densities for $|V_{tb}|^2$ and $|V_{tb} f_1^L|^2$.

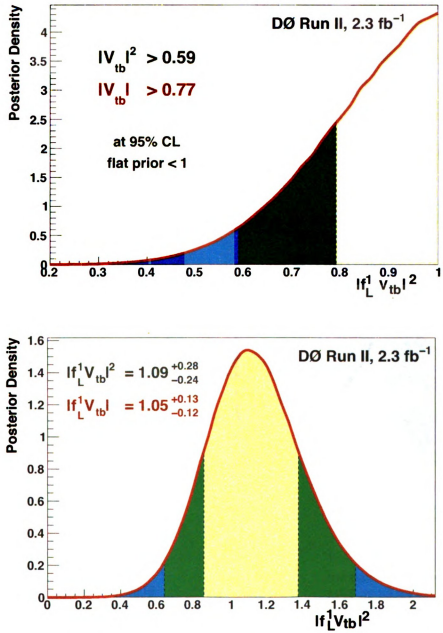

Figure 9.10: Posterior probability densities for $|V_{tb}|^2$ (left) and $|V_{tb} f_1^L|^2$ (right). The color bands represent different confidence bounds: 68.3 %, 95.4 % and 99.7 %.

9.8 Event Display

Figures 9.11 and 9.12 presents a possible Single Top event candidate. This event is identified as having three jets, of which two are considered b-tagged, a muon, and a neutrino in the form of MET.

In XY view, the SMT barrel hits are represented by red dots and the CFT axial fiber hits by blue dots. The outer part represents the calorimeter energy deposits, where the red portion corresponds to EM deposits and the blue to Hadronic.

The lego view, represents the calorimeter (η, ϕ) space. The circles correspond to the cone radius and the jet widths. Muons are represented in green, the corrected MET is represented in yellow, and the calorimeter deposits follow the same convention as in the XY view.

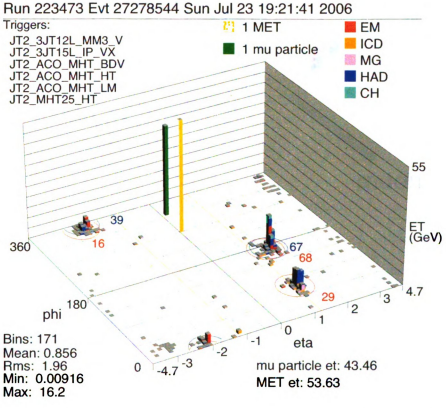

Figure 9.11: Possible candidate event display. The event contains three jets out of wich two are b-tagged, a muon, and a neutrino. Lego view of the DØ detector.

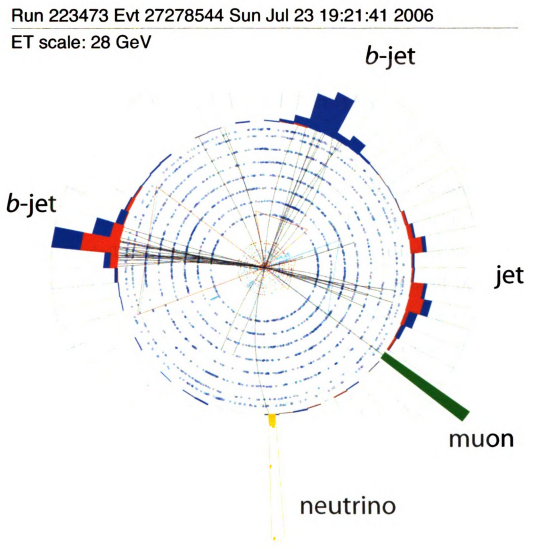

Figure 9.12: Possible candidate event display. The event contains three jets out of wich two are b-tagged, a muon, and a neutrino. XY view of the DØ detector.

Chapter 10

Results and Conclusions

This dissertation presents the results of the observation of Single Top using 2.3 fb^{-1} of Data collected with the DØ detector at the Fermilab Tevatron collider. The analysis includes the Single Top muon+jets and electron+jets final states for events with two to four jets with at least one jet b-tagged. Furthermore, Boosted Decision Trees are employed as a method to separate the Single Top signal from the overwhelming background. The resulting Single Top cross section measurement is:

$$\sigma(p\bar{p} \rightarrow tb + X, tqb + X) = 3.74\ ^{+0.95}_{-0.74}\ \text{pb}, \tag{10.1}$$

where the errors include both statistical and systematic uncertainties. The probability to measure a cross section at this value or higher in the absence of signal is $p = 1.9 \times 10^{-6}$. This corresponds to a standard deviation Gaussian equivalence of 4.6. When combining this result with two other analysis methods, the resulting cross section measurement is:

$$\sigma(p\bar{p} \rightarrow tb + X, tqb + X) = 3.94 \pm 0.88\ \text{pb}, \tag{10.2}$$

and the corresponding measurement significance is 5.0 standard deviations.

In addition, using the cross section measurement, a Bayesian posterior for $|V_{tb}|^2$

is obtained in the closed interval [0,1]. The measurement does not assume unitarity of the CKM matrix or the existence of three quark generations. The resulting limit for the CKM matrix element V_{tb} is:

$$|V_{tb}| > 0.78 \tag{10.3}$$

at 95% C.L. within the Standard Model. When the upper limit constraint on the $|V_{tb}|^2$ posterior is removed, the $V-A$ coupling strength is meassured to be:

$$|V_{tb}\, f_1^L| = 1.05\ ^{+0.13}_{-0.12} \tag{10.4}$$

where f_1^L is the left-handed Wtb coupling.

Appendix A

Decision Tree Outputs

In this Appendix, the boosted decision tree discriminant outputs are shown. First for all the 24 channels combined (Figure A.1); second, combining reconstruction versions and leptons but separated by number of jets and number of b-tagged jets (Figure A.2); third, separately for each of the 24 channels (separated by jet multiplicity Figures A.3, A.4, and A.5; and finally considering only the high discriminant region, $DToutput > 0.8$ where mostly signal is expected to be found (Figures A.6 to A.8).

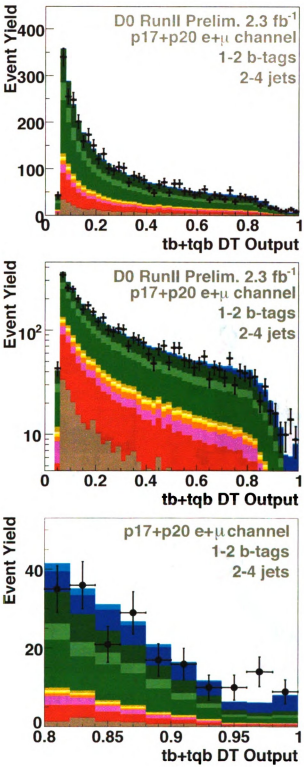

Figure A.1: Decision trees discriminant output for all 24 channels combined. The Single Top contribution in this plot is normalized to the measured cross section. Same distribution on linear scale (above), log scale (middle) and a zoom in to the signal region (below).

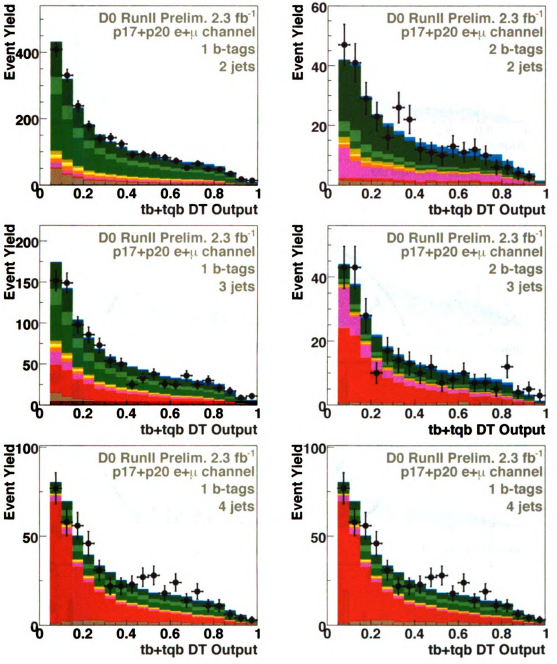

Figure A.2: Decision trees discriminant output for the e,μ+jets combination in RunIIa+b data. The total Single Top contribution in this plots is normalized to the measured cross section. [Rows: top =2 jets, center =3 jets, bottom =4 jets, columns: left =1 b-tag, right =2 b-tags.]

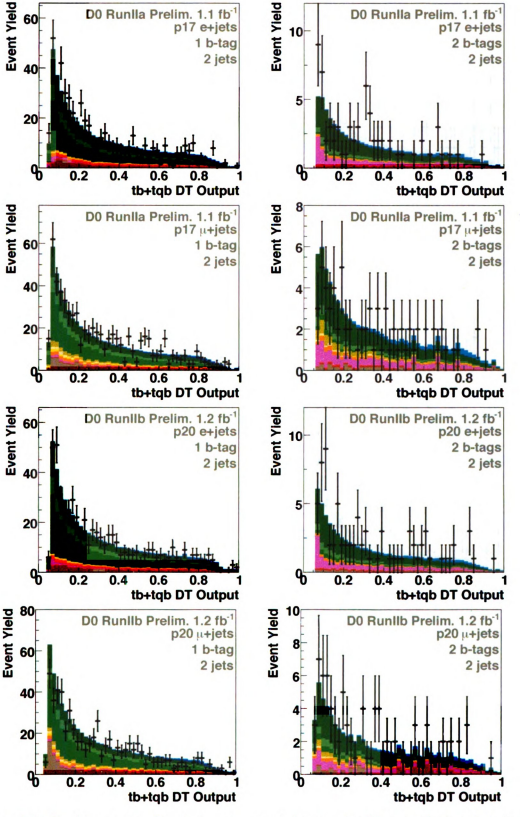

Figure A.3: Decision trees discriminant output for event with exactly two jets in the final state. One b-jet (left) two b-jet (right).

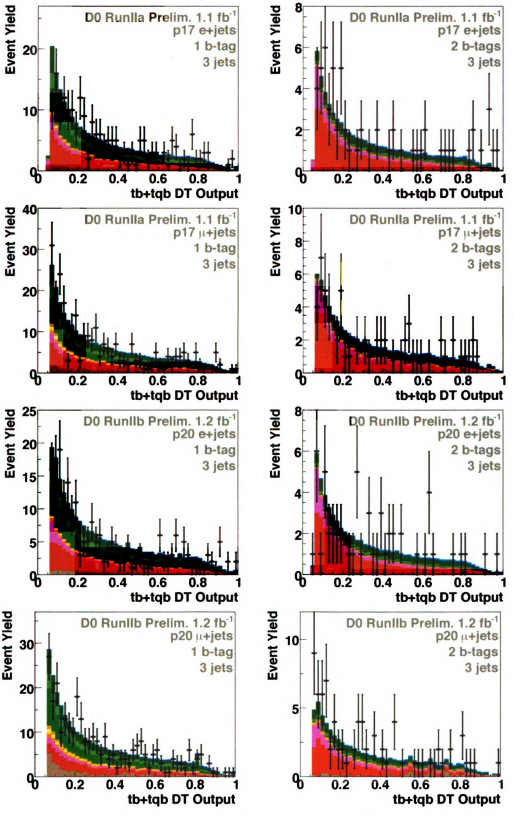

Figure A.4: Decision trees discriminant output for event with exactly two jets in the final state. One b-jet (left) two b-jet (right).

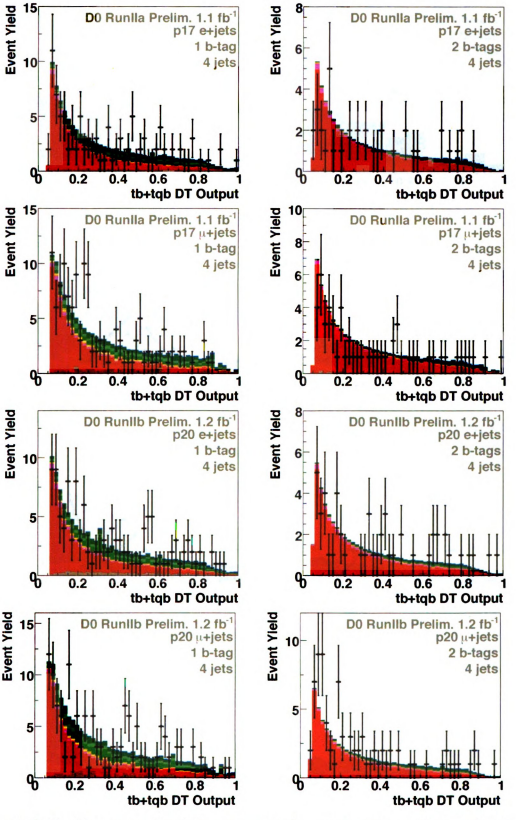

Figure A.5: Decision trees discriminant output for event with exactly two jets in the final state. One b-jet (left) two b-jet (right).

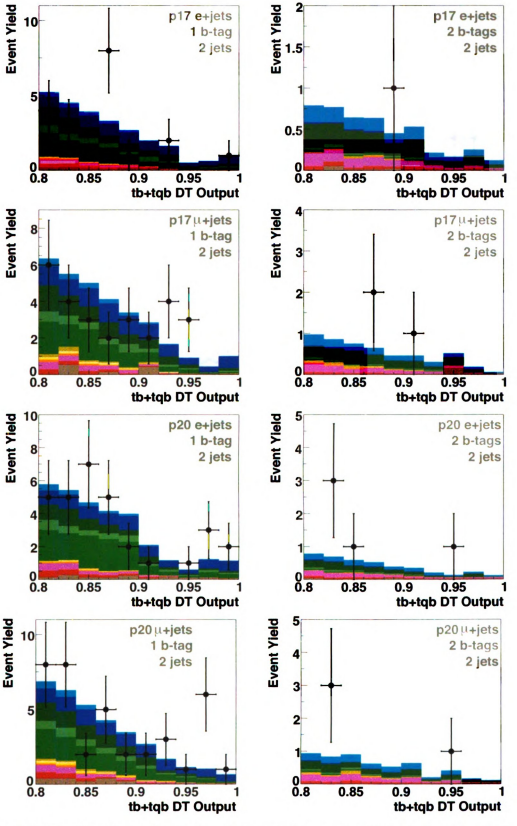

Figure A.6: Decision trees discriminant output for event with exactly two jets in the final state. One b-jet (left) two b-jet (right). Signal region only, $O_{DT} > 0.8$.

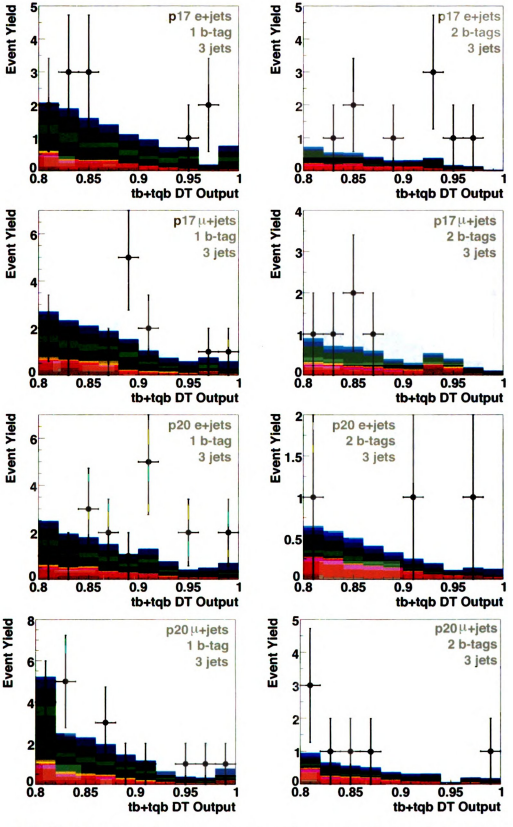

Figure A.7: Decision trees discriminant output for event with exactly two jets in the final state. One b-jet (left) two b-jet (right). Signal region only, $O_{DT} > 0.8$.

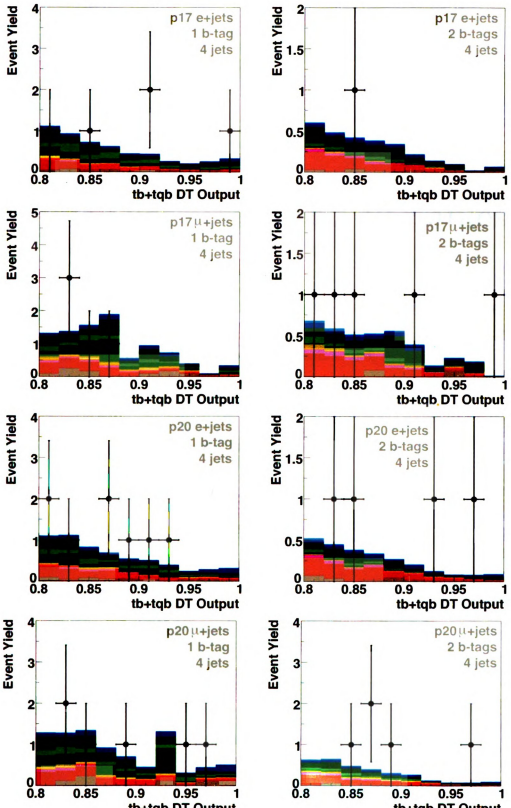

Figure A.8: Decision trees discriminant output for event with exactly two jets in the final state. One b-jet (left) two b-jet (right). Signal region only, $O_{DT} > 0.8$.

Appendix B

Plots of Discriminating Variables

Figures B.1 to B.21 show various kinematic distributions in the final samples:

- transverse momentum of the lepton (Figures B.1, B.2, and B.3)
- missing transverse energy (Figures B.4, B.5, and B.6),
- transverse energy of the leading jet (Figures B.7, B.8, and B.9),
- transverse energy of the second leading jet (Figures B.10, B.11, and B.12),
- scalar transverse energy sum (Figures B.13, B.14, and B.15),
- reconstructed top quark mass (Figures B.16, B.17, and B.18); and
- pseudorapidity of the light quark jet times lepton charge (Figures B.19, B.20, and B.21).

Each figure corresponds to a given jet multiplicity, the left column correspond the the Runn IIa period and the right column to the Run IIb period.

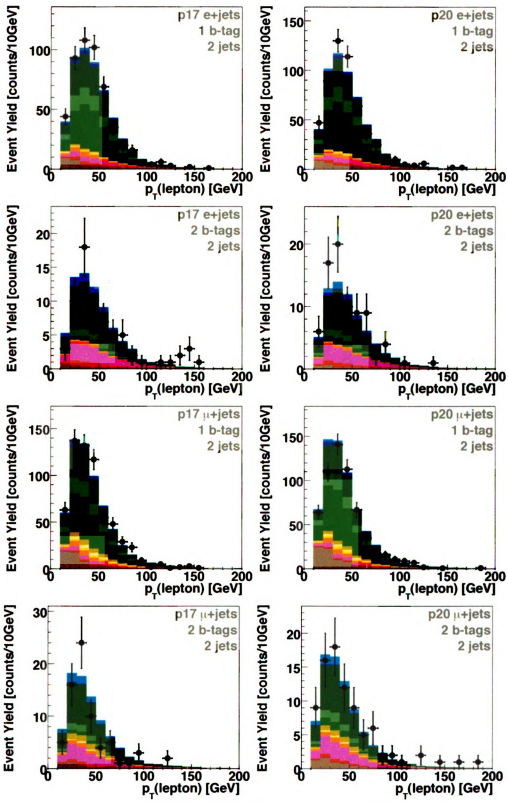

Figure B.1: The transverse momentum of the lepton for channels with exactly two jets in the final state. Run IIa (left) and Run IIb (right). Electron (top four) muon (bottom four). Alternating rows 1-btag and 2-btag.

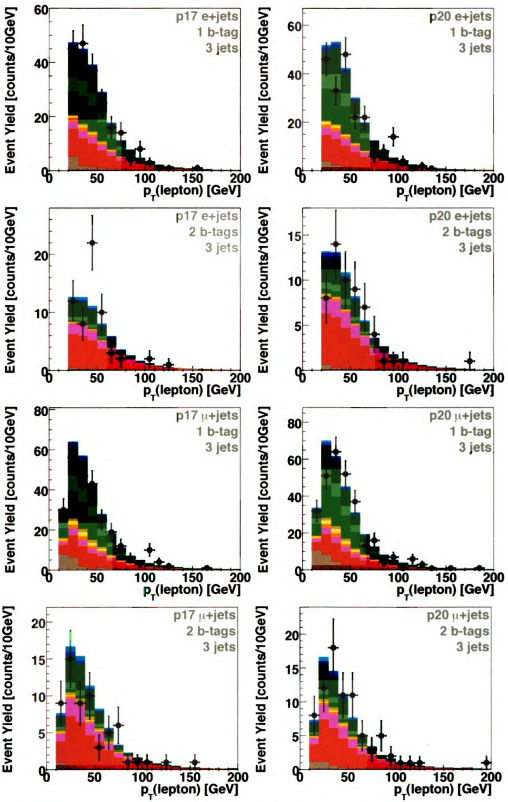

Figure B.2: The transverse momentum of the lepton for channels with exactly three jets in the final state. Run IIa (left) and Run IIb (right). Electron (top four) muon (bottom four). Alternating rows 1-btag and 2-btag.

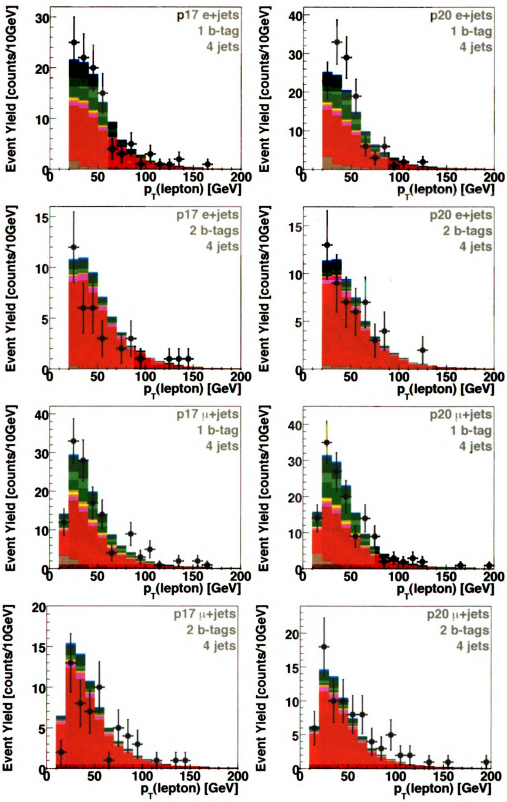

Figure B.3: The transverse momentum of the lepton for channels with exactly four jets in the final state. Run IIa (left) and Run IIb (right). Electron (top four) muon (bottom four). Alternating rows 1-btag and 2-btag.

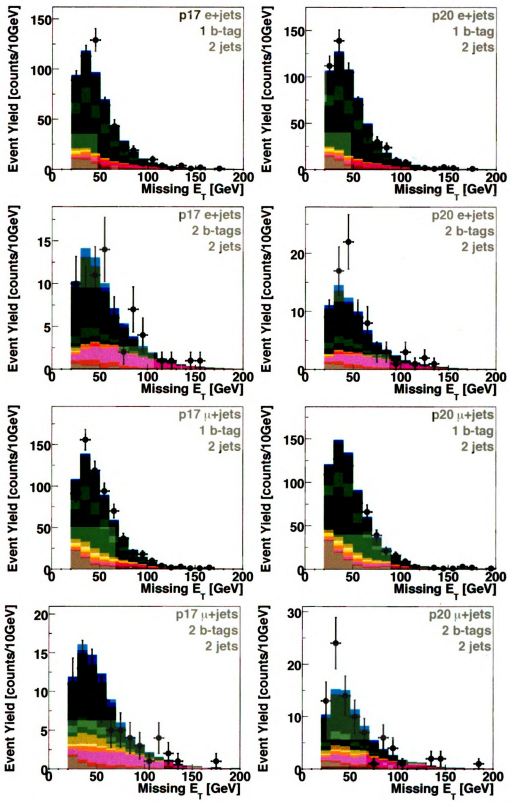

Figure B.4: The missing transverse energy for channels with exactly two jets in the final state. Run IIa (left) and Run IIb (right). Electron (top four) muon (bottom four). Alternating rows 1-btag and 2-btag.

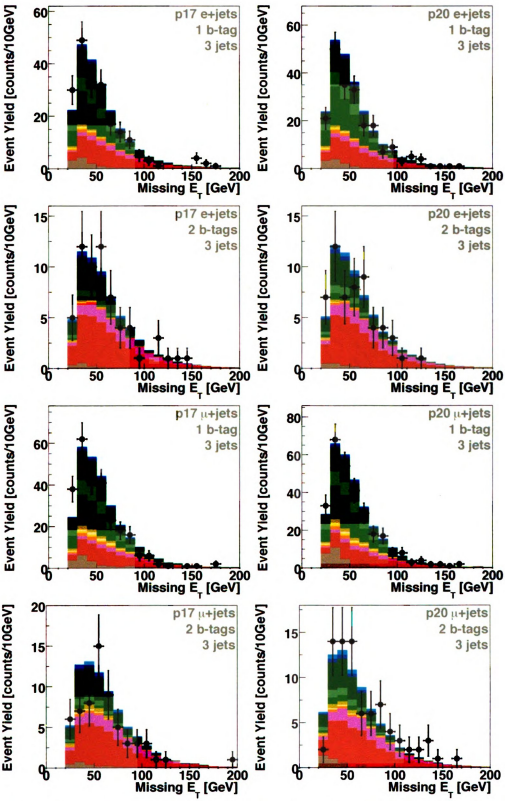

Figure B.5: The missing transverse energy for channels with exactly three jets in the final state. Run IIa (left) and Run IIb (right). Electron (top four) muon (bottom four). Alternating rows 1-btag and 2-btag.

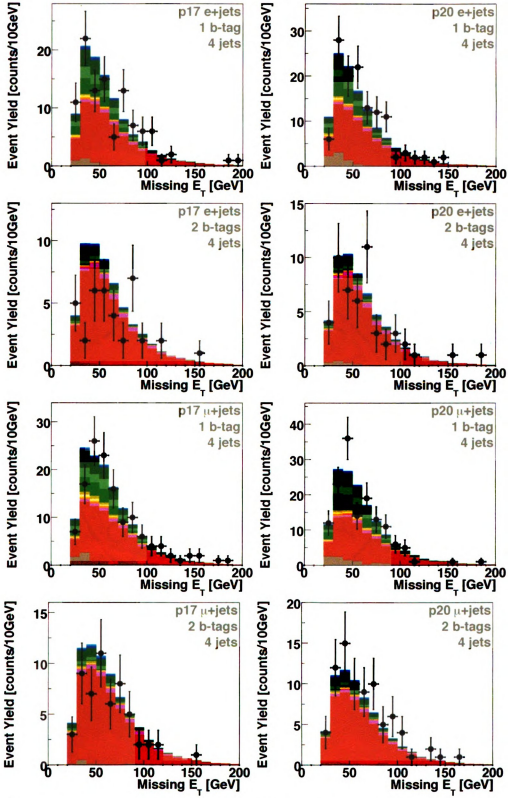

Figure B.6: The missing transverse energy for channels with exactly four jets in the final state. Run IIa (left) and Run IIb (right). Electron (top four) muon (bottom four). Alternating rows 1-btag and 2-btag.

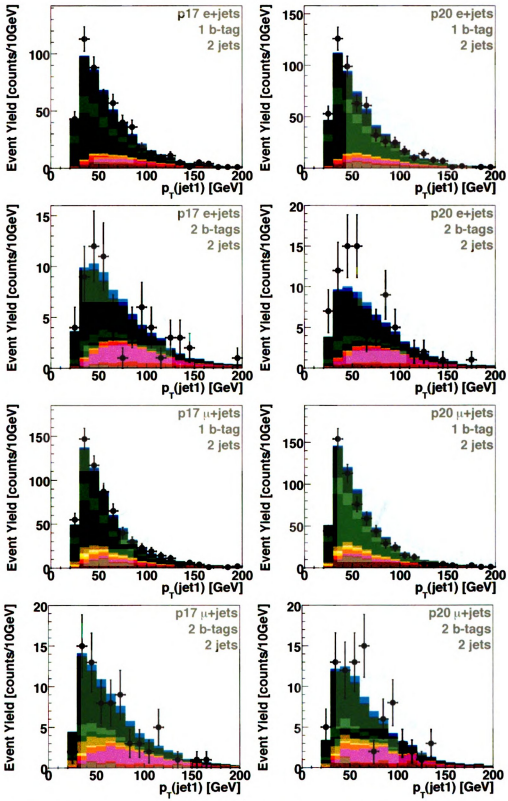

Figure B.7: The transverse energy of the leading jet for channels with exactly two jets in the final state. Run IIa (left) and Run IIb (right). Electron (top four) muon (bottom four). Alternating rows 1-btag and 2-btag.

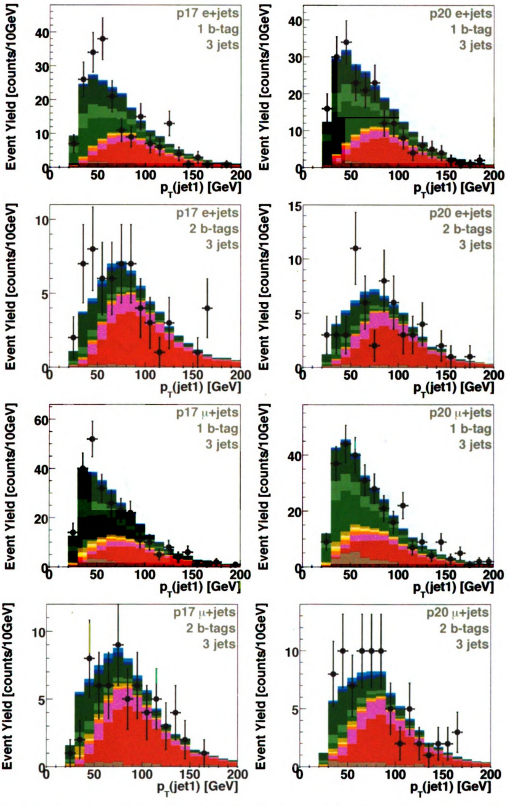

Figure B.8: The transverse energy of the leading jet for channels with exactly three jets in the final state. Run IIa (left) and Run IIb (right). Electron (top four) muon (bottom four). Alternating rows 1-btag and 2-btag.

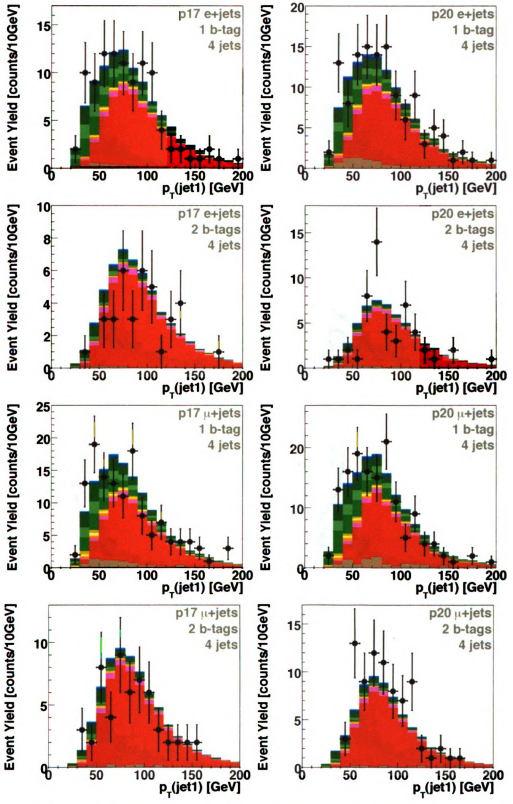

Figure B.9: The transverse energy of the leading jet for channels with exactly four jets in the final state. Run IIa (left) and Run IIb (right). Electron (top four) muon (bottom four). Alternating rows 1-btag and 2-btag.

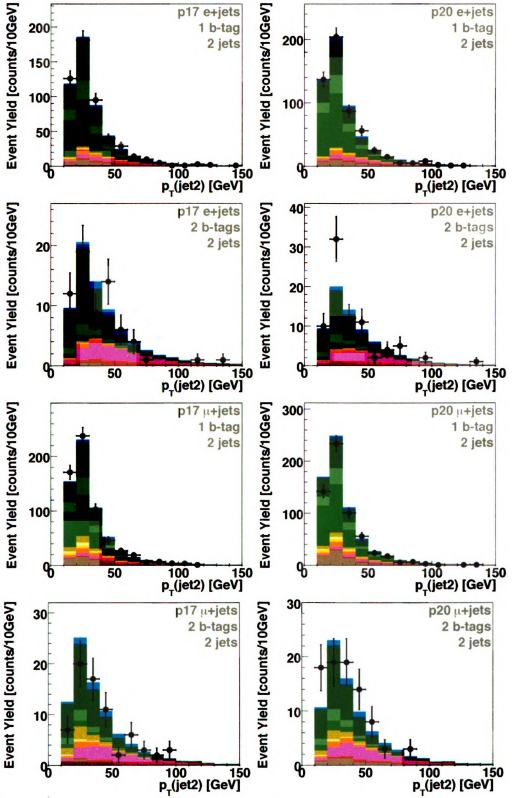

Figure B.10: The transverse energy of the second leading jet for channels with exactly two jets in the final state. Run IIa (left) and Run IIb (right). Electron (top four) muon (bottom four). Alternating rows 1-btag and 2-btag.

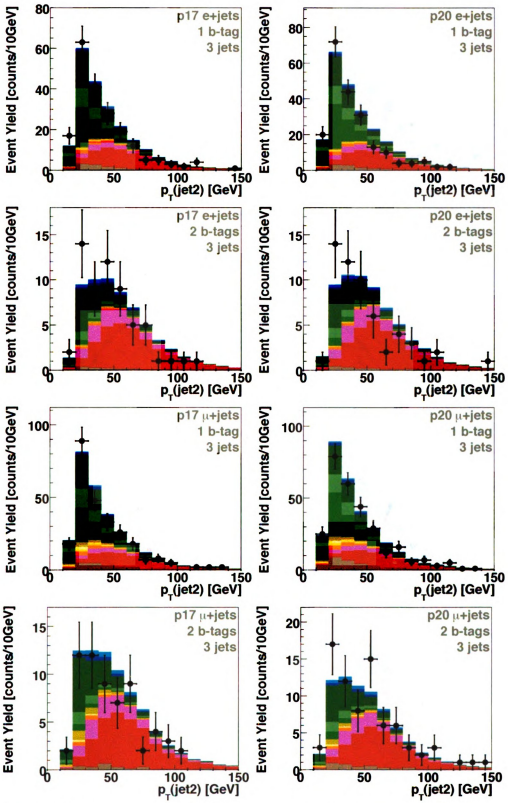

Figure B.11: The transverse energy of the second leading jet for channels with exactly three jets in the final state. Run IIa (left) and Run IIb (right). Electron (top four) muon (bottom four). Alternating rows 1-btag and 2-btag.

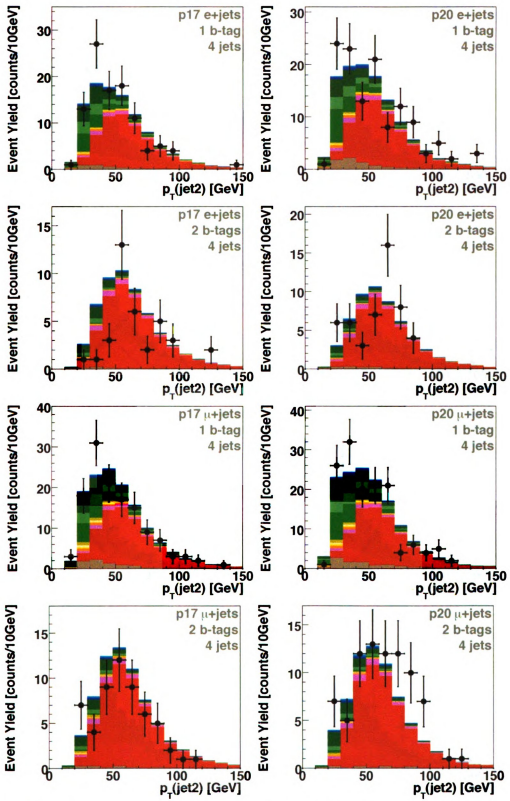

Figure B.12: The transverse energy of the second leading jet for channels with exactly four jets in the final state. Run IIa (left) and Run IIb (right). Electron (top four) muon (bottom four). Alternating rows 1-btag and 2-btag.

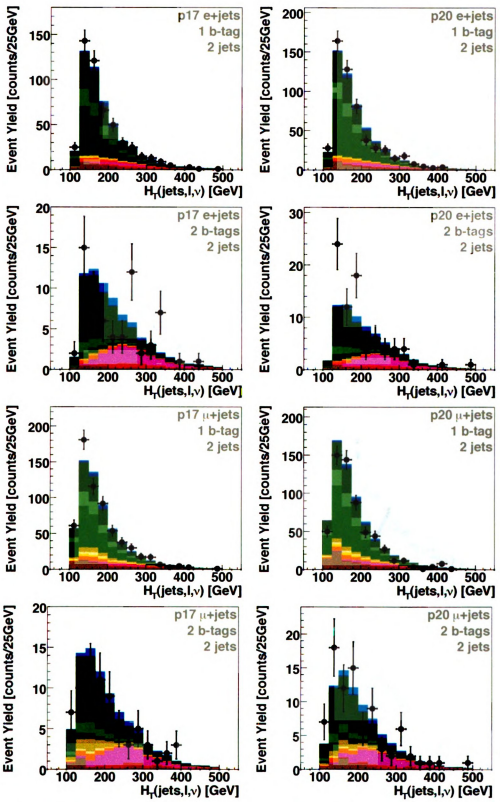

Figure B.13: The scalar transverse energy sumfor channels with exactly two jets in the final state. Run IIa (left) and Run IIb (right). Electron (top four) muon (bottom four). Alternating rows 1-btag and 2-btag.

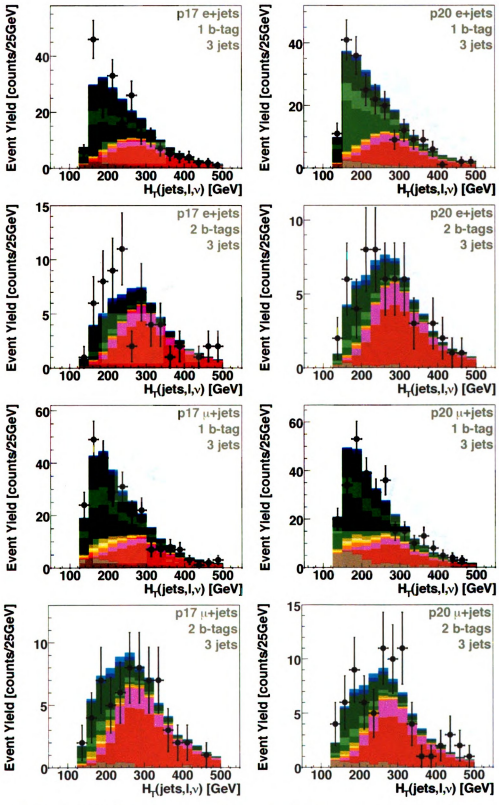

Figure B.14: The scalar transverse energy sum for channels with exactly three jets in the final state. Run IIa (left) and Run IIb (right). Electron (top four) muon (bottom four). Alternating rows 1-btag and 2-btag.

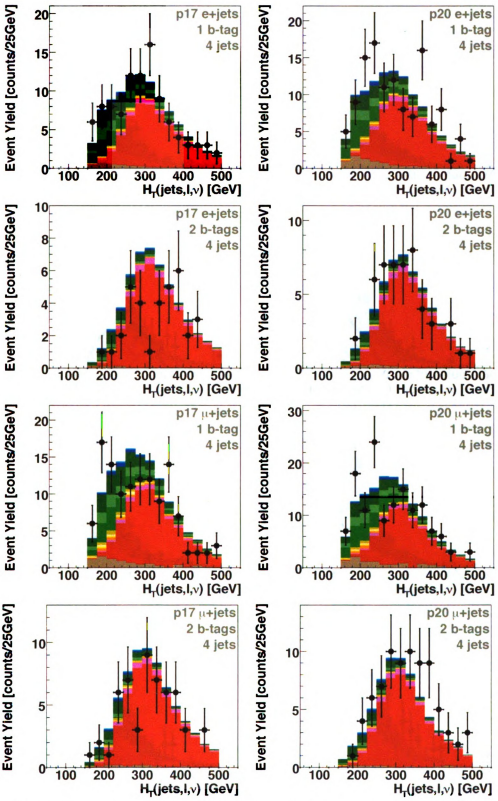

Figure B.15: The scalar transverse energy sum for channels with exactly four jets in the final state. Run IIa (left) and Run IIb (right). Electron (top four) muon (bottom four). Alternating rows 1-btag and 2-btag.

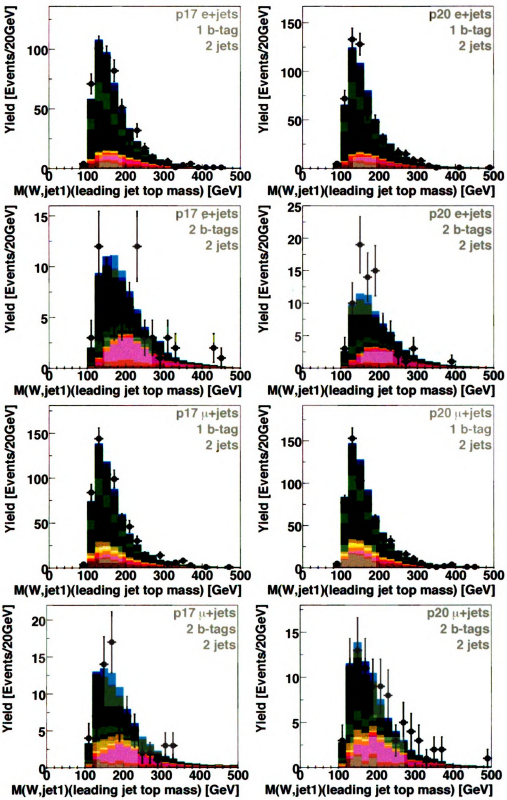

Figure B.16: The top quark mass for channels with exactly two jets in the final state. Run IIa (left) and Run IIb (right). Electron (top four) muon (bottom four). Alternating rows 1-btag and 2-btag.

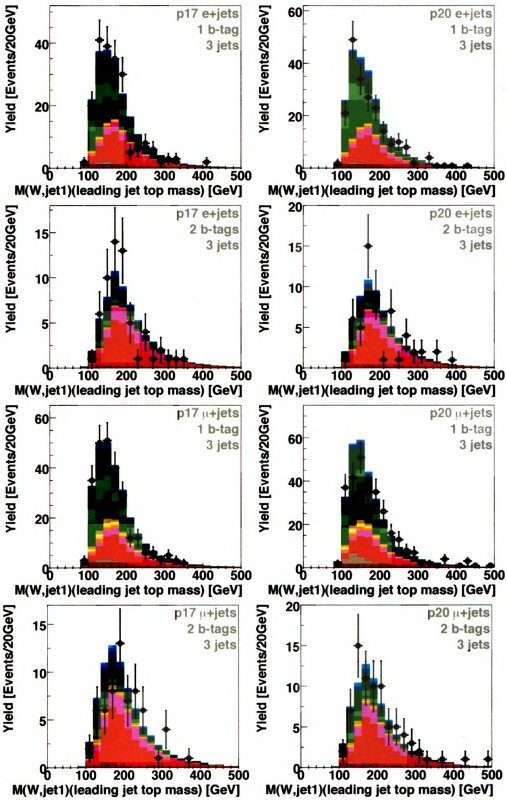

Figure B.17: The top quark mass for channels with exactly three jets in the final state. Run IIa (left) and Run IIb (right). Electron (top four) muon (bottom four). Alternating rows 1-btag and 2-btag.

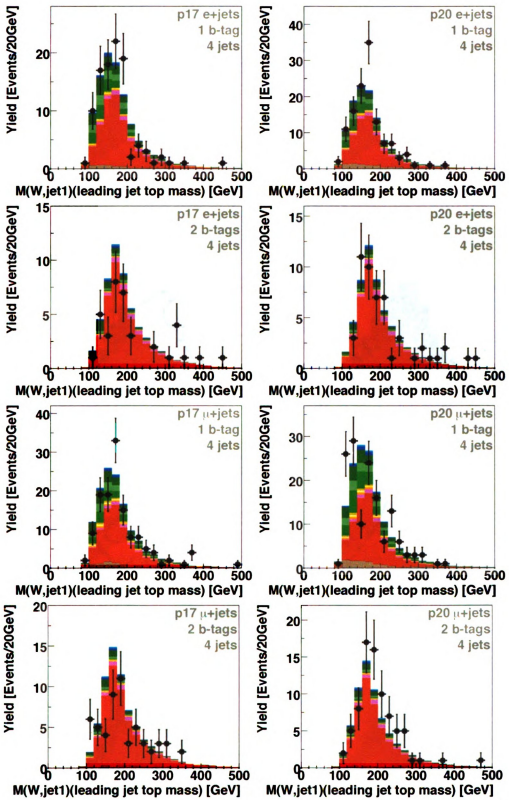

Figure B.18: The top quark mass for channels with exactly four jets in the final state. Run IIa (left) and Run IIb (right). Electron (top four) muon (bottom four). Alternating rows 1-btag and 2-btag.

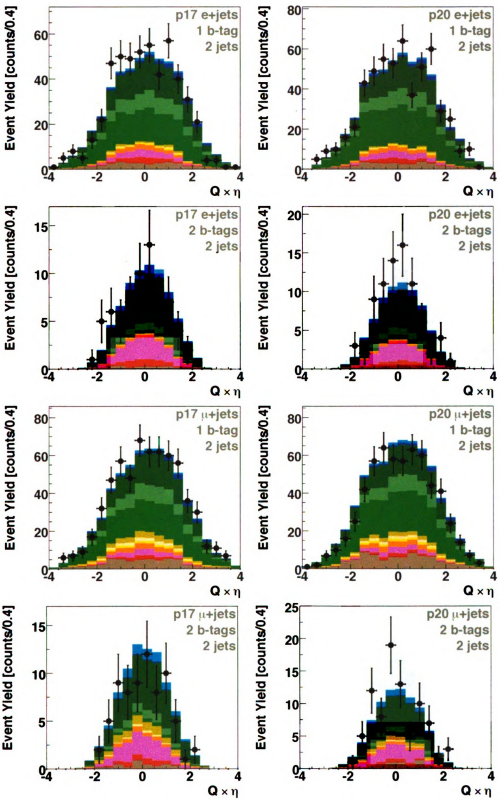

Figure B.19: The pseudorapidity of the light quark jet times lepton charge for channels with exactly two jets in the final state. Run IIa (left) and Run IIb (right). Electron (top four) muon (bottom four). Alternating rows 1-btag and 2-btag.

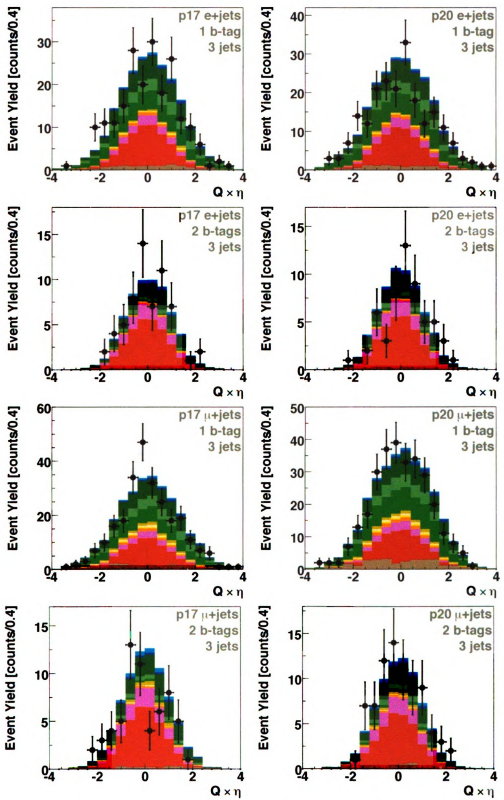

Figure B.20: The pseudorapidity of the light quark jet times lepton charge for channels with exactly three jets in the final state. Run IIa (left) and Run IIb (right). Electron (top four) muon (bottom four). Alternating rows 1-btag and 2-btag.

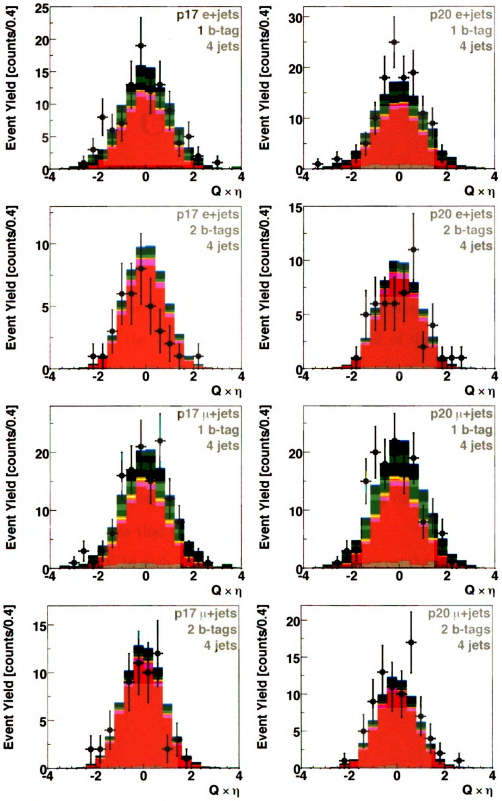

Figure B.21: The pseudorapidity of the light quark jet times lepton charge for channels with exactly four jets in the final state. Run IIa (left) and Run IIb (right). Electron (top four) muon (bottom four). Alternating rows 1-btag and 2-btag.

Appendix C

Systematic Uncertainty Tables

Tables C.1–C.24 show the flat systematic uncertainties on the signal and background samples for the all of the 24 channels in the analysis. All of the shape changing systematics are treated separately in the calculation and are presented in Appendix D.

Note that due to the normalization to data before b tagging, the $Wb\bar{b}$, $Wc\bar{c}$, and Wjj tagged yield estimates are not affected by any of the systematic uncertainties that affect the overall yield. The exception to this is b tagging, which is applied after normalization. There is still an effect on the shapes of distributions from the uncertainty components that depend on event kinematics.

The row "WQCD" in each Table includes the uncertainty on the W+jets normalization and on the multijets normalization. Note that the anticorrelation between these two uncertainties is included by giving a negative sign to this uncertainty in multijets samples.

Single-Tagged Two-Jet Muon Channel Percentage Errors

	$t\bar{t}ll$	$t\bar{t}lj$	Wbb	Wcc	Wlp	Zbb	Zcc	Zlp	dibosons	multijet	tb	tqb	$tb+tqb$
Luminosity	6.1	6.1	—	—	—	6.1	6.1	6.1	6.1	—	6.1	6.1	6.1
Xsect.	12.7	12.7	—	—	—	5.8	5.8	5.8	5.8	—	11.2	7.4	8.4
Branching frac.	1.5	1.5	—	—	—	—	—	—	—	—	1.5	1.5	1.5
PDF	—	—	—	—	—	—	—	—	—	—	3.0	3.0	3.0
Triggers	5.0	5.0	—	—	—	5.0	5.0	5.0	5.0	—	5.0	5.0	5.0
Lumi. rewtg.	1.0	1.0	—	—	—	1.0	1.0	1.0	1.0	—	1.0	1.0	1.0
Prim. vertex	1.4	1.4	—	—	—	1.4	1.4	1.4	1.4	—	1.4	1.4	1.4
Lepton ID	2.5	2.5	—	—	—	2.5	2.5	2.5	2.5	—	2.5	2.5	2.5
Jet frag.	0.7	0.7	—	—	—	4.0	4.0	4.0	0.7	—	0.7	0.7	0.7
ISR/FSR	3.0	3.0	—	—	—	8.0	8.0	8.0	0.6	—	0.6	0.6	0.6
b-jet frag.	2.0	2.0	—	—	—	2.0	—	—	—	—	2.0	2.0	2.0
Jet ID	1.0	1.0	—	—	—	1.0	1.0	1.0	1.0	—	1.0	1.0	1.0
Jet res.	4.0	4.0	—	—	—	4.0	4.0	4.0	4.0	—	4.0	4.0	4.0
S_{HF} W	—	—	13.7	13.7	−0.8	—	—	—	—	—	—	—	—
S_{HF} ratio	—	—	5.0	−5.0	—	—	—	—	—	—	—	—	—
S_{HF} Z	—	—	—	—	—	20.0	20.0	—	—	—	—	—	—
IKS	—	—	1.8	1.8	1.8	—	—	—	—	−40.0	—	—	—

Table C.13: p17 muon channel uncertainties, requiring exactly one tag and two jets.

Single-Tagged Four-Jet Muon Channel Percentage Errors

	$t\bar{t}ll$	$t\bar{t}lj$	Wbb	Wcc	Wlp	Zbb	Zcc	Zlp	dibosons	multijet	tb	tqb	$tb+tqb$
Luminosity	6.1	6.1	—	—	—	6.1	6.1	6.1	6.1	—	6.1	6.1	6.1
Xsect.	12.7	12.7	—	—	—	5.8	5.8	5.8	5.8	—	11.2	7.4	8.4
Branching frac.	1.5	1.5	—	—	—	—	—	—	—	—	1.5	1.5	1.5
PDF	—	—	—	—	—	—	—	—	—	—	3.0	3.0	3.0
Triggers	10.0	10.0	—	—	—	10.0	10.0	10.0	10.0	—	10.0	10.0	10.0
Lumi. rewtg.	1.0	1.0	—	—	—	1.0	1.0	1.0	1.0	—	1.0	1.0	1.0
Prim. vertex	1.4	1.4	—	—	—	1.4	1.4	1.4	1.4	—	1.4	1.4	1.4
Lepton ID	2.5	2.5	—	—	—	2.5	2.5	2.5	2.5	—	2.5	2.5	2.5
Jet frag.	0.7	0.7	—	—	—	4.0	4.0	4.0	4.7	—	4.7	4.7	4.7
ISR/FSR	0.6	0.6	—	—	—	8.0	8.0	8.0	12.6	—	12.6	12.6	12.6
b-jet frag.	2.0	2.0	—	—	—	2.0	—	—	—	—	2.0	2.0	2.0
Jet ID	1.0	1.0	—	—	—	1.0	1.0	1.0	1.0	—	1.0	1.0	1.0
Jet res.	4.0	4.0	—	—	—	4.0	4.0	4.0	4.0	—	4.0	4.0	4.0
S_{HF} W	—	—	13.7	13.7	−0.7	—	—	—	—	—	—	—	—
S_{HF} ratio	—	—	5.0	−5.0	—	—	—	—	—	—	—	—	—
S_{HF} Z	—	—	—	—	—	20.0	20.0	—	—	—	—	—	—
IKS	—	—	3.9	3.9	3.9	—	—	—	—	−54.0	—	—	—

Table C.23: p20 muon channel uncertainties, requiring exactly one tag and four jets.

Single-Tagged Four-Jet Electron Channel Percentage Errors

	$t\bar{t}ll$	$t\bar{t}lj$	Wbb	Wcc	Wlp	Zbb	Zcc	Zlp	dibosons	multijet	tb	tqb	$tb+tqb$
Luminosity	6.1	6.1	—	—	—	6.1	6.1	6.1	6.1	—	6.1	6.1	6.1
Xsect.	12.7	12.7	—	—	—	5.8	5.8	5.8	5.8	—	11.2	7.4	8.4
Branching frac.	1.5	1.5	—	—	—	—	—	—	—	—	1.5	1.5	1.5
PDF	—	—	—	—	—	—	—	—	—	—	3.0	3.0	3.0
Triggers	5.0	5.0	—	—	—	5.0	5.0	5.0	5.0	—	5.0	5.0	5.0
Lumi. rewtg.	1.0	1.0	—	—	—	1.0	1.0	1.0	1.0	—	1.0	1.0	1.0
Prim. vertex	1.4	1.4	—	—	—	1.4	1.4	1.4	1.4	—	1.4	1.4	1.4
Lepton ID	2.5	2.5	—	—	—	2.5	2.5	2.5	2.5	—	2.5	2.5	2.5
Jet frag.	0.7	0.7	—	—	—	4.0	4.0	4.0	4.7	—	4.7	4.7	4.7
ISR/FSR	0.6	0.6	—	—	—	8.0	8.0	8.0	12.6	—	12.6	12.6	12.6
b-jet frag.	2.0	2.0	—	—	—	2.0	—	—	—	—	2.0	2.0	2.0
Jet ID	1.0	1.0	—	—	—	1.0	1.0	1.0	1.0	—	1.0	1.0	1.0
Jet res.	4.0	4.0	—	—	—	4.0	4.0	4.0	4.0	—	4.0	4.0	4.0
S_{HF} W	—	—	13.7	13.7	−0.7	—	—	—	—	—	—	—	—
S_{HF} ratio	—	—	5.0	−5.0	—	—	—	—	—	—	—	—	—
S_{HF} Z	—	—	—	—	—	13.7	13.7	—	—	—	—	—	—
IKS	—	—	1.8	1.8	1.8	—	—	—	—	−30.0	—	—	—

Table C.9: p17 electron channel uncertainties, requiring exactly one tag and four jets.

Double-Tagged Three-Jet Muon Channel Percentage Errors

	$t\bar{t}ll$	$t\bar{t}lj$	Wbb	Wcc	Wlp	Zbb	Zcc	Zlp	dibosons	multijet	tb	tqb	$tb+tqb$
Luminosity	6.1	6.1	—	—	—	6.1	6.1	6.1	6.1	—	6.1	6.1	6.1
Xsect.	12.7	12.7	—	—	—	5.8	5.8	5.8	5.8	—	11.2	7.4	8.4
Branching frac.	1.5	1.5	—	—	—	—	—	—	—	—	1.5	1.5	1.5
PDF	—	—	—	—	—	—	—	—	—	—	3.0	3.0	3.0
Triggers	10.0	10.0	—	—	—	10.0	10.0	10.0	10.0	—	10.0	10.0	10.0
Lumi. rewtg.	1.0	1.0	—	—	—	1.0	1.0	1.0	1.0	—	1.0	1.0	1.0
Prim. vertex	1.4	1.4	—	—	—	1.4	1.4	1.4	1.4	—	1.4	1.4	1.4
Lepton ID	2.5	2.5	—	—	—	2.5	2.5	2.5	2.5	—	2.5	2.5	2.5
Jet frag.	0.1	0.1	—	—	—	4.0	4.0	4.0	3.7	—	3.7	3.7	3.7
ISR/FSR	2.8	2.8	—	—	—	8.0	8.0	8.0	5.2	—	5.2	5.2	5.2
b-jet frag.	2.0	2.0	—	—	—	2.0	—	—	—	—	2.0	2.0	2.0
Jet ID	1.0	1.0	—	—	—	1.0	1.0	1.0	1.0	—	1.0	1.0	1.0
Jet res.	4.0	4.0	—	—	—	4.0	4.0	4.0	4.0	—	4.0	4.0	4.0
S_{HF} W	—	—	13.7	13.7	−0.8	—	—	—	—	—	—	—	—
S_{HF} ratio	—	—	5.0	−5.0	—	—	—	—	—	—	—	—	—
S_{HF} Z	—	—	—	—	—	20.0	20.0	—	—	—	—	—	—
IKS	—	—	1.8	1.8	1.8	—	—	—	—	−51.0	—	—	—

Table C.20: p20 muon channel uncertainties, requiring exactly two tags and three jets.

Single-Tagged Four-Jet Muon Channel Percentage Errors

	$t\bar{t}ll$	$t\bar{t}lj$	Wbb	Wcc	Wlp	Zbb	Zcc	Zlp	dibosons	multijet	tb	tqb	$tb+tqb$
Luminosity	6.1	6.1	—	—	—	6.1	6.1	6.1	6.1	—	6.1	6.1	6.1
Xsect.	12.7	12.7	—	—	—	5.8	5.8	5.8	5.8	—	11.2	7.4	8.4
Branching frac.	1.5	1.5	—	—	—	—	—	—	—	—	1.5	1.5	1.5
PDF	—	—	—	—	—	—	—	—	—	—	3.0	3.0	3.0
Triggers	5.0	5.0	—	—	—	5.0	5.0	5.0	5.0	—	5.0	5.0	5.0
Lumi. rewtg.	1.0	1.0	—	—	—	1.0	1.0	1.0	1.0	—	1.0	1.0	1.0
Prim. vertex	1.4	1.4	—	—	—	1.4	1.4	1.4	1.4	—	1.4	1.4	1.4
Lepton ID	2.5	2.5	—	—	—	2.5	2.5	2.5	2.5	—	2.5	2.5	2.5
Jet frag.	0.7	0.7	—	—	—	4.0	4.0	4.0	4.7	—	4.7	4.7	4.7
ISR/FSR	0.6	0.6	—	—	—	8.0	8.0	8.0	12.6	—	12.6	12.6	12.6
b-jet frag.	2.0	2.0	—	—	—	2.0	—	—	—	—	2.0	2.0	2.0
Jet ID	1.0	1.0	—	—	—	1.0	1.0	1.0	1.0	—	1.0	1.0	1.0
Jet res.	4.0	4.0	—	—	—	4.0	4.0	4.0	4.0	—	4.0	4.0	4.0
S_{HF} W	—	—	13.7	13.7	−0.7	—	—	—	—	—	—	—	—
S_{HF} ratio	—	—	5.0	−5.0	—	—	—	—	—	—	—	—	—
S_{HF} Z	—	—	—	—	—	20.0	20.0	—	—	—	—	—	—
IKS	—	—	1.8	1.8	1.8	—	—	—	—	−30.0	—	—	—

Table C.21: p17 muon channel uncertainties, requiring exactly one tag and four jets.

Appendix D

JES, TRF, and RWT Systematic Uncertainties

Table D.1 shows the normalization part of the uncertainty from the jet energy scale and the taggability plus tag-rate functions, for the signal acceptances and for the combined backgrounds. These values are not included in the tables in Appendix C because they are not treated separately as flat systematics, but are included at the same time as the shape-changing part of the uncertainty is included. The JES normalization uncertainties are included on the $t\bar{t}$, Z+jets, and diboson backgrounds as well as the signal uncertainties, and the shape part is in addition applied to the W+jets, $t\bar{t}$, Z+jets, and diboson backgrounds. The TRF normalization and shape uncertainties are applied to all MC samples. Figure 7.6 shows the size of the reweighting uncertainties (error bars on points).

The JES uncertainties as used in the analysis are shown in Figs. D.1–D.3 for the signal boosted decision tree discriminant output. The signal TRF uncertainties are shown in Figs. D.1–D.3, and the ALPGEN reweighting function uncertainties in for the backgrounds is shown in Figs. D.7 and D.9. Similar distributions for JES and TRF background uncertainties can be found in Reference [90].

JES and TRF Normalization Uncertainties

	Run IIa						Run IIb					
	1-tag			2-tags			1-tag			2-tags		
	2 jets	3 jets	4 jets	2 jets	3 jets	4 jets	2 jets	3 jets	4 jets	2 jets	3 jets	4 jets
Jet Energy Scale												
tb+tqb (e)	1.5%	5.9%	11.7%	2.8%	2.1%	7.6%	2.1%	5.6%	12.4%	3.8%	1.8%	8.1%
tb+tqb (μ)	1.7%	5.9%	11.7%	3.1%	1.8%	8.8%	2.4%	4.9%	13.1%	4.0%	1.1%	8.4%
Background (e)	0.1%	0.1%	2.0%	1.0%	1.4%	1.2%	0.1%	0.3%	2.1%	1.2%	1.9%	1.0%
Background (μ)	0.8%	0.4%	1.9%	0.2%	1.3%	1.0%	0.5%	0.2%	1.7%	0.4%	1.8%	0.5%
Taggability and Tag-Rate Functions												
tb+tqb (e)	4.5%	3.4%	2.5%	10.8%	10.5%	10.1%	4.7%	3.6%	2.8%	10.8%	10.6%	10.4%
tb+tqb (μ)	4.2%	3.1%	2.3%	10.5%	10.2%	9.9%	4.7%	3.7%	2.9%	10.5%	10.4%	10.2%
Background (e)	5.7%	4.5%	2.4%	10.7%	10.1%	9.3%	7.0%	5.5%	3.0%	11.4%	10.4%	9.2%
Background (μ)	5.4%	4.3%	2.1%	10.2%	9.8%	9.0%	6.5%	5.3%	3.3%	10.9%	10.1%	9.2%

Table D.1: Normalization uncertainties on the signal and combined backgrounds from the jet energy scale and the taggability plus tag-rate functions for each analysis channel.

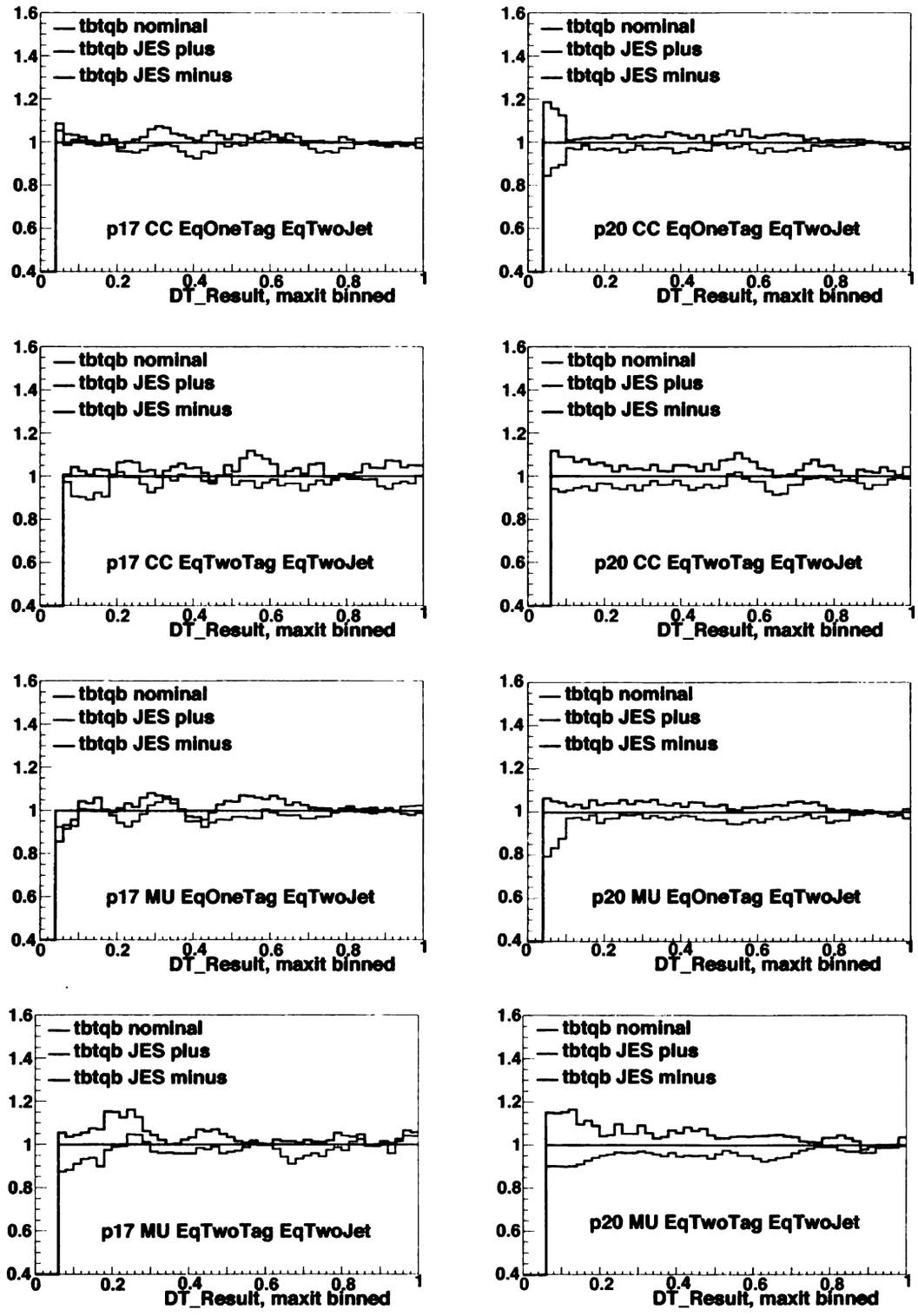

Figure D.1: Systematic shift when varying the JES signal distributions by $\pm 1\sigma$ for the BDT discriminant outputs of events with exactly two jets. Run IIa (left) and Run IIb (right). Electron (top four) muon (bottom four). Alternating rows 1-btag and 2-btag.

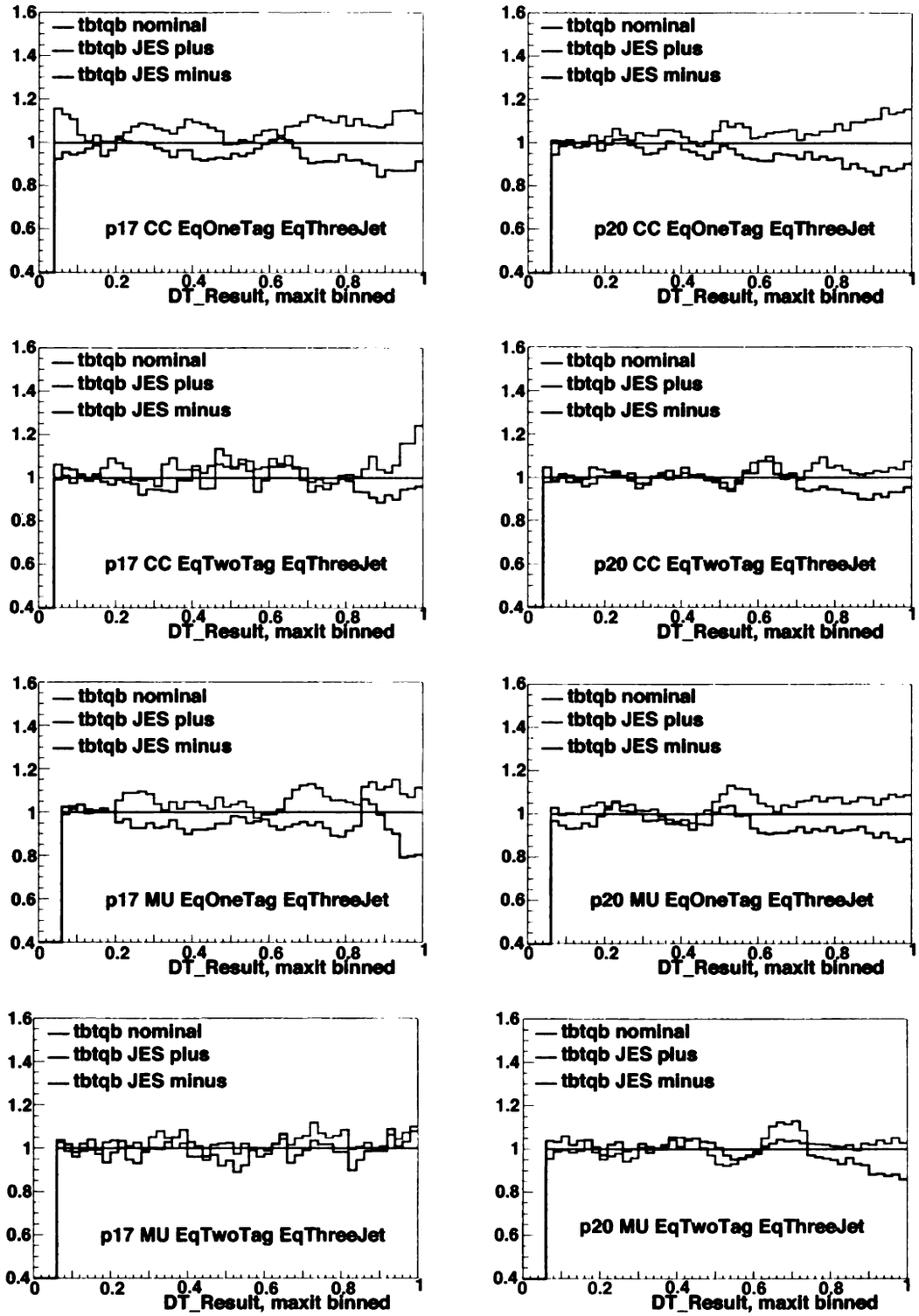

Figure D.2: Systematic shift when varying the JES signal distributions by $\pm 1\sigma$ for the BDT discriminant outputs of events with exactly two jets. Run IIa (left) and Run IIb (right). Electron (top four) muon (bottom four). Alternating rows 1-btag and 2-btag.

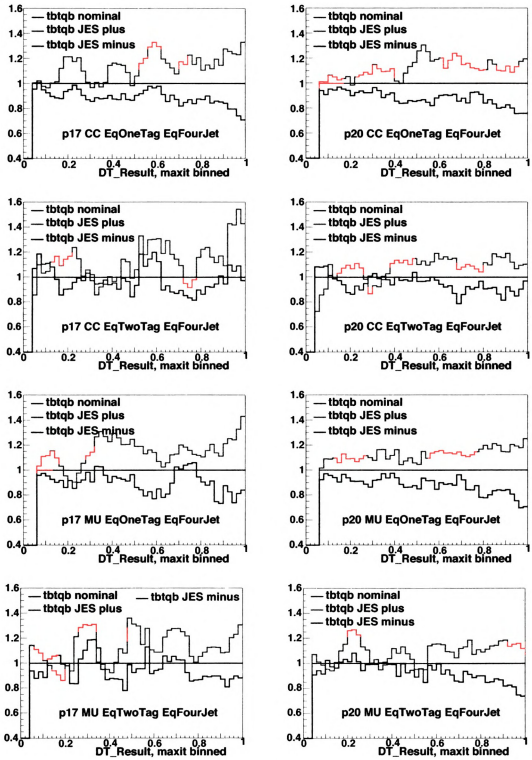

Figure D.3: Systematic shift when varying the JES signal distributions by $\pm 1\sigma$ for the BDT discriminant outputs of events with exactly two jets. Run IIa (left) and Run IIb (right). Electron (top four) muon (bottom four). Alternating rows 1-btag and 2-btag.

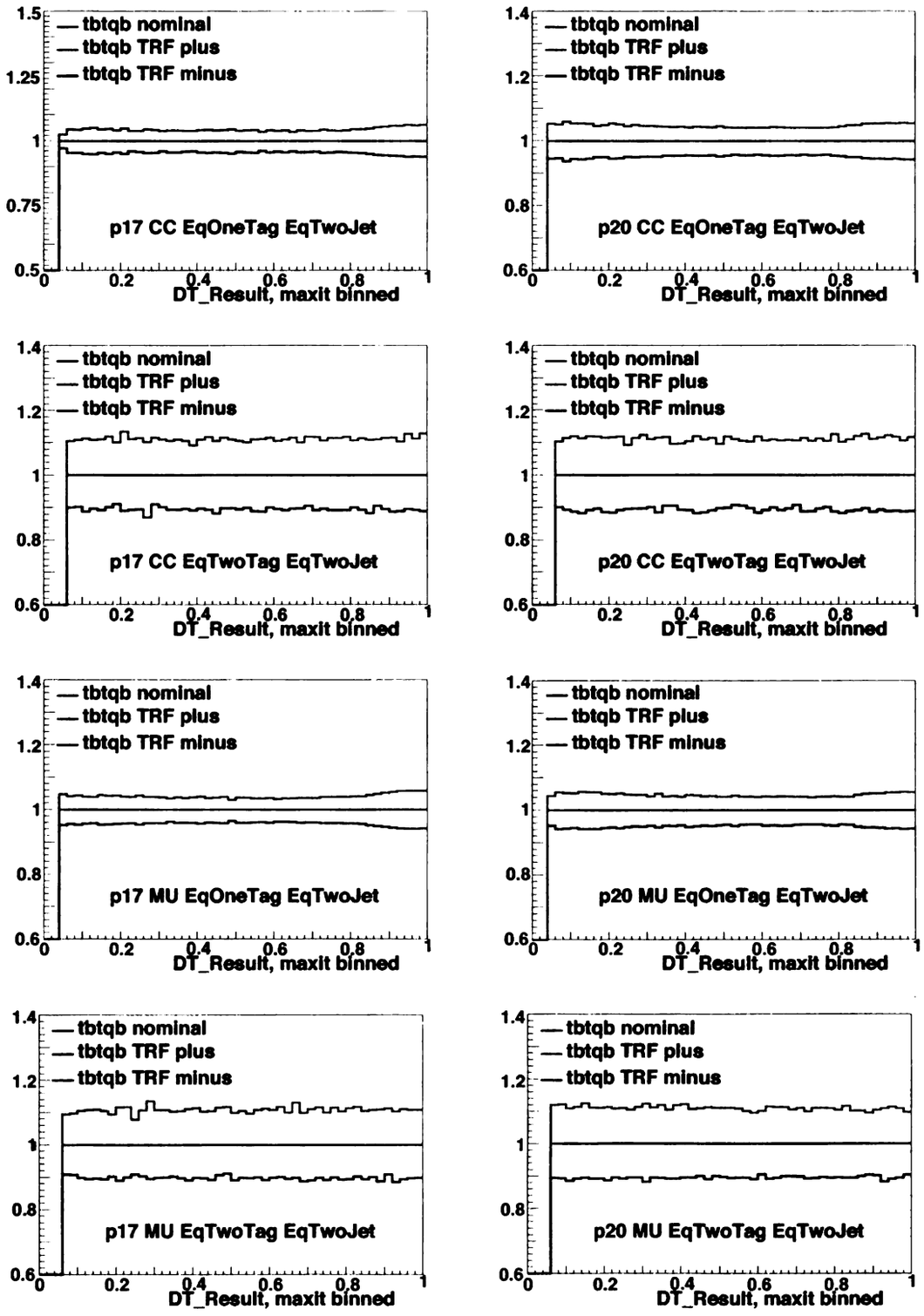

Figure D.4: Systematic shift when varying the TRF signal distributions by $\pm 1\sigma$ for the BDT discriminant outputs of events with exactly two jets. Run IIa (left) and Run IIb (right). Electron (top four) muon (bottom four). Alternating rows 1-btag and 2-btag.

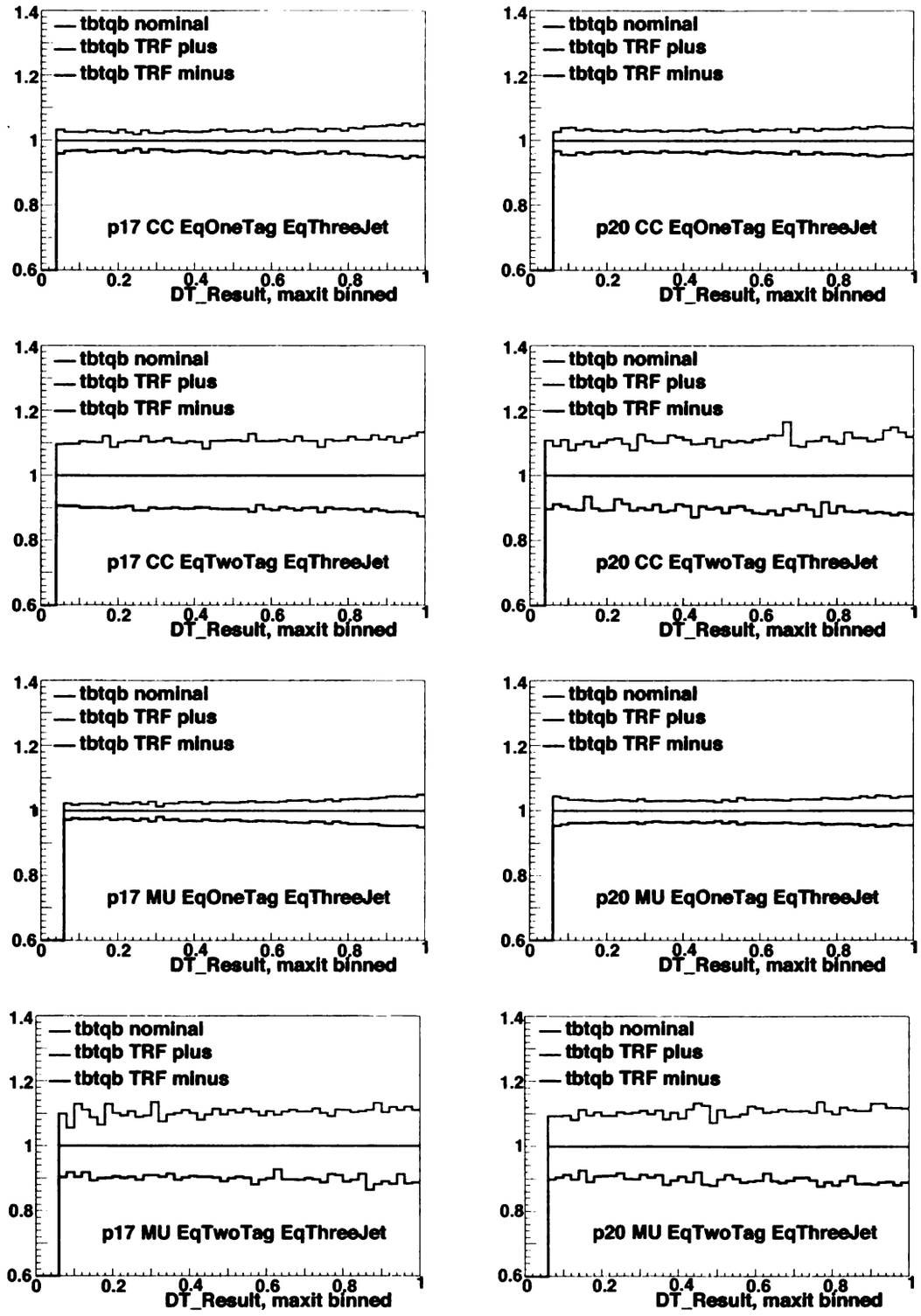

Figure D.5: Systematic shift when varying the TRF signal distributions by $\pm 1\sigma$ for the BDT discriminant outputs of events with exactly two jets. Run IIa (left) and Run IIb (right). Electron (top four) muon (bottom four). Alternating rows 1-btag and 2-btag.

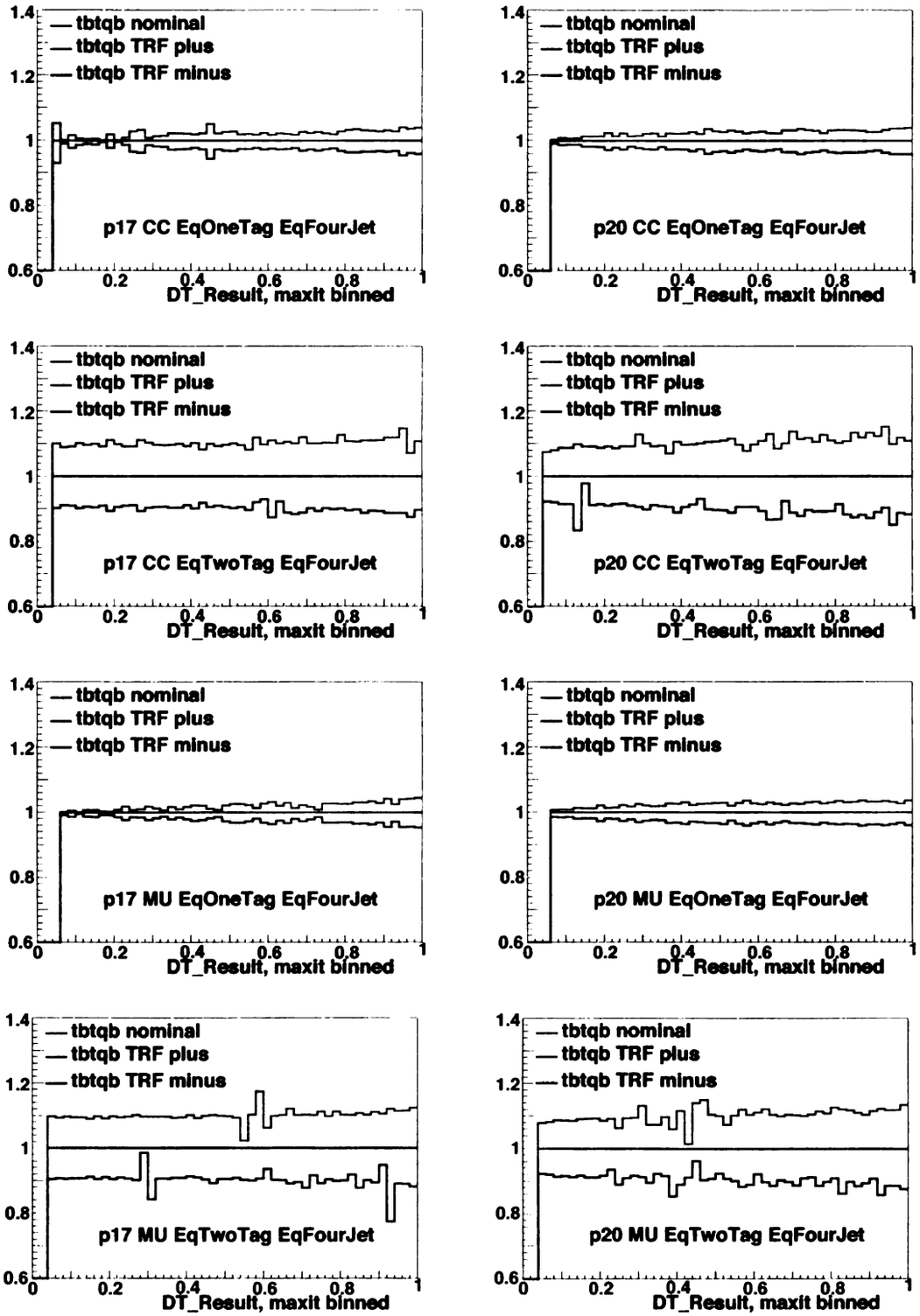

Figure D.6: Systematic shift when varying the TRF signal distributions by $\pm 1\sigma$ for the BDT discriminant outputs of events with exactly two jets. Run IIa (left) and Run IIb (right). Electron (top four) muon (bottom four). Alternating rows 1-btag and 2-btag.

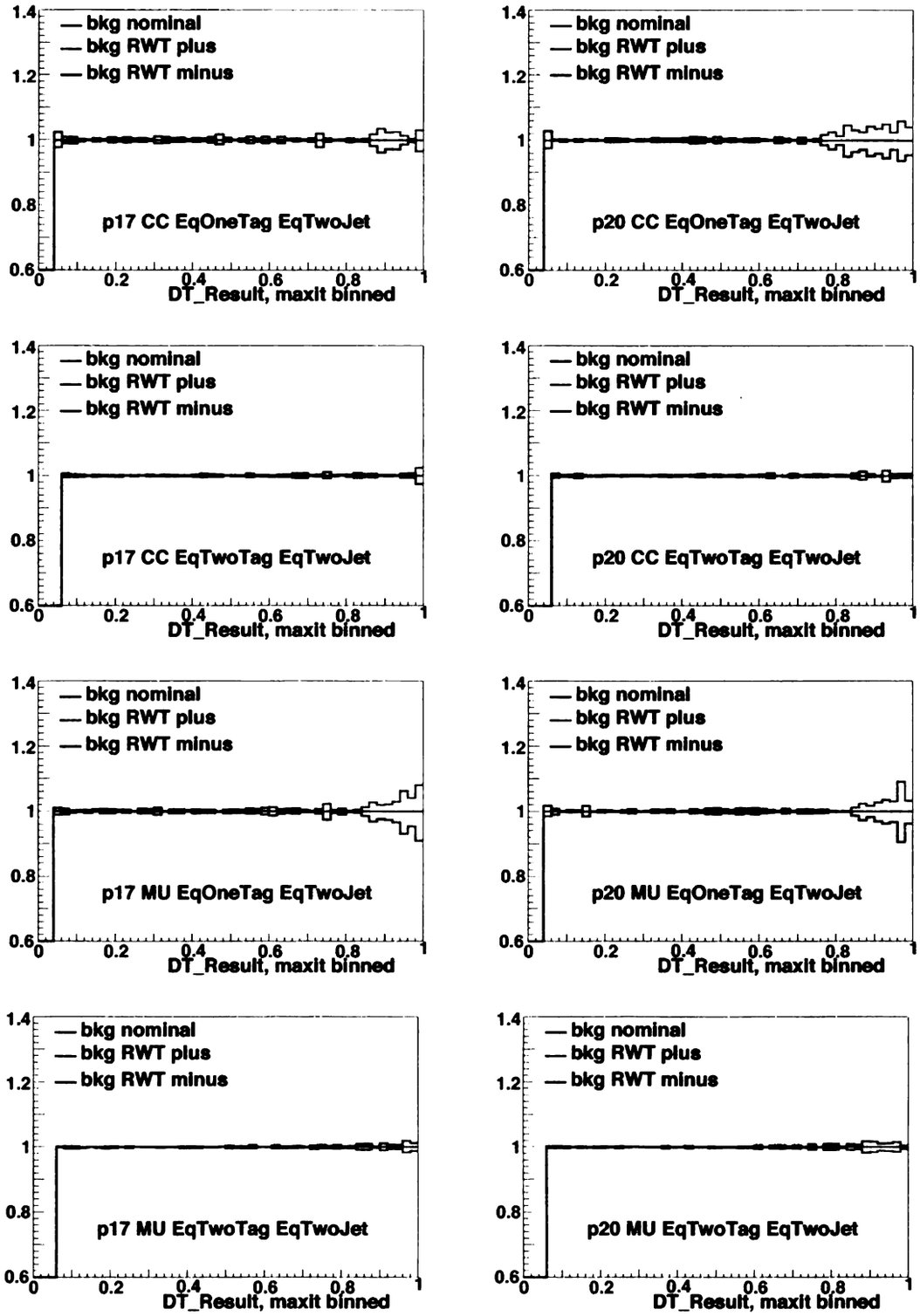

Figure D.7: Systematic shift when varying the RWT background distributions by $\pm 1\sigma$ for the BDT discriminant outputs of events with exactly two jets. Run IIa (left) and Run IIb (right). Electron (top four) muon (bottom four). Alternating rows 1-btag and 2-btag.

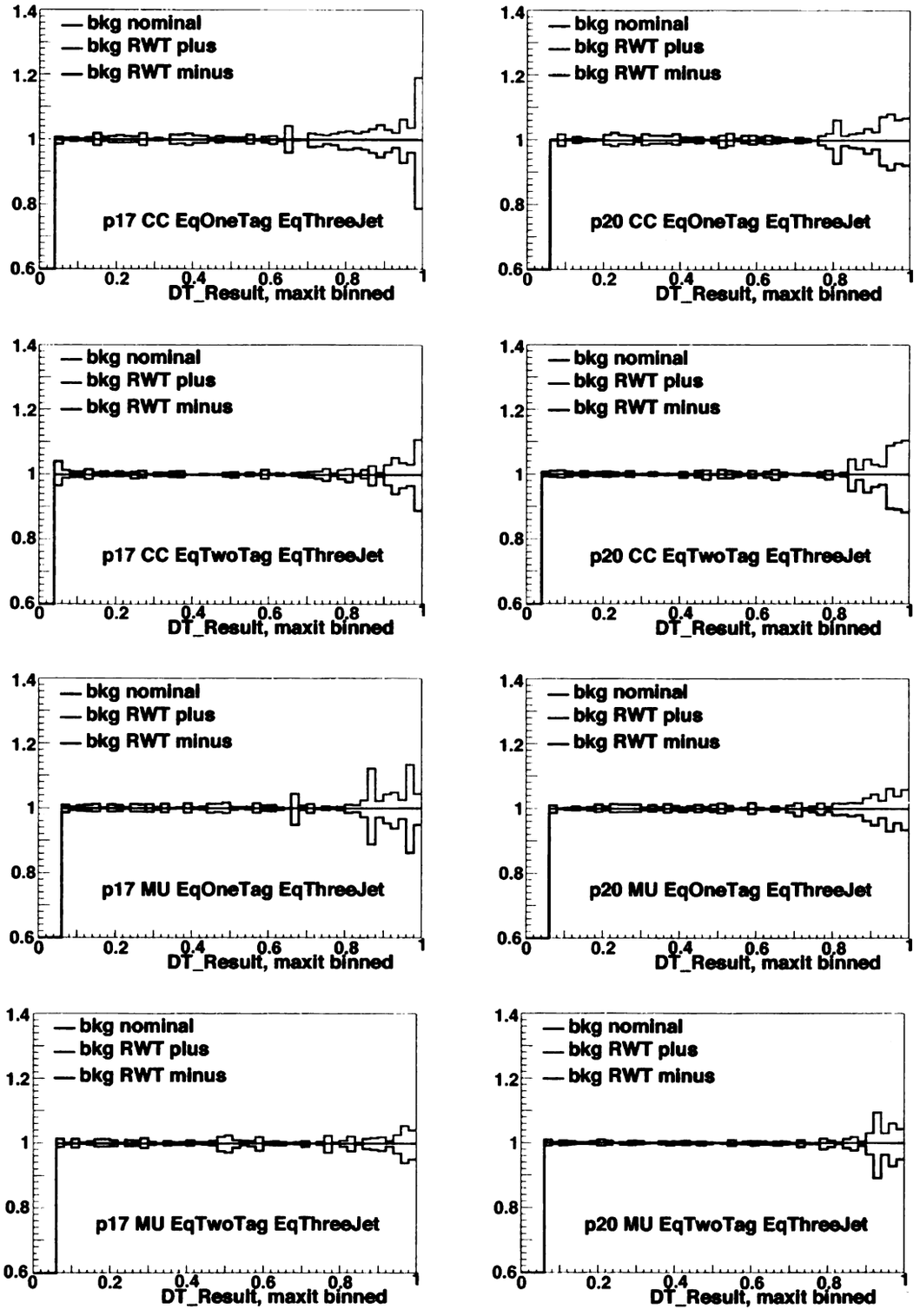

Figure D.8: Systematic shift when varying the RWT background distributions by $\pm 1\sigma$ for the BDT discriminant outputs of events with exactly two jets. Run IIa (left) and Run IIb (right). Electron (top four) muon (bottom four). Alternating rows 1-btag and 2-btag.

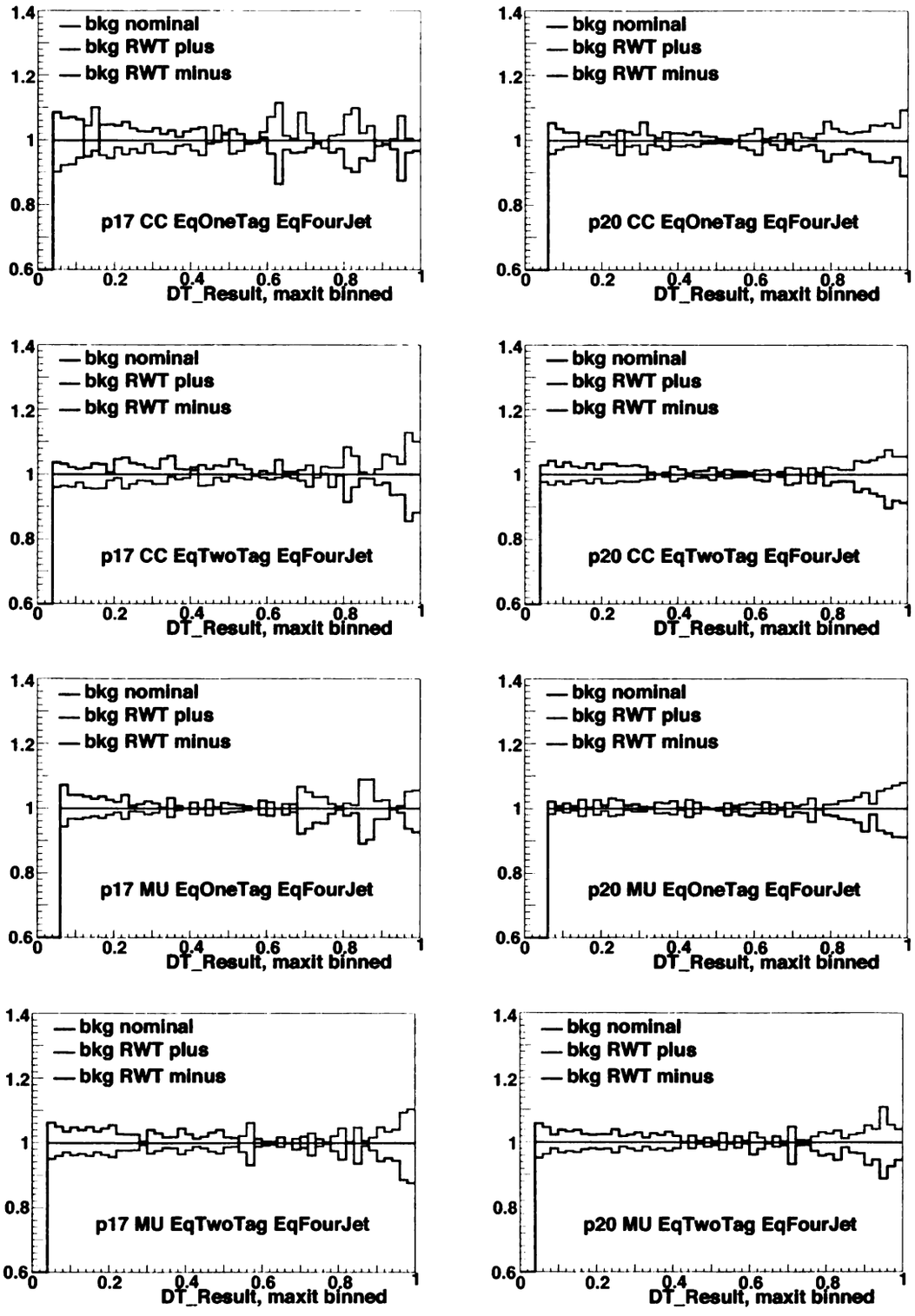

Figure D.9: Systematic shift when varying the RWT background distributions by $\pm 1\sigma$ for the BDT discriminant outputs of events with exactly two jets. Run IIa (left) and Run IIb (right). Electron (top four) muon (bottom four). Alternating rows 1-btag and 2-btag.

Appendix E

Cross Check Samples

In this Appendix, 6 variable distributions are shown for the W+jets and $t\bar{t}$ cross-check samples. The background model reproduces the data in each channel within the uncertainties confirming the validity of the samples in regions dominated by backgrounds.

The cross-check samples defined in Section 7.5, have all the same selection as the main sample, plus the following cuts:

- "W+jets" (2 jets, 1 tag, $H_T < 175$ GeV).
- "$t\bar{t}$" (4 jets, 1–2 tags, $H_T > 300$ GeV).

Figures E.7 and E.8 show the BDTs discriminant output for the the cross check samples in both linear and log scale.

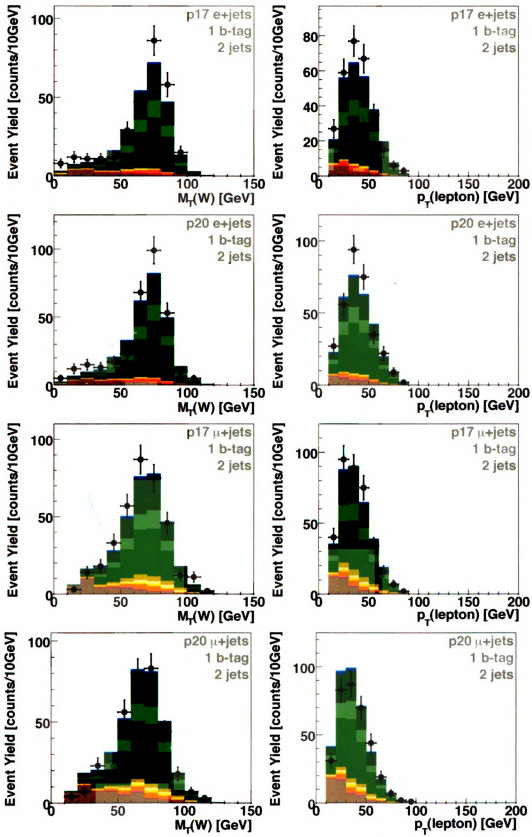

Figure E.1: Cross-check plots for several variables in the W+jets cross-check sample.

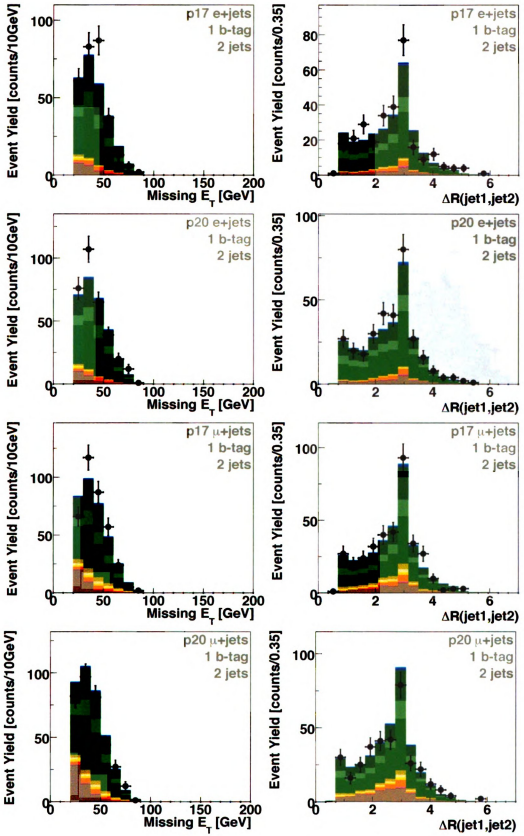

Figure E.2: Cross-check plots for several variables in the W+jets cross-check sample.

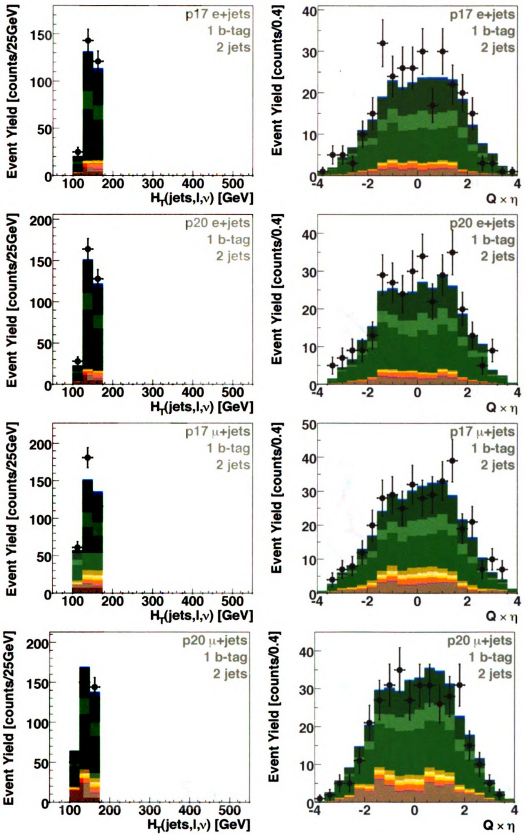

Figure E.3: More cross-check plots for variables in the W+jets cross-check sample.

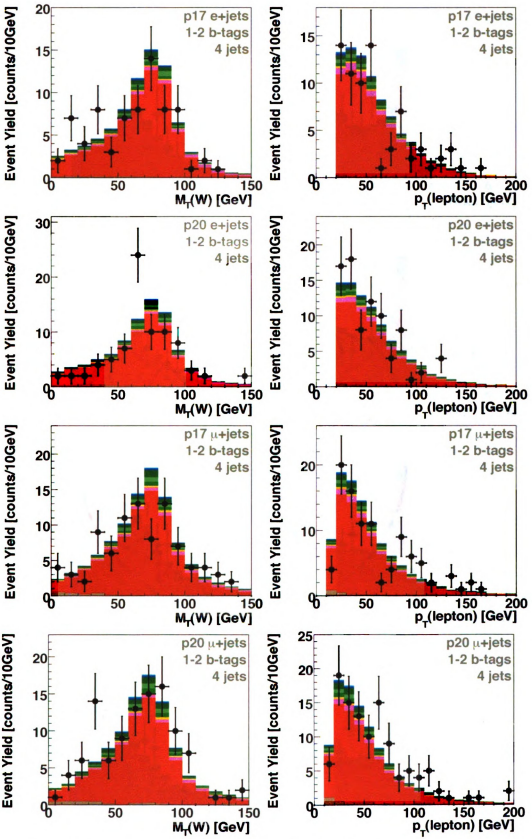

Figure E.4: Cross-check plots for several variables in the $t\bar{t}$ cross-check sample.

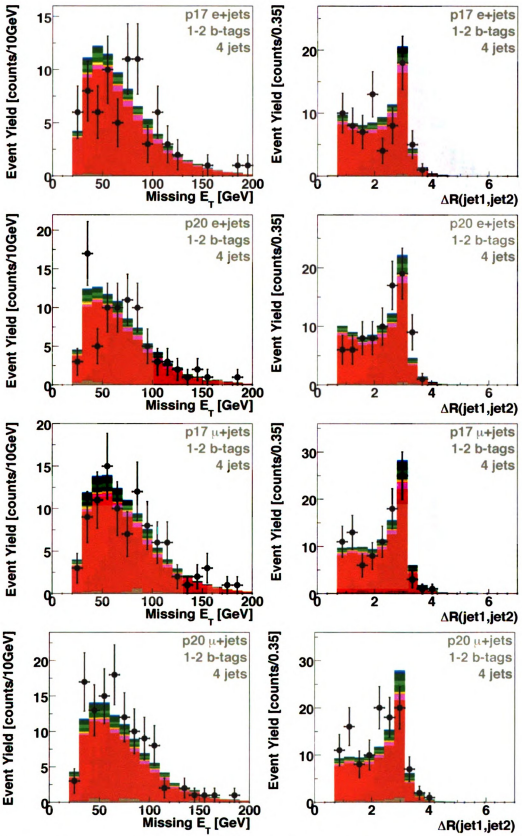

Figure E.5: Cross-check plots for several variables in the $t\bar{t}$ cross-check sample.

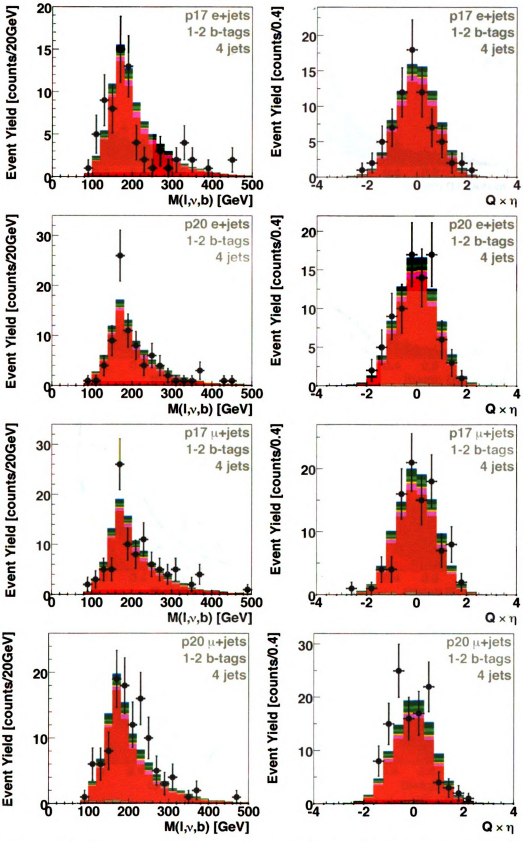

Figure E.6: More cross-check plots for variables in the $t\bar{t}$ cross-check sample.

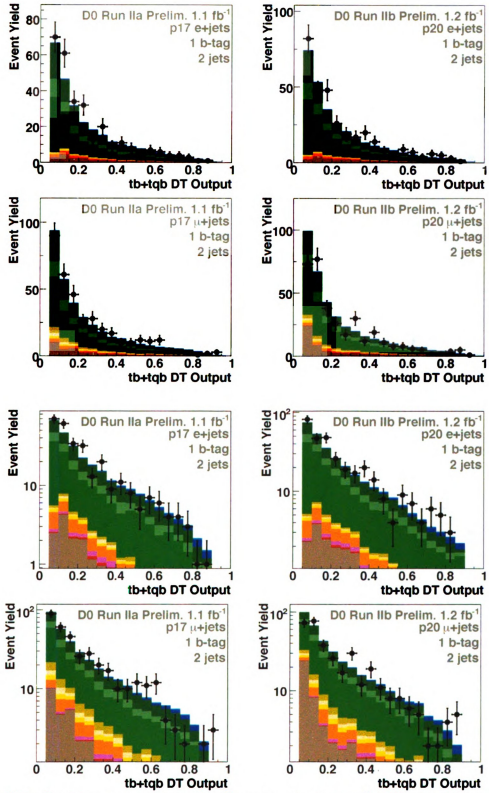

Figure E.7: Decision tree outputs for the cross-check sample "W+jets" on a linear scale. Upper row: electron channel; second row: muon channel. Left column: Run IIa; right column: Run IIb. The last two rows are the same plots that are in first and second row but in log scale

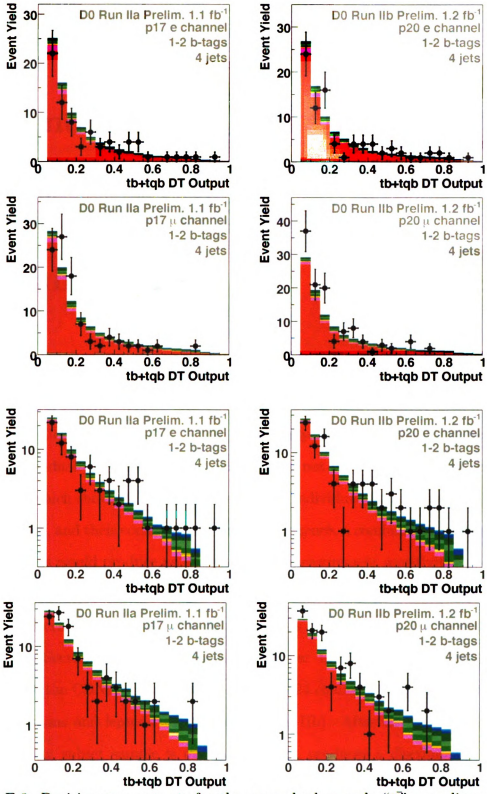

Figure E.8: Decision tree outputs for the cross-check sample "$t\bar{t}$" on a linear scale. Upper row: electron channel; second row: muon channel. Left column: Run IIa; right column: Run IIb. The last two rows are the same plots that are in first and second row but in log scale

Appendix F

Combination of Single Top Measurements

This Appendix presents the combination result of the three DØ Single Top analysis methods: Boosted Decision Trees (BDT) [90], Bayesian Neural Networks (BNN) [132] and Matrix Element (ME) [133]. These three analyses measure the Single Top cross section individually; however, these analyses are not fully correlated (as such, see Figure F.1 which shows 2-D plots comparing the individual analysis pseudo-datasets cross sections, and their correlations). As a consequence, a combination of these three measurements would produce an increase in the measurement sensitivity.

The combination uses a Bayesian Neural Network (CBNN) [139], which is trained using the discriminant outputs from each analysis as inputs, and the second subset sample (see Section 9.2) for the training. Similar to the Boosted Decision Trees (Chapter 9), the CBNN is trained for each of the 24 channels (2,3, and 4 jets - 1 and 2 b-jets - muons and leptons - Run IIa and Run IIb). After the CBNN is trained, the measuring subset sample is evaluated, which produces a discriminant output. Figure F.2 presents the resulting CBNN discriminant for all channels combined and the discriminant outputs from all the three Single Top analyses.

Following the same procedure outlined in Section 9.3, the CBNN discriminant

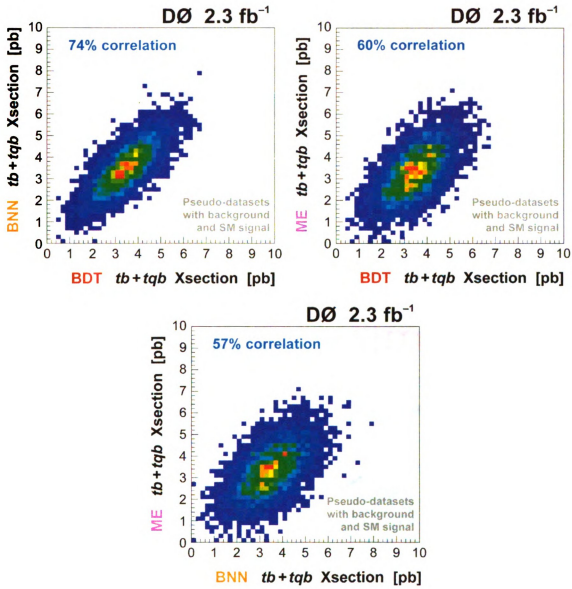

Figure F.1: Correlations among the three Single Top analyses pseudo-datasets: (BNN vs BDT), (ME vs. BDT), and (ME vs. BNN).

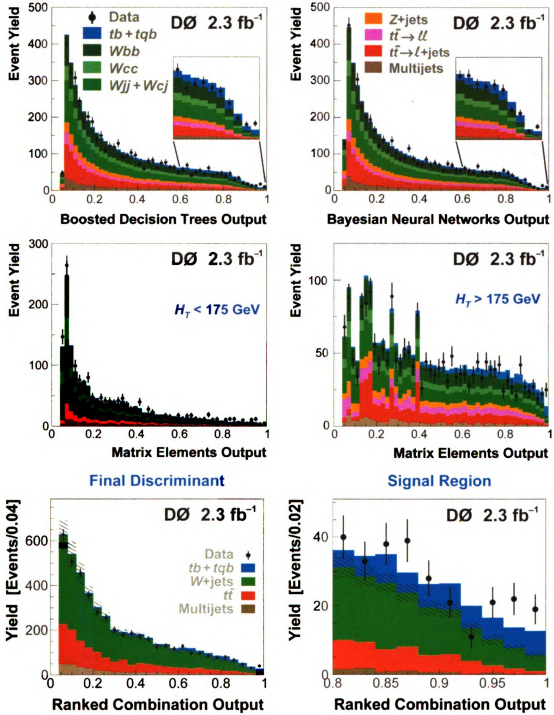

Figure F.2: Discriminant output for the three analyses methods. The bottom row corresponds to the combined BNN output discriminant, and a zoom into the signal region (BNN discriminant > 0.8).

output is used to build a posterior density from which the Single Top cross section measurement is obtained. The measured cross section is

$$\sigma(p\bar{p} \rightarrow tb + X, tqb + X) = 3.94 \pm 0.88 \text{ pb}, \tag{F.1}$$

where the errors include both statistical and systematic uncertainties. This measurement has a p-value of 2.5×10^{-7}, corresponding to a significance of 5.0 standard deviations. Table F.1 shows the individual analyses measurements and sensitivities together with the combined result. Figure F.3 shows the measurements posterior densities, and the corresponding pseudo-datasets ensembles.

Single Top Results with DØ 2.3 fb^{-1} of data

		Significance	
Analysis Method	Cross Section	Expected	Observed
Boosted Decision Trees	$3.74\ ^{+0.95}_{-0.79}$ pb	4.3 σ	4.6 σ
Bayesian Neural Networks	$4.70\ ^{+1.18}_{-0.93}$ pb	4.1 σ	5.4 σ
Matrix Element	$4.30\ ^{+0.99}_{-1.20}$ pb	4.1 σ	4.9 σ
Combination	3.94 ± 0.88 pb	4.5 σ	5.0 σ

Table F.1: Single Top cross section measurements.

Using the Single Top cross section measurement from the CBNN, a Bayesian posterior for $|V_{tb}|^2$ is built in the closed interval zero to one, $[0, 1]$. From this posterior, the limit $V_{tb} > 0.78$ is extracted at 95% C.L. within the Standard Model. If the upper limit constrain on the interval is removed, the resulting measurement for $|V_{tb}f_1^L|$ is:

$$|V_{tb}f_1^L| = 1.07\ ^{+0.11}_{-0.12} \tag{F.2}$$

which corresponds to the strength of the electroweak $V - A$ coupling. The full details of the measurement can be found in Reference [57]. Figure F.4 shows the posterior

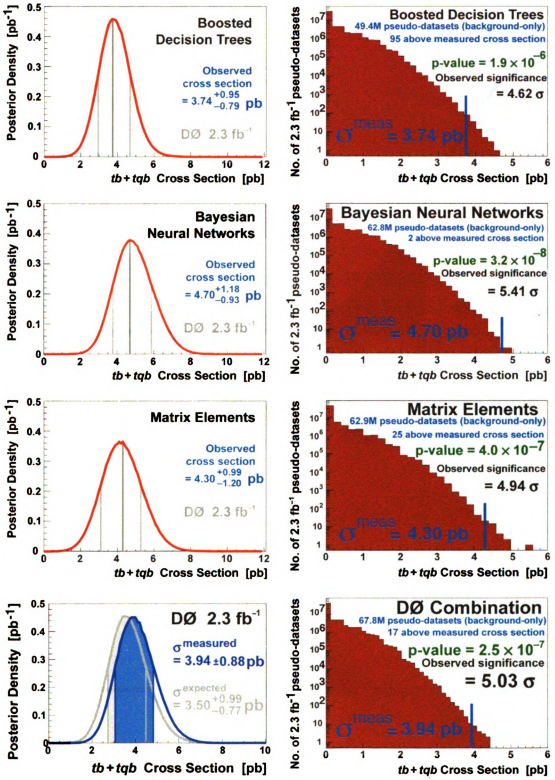

Figure F.3: Posterior probability densities (left column) and significance measurements (right column) for the BDT, BNN, ME, and the combination of the three analyses methods.

probability densities for $|V_{tb}|^2$ and $|V_{tb}f_1^L|^2$.

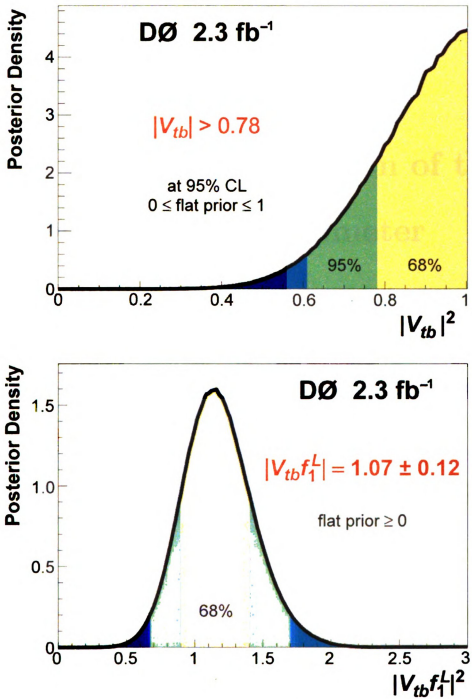

Figure F.4: Posterior probability densities for $|V_{tb}|^2$ (left) and $|V_{tb}f_1^L|^2$ (right). The color bands represent different confidence bounds: 68.3 %, 95.4 % and 99.7 %.

Appendix G

Design and Implementation of the New DØ Level-1 Calorimeter Trigger

In this Appendix, the upgrades of the DØLevel 1 Calorimeter trigger are presented. Special focus is put on the ADF (Analog to Digital Filters) cards with which I worked as part of my service work for the DØ experiment. Some of my hardware related task included the development of a work bench to test over 100 ADF-cards. The testing avoided any complications and/or malfunctions of the cards during the installation process of the system at DØ and current performance on the trigger system.

The full report on the Level-1 Calorimeter trigger was published in *Nuclear Instruments and Methods in Physics Research A 584, 75 (2008).* Excerpts from the original paper are presented below.

G.1 Introduction

Increasing luminosity at the Fermilab Tevatron collider has led the D0 collaboration to make improvements to its detector beyond those already in place for Run IIa,

which began in March 2001. One of the cornerstones of this Run IIb upgrade is a completely redesigned level-1 calorimeter trigger system. The new system employs novel architecture and algorithms to retain high efficiency for interesting events while substantially increasing rejection of background. We describe the design and implementation of the new level-1 calorimeter trigger hardware and discuss its performance during Run IIb data taking. In addition to strengthening the physics capabilities of D0, this trigger system will provide valuable insight into the operation of analogous devices to be used at LHC experiments.

In the following we describe the Level-1 Calorimeter Trigger System (L1Cal) designed for operation during Run IIb. Section G.2 discusses the motivation for replacing the L1Cal trigger, which was used in Run I and Run IIa. Algorithms used in the new system and their simulation are described in Section G.3, while the hardware designed to implement these algorithms is detailed in Sections G.4, G.5, G.6, and G.7. Mechanisms for online control and monitoring of the new L1Cal are outlined in Sections G.8 and G.9. This article then concludes with a discussion of early calibration and performance results in Sections G.10.

G.2 Motivation for the L1Cal Upgrade

By the time of the start of Run IIa in 2001, there was already a tentative plan in place for an extension to the run with accompanying upgrades to the accelerator complex [142], leading to an additional 2–6 fb^{-1} of integrated luminosity beyond the original goal of 2 fb^{-1}. This large increase in statistical power opens new possibilities for physics at the Tevatron such as greater precision in critical measurements like the top quark mass and W boson mass, the possibility of detecting or excluding very rare Standard Model processes (including production of the Higgs boson), and greater sensitivity for beyond the Standard Model processes like supersymmetry.

At a hadron collider like the Tevatron, however, only a small fraction of the

collisions can be recorded, and it is the trigger that dictates what physics processes can be studied and what is left unexplored. The trigger for the D0 experiment in Run IIa had been designed for a maximum luminosity of 1×10^{32} $cm^{-2}s^{-1}$, while the peak luminosities in Run IIb are expected to go as high as 3×10^{32} $cm^{-2}s^{-1}$. In the three-level trigger system employed by D0, only the L3 trigger can be modified to increase its throughput; the maximum output rates at L1 and L2 are imposed by fundamental features of the subdetector electronics. Thus, fitting L1 and L2 triggers into the bandwidth limitations of the system can only be accomplished by increasing their rejection power. While an increase in the transverse energy thresholds at L1 would have been a simple way to achieve higher rejection, such a threshold increase would be too costly in efficiency for the physics processes of interest. The D0 Run IIb Trigger Upgrade [144] was designed to achieve the necessary rate reduction through greater selectivity, particularly at the level of individual L1 trigger elements.

The L1Cal trigger used in Run I and in Run IIa [147] was based on counting individual trigger towers above thresholds in transverse energy (E_T). Because the energy from electrons/photons and especially from jets tends to spread over multiple TTs, the thresholds on tower E_T had to be set low relative to the desired electron or jet E_T. For example, an EM trigger tower threshold of 5 GeV is fully efficient only for electrons with E_T greater than about 10 GeV, and a 5 GeV threshold for EM+HD tower E_T only becomes 90% efficient for jet transverse energies above 50 GeV.

The primary strategy of the Run IIb upgrade of L1Cal is therefore to improve the sharpness of the thresholds for electrons, photons and jets by forming clusters of TTs and comparing the transverse energies of these clusters, rather than individual tower E_Ts, to thresholds.

The design of clustering using sliding windows (see Section G.3) in Field Programmable Gate Arrays (FPGAs) meets the requirements of this strategy, and also

opens new possibilities for L1Cal, including sophisticated use of shower shape and isolation; algorithms to find hadronic decays of tau leptons through their characteristic transverse profile; and requirements on the topology of the electrons, jets, taus, and missing transverse energy in an event.

G.3 Algorithms for the Run IIb L1Cal

Clustering of individual TTs into EM and Jet objects is accomplished in the Run IIb L1Cal by the use of a sliding windows (SW) algorithm. This algorithm performs a highly parallel cluster search in which groups of contiguous TTs are compared to nearby groups to determine the location of local maxima in E_T deposition. Variants of the SW algorithm have been studied extensively at different HEP experiments [148], and have been found to be highly efficient at triggering on EM and Jet objects, while not having the latency drawbacks of iterative clustering algorithms. For a full discussion of the merits of the sliding windows algorithm, see [149].

The implementation of the sliding windows algorithm in the D0 calorimeter trigger occurs in three phases. In the first phase, the digitized transverse energies of several TTs are summed into Trigger Tower Clusters (TTCL). These TTCL sums, based on the size of the EM or Jet sliding window, are constructed for every point in trigger tower space, and are indexed by the η, ϕ coordinate of one of the contributing TTs, with different conventions being used for different algorithms (see Sections ?? and ??). This process, which yields a grid of TTCLs that share energy with their close neighbors, is shown in the first and second panels of Fig. G.1.

In the second phase, the TTCLs are analyzed to determine locations of large energy deposits called local maxima (LM). These LM are chosen based on a comparison of the magnitude of the E_T of a TTCL with that of its adjacent TTCLs. Multiple counting of Jet or EM objects is avoided by requiring a spatial separation between adjacent local maxima as illustrated in the third panel of Fig. G.1.

In the third phase, additional information is added to define an output object. In the case of Jet objects, shown in the fourth panel of Fig. G.1, energy of surrounding TTs is added to the TTCL energy to give the total Jet object energy. EM and Tau objects are also refined in this phase using isolation information (see Sections ?? and ??).

Results for the entire calorimeter can be obtained very quickly using this type of algorithm by performing the LM finding and object refinement phases of the algorithm in parallel for each TTCL.

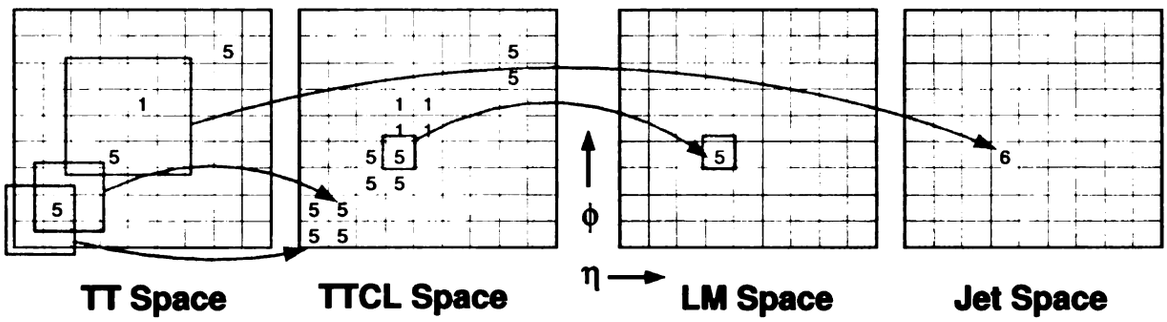

Figure G.1: The stages of algorithm flow for the sliding windows algorithm. In this example, which corresponds to the Run IIb Jet algorithm, a 2×2 TT TTCL is used, indexed by the position of its smallest η, ϕ TT. Baseline subtracted TT energies are indicated by numbers, and local maxima are required to be separated by at least 1 TT. Jet objects are defined as the E_T sum of the 4×4 TTs centered on the TTCL. Light gray regions in the diagrams indicate areas for which the object in question cannot be constructed because of boundary effects.

G.4 Hardware Overview

The algorithms described previously are implemented in several custom electronics boards designed for the new L1Cal. An overview of the main hardware elements of the Run IIb L1Cal system is given in Fig. G.2. Broadly, these elements are divided into three groups.

1. The *ADF System*, containing those elements that receive and digitize analog

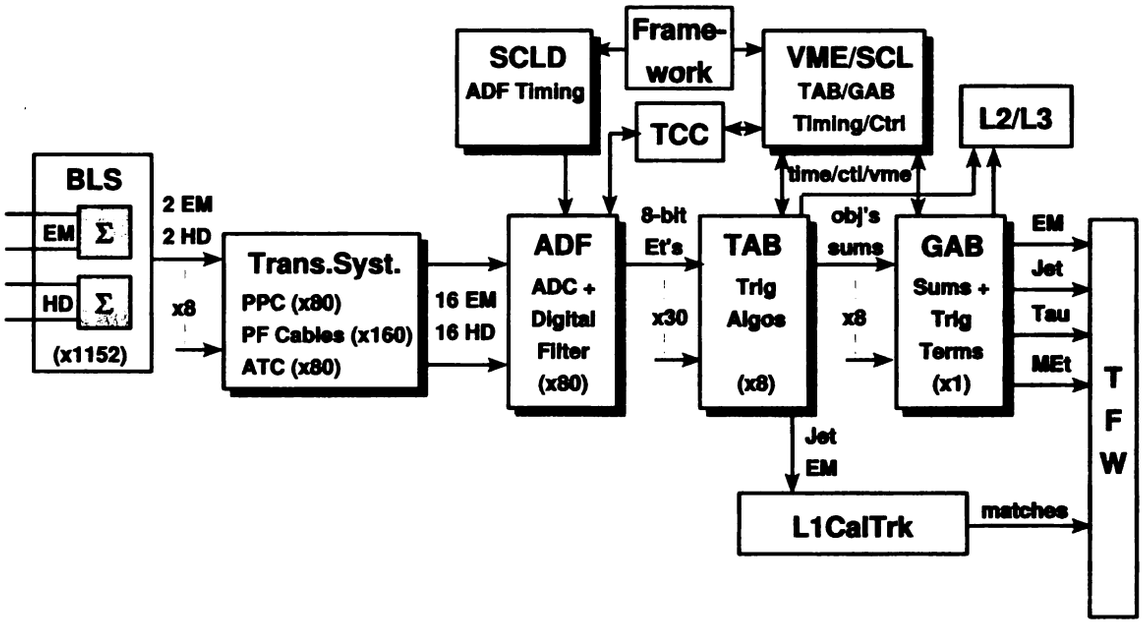

Figure G.2: A block diagram of the main hardware elements of the Run IIb L1Cal system and their interconnections.

TT signals from the BLS cards, and perform TT-based signal processing.

2. The *TAB/GAB System*, where algorithms are run on the digitized TT signals to produce trigger terms.

3. The *Readout System*, which inserts L1Cal information into the D0 data path for permanent storage.

The L1Cal also communicates with other elements of the D0 trigger and data acquisition (DAQ) system, including the following.

- The *Trigger Framework* (TFW), which delivers trigger decisions and synchronizes the entire D0 DAQ. From the L1Cal point of view, the TFW sends global timing and control signals (see Table G.1) to the system over *Serial Command Links* (SCL) and receives the L1Cal and/or terms.

- The L1Cal *Trigger Control Computer* (L1Cal TCC), which configures and mon-

itors the system.

- The *Level-1 Cal-Track Match* trigger system (L1CalTrk), another L1 trigger system that performs azimuthal matching between L1CTT tracks and L1Cal EM and Jet objects.

Within the L1Cal, the ADF system consists of the *Transition System*, the *Analog and Digital Filter* cards (ADF), and the *Serial Command Link Distributor* (SCLD). The Transition System, consisting of *Patch Panels*, *Patch Panel Cards* (PPC), *ADF Transition Cards* (ATC), and connecting cables, adapts the incoming BLS signal cables to the higher density required by the ADFs. These ADF cards, which reside in four 6U VME-64x crates [150], filter, digitize and process individual TT signals, forming the building blocks of all further algorithms. They receive timing and control signals from the SCL via a *Serial Command Link Distributor* card (SCLD).

Trigger algorithms are implemented in the L1Cal in two sets of cards: the *Trigger Algorithm Boards* (TAB) and the *Global Algorithm Board* (GAB), which are housed in a single 9U crate with a custom backplane. The TABs identify EM, Jet and Tau objects in specific regions of the calorimeter using the algorithms described in Section G.3 and also calculate partial global energy sums. The GAB uses these objects and energy sums to calculate and/or terms, which the TFW uses to make trigger decisions. Finally, the *VME/SCL card*, located in the L1Cal Control Crate, distributes timing and control signals to the TABs and GAB and provides a communication path for their readout.

The architecture of the L1Cal system and the number of custom elements required, summarized in Table G.2, is driven by the large amount of overlapping data required by the sliding windows algorithm. In total, more than 700 Gbits of data per second are transmitted within the system. Of this, each local maximum calculation requires 4.4 Gbits/s from 72 separate TTs. The most cost effective solution to this problem, which still results in acceptable trigger decision latency, is to deal with all data as serial

SCL	ADF	TAB/GAB	Description
INIT	—	yes	initialize the system
CLK7	yes	yes	132 ns Tevatron RF clock
TURN	yes	yes	marks the first crossing of an accelerator turn
REALBX	yes	—	flags clock periods containing real beam crossings
BX_NO	—	yes	counts the 159 bunch crossings in a turn
L1ACCEPT	yes	yes	indicates that an L1 Accept has been issued by the TFW
MONITOR	yes	—	initiates collection of ADF monitoring data
L1ERROR	—	yes	a TAB/GAB error condition transmitted to the SCL hub
L1BUSY	—	yes	asserted by the TABs/GAB until an observed error is cleared
—	ADF MON	—	allows TCC to freeze ADF circular buffers
—	ADF TRIG	—	allows TCC to fake a MONITOR signal on the next L1 Accept
—	—	TAB RUN	TAB/GAB data path synchronization signal
—	—	TAB TRIG	pulse to force writing to TAB/GAB diagnostic memories
—	—	TAB FRM	used for synchronization of TAB/GAB VME data under VME/SCL control
—	—	TAB ADDR	internal address for TAB/GAB VME read/write operations
—	—	TAB DATA	data for TAB/GAB VME read/write operations

Table G.1: Timing and control signals used in the L1Cal system. Included are D0 global timing and control signals (SCL) used by the ADFs and the TAB/GAB system, as well as intra-system communication and synchronization flags described later in the text.

Board	Input TT Region	Output TT Region	Total Number
PPC	4×4	4×4	80
ATC	4×4	4×4	80
ADF	4×4	4×4	80
SCLD	all	all	1
TAB	40×12	31×4	8
GAB	all	all	1
VME/SCL	all	all	1

Table G.2: A summary of the main custom electronics elements of the L1Cal system. For each board, the TT region (in $\eta \times \phi$) that the board receives as input and sends on as output is given as well as the total number of each board type required in the system.

bit-streams. Thus, all intra-system data transmission is done bit-serially using the Low Voltage Differential Signal (LVDS) protocol and nearly all algorithm arithmetic is performed bit-serially as well, at clock speeds such that all bits of a data word are examined in the 132 ns Tevatron bunch crossing interval. Examples of a bit-serial adder and comparator are shown in Fig. G.3. The only exception to this bit-serial arithmetic rule is in the calculation of Tau object isolation, which requires a true divide operation (see Section G.3) and thus introduces an extra 132 ns of latency to the trigger term calculation. Even with this extra latency, the L1Cal results arrive at the TFW well within the global L1 decision time budget.

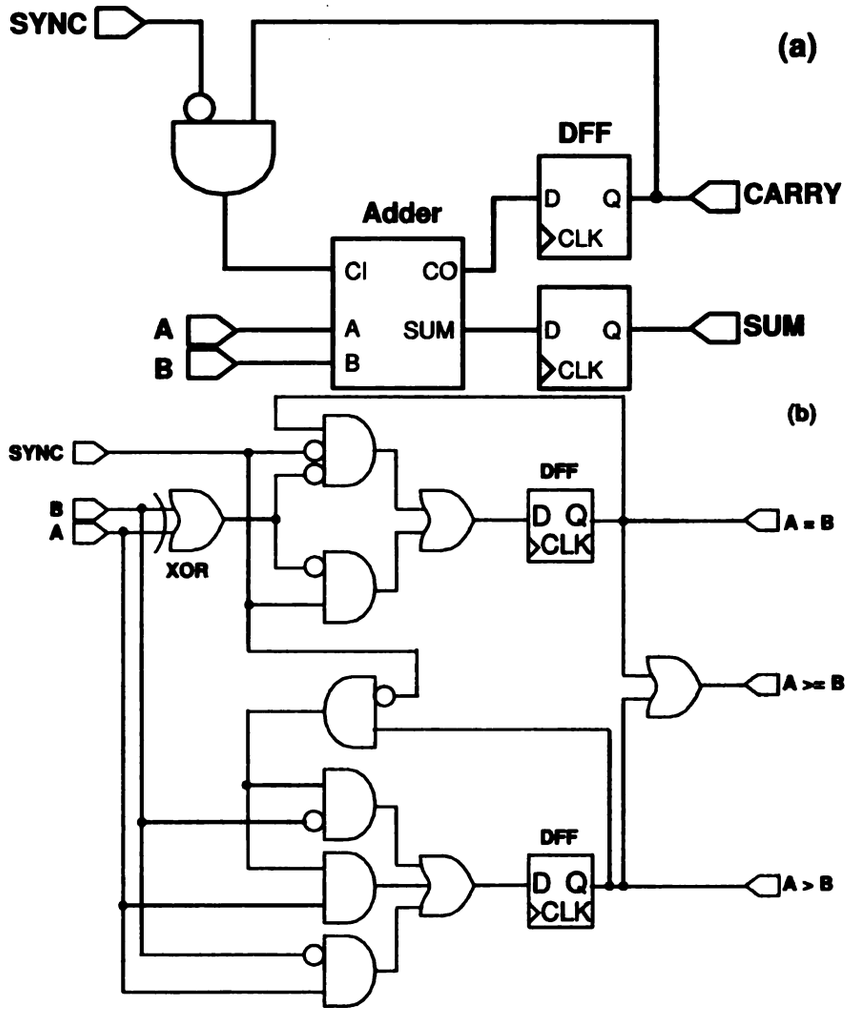

Figure G.3: Logic diagrams for a Bit-serial adder (a) and a bit-serial comparator (b).

G.5 The ADF System

G.5.1 Transition System

Trigger pick-off signals from the BLS cards of the EM and HD calorimeters are transmitted to the L1Cal trigger system, located in the Movable Counting House (MCH), through 40–50 m long coaxial ribbon cables. Four adjacent coaxial cables in a ribbon carry the differential signals from the EM and HD components of a single TT. Since there are 1280 BLS trigger cables distributed among ten racks of the original

L1Cal trigger electronics, the L1Cal upgrade was constrained to reuse these cables. However, because the ADF input signal density is much larger than that in the old system (only four crates are used to house the ADFs as opposed to 10 racks for the old system's electronics) the cables could not be plugged directly into the upgraded L1Cal trigger electronics; a transition system was needed.

The transition system is composed of passive electronics cards and cables that route signals from the BLS trigger cables to the backplane of the ADF crates (see Section G.5.2). It was designed to allow the trigger cables to remain within the same Run I/IIa rack locations. It consists of the following elements.

- Patch Panels and Patch Panel Cards (PPC): A PPC receives the input signals from 16 BLS trigger cables and transmits the output through a pair of Pleated Foil Cables. A PPC also contains four connectors which allow the monitoring of the signals. Eight PPCs are mounted two to a Patch Panel in each of the 10 racks originally used for Run I/IIa L1Cal electronics.

- Pleated Foil Cables: Three meter long Pleated Foil Shielded Cables (PFC), made by the 3M corporation [151], are used to transfer the analog TT output signals from the PPC to the ADF cards via the ADF Transition Card. There are two PFCs for each PPC for a total of 160 cables. The unbalanced characteristic impedance specification of the PFC is 72 Ω, which provides a good impedance match to the BLS trigger cables.

- ADF Transition Card (ATC): The ATCs are passive cards connected to the ADF crate backplane. These cards receive the analog TT signals from two PFCs and transmit them to the ADF card. There are 80 ATCs that correspond to the 80 ADF cards. Each ATC also transmits the three output LVDS cables of an ADF card to the TAB crate – a total of 240 LVDS cables.

G.5.2 ADF Cards

The *Analog and Digital Filter* cards (ADF) are responsible for sending the best estimate of the transverse energy (E_T) in the EM and HD sections of each of the 1280 TTs to the eight TAB cards for each Tevatron beam crossing. The calculation of these E_T values by the 80 ADF cards is based upon the 2560 analog trigger signals that the ADF cards receive from the BLS cards, and upon the timing and control signals that are distributed throughout the D0 data acquisition system by the Serial Command Links (SCL). The ADF cards themselves are 6U $\times$ 160 mm, 12-layer boards designed to connect to a VME64x backplane using P0, P1 and P2 connectors. The ADF system is set up and monitored, over VME, by a Trigger Control Computer (TCC), described in Section G.8.

G.5.3 Signal Processing in the ADFs

Each ADF card, as shown schematically in Fig. G.4, uses 32 analog trigger signals corresponding to the EM and HD components of a 4×4 array of Trigger Towers. Each differential, AC coupled analog trigger signal is received by a passive circuit that terminates and compensates for some of the characteristics of the long cable that brought the signal out of the collision hall. Following this passive circuit the active part of the analog receiver circuit rejects common mode noise on the differential trigger signal, provides filtering to select the frequency range of the signal caused by a real Tevatron energy deposit in the Calorimeter, and provides additional scaling and a level shift to match the subsequent ADC circuit.

The analog level shift in the trigger signal receiver circuit is controlled, separately for each of the 32 channels on an ADF card, by a 12 bit pedestal control DAC, which can swing the output of the ADC that follows it from slightly below zero to approximately the middle of its full range. This DAC is used both to set the pedestal of the signal coming out of the ADC that follows the receiver circuit and

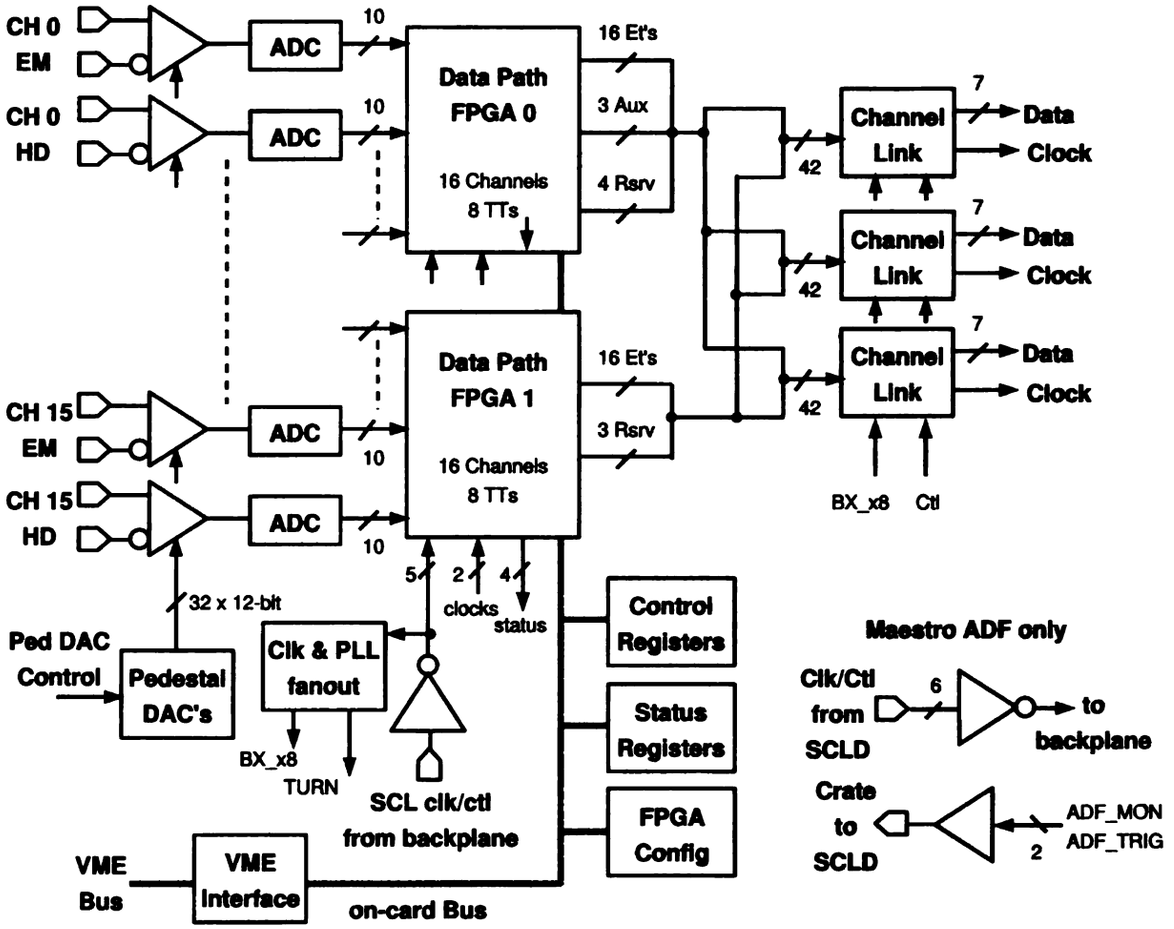

Figure G.4: ADF card block diagram.

as an independent way to test the full signal path on the ADF card. During normal operation, we set the pedestal at the ADC output to 50 counts which is a little less than 5% of its full scale range. This offset allows us to accommodate negative fluctuations in the response of the BLS circuit to a zero-energy signal.

The 10 bit sampling ADCs [152] that follow the receiver circuit make conversions every 33 ns – four times faster than the Tevatron BX period of 132 ns. This conversion rate is used to reduce the latency going through the pipeline ADCs and to provide the raw data necessary to associate the rather slow rise-time trigger signals (250 ns typical rise-time) with the correct Tevatron beam crossing. Although associating energy deposits in the Calorimeter with the correct beam crossing is not currently an

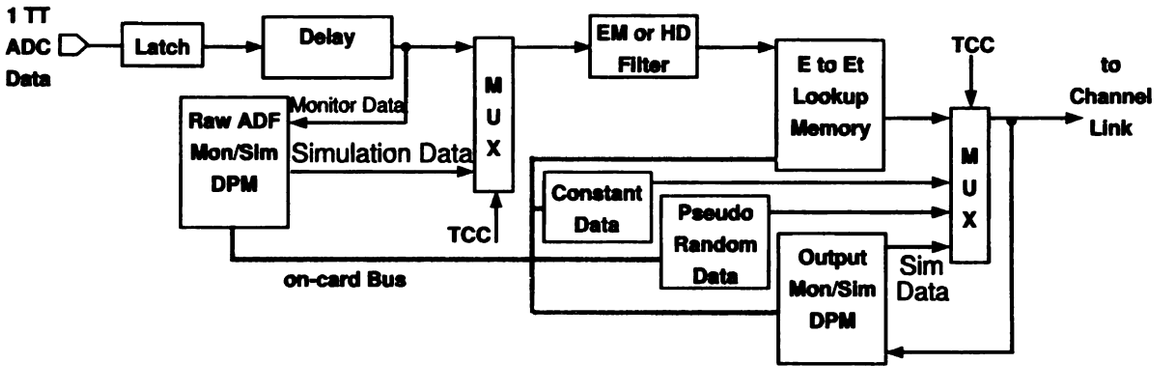

Figure G.5: Block diagram of signal processing for a single TT in the ADF.

issue since actual proton-antiproton collisions only occur every 396 ns, rather than every 132 ns as originally planned, the oversampling feature has been retained for the flexibility it provides in digital filtering.

On each ADF card the 10 bit outputs from the 32 ADCs flow into a pair of FPGAs [153], called the *Data Path FPGAs*, where the bulk of the signal processing takes place. This signal processing task, shown schematically in Fig. G.5, is split over two FPGAs with each FPGA handling all of the steps in the signal processing for 16 channels. Two FPGAs were used because it simplified the circuit board layout and provided an economical way to obtain the required number of I/O pins.

The first step in the signal processing is to align in time all of the 2560 trigger signals. The peak of the trigger signals from a given beam crossing arrive at the L1Cal at different times because of different cable lengths and different channel capacitances. These signals are made isochronous using variable length shift registers that can be set individually for each channel by the TCC. Once the trigger signals have been aligned in time, they are sent to both the Raw ADC Data Circular Buffers where monitoring data is recorded and to the input of the Digital Filter stage.

The Raw ADC Data Circular Buffers are typically set up to record all 636 of the ADC samples registered in a full turn of the accelerator. This writing operation can be stopped by a signal from the TCC, when an L1 Accept flagged with a special

Collect Status flag is received by the system on the SCL, or in a *self-trigger* mode where any TT above a programmable threshold causes writing of all Circular Buffers to stop. Once writing has stopped, all data in the buffers can be read out using the TCC, providing valuable monitoring information on the system's input signals. The Raw ADC Data Circular Buffers can also be loaded by the TCC with simulated data, which can be inserted into the ADF data path instead of real signals for testing purposes.

The Digital Filter in the signal processing path can be used to remove high frequency noise from the trigger signals and to remove low frequency shifts in the baseline. This filter is currently configured to select the ADC sample at the peak of each analog TT signal. This mode of operation allows the most direct comparison with data taken with the previous L1Cal and appears to be adequate for the physics goals of the experiment.

The 10 bit output from the Digital Filter stage has the same scale and offset as the output from the ADCs. It is used as an address to an *E to E_T Lookup Memory*, the output of which is an eight bit data word corresponding to the E_T seen in that TT. This E to E_T conversion is normally programmed such that one output count corresponds to 0.25 GeV of E_T and includes an eight count pedestal, corresponding to zero E_T from that TT.

The eight bit TT E_T is one of four sources of data that can be sent from the ADF to the TABs under control of a multiplexer (on a channel by channel and cycle by cycle basis). The other three multiplexer inputs are a fixed eight-bit value read from a programmable register, simulation data from the Output Data Circular Buffer, and data from a pseudo-random number generator.

The latter two of these sources are used for system testing purposes. During normal operation, the multiplexers are set up such that TT E_T data is sent to the TABs on those bunch crossing corresponding to real proton-antiproton collisions,

while the fixed pedestal value (eight counts) is sent on all other accelerator clock periods. If noise on a channel reaches a level where it significantly impacts the D0 trigger rate, then this channel can be disabled, until the problem can be resolved, by forcing it to send the fixed pedestal on all accelerator clock periods, regardless of whether they contain a real crossing or not. Typically, less than 10 (of 2560) TTs are excluded in this manner at any time.

Data is sent from the ADF system to the TAB cards using a National Semiconductor Channel Link chip set with LVDS signal levels between the transmitter and receiver [154]. Each Channel Link output from an ADF card carries the E_T data for all 32 channels serviced by that card. A new frame of E_T data is sent every 132 ns. All 80 ADF cards begin sending their frame of data for a given Tevatron beam crossing at the same point in time. Each ADF card sends out three identical copies of its data to three separate TABS, accommodating the data sharing requirements of the sliding windows algorithm.

G.5.4 Timing and Control in the ADF System

The ADF system receives timing and control signals listed in Table G.1 over one of the Serial Command Links [141]. Distribution of these signals from the SCL to the 80 ADF cards is accomplished by the *SCL Distributor* (SCLD) card. The SCLD card receives a copy of the SCL information using a D0-standard SCL Receiver mezzanine card and fans out the signals mentioned in Table G.1 to the four VME-64x crates that hold the 80 ADF cards using LVDS level signals. In addition, each ADF crate sends two LVDS level signals (`ADF_MON` and `ADF_TRIG`) back to the SCLD card, allowing TCC to cause synchronous readout of the ADFs.

Within an ADF crate, the ADF card at the mid-point of the backplane (referred to as the *Maestro*) receives the SCLD signals and places them onto spare, bused VME-64x backplane lines at TTL open collector signal levels. All 20 of the ADF

cards in a crate pick up their timing and control signals from these backplane lines. To ensure a clean clock, the CLK7 signal is sent differentially across the backplane and is used as the reference for a PLL on the ADFs. This PLL provides the jitter-free clock signal needed for LVDS data transmission to the TABs and for ADC sampling timing.

G.5.5 Configuring and Programming the ADF System

The ADF cards are controlled over a VME bus using a VME-slave interface implemented in a PAL that is automatically configured at power-up. Once the VME interface is running, the TCC simultaneously loads identical logic files into the two data path FPGAs on each card. Since each data path FPGA uses slightly different logic (*e.g.*, the output check sum generation), the FPGA *flavor* is chosen by a single ID pin. After TCC has configured all of the data path FPGAs, it then programs all control-status registers and memory blocks in the ADFs. Information that is held on the ADF cards that is critical to their Physics triggering operation is protected by making those programmable features "read only" during normal operation. TCC must explicitly unlock the write access to these features to change their control values. In this way no single failed or mis-addressed VME cycle can overwrite these critical data.

G.6 ADF to TAB Data Transfer

Digitized TT data from each ADF's 4×4, $\eta \times \phi$ region are sent to the TABs for further processing, as shown in Fig. G.6. To accommodate the high density of input on the TABs, the 8-bit serial trigger-tower data are transmitted using the channel-link LVDS chipset [154], which serializes 48 CMOS/TTL inputs and the transmission clock onto seven LVDS channels plus a clock channel. In the L1Cal system, the input to the

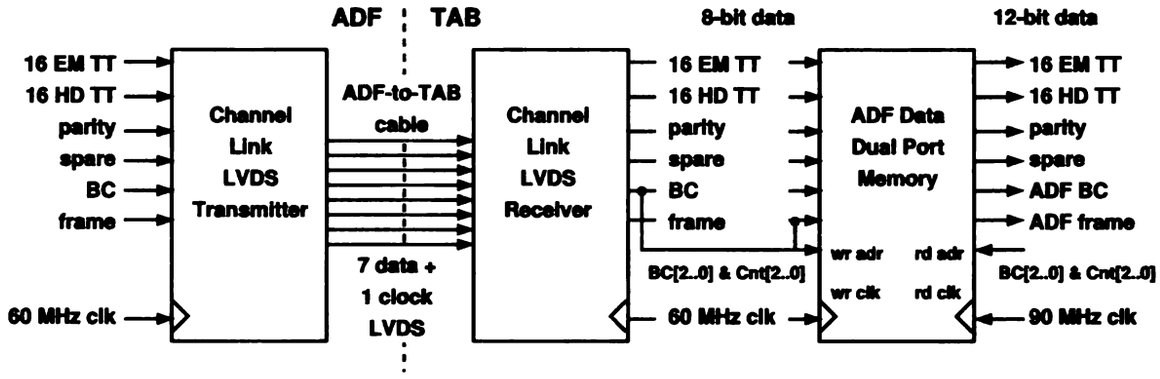

Figure G.6: ADF to TAB data transmission, reception and the dual-port-memory transition from 8-bit to 12-bit data.

transmitter is 60 MHz TTL (eight times the bunch crossing rate), which is stepped up to 420 MHz for LVDS transmission.

Each ADF sends three identical copies of 36 8-bit words to three different TABs on each bunch crossing. This data transmission uses eight LVDS channels - seven data channels containing six serialized data words each, and one clock - on Gore cables with 2mm HM connectors [155]. The 36 data words consist of the digitized E_T of 16 EM and 16 HD TTs and four control words. The bunch crossing number control word indicates which accelerator crossing produced the ADF data being transmitted, and is used throughout the system for synchronization. The frame-bit control word is used to help align the least significant bits of the other data words. The parity control word is the logical XOR of every other word and is used to check the integrity of the data transmission. Finally, one control word is reserved for future use.

While the ADF logic is 8-bit serial (60 MHz) the TAB logic is 12-bit serial (90 MHz). To cross the clock domains, the data passes through a dual-port memory with the upper four bits padded with zeros. The additional bit space is required to accommodate the sliding windows algorithm sums.

The dual port memory write address is calculated from the frame and bunch crossing words of the ADF data. The least significant address bits are a data word

bit count, which is reset by the frame signal, while the most significant address bits are the first three-bits of the bunch crossing number. This means that the memory is large enough to contain eight events of eight-bit serial data.

By calculating the read address in the same fashion, but from the TAB frame and bunch crossing words, the dual-port memory crosses 60 MHz/90 MHz clock domains, maintains the correct phase of the data, and synchronizes the data to within eight crossings all at the same time. This means the TAB timing can range between a minimal latency setting where the data is retrieved just after it is written and a maximal latency setting where the data is retrieved just before it is overwritten. If the TAB timing is outside this range, the data from eight previous or following crossings will be retrieved.

Although off-the-shelf components were used within their specifications, operating 240 such links reliably was found to be challenging. Several techniques were employed to stabilize the data transmission. Different cable lengths (between 2.5 and 5.0 m) wer used to match the different distances between ADF crates and the TAB/GAB crate. The DC-balance and pre-emphasis features of the channel-link chipset [154] were also used, but deskewing, which was found to be unreliable, was not.

G.7 The TAB/GAB System

G.7.1 Trigger Algorithm Board

The Trigger Algorithm Boards (TABs) find EM, Jet and Tau candidates using the sliding windows algorithm and perform preliminary sums for total and missing E_T calculations. Each TAB is a double-wide 9U $\times$ 400 mm, 12-layer card designed for a custom backplane. The main functional elements of the TAB are shown in Fig. G.7.

In the TAB's main trigger data path, LVDS cables from 30 ADFs are received at the back of the card using feedthrough connectors on the backplane. The data from

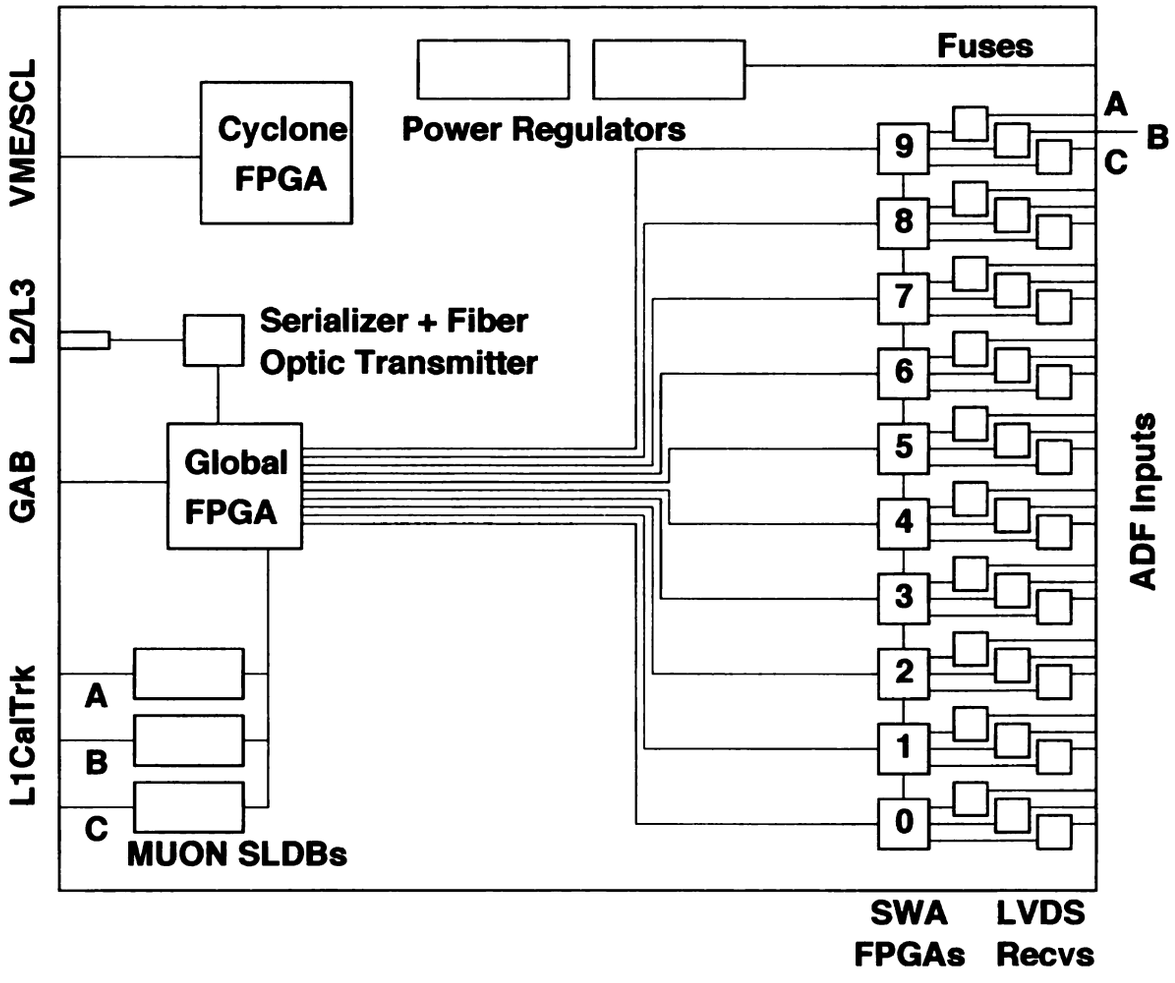

Figure G.7: Block diagram of the TAB.

these cables are extracted using Channel Link receivers[154] and sent, as individual bit-streams for each TT, to ten TAB sliding windows algorithm (SWA) FPGAs [156] for processing. These chips also pass some of their data to their nearest neighbors to accommodate the data sharing requirements of the sliding windows algorithms. The algorithm output from each SWA is sent to a single TAB global FPGA [156]. The global FPGA calculates regional sums and sends the results out the front of the board to the GAB, over the same type of cables used for ADF to TAB data transmission (see Section G.6) using embedded LVDS functionality in the FPGA. This data transmission occurs at a clock rate of 636 MHz.

The global FPGA also sends three copies of Jet and EM object information for each bunch crossing to the L1CalTrk system for processing using Gbit/s serial link transmitter daughter cards (MUON SLDB) [141]. Upon receiving an L1 accept from the D0 TFW, the TAB global chip also sends data out on a serial fiber-optic link [157] for use by the L2 trigger and for inclusion in the D0 event data written to permanent storage on an L3 accept.

Low-level board services are provided by the TAB Cyclone chip [158], which is configured by an on-board serial configuration device [159] on TAB power-up. These services include providing the path for power-up and configuration of the other FPGAs on the board, under the direction of the VME/SCL card; communicating with VME and the D0 SCL over the specialized VME/SCL serial link; and fanning out the 132 ns detector clock using an on-board clock distribution device [160].

G.7.2 Global Algorithm Board

The global algorithm board (GAB) receives data containing regional counts of Jet, EM, and Tau physics objects calculated by the TABs and produces a menu of and/or terms, which is sent to the D0 trigger framework. Like the TAB, the GAB is a double-wide 9U $\times$ 400 mm, 12-layer circuit board designed for a custom backplane. Its main functional elements are shown in Fig. G.8.

LVDS receivers, embedded in four Altera Stratix FPGAs (LVDS FPGAs) [156] each receive the output of two TABs, synchronizing the data to the GAB 90 MHz clock using a dual-port memory. The synchronized TAB data from all four LVDS FPGAs is sent to a single GAB S30 FPGA [156], which calculates and/or terms, and sends them to the trigger framework through TTL-to-ECL converters [161]. There are five 16-bit outputs on the GAB, although only four are used by the framework.

Much like the TABs, upon receiving an L1 accept, the GAB S30 sends data to L2 and L3 on a serialized fiber-optic link [157]. Also as on the TABs, a Cyclone FPGA

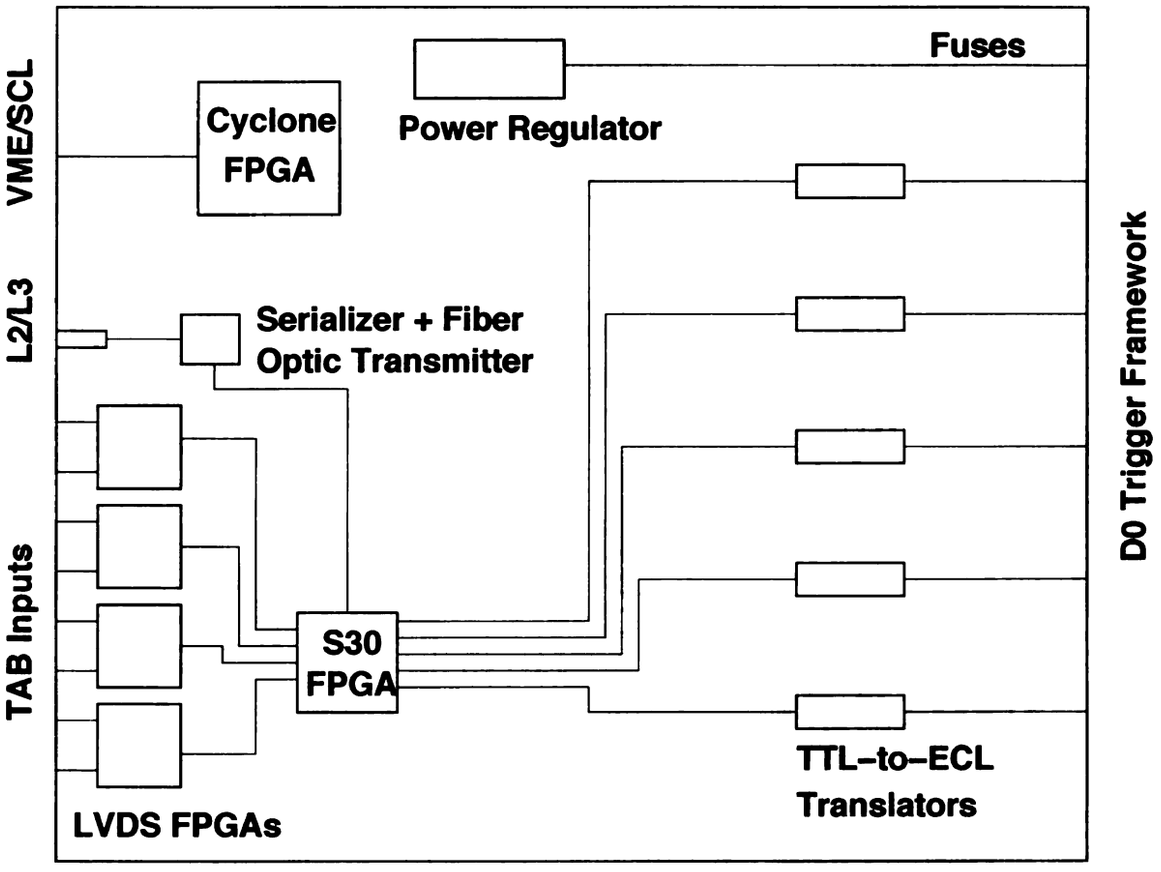

Figure G.8: Block diagram of the GAB.

[158] provides low-level board services.

G.8 Online Control

Most components of the D0 trigger and data acquisition system are programmable. The Online System allows this large set of resources and parameters to be configured to support diverse operational modes – broadly speaking, those used during proton-antiproton collisions in the Tevatron (*physics modes*) and those used in the absence of colliding beams (*calibration/testing modes*), forming a large set of resources and parameters needing to be configured before collecting data.

The L1Cal fits seamlessly into this Online System, with its online control software

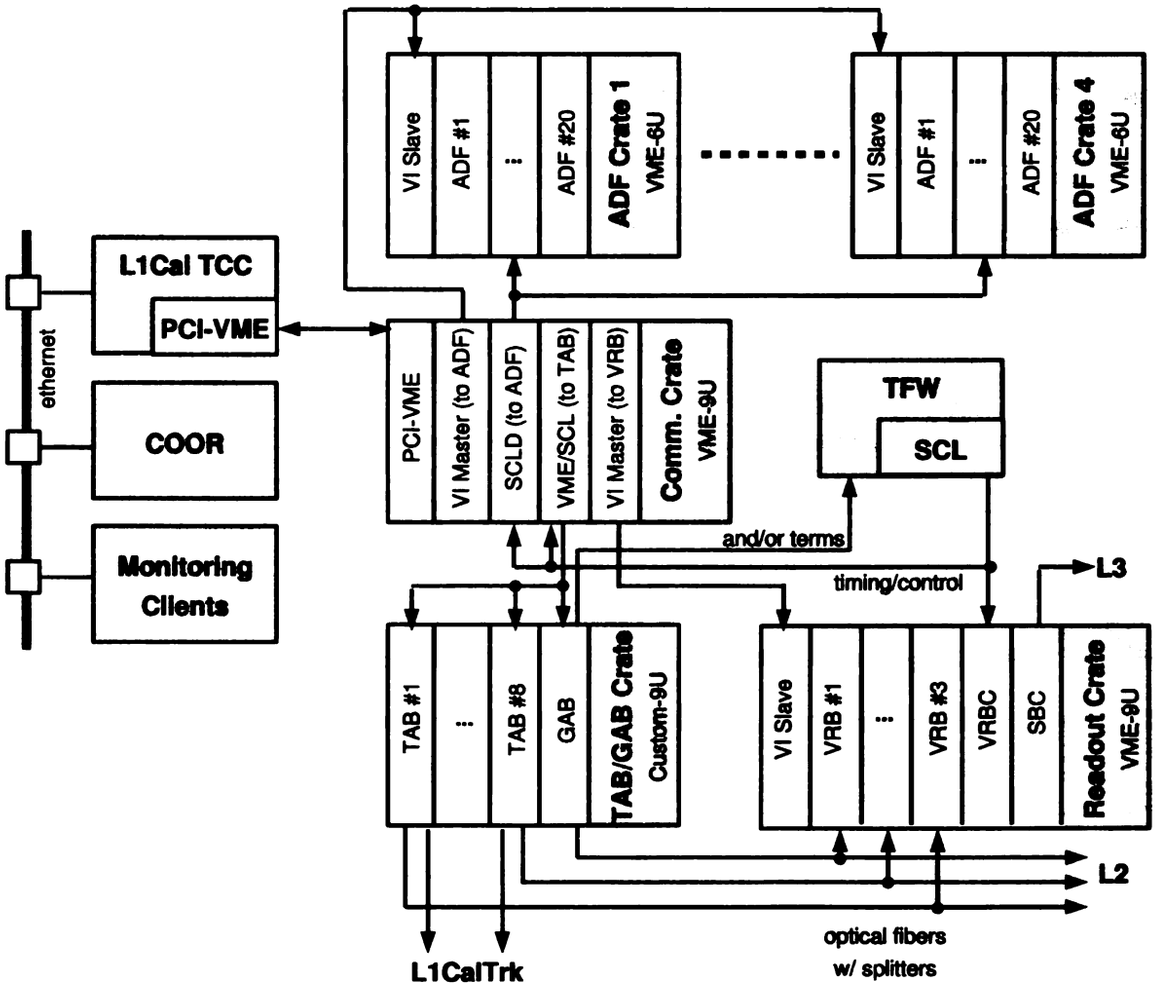

Figure G.9: Communications in the L1Cal system.

hiding the complexity of the underlying hardware, while making the run time programming of the L1Cal Trigger accessible to all D0 users in simple and logical terms. A diagram of the L1Cal, from an online data and control point of view, is shown in Fig. G.9. The main elements of L1Cal online control are listed below, with those aspects specific to L1Cal described in more detail in the following sections. For more information on D0-wide components see [141].

- The Trigger Framework (TFW) delivers global D0 timing and control signals to the L1Cal and collects and/or terms from the GAB as described in Section

G.4.

- COOR [141], a central D0 application, coordinates all trigger configuration and programming requests. Global trigger lists, containing requirements and parameters for all triggers used by the experiment, are specified using this application as are more specific trigger configurations (several of which may operate simultaneously) used for calibration and testing.

- The L1Cal Trigger Control Computer (TCC), a PC running the Linux operating system, provides a high level interface between COOR and the L1Cal hardware and allows independent expert control of the system.

- The Communication Crate contains cards that provide an interface between the L1Cal custom hardware in the ADF and TAB/GAB crates, and the L1Cal TCC and SCL.

- The L1Cal Readout Crate allows transmission of L1Cal data to the L3 trigger system.

- Monitoring Clients, consisting of software that may run on a number of local or remote computers, display information useful for tracking L1Cal operational status.

G.9 Managing Monitoring Information

The monitoring resources available in the ADF, TAB and GAB cards are described in Sections G.5.3.This information is collected by the TCC Control Software and is made available to Monitoring Clients via the Monitoring Interface. During normal operation, monitoring data are collected approximately every five seconds when the *Collect Status* qualifier is asserted on the SCL along with `L1ACCEPT`. If data flow has

stopped, monitoring data are still collected from the L1Cal, initiated by the TCS, which times out after six seconds of inactivity.

Monitored data include the following.

- The ADF output E_T of all TTs for all 36 active bunch crossings of the accelerator turn containing the **L1ACCEPT** for which the *Collect Status* signal is asserted.

- The bunch crossing number within this turn that identifies the **L1ACCEPT**.

- The contents of all error and status registers in the TABs and GAB (associated with each SWA and Global chip on the TABs and with the LVDS and S30 chips on the GAB). These registers indicate, among other information, synchronization errors on data transfer links, parity errors on each transfer, and bunch crossing number mismatches at various points in the TAB/GAB signal processing chain.

Monitoring information is displayed in the D0 control room and remotely using Monitoring Client GUIs. This application, written in Python [168] with Tkinter [169], requests and receives data from the TCS via calls to ITC. It displays average pedestal values and RMSs for each TT, to aid in the identification of noisy or dead channels, as well as system status information.

Another tool for monitoring data quality in the control room is a suite of Root-based [172] software packages called *Examine*. The L1Cal Examine package receives a stream of data from L3 and displays histograms of various quantities related to L1Cal performance, including comparisons between L1Cal and calorimeter precision readout estimates of TT energies. Data distributions can be compared directly to reference curves provided on the plots, which can be obtained either from an earlier sample of data or from simulation.

G.10 Calibration of the L1Cal

Several methods are employed to ensure that the E_T of individual trigger towers, used in the system, is correctly calibrated – *i.e.*, that one output count corresponds to 0.25 GeV of E_T and that the zero-E_T baseline is set to eight counts.

G.10.1 Online Pedestal Adjustment and Noise

The most frequently used of these procedures is a tool, run as part of the TCS, which samples ADC-level data from the ADFs when no true energy is expected to be deposited in the calorimeter. Based on this data, corrections to the DAC values used to set each channel's zero-energy baseline are calculated and can be downloaded to the system.

This online pedestal adjustment is performed every few days because of periodic pedestal shifts that occur in a small number of channels – typically less than ten. These pedestal shifts arise because of synchronous noise, with a period of 132 ns, observed in the system due largely to pickup from the readout of other, nearby detector systems. Although the amplitude of this noise varies from channel to channel (it is largest in only a handful of TTs), its phase is stable over periods of several stores of particle beams in the Tevatron, which sets the timescale for pedestal readjustment.

G.10.2 Calorimeter Pulser

The calorimeter pulser system [141], which injects carefully calibrated charge pulses onto the calorimeter preamps, is also used by the L1Cal to aid in the identification of dead and noisy channels. Special software compares E_T values observed in the ADFs with expectations based on the pattern of preamps pulsed and the pulse amplitudes used. Results are displayed graphically to allow easy identification of problematic channels. In addition to its utility in flagging bad channels, this system also provides

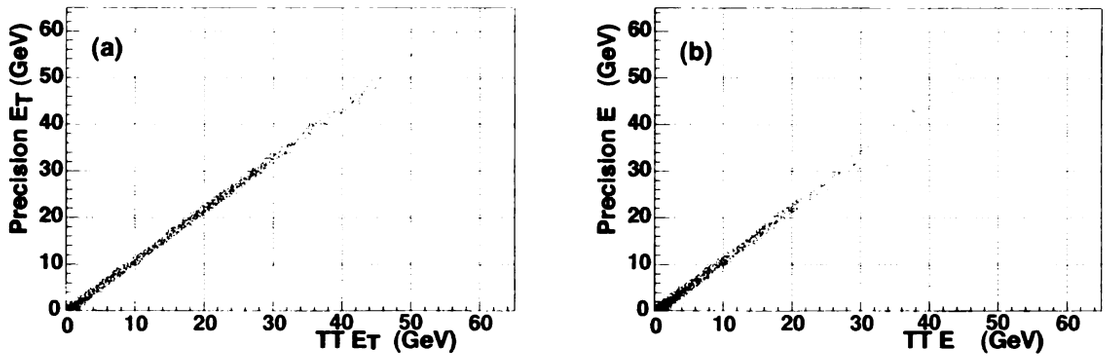

Figure G.10: Precision versus TT E_T for one EM (a) and one HD (b) trigger tower. The linear relationship with slope=1 indicates the good calibration of the tower. The excursion away from an absolute correlation is an indication of the inherent noise of the system.

a quick way to check that the L1Cal signal path is properly cabled.

G.10.3 Offline Gain Calibration

The desired TT response of the L1Cal, 0.25 GeV per output count, is determined by comparing offline TT E_T's to the corresponding sums of precision readout channels in the calorimeter, which have already been calibrated against physics signals. For this purpose, data taken during normal physics running of the detector are used. An example can be seen in Fig. G.10. Gain calibration constants, for use in the ADF E_T Lookup Memories, are derived from the means of distributions of the ratio of TT to precision readout channel sums for each EM and HD TT.

Gain coefficients derived in this way have been determined to be stable to within ~2% over periods of months. Thus, this type of calibration is normally performed only after extended Tevatron shutdown periods.

Bibliography

[1] C. Amsler et al. Review of particle physics. *Phys. Lett.*, B667:1, 2008.

[2] Particle Data Group, 2008. http://pdg.lbl.gov/.

[3] Andreas Hocker, H. Lacker, S. Laplace, and F. Le Diberder. A New approach to a global fit of the CKM matrix. *Eur. Phys. J.*, C21:225-259, 2001.

[4] C. D. Froggatt and H. B. Nielsen. Trying to understand the standard model parameters. *Surveys High Energ. Phys.*, 18, 2003.

[5] D. L. Bennett and H. B. Nielsen. Gauge couplings calculated from multiple point criticality yield $\alpha^{-1} = 137 \pm 9$: At last, the elusive case of U(1). *Int. J. Mod. Phys.*, A14:3313-3385, 1999.

[6] Q.H. Cao, R. Schwienhorst, J.A. Benitez, R. Brock, and C.P. Yuan. Next-to-leading order corrections to single top quark production and decay at the tevatron: 2: t-channel process. *Phys. Rev. D*, **72**:094027, 2005.

[7] Q.H. Cao, R. Schwienhorst, and C.P. Yuan. Next-to-leading order corrections to single top quark production and decay at the tevatron: 1: s-channel process. *Phys. Rev. D*, **71**:054023, 2005.

[8] Wikipedia. Standard model — wikipedia, the free encyclopedia, 2009. [Online; accessed 8-July-2009].

[9] Wikimedia Commons. Mecanismo de higgs, 2009. http://commons.wikimedia.org/wiki/File:Mecanismo_de_Higgs_PH.png.

[10] V. D. Barger and R. J. N. Phillips. *Collider Physics (Frontiers in Physics)*. Addison Wesley Publishing Company, 1987.

[11] A. Heinson, 2008. http://www-d0.fnal.gov/~heinson/.

[12] T .Tait and C.-P. Yuan. Single top quark production as a window to physics beyond the standard model. *Phys. Rev.*, D63:014018, 2001.

[13] Fermilab National Accelerator Laboratory, 2008. http://www.fnal.gov.

[14] Accelerator Concepts Rookie Books, 2009. http://www-bdnew.fnal.gov/operations/rookie_books/rbooks.html.

[15] V.M. Abazov et al. The upgraded DØ detector. *Nucl. Instr. and Meth. A*, **565**:463, 2006.

[16] Beam division Fermilab National Accelerator Laboratory, 2008. http://www-bd.fnal.gov.

[17] G. Borissov. Ordering a chaos or .. technical details of aa tracking All DØ Meeting. 2003. http://www-d0.fnal.gov/atwork/adm/d0_private/2003-02-28/adm_talk.ps.

[18] G. Blazey et. al. Run ii jet physics. *DØ Note*, **3750**, 2000.

[19] The Single Top Working Group. Single top quark production in 2.3 fb^{-1} of data — signal and background modeling and event selection. *DØ Note*, **5810**, 2009.

[20] P. Calfayan et al. Muon identification certification for p17 data. *DØ Note*, **5157**, 2006.

[21] S. Cho et al. Muon identification certification for p20 data. *DØ Note*, **5824**, 2008.

[22] J. Hays et al. Single electron efficiencies in p17 data and monte-carlo using p18.05.00 d0correct. *DØ Note*, **5105**, 2006.

[23] J. Atramentov et al. Electron and photon identification with p20 data. *DØ Note*, **5761**, 2008.

[24] A. Schwartzman and C. Tully. Primary vertex reconstruction by means of adaptive vertex fitting. *DØ Note*, **4918**, 2005.

[25] V. M. Abazov et al. Multivariate searches for single top quark production with the DØ detector. *PRD*, **75**:092007, 2007.

[26] Makoto Kobayashi and Toshihide Maskawa. CP Violation in the Renormalizable Theory of Weak Interaction. *Prog. Theor. Phys.*, 49:652–657, 1973.

[27] V. M. Abazov et al. Observation of Single Top Quark Production. *arXiv:0903.0850*, 2009.

[28] T. Aaltonen et al. First Observation of Electroweak Single Top Quark Production. *arXiv:0903.0885*, 2009.

[29] D. Kau. *Evidence for Single Top Quark Production Using Bayesian Neural Networks.* PhD thesis, Florida State University, 2007.

[30] J. Mitrevski. *Measurement of Single Top Quark Production at DØ Using a Matrix Element Method.* PhD thesis, Columbia University, 2007.

[31] T. Gadfort. *Measuring Single-Top Production at DØ.* PhD thesis, University of Washington, 2007.

[32] P. Perea. *Search for t-Channel Single Top Quark Production in ppbar Collisions at 1.96 TeV.* PhD thesis, University of California, Riverside, 2006.

[33] S. Jabeen. *Search for Single Top Quarks Produced in the s-Channel via Electroweak Interactions at sqrt(s) = 1.96 TeV at the Tevatron.* PhD thesis, University of Kansas, 2006.

[34] Benoit Clement. *Production Electrofaible du Quark Top au Run II de l'Experience DØ.* PhD thesis, IReS de Strasbourg, 2006.

[35] M. Angelou. *Recherche de la Production Electrofaible du Quark Top dans l'Experience DØ.* PhD thesis, DAPNIA/SPP Saclay, 2005.

[36] E. Busato. *Recherche de la Production Electrofaible du Quark Top dans le Canal Electron+Jets dans l'Experience DØ aupres du Tevatron.* PhD thesis, Université Paris VI, 2005.

[37] D. Gillberg. *Single Top Discovery.* PhD thesis, Simon Fraser University, 2009.

[38] M. Pangilinan. *in preparation.* PhD thesis, Brown University, 2009.

[39] A. Tanasijczuk. *in preparation.* PhD thesis, Universidad de Buenos Aires, 2009.

[40] S. F. Novaes. Standard model: An Introduction. *hep-ph/0001283*, 1999.

[41] D. Griffiths. *Introduction to elementary particles.* Weinheim, USA: Wiley-VCH, 1987.

[42] M. Kaku. *Quantum Field Theory, a modern introduction.* Oxford University Press, 1993.

[43] E. Brubaker et. al. Combination of CDF and D0 results on the mass of the top quark. *hep-ex/0603039*, 2006.

[44] S. Abachi et al. Observation of the top quark. *Phys. Rev. Lett.*, **74**:2632, 1995.

[45] F. Abe et al. Observation of top quark production in $p\bar{p}$ collisions. *Phys. Rev. Lett.*, **74**:2626, 1995.

[46] C.-P. Yuan. A New Method to Detect a Heavy Top Quark at the Tevatron. *Phys. Rev.*, D41:42, 1990.

[47] S. Willenbrock and D. Dicus. Production of Heavy Quarks from W Gluon Fusion. *Phys. Rev.*, D34:155, 1986.

[48] The Single Top Working Group. First direct measurement of $|V_{tb}|$. *DØ Note*, **5440**, 2007.

[49] A. Abulencia et al. Measurement of the t anti-t production cross section in p anti-p collisions at $\sqrt{s}$ = 1.96-tev. *Phys. Rev. Lett.*, **97**:082004, 2006.

[50] A. Abulencia et al. Measurement of the $t\bar{t}$ production cross section in $p\bar{p}$ collisions at $\sqrt{s} = 1.96$-tev in the all hadronic decay mode. *Phys. Rev. D*, **74**:072005, 2006.

[51] A. Abulencia et al. Measurement of the t anti-t production cross section in p anti-p collisions at s**(1/2) = 1.96-tev using missing e(t) + jets events with secondary vertex b-tagging. *Phys. Rev. Lett.*, **96**:202002, 2006.

[52] A. Quandt. Top quark physics at hadron colliders. *The European Journal*, C48:835, 2006.

[53] Nikolaos Kidonakis. Single top production at the Tevatron: Threshold resummation and finite-order soft gluon corrections. *Phys. Rev.*, D74:114012, 2006.

[54] Abazov et. al. Measurement of B($t \rightarrow$ Wb) /B($t \rightarrow$ Wq) at $\sqrt{s}$ = 1.96-TeV. *Phys. Lett.*, B639:616–622, 2006.

[55] Acosta et. al. Measurement of $B(t \rightarrow Wb)/B(t \rightarrow Wq)$ at the Collider Detector at Fermilab. *Phys. Rev. Lett.*, 95:102002, 2005.

[56] V.M. Abazov et al. Evidence for single top quarks and first direct measurement of $|v_{tb}|$. *Phys. Rev. Lett.*, **98**:181802, 2007.

[57] The Single Top Working Group. Measurement of $|v_t b|$ using the single top quark observation analyses from 2.3 fb^{-1} of data. *DØ Note*, **5816**, 2009.

[58] A. Heinson, A. S. Belyaev, and E. E. Boos. Single top quarks at the Fermilab Tevatron. *Phys. Rev.*, D56:3114–3128, 1997.

[59] G. Mahlon and S.J.Parke. Improved spin basis for angular correlation studies in single top quark production at the Tevatron. *Phys. Rev.*, D55:7249–7254, 1997.

[60] E. E. Boos and A. V. Sherstnev. Spin effects in processes of single top quark production at hadron colliders. *Phys. Lett.*, B534:97–105, 2002.

[61] Q.H. Cao and C.P. Yuan. Single top quark production and decay at next-to-leading order in hadron collision. *Phys. Rev. D*, **71**:054022, 2005.

[62] H.-J. He, T. Tait, and C.-P. Yuan. New topflavor models with seesaw mechanism. *Phys. Rev.*, D62:011702, 2000.

[63] S. Ellis M. Bowen and M. Strassler. In search of lonely top quarks at the tevatron. *Phys. Rev. D*, **72**:074016, 2005.

[64] S. Ellis M. Bowen and M. Strassler. In search of lonely top quarks at the tevatron. *ACTA PHYS.POLON.B*, 36:271, 2005.

[65] (Ed.) F.T. Cole, (Ed.) E.L. Goldwasser, and (Ed.) R.R. Wilson. National Accelerator Laboratory design report January 1968. 1968. FERMILAB-DESIGN-1968-01.

[66] Pushpalatha C. Bhat and William J. Spalding. Fermilab collider Run II: Accelerator status and upgrades. *AIP Conf. Proc.*, 753:30–41, 2005.

[67] TeVI Group. Design Report Tevatron 1 project. 1984. FERMILAB-DESIGN-1984-01.

[68] S. Abachi et al. The DØ detector. *Nucl. Instr. and Meth. A*, **338**:185, 1994.

[69] T. L. Edwards et al. Determination of the effective inelastic $p\bar{p}$ cross-section for the DØ Run II luminosity measurement. 2004. FERMILAB-TM-2278-E.

[70] Fermilab National Accelerator Laboratory. DØ algorithms group. how to run reco, 2008. http://www-d0.fnal.gov/computing/algorithms/howto/howtoreco.html.

[71] A. Khanov. Htf: Histogramming method for finding tracks, the algorithm description. *DØ Note*, **3778**, 2000.

[72] A. Schwartzman and M. Narain. Probabilistic primary vertex selection. *DØ Note*, **4042**, 2002.

[73] J. Kozminski et al. Electron likelihood in p14. *DØ Note*, **4449**, 2004.

[74] A. Kumar, B. Choudhary, J. Kozminski, R. Kehoe, J. Hays, and J. Stark. Electron likelihood study. *DØ Note*, **4769**, 2005.

[75] Muon ID and Algorithms group web page, 2008. http://www-d0.fnal.gov/computing/algorithms/muon/muon_algo.html.

[76] O. Peters. Muon segment reconstruction - linked list algorithm. Technical report, Fermilab, 2001.

[77] J.-R. Vlimant et. al. Technical description of the t42 algorithm for calorimeter noise suppression. *DØ Note*, **4146**, 2003.

[78] A. Harel. Jet id optimization. *DØ Note*, **4919**, 2006.

[79] A. Harel and J. Kvita. p20 jetid efficiencies and scale factors. *DØ Note*, **5634**, 2008.

[80] Preliminary p17 jes for data and mc (jetcorr v07-01-02), 2004. http://www-d0.fnal.gov/phys_id/jes/d0_private/certified/certified_jes.html.

[81] L. Swayer et. al. Missing et reconstruction. *DØ Note*, **3957**, 2003.

[82] S. Trincaz-Duvoid and P. Verdier. Missing et reconstruction in p17. *DØ Note*, **4474**, 2004.

[83] M. Anastasoaie, S. Robinson, and T. Scanlon. Performance of the nn b-tagging tool on p17 data. *DØ Note*, **5213**, 2006.

[84] M. Abolins et. al. Design and implementation of the new d0 level-1 calorimeter trigger. *Nucl. Instr. and Meth. A*, 584:75, 2008.

[85] DØ Common Samples Group webpage for p17 (RunIIa) data, 2008. http://www-d0.fnal.gov/Run2Physics/cs/skimming/fixPass2p170903.html.

[86] DØ Common Samples Group webpage for p20 (RunIIb) data, 2008. http://www-d0.fnal.gov/Run2Physics/cs/skimming/p20_pass2.html.

[87] B. Casey et. al. Determination of the run iib luminosity constants. *DØ Note*, **5559**, 2007.

[88] E. Boos, V. Bunichev, L. Dudko, V. Savrin, and V. Sherstnev. Method for simulating electroweak top-quark production events in the nlo approximation: Singletop event generator. *Physics of Atomic Nuclei*, **69**(8):1317, 2006.

[89] Comparison of t-channel $2 \rightarrow 3$ production at NLO with CompHEP samples. R. schwienhorst et. al.

[90] The Single Top Working Group. Observation of single top quark production in 2.3 $\mathrm{fb}^{-}1$ of data using boosted decision trees. *DØ Note*, **5811**, 2009.

[91] J. Pumplin et. al. New generation of parton distributions with uncertainties from global QCD analysis. *J. High Energy Physics*, **07**:012, 2002.

[92] T. Sjostrand, S. Mrenna, and P. Skands. PYTHIA 6.4 Physics and Manual. *J. High Energy Physics*, **05**:026, 2006.

[93] S. Jadach, Z. Was, R. Decker, and J.H. Kuhn. The tau decay library TAUOLA: Version 2.4. *Comput. Phys. Commun.*, **76**:361–380, 1993.

[94] D.J. Lange. The EvtGen particle decay simulation package. *Nucl. Instrum. Meth.*, **A462**:152–155, 2001.

[95] M. Mangano, M. Moretti, F. Piccinini, R. Pittau, and A.D. Polosa. ALPGEN, a generator for hard multiparton processes in hadronic collisions. *J. High Energy Physics*, **07**:001, 2003.

[96] S. Hoche et. al. Matching parton showers and matrix elements. *hep-ph/0602031*, 2006.

[97] D. Gillberg. Heavy flavour removal and determination of weighting factors for ALPGEN w+jets monte carlo. *DØ Note*, **5129**, 2006.

[98] Y. Fisyak and J. Womersley. D0gstar DØ geant simulation of the total apparatus response. *DØ Note*, **3191**, 1997.

[99] GEANT. CERN library long writeup. Technical Report W5013, CERN, 1994.

[100] N. Kidonakis. Single top quark production at the tevatron: threshold resummation and finite-order soft gluon corrections. *Phys. Rev. D*, 74:114012, 2006.

[101] N. Kidonakis and R. Vogt. Next-to-next-to-leading order soft gluon corrections in top quark hadroproduction. *Phys. Rev. D*, 68:114014, 2003.

[102] T. Nunnemann. The mcfm (n)nlo calculations of the diboson cross sections and their uncertainties, MCFM version 3.4.5. http://www-clued0.fnal.gov/~nunne/cross-sections/mcfm_cross-sections.html.

[103] E. Barberis et. al. The matrix method and its error calculation. *DØ Note*, **4564**, 2004.

[104] R. Schwienhorst and E. Perez. Uncertainty calculation for combined w+jets and qcd backgrounds in analyses with w+jets signatures. *DØ Note*, **4597**, 2004.

[105] V.M. Abazov et al. Evidence for production of single top quarks. *Phys. Rev. D*, **78**:012005, 2008.

[106] N. Makovec and J.-F. Grivaz. Shifting, smearing and removing simulated jets. *DØ Note*, **4914**, 2005.

[107] DØ V+jets group web page, 2008. https://plone4.fnal.gov/P1/D0Wiki/physics/VplusJets/

[108] CVS repository V+jets group, 2008. http://cdcvs0.fnal.gov/cgi-bin/public-cvs/cvsweb-public.cgi/vjets_cafe/?cvsroot=d0cvs.

[109] H. Schellman. Run iib longitudinal beam shape. *DØ Note*, **5540**, 2007.

[110] H. Schellman. The longitudinal shape of the luminous region at DØ. *DØ Note*, **5142**, 2006.

[111] V.M. Abazov et. al. Measurement of the shape of the boson rapidity distribution for $p\bar{p} \rightarrow Z/gamma^* \rightarrow e^+e^- + X$ events produced at $\sqrt{s}$ of 1.96-TeV. *Phys. Rev.*, D76:012003, 2007.

[112] M. Shamim and T. Bolton. z p_t reweight. *DØ Note*, **5565**, 2008.

[113] S. Muanza. A compilation of mcfm v5.1 cross section. *DØ Note*, **5406**, 2007.

[114] Y. Peters et. al. Study of the w+jets heavy flavor scale factor in p17. *DØ Note*, **5300**, 2006.

[115] D. Bowser-Chao and D.L. Dzialo. Comparison of the use of binary decision trees and neural networks. *Phys. Rev. D*, **47**:1900, 1993.

[116] L. Breiman, J. Friedman, C.J. Stone, and R.A. Olshen. *Classification and Regression Trees*. Wadsworth, Stamford, 1984.

[117] R. Tibshirani T. Hastie and J. Friedman. *The elements of statistical learning: data mining, inference, and prediction.* Springer, 2001.

[118] C. Gini. Variabilità e mutabilità. *Memorie di Metodologica Statistica*, 1912.

[119] B.P. Roe, H.-J. Yang, J. Zhu, Y. Liu, I. Stancu, and G. McGregor. Boosted decision trees as an alternative to artificial neural networks for particle identification. *Nucl. Instr. and Meth. A*, **543**:577, 2005.

[120] Kearns. M. Thoughts on hypothesis boosting, 1988. Unpublished manuscript.

[121] H.-J. Yang, B.P. Roe, and J. Zhu. Studies of boosted decision trees for miniboone particle identification. *Nucl. Instr. and Meth. A*, **555**:370, 2005.

[122] Y. Freund and R.E. Schapire. Experiments with a new boosting algorithm. *Machine Learning: Proceedings of the Thirteenth International Conference*, 148, 1996.

[123] Y. Freund and R.E. Schapire. A decision-theoretic generalization of on-line learning and an application to boosting. *Journal of computer system sciences*, **55**:119, 1997.

[124] R. E. Schapire. The boosting approach to machine learning an overview. *MSRI Workshop on Nonlinear Estimation and Classification, 2002*, 2002.

[125] E. Boos and L. Dudko. Optimized neural networks to search for higgs boson production at the tevatron. *Nucl. Instr. and Meth. A*, **502**:486, 2003.

[126] L. Dudko. Use of neural networks in a search for single top quark production 'at DØ. *AIP Conf. Proc.*, **583**:83, 2001.

[127] ROOT A Data Analysis Framework, 2008. http://root.cern.ch.

[128] N. Kidonakis and R. Vogt. Theoretical top quark cross section at the Fermilab Tevatron and the CERN LHC. *PRD*, 78(7):074005, October 2008.

[129] H. Schellman. The longitudinal shape of the luminous region at DØ. *DØ Note*, **5142**, 2006.

[130] H. Schellman. Run iib longitudinal beam shape. *DØ Note*, **5540**, 2007.

[131] Y. Peters, M. Begel, K. Hamacher, , and D. Wicke. Reweighting of the fragmentation function for the DØ monte carlo. *DØ Note*, **5325**, 2007.

[132] The Single Top Working Group. Observation of single top quark production in 2.3 fb$^-$1 of data using boosted decision trees. *DØ Note*, **5812**, 2009.

[133] The Single Top Working Group. Observation of single top quark production using the matrix element analysis technique in 2.3 fb^{-1} of data. *DØ Note*, **5811**, 2009.

[134] R. Schwienhorst Private communication

[135] R. Schwienhorst et. al. Statistical methods implemented in the package `top_statistics`. *DØ Note*, **5817**, 2008.

[136] S. Jain et. al. Computing limits using a bayesian approach in the package `top_statistics`. *DØ Note*, **5123**, 2006.

[137] I. Bertram et. al. A recipe for construction of confidence limits. *FERMILAB-*, **TM-2104**, 2000.

[138] S. Jain and H.B. Prosper. Analysis optimizations using bayes factors. *DØ Note*, **5260**, 2008.

[139] The Single Top Working Group. Combination of three single top quark cross section measurements from 2.3 fb^{-1} of data using a bayesian neural network. *DØ Note*, **5814**, 2009.

[140] *Tevatron Run II Handbook.*
`http://www-bd.fnal.gov/lug/`

[141] V.M. Abazov, *et al.*, Nucl. Instrum. and Methods **A 565**, 463 (2006).

[142] *The Tevatron Run II Upgrade Project.*
`http://www-bd.fnal.gov/run2upgrade/`

[143] R. Lipton, Nucl. Instrum. and Methods **A 566**, 104 (2006); M. Weber, Nucl. Instrum. and Methods **A 566**, 182 (2006).

[144] M. Abolins, *et al.*, IEEE Trans. on Nucl. Sci. **51**, 340 (2004).

[145] S. Abachi, *et al.*, Nucl. Instrum. and Methods **A 338**, 185 (1994).

[146] The right-handed D0 coordinate system is defined with the z-axis in the direction of the proton beam, with ϕ measuring the azimuthal angle in the plane transverse to the beam direction, with θ measuring the polar angle, and with the pseudo-rapidity, $\eta = -\ln[\tan(\theta/2)]$.

[147] M. Abolins, D. Edmunds, P. Laurens and B. Pi , Nucl. Instrum. and Methods **A 289**, 543 (1990).

[148] see for example:
the ATLAS Level-1 Trigger Group, *ATLAS Level-1 Trigger Technical Design Report*, `http://atlas.web.cern.ch/Atlas/GROUPS/DAQTRIG/TDR/tdr.html`
ATLAS TDR-12 (1998).
the CMS Collaboration, *The TriDAS Project Technical Design Report, Vol. 1: The Trigger Systems*,
`http://cmsdoc.cern.ch/cms/TDR/TRIGGER-public/trigger.html`,
CERN/LHCC 2000-38 (2000).
J. Alitti, *et al.*, Z. Phys. **C49**, 17 (1991).

[149] The D0 collaboration, *Run IIb Upgrade Technical Design Report*, Fermilab-Pub-02/327-E (2002).

[150] WIENER, Plein & Bauss Ltd.
`http://www.wiener-us.com/`

[151] 3M Corporation, Pleated foil shielded cable (90211 Series)
`http://www.3m.com`

[152] Analog Devices, 10-Bit 40 MSPS 3 V Dual A/D Converter (AD9218BST-40)
`http://www.analog.com`

[153] Xilinx, Virtex-II FPGA (XC2V1000-4FG456C)
`http://www.xilinx.com/`

[154] National Semiconductor, 48-bit Channel Link SER/DES (DS90CR483/4)
`http://www.national.com`

[155] W. L. Gore & Associates, Inc., Eye-Opener Millipacs 2 / Z-Pack 2mm HM Cable Connector (2MMS02xx)
`http://www.gore.com`

[156] Altera, Stratix Device Family (EP1Sxx)
`http://www.altera.com`
(EP1S20F780C7, EP1S20F780C6, EP1S10F780C6, and EP1S30F1020C6 devices are used for the TAB SWA, TAB global, GAB LVDS and GAB S30 FPGAs, respectively.)

[157] Agilent Technologies, Transmit/Receive Chip Set (HDMP-1022)
`http://www.agilent.com`
Stratos Optical Technologies, Optical Gbit Dual Transmitter (M2T-25-4-1-L)
`http://www.stratoslightwave.com`

[158] Altera, Cyclone Device Family (EP1C6Q240C7)
`http://www.altera.com`

[159] Altera, Serial Configuration Device (EPCS4SI8)
`http://www.altera.com`

[160] Cypress Semiconductor Corporation, Clock Distribution Buffer (CY29948AI)
`http://www.cypress.com`

[161] Fairchild Semiconductor, TTL to ECL Converter (FDLL4148)
`http://www.fairchildsemi.com`

[162] National Semiconductor, Differential Line Drivers/Receivers (DS90LV047/8 ATMTC) `http://www.national.com`

[163] As currently implemented the North, Central and South regions correspond to $3.2 < \eta < 1.0$, $1.0 < \eta < -1.0$, and $-1.0 < \eta < 3.2$, respectively.

[164] Altera, ACEX 1K Series FPGA (EP1K50QC208-2)
http://www.altera.com

[165] Because of the extra latency involved in the divide operation necessary for the calculation of the Tau algorithm isolation, this information is not available in time for transmission to the L1CalTrk system.

[166] GE Fanuc Embedded Systems, PCI to VME bus adapter (Model 618)
http://www.gefanucembedded.com

[167] *Vertical Interface Board Documentation.*
http://www-linac.fnal.gov/LINAC/hardware/vmesys/boards/vi/viInfo.html

[168] Python Programming Language – Official Website.
http://www.python.org

[169] TkInter Documentation Website.
http://wiki.python.org/moin/TkInter

[170] W3C: Extensible Markup Language Website.
http://www.w3.org/XML/

[171] The ADAPTIVE Communication Environment Website.
http://www.cs.wustl.edu/~schmidt/ACE.html

[172] R. Brun, *et al.*, *ROOT: An Object-Oriented Data Analysis Framework.*
http://root.cern.ch/root/

MICHIGAN STATE UNIVERSITY LIBRARIES
3 1293 03063 0903